Search for Supersymmetry in the 1-Lepton plus Jets Final States with the ATLAS Detector

von

Pedro Salvador Urrejola Pereira

Dissertation
zur Erlangung des Grades

DOKTOR DER NATURWISSENSCHAFTEN

vorgelegt dem

Fachbereich Physik, Mathematik und Informatik
der
Johannes Gutenberg-Universität Mainz

Mainz, den 11.02.2020

Datum der mündlichen Prüfung: 10.02.2020

Abstract

The LHC remarkable 7 and 8 TeV data taking campaigns were used to test precision measurements for standard model processes, search for physics beyond SM and for the search and consequent discovery of the higgs boson. After 2012 the LHC prepared for its first long shutdown during which the hardware and software of the machine were upgraded and prepared for the next runs at higher energies and collision rates. In 2015 the LHC started collecting data from 13 TeV center of mass proton proton collisions every 25 ns, reaching a peak luminosity of 5×10^{33} cm$^{-2}s^{-1}$ and a total delivered luminosity of 4.2 fb^{-1}.

This document presents searches for Supersymmetry in the final states with one lepton, jets and missing transverse energy. The analyses uses statistically independent control regions to control dominant Standard Model backgrounds, signal regions to probe for possible supersymmetric events and validation regions for validation purposes. A simultaneous fit to data normalizes the main backgrounds in the control regions using a profile likelihood method for precise background estimates in the signal regions.

The results and interpretation of 8 TeV one lepton analysis were re-interpreted in a much general supersymmetric framework as the phenomenological Supersymmetric Standard Model (pMSSM). The re-interpretation results were combined with the results from many other searches to cover all reachable regions of the phase space. The ATLAS analyses constrain to strong pMSSM production showed that all models with gluino masses below 700 GeV can be excluded. For models with neutralino LSP masses below 500 GeV, the previous limit extends to 1 TeV. For the models that could not be excluded by any of the searches, a study was done looking for blind spots in the parameter space, that could be covered by one lepton searches. The results showed that in most of the cases the leptons came from secondary channels, confirming that searches with no hard leptons are the most sensitive among a vast region of the phase space.

The document also presents the results of the ATLAS one lepton analysis using the full 2015 dataset at 13 TeV. The search was optimized for a simplified signal model assuming direct gluino pair production, both decaying in via lightest chargino to the lightest neutralino with 100% BR. The results were consistent with the null hypothesis and were interpreted as model independent upper limits, and as 95% CL exclusion limits for the gluino simplified models. The new limits extend the reach of previous searches in different regions. For low neutralino LSP masses, gluino masses of up to 1.6 TeV can be excluded, while for compressed scenarios gluino masses of only up to 870 GeVcan be excluded.

Kurzfassung

Die ausgezeichneten LHC Kampagnen bei 7 und 8 TeV wurden verwendet, um Präzisionsmessungen von Standardmodellprozesse durchzuführen, um Physik jenseits des SM zu suchen und um die Suche und anschließende Entdeckung des Higgs-Bosons zu machen. Nach 2012 bereitete sich der LHC auf seine erste lange Abschaltung vor, bei dem die Hardware und Software der Maschine für den nächsten Run mit höherer Energien und Kollisionsraten aktualisiert und vorbereitet wurden. Im Jahr 2015 begann der LHC Proton-Proton-Kollisionen bei einer Schwerpunktsenergie von 13 TeV und einer Rate von 25 ns zu sammeln und erreichete einer gelieferte integrierten Luminosität von insgesamt 4.2 fb^{-1} und eine instantanen Luminosität von 5×10^{33} $\text{cm}^{-2}s^{-1}$

In dieser Arbeit wird eine Suche nach Supersymmetrie mit einem Lepton, Jets und fehlender Transversalenergie vorgestellt. Die Analysen verwenden statistisch unabhängige Kontrollregionen, um dominante Standardmodell-Untergründe zu kontrollieren, Signalregionen, um nach möglichen supersymmetrischen Ereignissen zu suchen, und Validierungsregionen für Validierungszwecke. Eine simultane Anpassung normiert die Haupthuntergründe in den Kontrollregionen mit Hilfe einer Profile-Likelihood Methode für eine präzise Untergrunderwartung in den Signalregionen.

Die Ergebnisse und die Interpretation der 8 TeV 1-Lepton-Analyse wurden in Rahmen eines allgemeinen, supersymmetrischen Modells als die *phenomenological Supersymmetric Standard Model* (pMSSM) neu interpretiert. Die Ergebnisse der Neuinterpretation wurden mit den Ergebnissen anderer Suchen kombiniert, um einen möglichst großen Bereich des Phasenraums abzudecken. Die ATLAS Analysen schränken die starke pMSSM Produktion ein, sodass alle Modelle mit Gluino Massen unter 700 GeV ausgeschlossen werden können. Für Modelle mit Neutralino LSP Massen unter 500 GeV die vorherige Grenze steigt bis zum 1 TeV. Für jene Modelle, die durch keine der Suchen ausgeschlossen werden konnten, wird eine weitere Studie durchgeführt. Die Studie sucht nach Bereichen im Parameterraum, die mit dieser 1 Lepton Suchen abgedeckt werden könnten. Die Ergebnisse zeigten, dass die Leptonen in den meisten verbleibenden Modelle aus sekundären Kanälen heraus kommen. Dies bestätigt, dass Suchen ohne *harte* Leptonen in einem weiten Bereich des Phasenraums am sensitivsten sind.

In dieser Arbeit werden auch die Ergebnisse der ATLAS 1 Lepton Analyse mit dem vollem 2015 Datensatz bei 13 TeV präsentiert. Die Suche wurde für ein vereinfachtes Signalmodell optimiert, das direkte Paarproduktion von Gluinos voraussetzt, wobei beide Gluinos über das leichteste Chargino zum leichtesten Neutralino mit 100% BR zerfallen. Die beobachteten Daten stimmten mit der Nullhypothese überein und wurden als modellunabhängige Obergrenzen und als Ausschlussgrenzen in den betrachteten Regionen interpretiert. Diese neuen Grenzen reichen weiter als die von den vorherigen Suchen in verschiedenen Regionen. Bei niedrigen Neutralino LSP Massen können Gluino Massen bis zu 1, 6 TeV ausgeschlossen werden, während bei komprimierten Szenarien Gluino Massen nur bis zu 870 GeV ausgeschlossen werden können.

Contents

Introduction

Describing nature and the changes we see in it has been a long lasting and still open quest for the human being. The pre-Socratic Greek philosophers called natural philosophers were one of the first known thinkers trying to understand nature avoiding the usual mythological explanations, possibly setting the first stones for the independence of science from religion. They might have been the first people exploring the concepts of matter and its fundamental constituents[1]. Probably the only or at least most cited atomist in physics papers is Democritus (460-370 BC), he supposed that *everything* was built by tiny and invisible pieces that were unalterable and eternal. He called such pieces *atoms* which means indivisible. Between these atoms there was presumed an infinite void or vacuum, that he considered to be necessary for local motion. Another crucial characteristic of Democritus atoms, besides their indivisibility and eternity was diversity. There were different types of atoms, so they could be used to create different objects and beings including earth, water, fire, air and everything including himself. After an object disintegrate, its atoms would disperse and could be used to build something else.

Among the pre-Socratic there were different theories, but theirs was only an abstract debate as no real evidence of their conjectures could be proven. Many centuries needed to pass until several advances in philosophy, mathematics and optics from the eastern world migrated to the western world, together with the creation of new technical equipment such as the telescope or the vacuum pump and the idea that such experimental devices are as valid as simple observation when studying nature, pavemented the way for the Renaissance. The works of Alhazen, Fakhr al-Din al-Razi, Roger Bacon, Leonardo Da Vinci, Nicolas Copernicus, Galileo Galilei, Rene Descartes, Johannes Keppler, Robert Boyle and Isaac Newton between many others during the first half of the second millennium of the present era finally put an end to the Aristotelian era giving science and the study of nature a complete new meaning to society. Such a revolution improved drastically the way of making science, including experimental technology as the main tool for it, changing radically our conception of matter, its constituents and interactions.

After two millenniums John Dalton (1766-1844) revisited the concept of the atom. He studied the gases and its properties following the work of Robert Boyle (1627-1691) and his law of gases (Boyle's Law), Lavoiser's law of conservation of mass and Proust's law of definite proportions. Dalton thought that gases must consist of small particles. He used the name atom to name these tiny particles of matter. Dalton's theory held that every substance is composed of atoms in different proportions and that all atoms of one element were identical and different to the atoms of other elements. He also stated that each atom differed from other atoms in its mass. In the XIX century many more elements were discovered and a new classification different to the one proposed early by Lavoiser was needed. Many philosophers, chemists, physicist, and thinkers, helped to the development of new ideas, theories and laws. One of them was Dimitri Mendeleev (1834-1907) commonly credited for the creation of the

[1]The concept of fundamental constituents will be used in this text as the basic blocks of all known matter that cannot be further divided

modern periodic table in which elements are ordered in different periodic groups related to their properties. One of the biggest breakthrough it was the removal of the *Caloric* as an element, after the first law of thermodynamics replaced the old caloric theory. Mendeleev was able to put order to Dalton's atomic theory allowing him to correct individual atomic weights and to identify empty places for not yet discovered elements such as Galium and Germanium.

The indivisibility of Dalton's atom did not to last for long. After discovering the electron in the 1890's, using cathode ray tubes, Joseph John Thomson (1856-1940) postulated its Plum-pudding model that pictured atom as an homogeneously positive charged sphere, with tiny negatively charged electrons like plums in a pudding. But Thomson's model was also not to last, as around 1911 one of the most important experiments performed by Ernest Rutherford (1871-1937) contradicted Thomson's results. The Rutherford experiment consisted in bombarding a thin film of gold foil with a beam of α particles coming from recently discovered radioactive material. The experimental results showed that most of the α particles passed trough the foil almost unaffected, while few of them being deflected from their original trajectory. From the deflected particles, few of them were deflected in at very large angles, including particles to scatter back in the direction from where they came. The only possible explanation was that the atom consisted in on a tiny positively charged nucleus where almost all of the atoms mass was contained, surrounded by very light and tiny electrons orbiting around the nucleus. This model was one of the greatest breakthrough in the quest for describing nature and its constituents, however its tested to have deep theoretical problems. The biggest problem is that if the electrons orbit like planets, they must be accelerated and thus must emit electromagnetic radiation, making them loose energy, and eventually fall into the nucleus, making this a very unstable atom.

With the rising of the quantum theory in the early 1900s by the hand of many researchers as Max Plank, Albert Einstein, Niels Bohr, Louis de Broglie, Werner Heisenberg and many others the picture of the atom we have today has changed quite a lot. Even though Rutherford's atom idea was proven incorrect, it was the last classical explanation to the modeling of the atom. Todays atom may only be explained and interpreted using a non classical non deterministic explanation based on quantum physics, where the nucleus is quite similar to Rutherford's nucleus, but where electrons are only likely to be found within different volumes of space called orbitals. The complexity of the explanation of the quantum model of the atom, has made it rather difficult to remove the classical and simpler Rutherford's model from the minds of people not close to scientific research. For some years it was thought that the newly discovered tiny nucleus was now one fundamental piece just as the electron, but it was not until the discovery of the neutron in 1932 by James Chadwick that this idea was proven wrong.

The neutron was soon to be used as a new experimental tool to test the nuclear structure. Bombarding nucleus with neutrons, which were not affected by electric interactions, helped probing the nucleus much deeper. This lead quickly to the fission of uranium atoms, and to discovery of new radioactive elements during the 30's. Further discoveries in the 30s and 40s including the discovery of pions from cosmic rays, together with the arrival of the first high energy particle accelerators led to the discovery of many different hadron and resonances during the 50s and 60s. In the 60s a quark model was proposed independently by Murray Gell-Mann and George Zweig as a theoretical way of naturally ordering the particle zoo composed by all these new discovered hadrons, proposing that protons might not be elementary particles. But it was not until the late 60s and 70s when deep inelastic scattering experiments at the Stanford Linear Accelerator Center helped probing the protons even deeper by smashing electrons against protons. Deep inelastic scattering experiments proved not only that protons had an internal structure, additionally the experiments helped understanding the behavior of these internal particles when interacting with the electron. The higher the energy of the probing electron, the more complex the structure of the proton

appear. Deep inelastic scattering experiments can be thought as extensions of the Rutherford's experiment, but with much higher relative energy between the scattered particles, refining the resolution at which the nucleus structure is tested. Deep inelastic scattering helped building the parton distribution functions, that quantize the fraction of energy taken by a proton constituent in a collision. The previous experiments paved the way for a variety of very powerful particle colliders such as the Tevatron at Fermilab in Batavia-USA, LEP at CERN in Geneva-Switzerland, the HERA at DESY in Hamburg Germany, KEKB at KEK in Tsukuba-Japan, RHIC at the Brookhaven National Laboratory in USA between others. With this accelerators and their detectors, new composite and elemental particles were discovered, and the interactions between them started to be better understood. On the theory side, all these discoveries were summarized during the second half of the 20th century within the Standard Model (SM) of particle physics, a model developed in several stages by many scientists around the world. The standard model predicted the existence of new fundamental particles that were not discovered yet, and gained more credibility in the dawn of the 20th century after the discovery of the top quark by the CDF and DØ experiments at Fermilab in 1995 and the discovery of the tau neutrino by the DONUT experiment also at Fermilab in 2000.

With the discovery of the top and the tau neutrino, the particle content of the model was almost completely discovered by experiments. The only remaining particle to be discovered was the higgs boson. The higgs boson, was introduced to the standard model as a theoretical tool to elegantly explain the generation of mass of the fundamental particles without violating gauge symmetry. The higgs particle was finally discovered independently by the ATLAS and CMS experiments in the Large Hadron Collider in 2012. The discovery of the higgs particle closed a chapter in the history of the SM as all the predicted fundamental particles have now been discovered. Nevertheless there are still some open questions within the SM, such as where do neutrino masses come from, what is the nature of dark matter and dark energy, or why is the weak force is several orders of magnitude as strong as gravity. One of the preferred beyond the standard model theory among physicists is Supersymmetry (SUSY) that postulates a symmetry between matter and its interactions. SUSY can deliver theoretical solutions to many of the SM problems. One of the major goals of the LHC, and of previous and future particle accelerators, was to find evidence of new physics including SUSY. The LHC can be also thought as a tool that probe even deeper the proton structure, but is also used for additional general purpose research. In this thesis an emphasis is given to the search of SUSY in final states containing one lepton, jets and missing transverse energy using the ATLAS detector. The results proved to be consistent with the SM predictions and thus have been interpreted to set limits on possible SUSY parameters such as the masses of hypothetical supersymmetric particles. There are still many open questions that go even beyond the particle physics realm. History has proven that each answer comes with new questions and that human knowledge is always changing and evolving. The quest of describing nature and the changes we see in it is far from over.

Chapter 1

The Standard Model

The Standard Model (SM) of particle physics provides the most accurate description for the electromagnetic, weak and strong interactions. To include such interactions accurately, the Lorentz invariant lagrangian is built to be invariant under the $SU(3)_C \times SU(2)_L \times U(1)_Y$ gauge symmetry group. The subscripts C (*Color*), L (*Left*) and Y (*hYpercharge*) relate to how these interactions manifest.

1.1 The Standard Model particle spectrum

The SM describes in a simple way the nature of quantum interactions between all fundamental particles known so far. Some of these particles like the electron, were discovered before the existence of the model. Others were initially included as a theoretical need and were experimentally discovered decades later. These particles are classified according to their properties and behavior. There are 12 matter fields with half-unit spin called *fermions*. 12 gauge or interaction fields with spin 1 called gauge *bosons*, which are often referred as mediators. There is one additional spin 0 scalar field called the Higgs boson.

Generation	I	II	III
Quarks	up u $m_u = 2.3^{+0.7}_{-0.5}$ MeV	charm c $m_c = 1.275 \pm 0.025$ GeV	top t $m_t = 173.21 \pm 0.51 \pm 0.71$ GeV
	down d $m_d = 4.8^{+0.5}_{-0.3}$ MeV	strange s $m_s = 95 \pm 5$ MeV	bottom b $m_b = 4.18 \pm 0.03$ GeV
Leptons	neutrino e ν_e $m_{\nu_e} < 2$ eV	neutrino mu ν_μ $m_{\nu_\mu} < 0.19$ MeV	neutrino tau ν_τ $m_{\nu_\tau} < 18.2$ MeV
	electron e $m_e = 0.511$ MeV	muon μ $m_\mu = 105.658$ MeV	tau τ $m_\tau = 1776.86 \pm 0.12$ MeV

`Table 1.1:` The 12 elementary fermions that conform matter grouped by generation. The particle masses are included [1].

photon	Z-boson	W-boson	gluon	Higgs
γ	Z	$W^{\pm}$	g	h
$m_\gamma = 0$ eV	$m_Z = 91.188 \pm 0.098$GeV	$m_W = 80.385 \pm 0.015$GeV	$m_g = 0$eV	$m_h = 126.0 \pm 0.4$GeV

`Table 1.2:` SM interaction boson fields with their masses. [1]. All gauge bosons have spin 1 while the Higgs boson has spin 0

The 12 fermions and their antiparticles[1] are the constituents of all the known matter. Astronomical observations [5] show however, that ordinary matter adds up to only 5% of the total content of the universe. The remaining 95% is still unknown and is usually called "Dark Matter" and "Dark Energy". The fermion group can be further divided into two subgroups: *Leptons* and *quarks*. Leptons do not interact via the strong interaction while quarks do. This difference is crucial to understand the behavior of quarks at low energies. One example is quark confinement, which makes it impossible to find free quarks at low energies. Instead they appear in bound states called *hadrons*. There are 2 types of hadrons: *Mesons* which are bound states of a quark and an antiquark and *baryons* that are bound states of three quarks[2]. All fermions can be organized in three generations sharing the same quantum numbers. A schematic representation of all fermions arranged by generations is shown in Table 1.1.

The 12 gauge eigenstates or interaction particles are: One gauge boson B from $U(1)_Y$. Three gauge bosons W from $SU(2)_L$. Eight gauge bosons G from $SU(3)_C$. The mixing of B and the neutral W boson produces two electrically neutral mass eigenstates: The photon γ, and the Z boson. The two remaining electrically charged W gauge bosons mix to produce the two charged mass eigenstates W^+ and W^-.

The Higgs boson, is the remaining massive eigenstate of the Higgs gauge scalar field, that was introduced to the SM to give mass to all massive particles of the SM. Initially the Higgs mechanism, that will be discussed in detail in section 1.3, was a theoretical solution to the mass problem of the SM. Later in August 2012 both ATLAS and CMS collaborations published the discovery of a new particle compatible to the SM Higgs boson. A schematic representation of all gauge boson mass eigenstates plus the Higgs boson is presented in Table 1.2.

1.2 The Standard Model interactions

The SM describes the physics between fundamental particles including three fundamental interactions: Strong interactions described by Quantum Chromodynamics (QCD) plus electromagnetic and weak interactions which are described by the electroweak theory (EW). It also includes fermion and gauge boson interactions with the Higgs sector. The SM lagrangian can be written in the form:

$$\mathcal{L}_{SM} = \mathcal{L}_{QCD} + \mathcal{L}_{EW} + \mathcal{L}_{Higgs} + \mathcal{L}_{Yukawa}. \tag{1.1}$$

Each term of the lagrangian above will be explained in the following sections.

[1] For neutrinos, the difference between particle and antiparticle depends on the treatment given. Two possible representations exist: Majorana neutrinos where both neutrino and antineutrino are the same particle, and Dirac Neutrinos where the antineutrino is a different particle. In the SM neutrinos are treated as massless Dirac neutrinos. Evidence on neutrino oscillations [2–4] introduce the need for massive neutrinos, making this ambivalence much more interesting, as the method to include a mass in each case would imply distinct underlying physics.

[2] In the last years physicists have detected new combinations of quark arrangement; tetra-quarks and penta-quarks, that are groups of 4 and 5 quarks respectively [6].

1.2.1 Electroweak interactions

Electricity and magnetism were initially seen and considered as two unrelated phenomena. Centuries later both phenomena were unified under the electromagnetic theory thanks to the work done by Faraday and Maxwell among many others. This unification closely resembles to what occurred later with electromagnetism and weak interactions, which were unified under the electroweak theory by Glashow, Salam and Weinberg in 1967 in the GSW theory [7].

Writing a relativistic quantum field theory of electrodynamics was accomplished by Dirac in 1927 with the foundation of Quantum Electrodynamics (QED) [8]. Assuming the existence of only one massive lepton (electron), and one massless gauge boson (photon), a lagrangian invariant under the Lorentz and $U(1)_{EM}$ transformations can be written without breaking Lorenz or $U(1)_{EM}$ symmetry. In the QED lagrangian, electrons are written as Dirac spinors while photons are inserted as a massless gauge bosons via minimal coupling to electrons in the covariant derivative, requiring local gauge invariance. But the SM must contain also massive bosons to account for weak interactions plus massless leptons for the neutrinos[3] making impossible to directly write an invariant lagragian.

As no right-handed neutrinos have yet been found, charge symmetry (C) must be broken. Also the results found by Chien-Shiung Wu in 1957 [9] on parity symmetry (P) violation in β decays, helped to understand the chiral nature of weak interactions. Years later, Christenson, Cronin, Fitch and Turlay [10] in year 1964 found the first evidence of CP violation in the decay of K^0 mesons. The nature of these discrete symmetries are explicit in the SM lagrangian density, which is written in terms of chiral fields, where the charged W bosons couple only to particles with left-handed chirality or to antiparticles with right-handed chirality[4]. To achieve this, left handed fields are written in $SU(2)_L$ doublets while right handed fields are written as $SU(2)_L$ singlets. As quarks also experience EW interactions, they are also represented in left doublets and right singlets. The chiral representation of leptons and quarks can be seen in Table 1.3.

Generation	I	II	III
Quarks	$\begin{pmatrix} u^i \\ d^i \end{pmatrix}_L$	$\begin{pmatrix} c^i \\ s^i \end{pmatrix}_L$	$\begin{pmatrix} t^i \\ b^i \end{pmatrix}_L$
	$u^i_R\ ,\ d^i_R$	$c^i_R\ ,\ s^i_R$	$t^i_R\ ,\ b^i_R$
Leptons	$\begin{pmatrix} \nu_e \\ e \end{pmatrix}_L$	$\begin{pmatrix} \nu_\mu \\ \mu \end{pmatrix}_L$	$\begin{pmatrix} \nu_\tau \\ \tau \end{pmatrix}_L$
	e_R	μ_R	τ_R

`Table 1.3:` Table with the left and right handed components of the SM fermions. The table shows only first generation particles. Similar notation is defined for antiparticles and for the second and third generations as well. The i sub-index included for quarks, is related to the color charge that will be explained in the next chapter.

[3] By the time the SM was developed, neutrinos were considered as massless particles. Today there is strong evidence for the existence of neutrino masses [2–4]

[4] For massless particles chirality and helicity are the same: For a left-handed massless particle the spin is oriented against the direction of motion while right-handed stands for the opposite. Helicity can be defined as the sign of the projection of the spin on the momentum direction. Chirality is harder to define and for the scope of this document it will be said that it is similar to helicity but just as mass, charge or spin it is inherent to the particle. This means that it is not modified by any change of reference frame, contrary to helicity. For a Dirac field chirality is defined using the γ_5 operator which has eigenvalues $+1$ and -1. A Dirac field can be projected on its left or right handed component using the left or right operators: $P_L = \frac{1}{2}(1-\gamma_5)$ and $P_R = \frac{1}{2}(1+\gamma_5)$

To simplify the notation, the doublets can be redefined as it follows:

$$\begin{aligned} L &= \begin{pmatrix} \nu_e \\ e \end{pmatrix}_L \qquad R = e_{_R} \\ Q &= \begin{pmatrix} u \\ d \end{pmatrix}_L \qquad U = u_{_R} \qquad D = d_{_R} \end{aligned} \tag{1.2}$$

An analogue notation is defined for second and third generation particles. As for EW interactions color charge plays no role, the i sub-index for the quark sector has been intentionally omitted. Note that L is a $SU(2)_L$ doublet while R is a singlet. Nevertheless each component is a two components Weil spinors, building the four components Dirac spinors:

$$\begin{aligned} L &= \begin{pmatrix} \nu_e \\ e \end{pmatrix}_L = \begin{pmatrix} \nu_{e_{_L}} \\ e_{_L} \end{pmatrix} \\ R &= e_{_R} \end{aligned} \tag{1.3}$$

where $e_{_L}$, $\nu_{e_{_L}}$ and $e_{_R}$ are the Weil spinors defined as:

$$\begin{aligned} e_{_L} \equiv P_{_L} e = \frac{1}{2}(1-\gamma_5)e = \begin{pmatrix} e_{_L} \\ 0 \end{pmatrix} \\ \nu_{e_{_L}} \equiv P_{_L} \nu = \frac{1}{2}(1-\gamma_5)\nu_e = \begin{pmatrix} \nu_{e_{_L}} \\ 0 \end{pmatrix} \\ e_{_R} \equiv P_{_R} e = \frac{1}{2}(1+\gamma_5)e = \begin{pmatrix} 0 \\ e_{_R} \end{pmatrix} \end{aligned} \tag{1.4}$$

With such representation it is impossible to write explicit mass terms for the fermions in the lagrangian as they are either gauge or Lorentz violating. Instead, the weak and electromagnetic interactions are unified in a $SU(2)_L \times U(1)_Y$ gauge invariant lagrangian, where all fermion and boson fields are massless. Fermion and boson masses are spontaneously acquired via the Higgs mechanism after electroweak symmetry breaking (EWSB) as discussed in chapter 1.3. Using the chiral representation, the lagrangian for electroweak interactions is written as follows:

$$\mathcal{L}_{EW} = \mathcal{L}_{Gauge} + \mathcal{L}_{Fermion}, \tag{1.5}$$

whith:

$$\mathcal{L}_{Gauge} = -\frac{1}{4} B_{\mu\nu} B^{\mu\nu} - \frac{1}{4} W^a_{\mu\nu} W^{\mu\nu}_a \tag{1.6}$$

and where $B_{\mu\nu}$ and $W^a_{\mu\nu}$ are the strength tensors associated to $U(1)_Y$ and $SU(2)_L$ respectively, where $a = 0, 1, 2$. Due to the noncommutative nature of $SU(2)_L$, the $W^a_{\mu\nu}$ tensor contains a self interaction term. Both terms are defined as follows:

$$B_{\mu\nu} = \partial_\mu B_\nu - \partial_\nu B_\mu \tag{1.7}$$

$$W^a_{\mu\nu} = \partial_\mu W^a_\nu - \partial_\nu W^a_\mu - g\epsilon_{abc} W^b_\mu W^c_\mu, \tag{1.8}$$

where g is the gauge coupling constant associated to $SU(2)_L$ and ϵ_{abc} is the antisymmetric or Levi-Civita tensor. The last term in the definition of $W^a_{\mu\nu}$ is responsible for trilinear and quartic self interactions of the W^a bosons.

On the other hand, the fermion part of the lagrangian (omitting the second and third generation for simplicity) has the following structure:

$$\begin{aligned} \mathcal{L}_{Fermion} &= i\overline{L}\gamma^\mu D^L_\mu L + i\overline{R}\gamma^\mu D^R_\mu R \\ &+ i\overline{Q}\gamma^\mu D^L_\mu Q + i\overline{U}\gamma^\mu D^R_\mu U + i\overline{D}\gamma^\mu D^R_\mu D \end{aligned} \tag{1.9}$$

where:

$$\begin{aligned} D_\mu^L L &= [\partial_\mu + \frac{i}{2} Y_{_L} g' B_\mu + \frac{i}{2} g W_\mu^a T^a] L \\ D_\mu^R R &= [\partial_\mu + \frac{i}{2} Y_{_R} g' B_\mu] R \\ D_\mu^L Q &= [\partial_\mu + \frac{i}{2} Y_{_Q} g' B_\mu + \frac{i}{2} g W_\mu^a T^a] Q \\ D_\mu^R U &= [\partial_\mu + \frac{i}{2} Y_{_U} g' B_\mu] U \\ D_\mu^R D &= [\partial_\mu + \frac{i}{2} Y_{_D} g' B_\mu] D. \end{aligned} \tag{1.10}$$

Here, the group structure is explicitly seen. The $U(1)_Y$ generators represented by the hypercharges $Y_{_L} = -1, Y_{_R} = -2, Y_{_Q} = 1/3, Y_{_U} = 4/3, Y_{_D} = -2/3$ are found by calculating the proper lepton and quark charges using the formula $Q = T_3 + Y$, where Q is the electric charge, and T_3 is the third component of the weak isospin ($T_3 = \pm 1/2$ for left handed chirality while $T_3 = 0$ for right handed chirality) The $SU(2)_L$ generators denoted as T^a are usually represented by the Pauli matrices satisfying the relation $[\sigma_a, \sigma_b] = 2i\epsilon_{abc}\sigma_c$. The coupling constants of the B and W bosons to the fermions represented by g' and g are universal within families.

1.2.2 Strong interactions

The strong interaction described by Quantum Chromodynamics (QCD) is the third fundamental interaction included in the SM. QCD can be written as a gauge theory invariant under the $SU(3)_C$ group. Each quark has one of the three types of strong or color charge, namely red, green and blue (r, g, b). Antiquarks have also three types of negative color charge, anti-red, anti-green and anti-blue $(\overline{r}, \overline{g}, \overline{b})$. Color charged particles interact strongly by the exchange of gluons which are massless bosons. Gluons have eight different color charge combinations[5]. As leptons do not carry color charge they do not interact with gluons and take no part in strong interactions. It is important to stress that color charge has no relation with flavor or electric charge, making QCD independent of EW interactions. The QCD lagrangian can be written as:

$$\mathcal{L}_{QCD} = \mathcal{L}_{Gauge} + \mathcal{L}_{Fermion}, \tag{1.11}$$

where:

$$\mathcal{L}_{Gauge} = -\frac{1}{4} G_{\mu\nu}^a G_a^{\mu\nu} \tag{1.12}$$

and $G_{\mu\nu}^a$ is the strength tensor associated to $SU(3)_C$:

$$G_{\mu\nu}^a = \partial_\mu G_\nu^a - \partial_\nu G_\mu^a - g_s f_{abc} G_\mu^b G_\mu^c, \tag{1.13}$$

where g_s is the gauge coupling constant associated to $SU(3)_C$, $a = 0, ..., 7$, and f_{abc} are the structure constants of the group[6]. Analog to $SU(2)_L$, the non commutative nature of $SU(3)_C$ allows trilinear and quartic self interactions terms for the gluons. No mass term is written nor needed as gluons are massless making $SU(3)_C$ a conserved symmetry. The fermionic part of the lagrangian can be written:

[5] $SU(3)$ allows for 9 possible color-anticolor states. Eight are arranged in an octet plus one in a singlet. The singlet is colorless thus cannot be accounted as a gluon carrying color charge

[6] f_{abc} is an antisymmetric tensor. $f_{123} = 1$, $f_{147} = f_{246} = f_{257} = f_{345} = f_{516} = f_{637} = 1/2$ and $f_{458} = f_{678} = \sqrt{3}/2$. The remaining constants are zero.

$$\mathcal{L}_{Fermion} = \overline{q}(i\gamma^\mu \partial_\mu)q - g_s(\overline{q}\gamma^\mu T_a q)G^a_\mu \tag{1.14}$$

where T_a are the $SU(3)_C$ generators. The usual representation takes the form of the Gell-Mann matrices λ_a ($T_a = \lambda_a/2$) with the relation $[\lambda_a, \lambda_b] = 2if_{abc}\lambda_c$. Analog to the lepton case, no mass term for the quarks can be written yet. The g_s coupling constant of gluons to quarks decreases with energy, which bears deep consequences. One is the impossibility to use the perturbative approach when studying QCD at low energies, thus the need for different approaches such as effective theories and the lattice formulation. At higher energies precise calculations using DGLAP [12] are possible and have been proven with excellent accuracy. Such effect is known as asymptotic freedom, meaning that at higher energies quarks interact weaker. Another phenomenon observed is the impossibility to isolate and measure color charge. This is known as quark confinement: If two hadrons (or one hadron and an electron) collide at high energies, one of the composite quarks might be pushed away from its partners in the bound state. The more energy it receives, the further it can be separated from its partners increasing the binding energy. At some point it is more efficient energetically for a pair of quark-antiquark to be produced, resulting in two hadrons. This process is called hadronization and plays a crucial role in hadron colliders. This is also why strong interactions are short ranged despite having massless gauge bosons like gluons as force carriers.

1.3 The Higgs sector, electroweak symmetry breaking and masses

As said before, explicit mass terms for gauge bosons or fermions can not be written in the SM as they violate gauge symmetry. Instead the Higgs sector is introduced to the SM to explain masses in a *natural* and elegant manner. In nature, besides gluons, there are three massive gauge bosons Z and $W^\pm$ plus one massless gauge boson γ. In order for the Higgs mechanism to give mass to the three massive gauge bosons, at least three degrees of freedom (d.o.g.) from the Higgs scalar fields are needed. To achieve that, one charged scalar Higgs doublet, invariant under $SU(2)_L \times U(1)_Y$ is introduced:

$$H = \begin{pmatrix} H^+ \\ H^0 \end{pmatrix} = \frac{1}{\sqrt{2}} \begin{pmatrix} \phi_1 + i\phi_2 \\ \phi_3 + i\phi_4 \end{pmatrix} \tag{1.15}$$

where H^+ and H^0 are complex scalar fields that can be written in terms of its real and complex components, having in total 4 d.o.f. The Higgs Lagrangian can be written as:

$$\mathcal{L}_{Higgs} = (D_\mu H)^\dagger (D^\mu H) - V(H^\dagger H) \tag{1.16}$$

with the covariant derivative defined by:

$$D_\mu = \left(\partial_\mu + \frac{i}{2}g' B_\mu + \frac{i}{2}g W^a_\mu T^a\right) \tag{1.17}$$

and a Higgs potential V given by:

$$V(H^\dagger H) = m^2 H^\dagger H + \lambda (H^\dagger H)^2. \tag{1.18}$$

The parameters in 1.18 need to satisfy $m^2 < 0$ and $\lambda > 0$ for the potential to have the desired shape. The signs of m^2 and λ are chosen arbitrarily to achieve EWSB. The shape of the potential usually called *mexican hat*, is displayed in figure 1.1 for the second component of the doublet H^0.

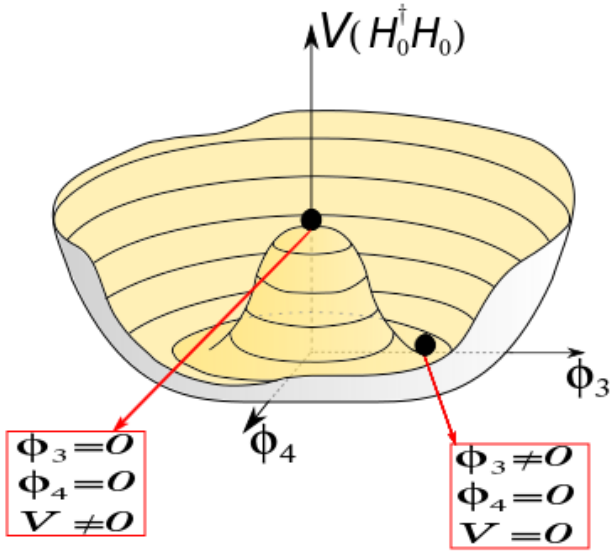

Figure 1.1: Higgs potential. When $\Phi = 0$ the potential is different than zero, while the potential has infinite degenerate minima where $V = 0$. Image based on [11].

If $\lambda < 0$ the potential would have no minimum, so it is required to be positive. If $m^2 > 0$ the potential will always grow with Φ and it would have a trivial minimum for $\Phi = 0$, which is invariant under $SU(2)_L \times U(1)_Y$. If we require $m^2 < 0$ the potential will have the required shape, and it will have a minimum for $\Phi \neq 0$. The minimum is infinite degenerate, in a circle around $\Phi = 0$ and the neutral component will acquire a vacuum expectation value (v.e.v.) represented by v:

$$\langle H \rangle = \frac{1}{\sqrt{2}} \begin{pmatrix} 0 \\ v \end{pmatrix} \tag{1.19}$$

It can be easily noticed that while the lagrangian in 1.16 is invariant under $SU(2)_L \times U(1)_Y$, the vacuum state in 1.19 is not. This is known as spontaneous symmetry breaking, in this case electroweak symmetry breaking (EWSB). The expression for v is found by minimizing the potential and finding the non trivial and stable minimum:

$$\left.\frac{\partial V(\Phi)}{\partial \Phi}\right|_{v/\sqrt{2}} = 2m^2\left(v/\sqrt{2}\right) + 4\lambda\left(v/\sqrt{2}\right)^3 = 0 \quad \Longrightarrow \quad v = \sqrt{\frac{-m^2}{\lambda}} \tag{1.20}$$

To preserve $U(1)_{EM}$ after EWSB only the neutral part of the doublet can acquire a v.e.v. With $m^2 < 0$ and $\lambda > 0$, the lagrangian in 1.16 does not represent a particle with mass m. Instead, to properly interpret it, an expansion around the minimum can be done shifting the field definition:

$$H = \frac{1}{\sqrt{2}} \begin{pmatrix} \theta_1 + i\theta_2 \\ v + h + i\theta_3 \end{pmatrix} \tag{1.21}$$

The fields θ_1, θ_2 and θ_3 are the so called Nambu-Goldston bosons, while h will represent the physical Higgs boson particle. The Nambu-Goldston bosons are the three degrees of freedom that will be absorbed by the the Z and $W^\pm$ gauge bosons resulting in mass terms for each. It is usual to make a gauge transformation to move to the unitary gauge, where $\theta_1' = \theta_2' = \theta_3' = 0$. Even though this is not mandatory, it will simplify the visualization of the EWSB effect. Working in the unitary gauge, the Higgs field presented in 1.21 looks like:

$$H = \frac{1}{\sqrt{2}} \begin{pmatrix} 0 \\ v + h(x) \end{pmatrix} \tag{1.22}$$

Replacing 1.22 in to 1.18 and omitting constant terms, the Higgs potential has the form:

$$V(H^\dagger H) = \lambda v^2 h^2 + \lambda v h^3 + \frac{\lambda}{4} h^4 \tag{1.23}$$

where a mass term for the physical Higgs boson is now explicit. Trilinear and quartic self interactions of the Higgs boson also appear.

1.3.1 Gauge boson masses

The mechanism that generate masses for the Z and $W^\pm$ gauge bosons is hidden in the kinetic terms of Higgs lagrangian in equation. The B_μ and the W^a_μ fields are included into the covariant derivative via minimal coupling to the Higgs fields. Replacing 1.22 in the dynamic part of 1.16 and expanding:

$$\begin{aligned} (D_\mu H)^\dagger (D^\mu H) &= \frac{1}{2}(\partial_\mu h)(\partial^\mu h) + \frac{g^2}{4} W^-_\mu W^{+\mu}(v+h)^2 \\ &+ \left[\frac{g'^2}{8} B^\mu_\mu - \frac{g' g}{4} B_\mu W^{3\mu} + \frac{g^2}{8} W^3_\mu W^{3\mu}\right](v+h)^2 \end{aligned} \tag{1.24}$$

where the anti-diagonal part of the $W^a_\mu T^a$ matrix has been reinterpreted as the charged $W^\pm$ bosons:

$$W^\pm_\mu = \frac{1}{\sqrt{2}}(W^1_\mu \mp i W^2_\mu) \tag{1.25}$$

The expression in 1.24 contains three terms: The first corresponds to the kinematic term of the physical Higgs boson. The second and third terms are multiplied by the quadratic term $(v+h)^2$. Inspecting only the component proportional to v^2, shows explicit mass terms for the gauge bosons. In addition, mixing terms of the neutral gauge bosons also appear:

$$\frac{g^2 v^2}{4} W^-_\mu W^{+\mu} + \left[\frac{g'^2 v^2}{8} B^\mu_\mu - \frac{g' g v^2}{4} B_\mu W^{3\mu} + \frac{g^2 v^2}{8} W^3_\mu W^{3\mu}\right] \tag{1.26}$$

The first term in 1.26, corresponds to the $W^\pm$ mass term. The second part includes the mixing term $B_\mu W^{3\mu}$ indicating that B_μ and W^3_μ are not physical particles, but linear combination of the mass eigenstates. To find the real mass eigenstates, both fields can be grouped in a two dimensional array mixed by a 2×2 mass matrix. Diagonalizing this matrix the physical particles Z and γ are obtained:

$$\begin{aligned} Z_\mu &= -B_\mu \sin\theta_W + W^3_\mu \cos\theta_W \\ \gamma_\mu &= B_\mu \cos\theta_W + W^3_\mu \sin\theta_W \end{aligned} \tag{1.27}$$

The θ_W is the Weinberg's angle given by $\tan\theta_W = (g'/g)$. After diagonalization, the mass terms for all four gauge bosons are found:

$$m^2_{W^\pm} = \frac{g^2 v^2}{4} \qquad m^2_Z = \frac{(g^2 + g'^2)v^2}{4} \qquad m^2_\gamma = 0 \tag{1.28}$$

It is important to notice g and g' as well as m_Z and $m_{W^\pm}$ are not independent. Instead, g and g' relate to each other via the Weinberg's angle as a consequence of electroweak unification:

$$\tan(\theta_W) = \frac{g'}{g} \qquad \text{and} \qquad \cos(\theta_W) = \frac{m_{W^\pm}}{m_Z} \tag{1.29}$$

1.3.2 Yukawa lagrangian and fermion masses

Fermion masses are included into the SM via the Yukawa lagrangian. With the inclusion of the Higgs scalar doublet, interaction terms between the scalar and fermion fields must be added to the lagrangian. After EWSB, interaction terms between the physical Higgs boson plus fermion mass terms appear, leaving neutrinos as massless particles. The Yukawa lagrangian has the form:

$$\mathcal{L}_{Yukawa} = -y^u_{ij}(\overline{Q}^i\tilde{\Phi})U^j - y^d_{ij}(\overline{Q}^i\Phi)D^j - y^l_{ij}(\overline{L}^i\Phi)R^j + h.c. \tag{1.30}$$

where y^l_{ij}, y^u_{ij} and y^d_{ij} are 3×3 arbitrary complex matrices denominated yukawa couplings. $\tilde{\Phi}$ is scalar doublet defined as $\tilde{\Phi} = i\sigma_2\Phi^*$, which is added to include the proper part (u^i_L) of the Q^i doublet into the mass terms of the up type quarks. To simplify, the left handed components of the fermion fields can be written in generations arrays:

$$u_L = \begin{pmatrix} u \\ c \\ t \end{pmatrix}_L \quad d_L = \begin{pmatrix} d \\ s \\ b \end{pmatrix}_L \quad l_L = \begin{pmatrix} e \\ \mu \\ \tau \end{pmatrix}_L \tag{1.31}$$

and similar for the right handed components. After EWSB, 1.22 can be replaced in 1.30 leading to explicit fermion mass terms proportional to v:

$$\overline{u_R}\mathcal{M}^u u_L + \overline{d_R}\mathcal{M}^d d_L + \overline{l_R}\mathcal{M}^l l_L + h.c. \tag{1.32}$$

where $\mathcal{M}^{(u,d,l)}_{ij} = y^{(u,d,l)}_{ij}(v/\sqrt{2})$ are 3×3 mass matrices. This includes mixing terms between the fermions coupling to the gauge bosons, proving that these are not real mass eigenstates. The weak interacting fermions f are a linear combination of the physical mass fermions f^m by rotations given by unitary matrices $U_L, U_R, D_L, D_R, L_L, L_R$:

$$u_{(L,R)} = U_{(L,R)}\cdot u^m_{(L,R)}, \quad d_{(L,R)} = D_{(L,R)}\cdot d^m_{(L,R)}, \quad l_{(L,R)} = L_{(L,R)}\cdot l^m_{(L,R)} \tag{1.33}$$

With these redefinition of the fermion fields, the mass matrices can be diagonalized:

$$U_R^{-1}\mathcal{M}^u U_L = diag(m_{u,c,t}),\ \ D_R^{-1}\mathcal{M}^d D_L = diag(m_{d,s,b}),\ \ L_R^{-1}\mathcal{M}^l L_L = diag(m_{e,\mu,\tau}) \tag{1.34}$$

So far this procedure seems reasonable, but there is a small and non trivial feature. The u^i_L fields has been rotated using the U_L matrix while the d^i_L have been rotated using the D_L matrix. But both u^i_L and d^i_L fields are part of the same $SU(2)_L$ doublet Q_i and should be then rotated with the same matrix in order to preserve $SU(2)_L$ gauge symmetry. If the same diagonalization matrix ($U^{ij}_L = D^{ij}_L$) is used for both (staying on the weak basis), then $\mathcal{M}^D$ cannot be fully diagonalized. However when using the mass basis as done above, both $\mathcal{M}^U$ and $\mathcal{M}^D$ can be diagonalized but $U^{ij}_L \neq D^{ij}_L$ and the components of Q_i will be independently rotated, leading to an explicit violation of $SU(2)_L$ gauge symmetry. This symmetry breaking introduces mixing terms to the interactions of quarks with the charged gauge bosons $W^\pm$, describing the only source of CP violation in the SM. To illustrate this, the interaction terms between fermions and weak gauge bosons given in 1.9 can be written using the physical bosons $W^\pm$, Z and γ given in 1.25 and 1.27. Looking only at the term including the charged W^+ interaction with quarks, included in the $D^L_\mu Q$ term, the lagrangian looks like:

$$\mathcal{L}^{W^+_\mu Q}_{Fermion} = \frac{g}{\sqrt{2}}\overline{u_L}\gamma^\mu d_L W^+_\mu \tag{1.35}$$

After diagonalizing the yukawa mass matrices in the mass basis, the previous expression takes the form:

$$\mathcal{L}^{W^+_\mu Q}_{Fermion} = \frac{g}{\sqrt{2}}\overline{u^m_L}U^\dagger_L\gamma^\mu D_L d^m_L W^+_\mu \tag{1.36}$$

Where the generation mixing of the quark mass eigenstates is now explicit and parametrized by the so-called Cabibbo-Cobayashi-Maskawa matrix:

$$V_{CKM} = U_L^\dagger \cdot D_L \tag{1.37}$$

In the neutral sector, the matrix is of the type $U_L^\dagger \cdot U_L$ which is equal to the identity. Hence no generation mixing is present for neutral currents. In the leptonic case, for massless neutrinos the diagonalization matrices ν_L are arbitrary. In such case they can be chosen ad-hoc such that $L_L^\dagger \cdot \nu_L = 1$ avidung flavor mixing in the lepton sector as required by experimental evidence.

1.3.3 Discovery of the Higgs boson

The EWSB process presented was only a theoretical approach to understand the origin of mass of subatomic particles. The idea of a fundamental boson as part of the mechanism was only a possibility, as no fundamental scalar boson had ever been discovered. This scenario changed drastically in 2012 with the discovery of a new particle by the ATLAS and CMS collaborations [15, 16] and the subsequent Nobel prize in 2013 for François Englert and Peter Higgs for their theoretical achievement [17,18]. The discovery is considered as a huge milestone for high energy physics and for the LHC. The particle found with a significance of 7σ was a boson with spin 0 with a mass of ~ 125 GeV and it is compatible with the SM predictions.

1.4 Problems and open questions

Despite being a robust and very complete model with an unprecedented precision, the SM as any man made model has its flaws.

One is the hierarchy problem [13,14]. In principle the problem is why do the weak scale is several $\sim 10^{19}$ orders of magnitude smaller than the Plank scale. When performing one-loop radiative corrections to the Higgs mass, lepton loops as the one in fig 1.2 are to be included.

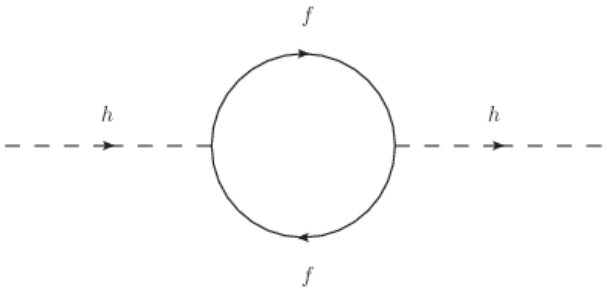

Figure 1.2: Quantum correction to the Higgs mass includes UV divergent diagrams as this fermion loop, proportional also to the fermion mass

The contribution to the Higgs mass coming only from this term looks like:

$$\delta m_h^2|_{fermion} = -\frac{|y_f|^2}{8\pi^2}[\Lambda^2 - 3m_f^2 \ln\left(\frac{\Lambda^2 + m_f^2}{m_f^2}\right) + \dots] \tag{1.38}$$

As seen in eq. 1.38 the whole contribution is proportional to the Yukaya coupling y_f. As Yukaya couplings are proportional to the fermion masses, the main contribution from the fermion loops to the Higgs mass comes from the top quark loops. It is seen that the correction

has a term proportional to Λ^2, where Λ is the energy scale below which the model is valid. There is also a logarithmic dependence on lambda, that plays a crucial role when computing the energy dependence of the parameter. To avoid ultra violet (UV) divergences from the Λ^2 term to obtain non divergent observables, a fine-tuned cancellation between the quantum corrections and the bare value must be performed. This procedure is however far from elegant and lacks of any explanation about the underlying physics behind such an ad-hoc tuning.

Another problem of the SM already mentioned, is the treatment of neutrinos as massless particles. The latest experiments on neutrino detection, demonstrates the existence of neutrino mixing and oscillations. Such oscillations would be impossible if neutrinos were massless. The mechanism for neutrinos to acquire a mass is still unknown and is a very active research field at the time being.

Gauge coupling unification is another SM *problem*. The SM is a renormalizable theory [19], and renormalization group equations (RGEs) for the SM parameters describe their dependence with the energy scale at which a process takes part. The logarithmic terms in eq. 1.38 are crucial for calculating this energy dependence. The SM gauge coupling constants energy scale dependance shows that g, g' and g_s tend to come closer as energy increases, but not reaching one unified value. Even though this is not a real problem of the model, there is the belief that all three interactions could be unified at a GUT[7] scale. The GUT scale must be below the Plank Scale, and after it another model should explain quantum interactions in which the three elementary forces are indistinguishable.

Another key aspect missing in the SM is Dark Matter (DM). This terminology is used to acknowledge for matter that is non-luminous and that can not be detected with telescopes. The existence of it, was initially postulated by Zwiki [22] to solve astrophysical observations regarding the velocity of galaxies moving in a cluster. Zwiki calculated the total mass of the Coma cluster indirectly, using the velocities of the galaxies found, by measuring the Doppler redshift of its spectra. Then he measured the amount of light observed from all the objects in the cluster. With this results he noticed that the measured velocities were almost 10 times faster as expected from the observations. He concluded that there must be around one hundred times more mass in the cluster as the amount measured by ordinary telescopes. The missing part was called Dark Matter. More evidence of DM was found looking at the rotation curve of the nearby galaxy M33 [23] and also using gravitational lensing in the case of the bullet cluster [24]. The existence of DM also plays an important role to explain the anisotropies of the cosmic microwave background CMB [5, 25]. The usual explanation that fits with all these observations is that DM must be massive, slower than light, non-baryonic and weakly interacting. The only particle that we know with such characteristics is the neutrino, and in the SM it is modeled as a massless particle. Anyhow, beyond any mechanism that could solve the SM neutrino mass problem, neutrinos are required to be light, and given their relic abundance, are too light to account for all the required DM.

[7] GUT: Grand Unification Theories [20, 21]. The GUT scale is the scale at which unification occurs.

Chapter 2

Supersymmetry

Developed in the 70's in parallel by Golfand and Likhtman [29] and by Volkov and Akulov [30], Supersymmetry (SUSY) [26–28] is one of the most popular beyond SM theory. To solve some of the SM problems, SUSY presumes the existence of additional fundamental particles that have not been found yet, postulating a new symmetry between fermionic and bosonic degrees of freedom. To build a supersymmetric Lagrangian, a superspace is defined with four spacetime coordinates x_μ ($\mu = 0, 1, 2, 3$) plus four extra Grassmann coordinates θ_i and $\overline{\theta}_i$ ($i = 1, 2$). With the additional Grassman coordinates fermion and boson fields can be written together in superfields, which are functions of the superspace. These superfields can be expanded in power series of θ_i and $\overline{\theta_i}$, and due to the nature of Grassmann variables, the expansion will have a finite number of terms. Each term in the expansion has one component field that can be either scalar, vector or a spinor depending on the Grassmann structure of it. A superfield for example could include a SM fermion as the electron and in the same object a boson field that is its supersymmetric partner, called selectron. If SUSY were a conserved symmetry, the two partner fields would have exactly the same mass. Since no extra particles with the SM masses have been observed, SUSY must be broken. With SUSY broken, the supersymmetric particles'are heavier than their SM partners, explaining why they have not been found, yet.

2.1 Minimal Supersymmetric Standard Model

2.1.1 MSSM Particle Content

The Minimal Supersymmetric Standard Model (MSSM) is the simplest supersymmetric extension of the SM where all SM particles have one supersymmetric partner that differs from each in half spin unit[1]. In the MSSM, SM fermion fields together with their scalar superpartners or *sfermions* lie on a *scalar superfield*. The same happens with the SM Higgs and its fermionic superpartner called *higgsino*. Vector boson fields and their supersymmetric partners, lie on a *vector superfield*. To construct the required interactions without introducing anomalies to the theory, two higgs-higgsino superfields are needed resulting in two Higgs doublets: H_u and H_d with their respective superpartners. Both Higgs fields will acquire vacuum expectation values v_u and v_d which will give mass to up-type and down-type quarks, respectively. Table 2.1 shows the particle content of the MSSM. In this table, the hypercharge is normalized such that electric charge is given by $Q = T_3 + Y/2$ where T_3 is the third component of the $SU(2)_L$ isospin.

With the particle content of the model, interaction terms can be written. This task must be done carefully. In the SM leptonic and baryon numbers are automatically conserved due

[1]There are SUSY models with more than one supersymmetric partner for each SM particle.

Superfields				$SU(3)_C$	$SU(2)_L$	$U(1)$
Gauge Multiplets						
$\widehat{G}$		g	$\widetilde{g}$	8	1	0
$\widehat{V}$		W^a	$\widehat{\widetilde{W}}^a$	1	3	0
$\widehat{V}'$		B	$\widehat{B}$	1	1	0
Matter Multiplets						
$\widehat{L}$	leptons	$\widetilde{L}^j = (\tilde{\nu}, \tilde{e}^-)_L$	$(\nu, e^-)_L$	1	2	-1
$\widehat{E}$		$\widetilde{E} = \tilde{e}^+_R$	e^c_L	1	1	2
$\widehat{Q}$	quarks	$\widetilde{Q}^j = (\tilde{u}, \tilde{d})_L$	$(u, d)_L$	3	2	1/3
$\widehat{U}$		$\widetilde{U} = \tilde{u}^*_R$	u^c_L	3^*	1	$-4/3$
$\widehat{D}$		$\widetilde{D} = \tilde{d}^*_R$	d^c_L	3^*	1	2/3
$\widehat{H}_u$	Higgs	H^i_u	$(\widetilde{H}^+_u, \widetilde{H}^0_u)_L$	1	2	1
$\widehat{H}_d$		H^i_d	$(\widetilde{H}^0_d, \widetilde{H}^-_d)_L$	1	2	-1

Table 2.1: MSSM particle spectrum. Where the transformation rules under gauge groups have been included. Table based on [27].

to $SU(3)_C \times SU(2)_L \times U(1)_Y$ gauge invariance. In a more general SUSY model, lepton and baryon number violating terms can exist. This can be handled defining a discrete symmetry called "R-Parity", that distinguishes regular from SUSY particles:

$$R \equiv (-1)^{3(B-L)+2S}. \tag{2.1}$$

For a SM particle $R = 1$ while for a SUSY particles $R = -1$. In the MSSM R-Parity is conserved, and as a consequence supersymmetric particles must be always produced in pairs. With R-Parity conserved, if any SUSY particle was created in a proton-proton collision, it could only decay into another lighter SUSY particle plus a SM particle. This decay chain will continue until a decay into the Lightest Supersymmetric Particle (LSP) that could not further decay, making the LSP stable[2]. An example of a possible decay chain can be seen in figure 2.1.

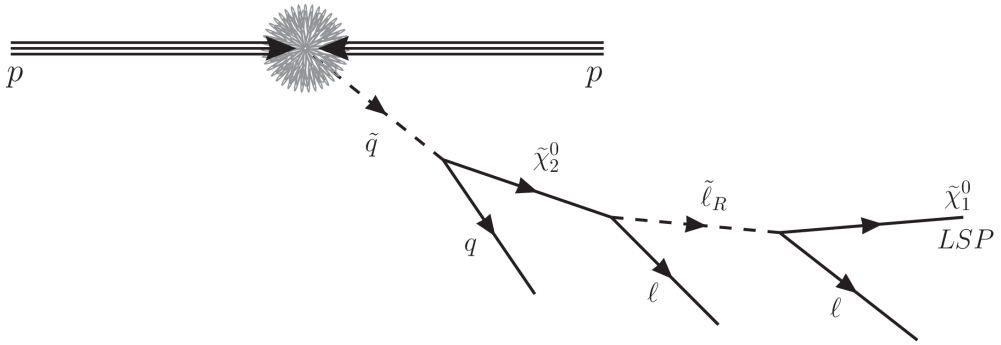

Figure 2.1: Example of a decay chain into the LSP in a pp collision conserving $R-$ parity. SUSY particles are often labeled with a *tilde*

Conserving the R symmetry, the most general superpotential with all the interaction terms can be written as:

$$W_{MSSM} = \epsilon_{ij}\left[h_l \widehat{H}^i_d \widehat{L}^j \widehat{E} + h_d \widehat{H}^i_d \widehat{Q}^j \widehat{D} - h_u \widehat{H}^i_u \widehat{Q}^j \widehat{U} - \mu \widehat{H}^i_u \widehat{H}^j_d\right] \tag{2.2}$$

[2]In R-Parity violating (RpV) models, the LSP is not stable and may decay directly into SM particles. These models can explain neutrino masses, but the LSP is no longer a good candidate for cold dark matter

Where the superfields labeled with a *hat* ($\widehat{\ }$) are the ones defined in Table 2.1. ϵ_{ij} mixes $SU(2)$ doublets. h_l, h_d and h_u are yukawa coupling constants which are 3×3 matrices in the generation space. μ is the Higgsino mass parameter. For simplicity, all generations labels have been omitted. At this point, all the superfields with their component fields and interactions are present, but SUSY is not broken yet. The dynamics of supersymmetry breaking is one among the most interesting fields in fundamental SUSY theories. In analogy to EWSB supersymmetry breaking, SUSY breaking cannot be achieved without gauge violation. Usually a hidden sector is included where SUSY is broken. The visible sector acknowledges SUSY breaking by interacting with the hidden sector via flavor blind messenger fields. Some of these models are mSUGRA [32], GMSB [33] and AMSB [34] that differentiate in the nature of the messenger interactions, whether it is mediated via gravity, gauge fields or anomalies. The implications of the different SUSY breaking scenarios are distinctive, fortunately all mechanisms lead to similar low energy terms, called *soft*[3] terms. The most general $R-$parity conserving soft potential written in terms of the component fields is given by:

$$\begin{aligned} V_{soft} &= m_u^2|H_u|^2 + m_d^2|H_d|^2 - m_{ud}^2(\epsilon_{ij}H_u^i H_d^j + h.c.) \\ &+M_{\tilde{Q}}^2\left[\tilde{t}_L^*\tilde{t}_L^* + \tilde{b}_L^*\tilde{b}_L^*\right] + M_{\tilde{U}}^2\tilde{t}_R^*\tilde{t}_R^* + M_{\tilde{D}}^2\tilde{b}_R^*\tilde{b}_R^* \\ &+M_{\tilde{L}}^2[\tilde{\nu}^*\tilde{\nu} + \tilde{\tau}_L^*\tilde{\tau}_L] + M_{\tilde{E}}^2\tilde{\tau}_R^*\tilde{\tau}_R + \frac{1}{2}\left[M_3\overline{\tilde{g}}\tilde{g} + M_2\overline{\widetilde{W}^a}\widetilde{W}^a + M_1\overline{\widetilde{B}}\widetilde{B}\right] \\ &+\frac{g}{\sqrt{2}m_W}\ \epsilon_{ij}\left[\frac{m_\tau A_\tau}{cos\beta}H_d^i\tilde{\ell}_L^j\tilde{\tau}_R^* + \frac{m_b A_b}{cos\beta}H_d^i\tilde{q}_L^j\tilde{b}_R^* - \frac{m_t A_t}{sin\beta}H_u^i\tilde{q}_L^j\tilde{t}_R^*\right] \end{aligned} \tag{2.3}$$

where $\tilde{q}_L, \tilde{\ell}_L$ are $SU(2)$ doublets given by $\tilde{\ell}_L \equiv \begin{pmatrix}\tilde{\nu}\\ \tilde{\tau}_L\end{pmatrix}, \tilde{q}_L \equiv \begin{pmatrix}\tilde{t}_L\\ \tilde{b}_L\end{pmatrix}$, $\tilde{t}$ and $\tilde{b}$ are the squarks and $\tilde{\nu}$ while $\tilde{\tau}$ are the sleptons. For simplicity, 2.3 is written using only third generation notation, thus squark, slepton, and fermion parameters are 3×3 matrices. $M_{\tilde{Q}}, M_{\tilde{U}}, M_{\tilde{D}}, M_{\tilde{L}}$ and $M_{\tilde{E}}$ are the mass parameters for the sfermions. M_1, M_2 and M_3 are the gaugino mass parameters while $\widetilde{W}, \widetilde{B}$ and $\widetilde{g}$ are the corresponding gauguinos called $Wino, Bino$ and $gluino$ respectively. The last line in eq. 2.3 correspond to the supersymmetric version of the yukawa couplings, corresponding to scalar triple vertices, where $A_{\{\tau,b,t\}}$ are trilinear scalar coupling parameters.

2.1.2 MSSM eigenstates

The particles introduced in the previous chapter correspond to interaction states and not necessarily to mass eigenstates of the theory. To obtain the mass eigenstates, all the fields containing the same quantum numbers can be grouped into multiplets where the mass matrices can be diagonalized to find mass eigenstates ant their masses. In Appendix A the mass eigenstates of the different sectors of the model are presented.

2.2 SUSY approach to some of the SM problems.

At the end of chapter 1 some of the SM problems or open questions were mentioned, in this chapter the SUSY approach for explaining such features will be discussed.

Regarding the hierarchy problem, as new particles are added to the particle spectrum, more loops will contribute to the renormalization of the Higgs mass and the theory is built in such a way that the loops including the new scalars can cancel exactly the UV divergences from the loops seen on figure 1.2.

[3]The *soft* adjective is used to express that the potential breaks SUSY preserving desired features such as cancellation of the UV divergences

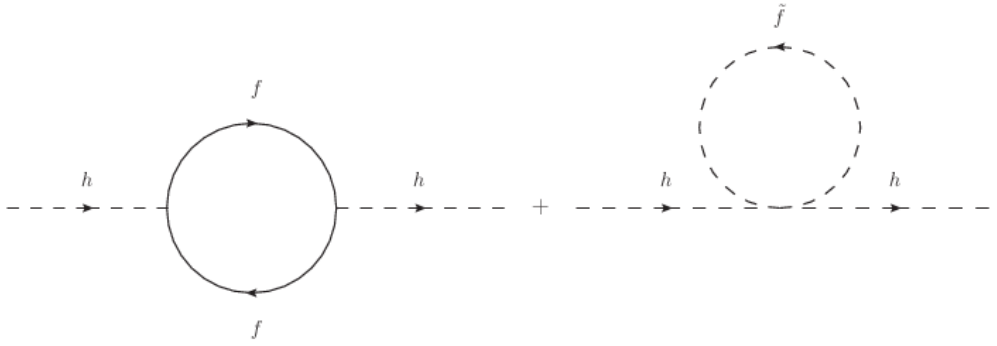

Figure 2.2: UV divergences of the Higgs mass coming from fermion loops are exactly canceled by scalar sfermion loops

In figure 2.2 the loop including a *sfermion* boson $\widetilde{f}$ (the superpartner of a fermion) contributes also to the Higgs mass as:

$$\delta m_h^2|_{sfermion} = \frac{3|y_f|^2}{8\pi^2}[\Lambda^2 - 3m_f^2 \ln\left(\frac{\Lambda^2 + m_f^2}{m_f^2}\right) + \dots] \tag{2.4}$$

The $hh\widetilde{f}\widetilde{f}$ coupling is also proportional to m_f^2 and the sign of the contribution is exactly the opposite because the first is a fermionic loop that carries a minus with it due to the anticommuting nature of fermions, while the second is a bosonic loop which has positive sign. In this way is how SUSY theories can cancel UV divergences to the Higgs mass without the need of *fine-tunning*. A similar procedure cancels UV divergences coming from bosonic loops in the SM, that are canceled when their fermion partners called gauginos are included.

About neutrino masses, they can be easily included in RpV SUSY theories by violating $R-$parity. When this happens, neutralinos can mix with the neutrinos sharing one unique mass matrix. Thanks to this mixing, after diagonalizing the neutralino-neutrino matrix, mass terms for the neutrinos appear. As already sated above $R-$parity conservation kept the LSP stable avoiding its decay, but once R parity is violated this no longer valid. In many RpV SUSY models the neutralino is not longer the best candidate for DM and the candidate can be the gravitino[4] that due to RpV could decay, but since they interact only gravitationally, their lifetime would be very long and could account for DM as a long lived particle.

Together with the natural solution to the hierarchy problem, the gauge coupling unification is one of the nicest features of SUSY. After including new particles to the theory and knowing that at some scale SUSY breaks, the RGEs change with respect to the SM. The SM RGEs would be valid from the weak scale up to the supersymmetry breaking scale M_{SUSY}, after which the RGEs for SUSY should be used up to the M_P scale or some intermediate scale if GUT or other type of theory is proposed. As said before within the SM the gauge coupling constants do not meet at a single point, but in the MSSM unification occurs at a scale of $\sim 10^16$ GeV for $M_{SUSY} \sim 1$ TeV. The gauge coupling unification is a hint for GUT and the fact that unification cannot be achieved in the Standard Model is also a hint that there might be new physics at an intermediate scale. Moreover coupling constant unification in the MSSM points to the fact that the new scale at which new physics could appear lies near the TeV scale.

The last point discussed on the SM problems was Dark Matter. As already discussed, R-Parity conserving SUSY theories have a natural candidate for DM when the neutralino is

[4]Gravitino is the SUSY partner of the graviton in supergravity theories

the LSP. Depending on the SUSY parameters, other scenarios may exist where for example the lightest chargino is the LSP. Such models are strongly disfavored, as the existence of a stable massive charged particle does not match neither with observations nor with the main DM requirements as neutrality. It was also said that many other SUSY scenarios count with gravitinos as a DM candidates.

2.3 Simplified models

In the previous chapters an introduction to the MSSM parameter spectrum was presented. The MSSM has more than 100 independent parameters mainly to parametrize SUSY breaking and performing experimental searches or phenomenological studies over such a large number of variables is quite hard. Normally a set of suppositions are needed to reduce the number of independent parameters, and this can be done by various means. Many models assume a specific SUSY breaking scenario with specific conditions at the GUT scale, reducing the number of independent parameters to only a few. In these models, the mass spectrum of SUSY particles at the weak scale is calculated running the RGEs from the high energy GUT scale to the weak scale. The parameter spectrum at low energy is then used as an input for calculating the production cross sections and decay rates of the SUSY particles. With the first results of the LHC detectors, most of the groups searching for SUSY focused on these type of models, where the most popular model was mSUGRA with only 5 independent parameters[5]: M_0 corresponding to a unified scalar mass, $M_{1/2}$ corresponding to a unified gaugino mass, A_0 corresponding to a unified trilinear scalar coupling, $\tan\beta$ that corresponds to the ratio of the two Higgs doublets *vevs*, and $sign(\mu)$ that is the sign of the Higgsino mass parameter. As no significant signals consistent with any of these models were found, the results were used to constrain the parameter space, typically setting lower limits to the possible values for the masses. Additionally, a different approach for SUSY searches became more popular and the groups started to interpret their results in terms of exclusion limits in the so called **simplified models** [36–39] aiming to cover as many topologies as possible. In simplified models, there is one specific production channel with 100 % branching ratio (BR) to a specific final state. A simplified model can be described by an effective Lagrangian that includes only the interactions of a small number of new particles reducing the relevant parameters to a small number of masses plus the production cross section. The channel with the best sensitivity for the one lepton analysis during the 2015 data taking period at 13 TeV, was the gluino pair production decaying via the lightest chargino to the lightest neutralino in a one step cascade. A diagram for such process can be found in chapter 4 in figure 7.2.

2.4 pMSSM: The phenomenological Minimal Supersymmetric Standard Model

The exclusion limits from the "high scale"[6] and "simplified" models already mentioned, helped to probe the sensitivity of each separated analyses to specific parts of the MSSM spectrum. This limits are far from fully exploring the vast parameter space of the MSSM,

[5]It must be said that performing a fine sampling of this five dimensional parameter space is also beyond the reach of any phenomenological study, where the main difficulty lies when simulating the different experimental signatures at the detectors. To deal with this difficulty and to harmonize the studies of thousands of physicists around the world, a set of specific benchmark scenarios were created [35]. Each scenario exhibit specific characteristics of the MSSM parameter space. These benchmark points are not only based on mSUGRA like scenarios.

[6]Here, "high scale" models means models in which a set of suppositions are done to define specific SUSY breaking scenarios plus specific unification conditions at the GUT scale such as mSUGRA, GMSB or AMSB

however combined to the strong constraints coming from flavor physics [40, 206–214] and other experimental results, a reduction and restriction of the MSSM parameters can be done resulting in the phenomenological MSSM (pMSSM) [41–43]. Making no assumption of physics at high scales and being inclusive with respect to production and decay channels, the pMSSM allows to cover a wide range of SUSY phenomenology and can be parameterized by 19 parameters. The main constraints included in the pMSSM used to reduce the number of parameters are:

- R parity conservation with the stability of the LSP.
- No new sources of CP violation are allowed assuming real soft parameters.
- Additional flavor changing neutral currents (FCNC) are absent.
- The LSP is a dark matter candidate if neutral in both charge and color.
- The first two generations of sfermions are mass degenerate, and their Yukawa couplings are negligible at sparticle production or precision observables.

In the study relevant for this thesis, the following extra requirements were made: To keep the physical states accessible to the LHC reach, an upper bound to the mass parameters of 4 TeV is applied, meaning that models where only a few light states are available with the rest being beyond reach will not be covered. Lower and upper bounds for some parameters are required to fit experimental constraints and to give a high density of points accessible by the LHC. The detailed requirements are given in detail in chapter 6.

In previous publications [44, 45] pMSSM models were also considered, where only the left-handed squarks of the first two generations, the two lightest neutralinos, and the lightest chargino were assumed to be within kinematic reach, with gluino masses up to 3 TeV while all the other SUSY particles were decoupled with masses equal to 5 TeV. These models cover a small spectrum of the MSSM parameter space and should not be confused with the more complete pMSSM models mentioned before which are the relevant ones regarding this thesis.

2.5 Experimental limits and status

Summarizing the latest results of SUSY searches is not an easy task, as there are several ways to search for SUSY. As already mentioned above, no statistically significant result consistent with any "high scale" or "simplified" model has yet been found in any of the final state scenarios where the searches have been performed. Therefore to show all the latest results and exclusion limits, a review paper would be needed and this is not the scope of these document. The reader is though encouraged to review all the public results in the web pages of the ATLAS [46] and the CMS [47] collaborations. Also it is important to mention that all limits on SUSY masses will depend on the underlying assumptions made. Nevertheless some of the most important and the latest results for similar searches will be shown below. The latest exclusion limits for mSUGRA scenarios with one lepton plus missing energy plus jets final state were published for 8 TeV collisions and are displayed in figure 2.3 where for large m_0 values gluino masses up to 1.2 TeV can be excluded.

In figure 2.4 the limits for a one step simplified model of gluino pair production decaying via lightest chargino to the neutralino LSP are shown for the same final state including soft leptons ($p_T < 25$ GeV) where a full statistical combination of all soft and hard lepton signal regions is possible. For the $x = 0.5$ grid, the combined limit on the gluino mass reaches up also to 1.2 TeV. It is interesting to notice how the soft and hard 1 lepton analyses complement each other, where the soft lepton analysis is powerful along the diagonal where the gluino and neutralino masses are almost degenerate, while the hard lepton channel is able to reach

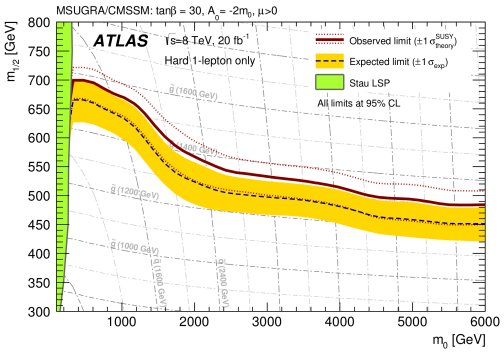

Figure 2.3: 95% CL exclusion limit from the one lepton channel in the $(m_0, m_{1/2})$ plane for the mSUGRA model with $\tan\beta = 30$, $A_0 = -2m_0$ and $\mu > 0$. In the green region the $\tilde{\tau}$ is the LSP. The gray lines in the background represent constant squark and gluino masses. The dashed blue line represents the expected limits where the yellow band accounts for experimental and theory uncertainties. The red line represents the observed limit where the dotted red line accounts for theoretical scale and PDF uncertainties on the signal cross section [48].

higher gluino masses. For the free x grid with $m_{\tilde{\chi}_1^0} = 60$ GeV a gluino mass up to 1.22 TeV can be excluded. More information on how these plots are produced will be explained in the last chapter where the interpretation of the 13 TeV results is discussed.

A summary diagram with a selection of the mass limits on new states or phenomena obtained with the ATLAS detector available before 13 TeV data taking is shown in figure 2.5.

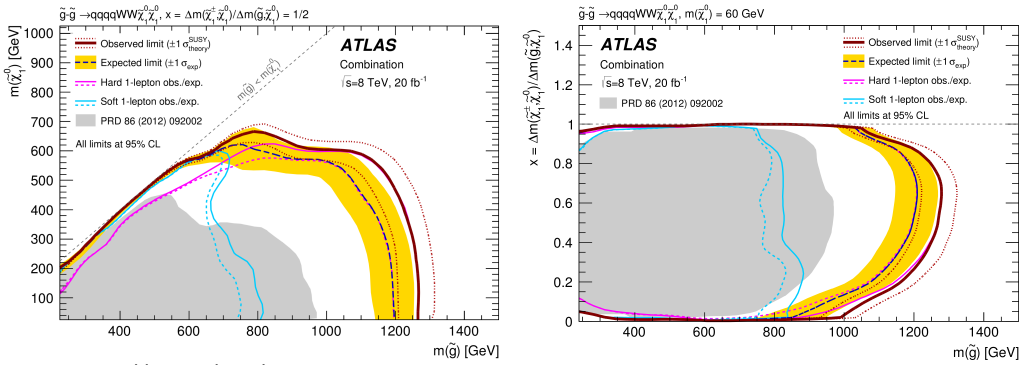

Figure 2.4: Left: 95% CL exclusion limit from the one lepton channel in the $(m_{\tilde{g}}, m_{\tilde{\chi}_1^0})$ plane for the gluino simplified model, where x=0.5. Right: 95% CL exclusion limit from the one lepton channel in the $(m_{\tilde{g}}, x)$ plane for the gluino simplified model, where $m_{\tilde{\chi}_1^0} = 60$ GeV. In both plots the dashed blue line represents the expected limits where the yellow band accounts for experimental and theory uncertainties. The red line represents the observed limit where the dotted red line accounts for theoretical scale and PDF uncertainties on the signal cross section. The individual soft and hard lepton limits are included. The gray area represent older limits by previous similar analyses with 7 TeV data [48]

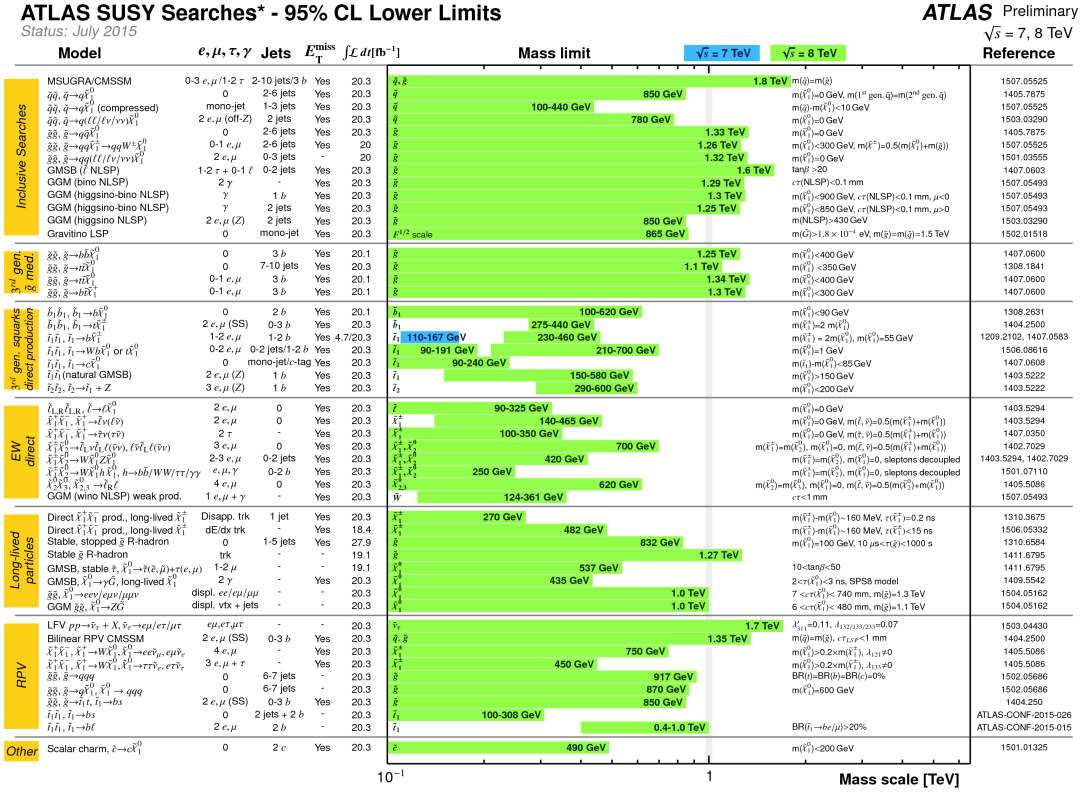

*Only a selection of the available mass limits on new states or phenomena is shown. All limits quoted are observed minus 1σ theoretical signal cross section uncertainty.

Figure 2.5: Selection of the mass limits published by the ATLAS collaboration before Run 2 [46].

Chapter 3

The Large Hadron Collider and the ATLAS detector

3.1 The Large Hadron Collider

The Large Hadron Collider (LHC) [50–53] is the biggest experiment ever built by humans. It is a proton-proton collider[1] built in a 27 kilometer underground ring located in the border between France and Switzerland near Geneva. It is built in the same tunnel where the Large Electron Positron Collider (LEP) [54] was located. A simple schematic view of the LHC injection chain [55] is presented in figure 3.1.

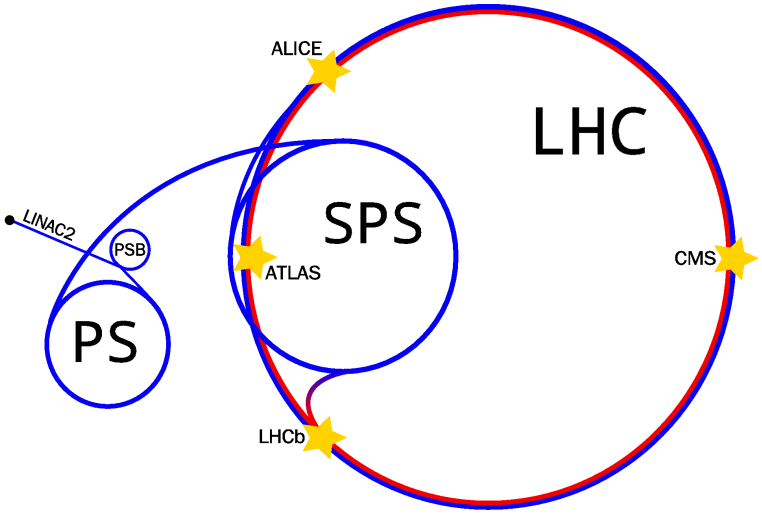

Figure 3.1: Proton paths from the LINAC2 to the LHC.

Initially, a bunch with roughly 10^{11} protons is accelerated by electric fields in the LINAC2 [56] linear accelerator, reaching an approximated velocity of 0.3c and an energy of 50 MeV. After LINAC2 the bunch is divided in four, and each packet enters in to one of the four 157 m circumference rings of the Proton Synchrotron Booster (PSB) [57]. The PBS magnetic fields are used to bend the trajectory of the protons, while its pulsating electric field accelerates them to a maximum of 1.4 GeV and a velocity of 0.91c. After the PSB, the bunches are

[1] It can also produce proton-lead, lead-lead and gold-gold collisions to study Quark-Gluon plasma

recombined and injected into the Proton Synchrotron (PS) [58], a 628 m circumference ring which accelerates the beam up to 25 GeV. At this point, protons reach a velocity of 0.999c and the energy given by the electric fields boosts the total energy and momentum of the protons without a significant velocity increase. After the PS, the bunches are injected to the Super Proton Synchrotron (SPS) [59], a 7 Km circumference ring that increases further the energy of the protons from 25 GeV up to 450 GeV. When the desired energy is reached, devices called kickers inject the bunches in to one of the two LHC vacuum beam pipes. In one beam pipe the bunches rotate clockwise and in the other counter-clockwise. The bunches are injected in synchronization with the bunches already in, forming groups called bunch trains. In the LHC it takes nearly 20 minutes for the protons to reach the desired energy of 6.3 TeV. A healthy beam can be used for hours adding on each run as much statistics as possible. In the 4 spots marked with a star in figure 3.1, the beams cross and it is here where the collisions take place. Surrounding the collision points is where the main detectors are built.

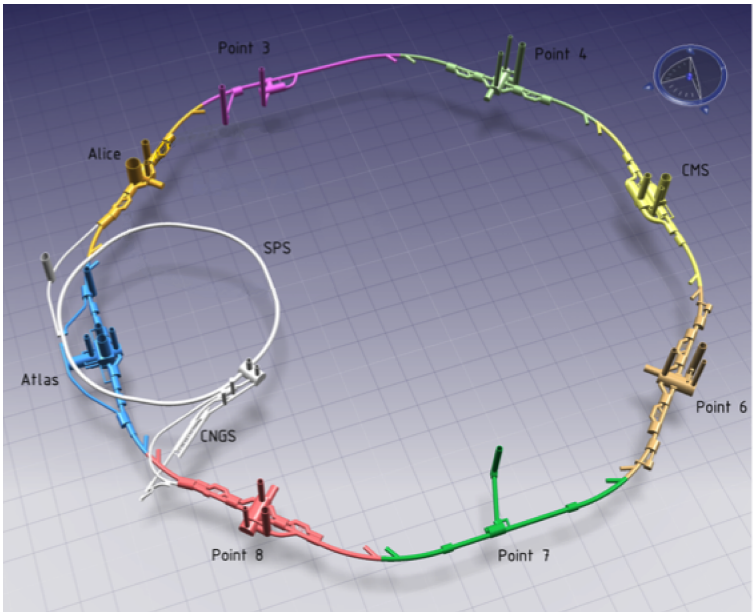

Figure 3.2: LHC ring octagonal shape [60].

The LHC ring consists of an octet with curved arcs between each straight section, as presented in figure 3.2. There are in total eight independent sectors or octants, defined as the section between the middle points of two consecutive straight sections. Each straight section is denoted as a *point*. In point 1 the ATLAS detector [61–63] is built, in points 2, 5 and 8, the ALICE [64], CMS [65] and LHCb [66] detectors are built. In points 2 and 8 the injection from the SPS to the LHC takes place. The radio frequency accelerator [67] is located at point 4. The main collimation installations are found in points 3 and 7 and the beam dump is found at point 6. In each of the arcs, 154 dipole magnets are used to bend the proton beam in to its desired trajectory, adding up to a total of 1232 dipoles. Each dipole is 14.3 m long, weighs 35 tons and it is cooled down to 1.9 K. The 8 T magnetic field needed to bend the protons trajectory is induced by strong electric currents of roughly 11 kA. These currents are too extreme to pass through traditional copper cables without melting them. Instead, the LHC dipole coils are made of Niobium-Titanium (NbTi), a superconductive material with a superconductive regime that lies below the temperature of the superfluid Helium (-271 °C) used to cool it. The remarkable properties of superfluid Helium such as a very high thermal conductivity and a very low coefficient of viscosity makes it the perfect cryogenic candidate.

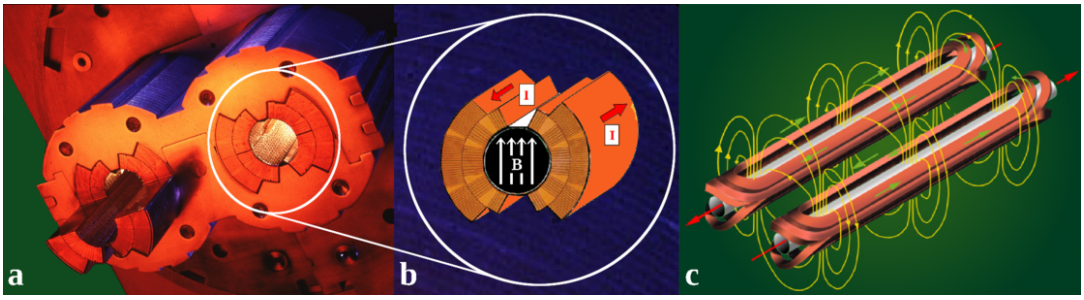

Figure 3.3: LHC Dipoles [68, 69].

As seen in figure 3.3a the LHC dipole system includes two beam pipes with a 2 in 1 magnet design. On each side two opposite currents are applied to generate a constant magnetic field perpendicular to the beam direction in the center of the beam (3.3b). The inner part of a dipole, beam direction, electric currents and magnetic fields are presented in figure 3.3c. The magnetic field acting over the protons generates a Lorenz force pointing to the center of the LHC ring, bending both beams to follow the LHC trajectory. The action of the magnetic field over the electric currents in the coils, generates a force on the coils pushing them apart along the LHC radial direction, tending to open the magnet. To avoid the coils from opening, they are surrounded and contained with non magnetic austenitic steel collars. The collars are also surrounded by a magnetic iron yoke confining the magnetic filed. This structure is shown in a transverse section of the dipole in figure 3.4.

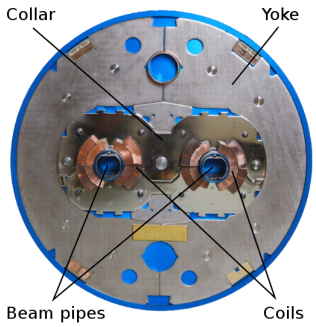

Figure 3.4: Transverse view of an LHC dipole magnet [50].

The dipole magnets have a defocussing effect over the beam, that is balanced by 392 superconducting quadrupole magnets. The LHC quadrupole magnets are used to keep the protons in tight bunches counteracting the coulomb force that tries to separate them. Each quadrupole focus the beam in one direction of the transverse plane while defocussing it in the other. This effect is shown in figure 3.5, where the magnetic field generated by the coils, and the shaping of the beam are presented. Quadrupole magnets with opposite currents are alternated between the dipoles focusing the beam in one direction and then in the other. The magnetic field of the focusing magnets has a steep gradient of 223 T/m, resulting in higher forces acting on protons far from the beam axis, and negligible forces acting on protons traveling close to it.

Besides dipole and quadrupole magnets, additional multipolar magnets are used to fine tune the beam. A triplet of quadrupole magnets at both ends of the detectors are used to utterly focus and collimate the beam towards collision. The beams can be focused as shown

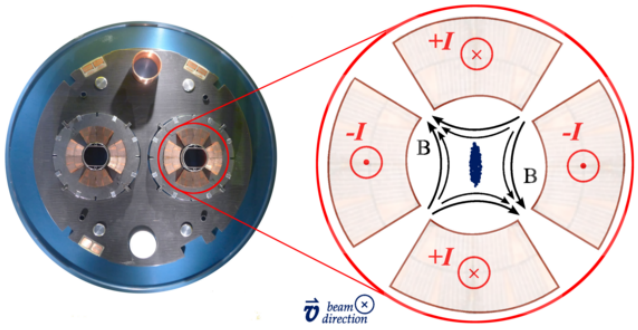

Figure 3.5: Transverse view of an LHC quadrupole magnet [50].

in figure 3.6 from 0.2 mm in the arcs to 16 µm at the interaction point, increasing the number of proton-proton interactions per bunch crossing.

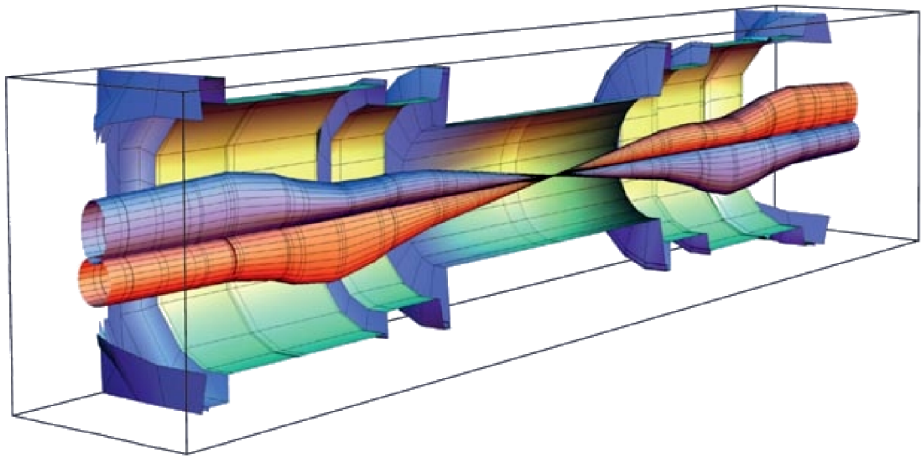

Figure 3.6: Proton beams being squeezed before interactions [70].

A key aspect of any particle collider is the instantaneous luminosity L that can deliver. Given a process cross section σ the event rate r associated to it will be determined by the luminosity as $r = L\sigma$. The Instantaneous luminosity accounts for the number of proton-proton interactions per unit area and time, and depends on key accelerator parameters: Number of particles per bunch N_p, number of bunches per beam k_b, the beam frequency f, the velocity of the particles v, the crossing angle between both beams σ_c, the average spread of the particles in a bunch, and the transverse size of the particle beam at the interaction point β^*. With these variables the instantaneous luminosity can be written as:

$$L = \frac{N_p^2 k_b f \gamma}{4\pi\varepsilon_n \beta^*} F \tag{3.1}$$

where γ is the relativistic Lorentz factor related to the velocity v of the particles, F is a reduction factor related to σ_c, and ε_n is the normalized emittance, which is proportional to the bunch spread. Integrating the instantaneous luminosity over time, the integrated luminosity is obtained, which is proportional to the event number of a process. When integrated over a full data taking period, gives the total amount of data provided by the LHC during that period.

In 2012 the LHC run with 4 TeV energy per bunch adding to an 8 TeV center of mass (c.o.m) energy. The runs were made with 50 ns bunch spacing reaching a peak luminosity of 7.7x10^{33}cm^{-2}s^{-1} and a total integrated luminosity of 20.3 fb^{-1}. During the first long shutdown (LS1) the LHC and its detectors were upgraded to change damaged parts and to reach the higher standards needed for Run 2. After the LHC started running again in 2015, the beam energy was increased to 6.5 TeV adding up to 13 TeV c.o.m energy. Some test runs were done with 50 ns bunch spacing while for the rest of the year it was changed to 25 ns with a base number of 2244 bunches per beam, with a nominal intensity of 1.15x10^{11} protons per bunch. The complete data taking period with 25 ns spacing added an integrated luminosity of 3.2 fb^{-1} with a peak luminosity of 5x10^{33}cm^{-2}s^{-1}.

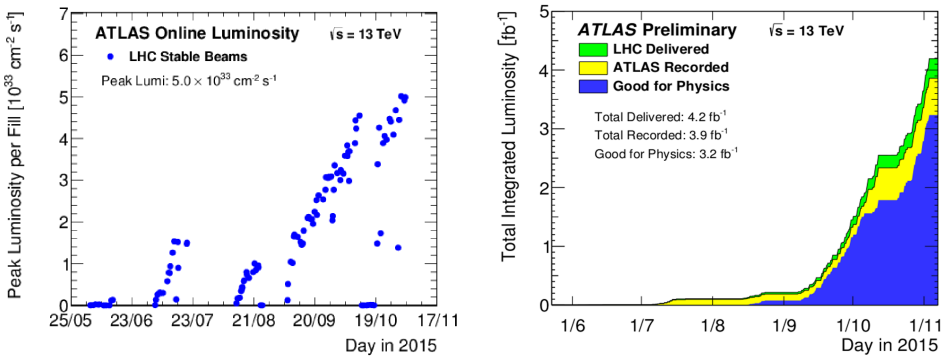

`Figure 3.7:` Instant and integrated luminosity during 2015 data taking period [71]

In figure 3.7 the instant luminosity and the integrated luminosity during the 2015 data taking period is shown. During 2015 there were problems leading to forced beam dumps and the unavailability of the LHC beam. Most of them were in the cryogenic system, mainly in one refrigerator. The issue was repaired in January 2016.

3.2 The ATLAS Detector

The ATLAS[2] detector [61–63] is one of the four main detectors of the LHC, and together with the CMS detector [65] conform the two main general-purpose detectors of the LHC. ATLAS consists of a 26 m diameter and 46 m length cylinder, filled with several layers of different sub-detectors, designed to cover a vast range of physical processes. In the barrel region, layers are added as concentric cylinders, while in the forward regions layers are added as discs one after another as presented in figure 3.8. The inner detector is the part of the ATLAS located closest to the interaction point and it is designed to get the tracks and momentum of charged particles. The next detector layers correspond to the two calorimeters which measure the energy of electrons photons and hadrons by *absorbing* them. Finally the outer most layers correspond to the muon detectors that work as tracking devices and measure the momentum of muons passing through. As important as the detecting devices, the superconducting toroidal and solenoid magnets are designed to bend electrically charged particles to differentiate particles from antiparticles and to calculate its momentum.

[2]ATLAS: A Toroidal LHC ApparatuS

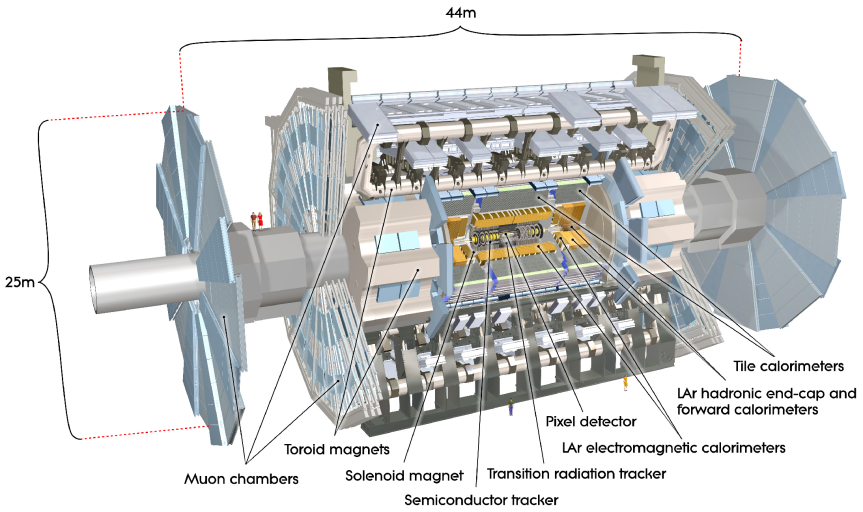

Figure 3.8: The ATLAS detector and its components. [61]

3.2.1 The ATLAS coordinate system

The origin of the ATLAS coordinate system [62] is located at the nominal interaction point at the center of the detector. As shown in figure 3.9a, the positive z axis is defined along the beam axis and points from the origin towards side A[3] of the ATLAS detector. The side of the detector with negative z is referred as side C. Side B is located at the transverse plane at $z = 0$ that is defined with the x axis pointing to the center of the LHC ring and the the y axis pointing up. The azimuthal angle ϕ is measured around the beam axis in the transverse plane from x to y, i.e. $\phi = \arctan(y/x)$, with $\phi \in \{-\pi, \pi\}$. The polar angle θ is measured from the z axis towards the transverse plane.

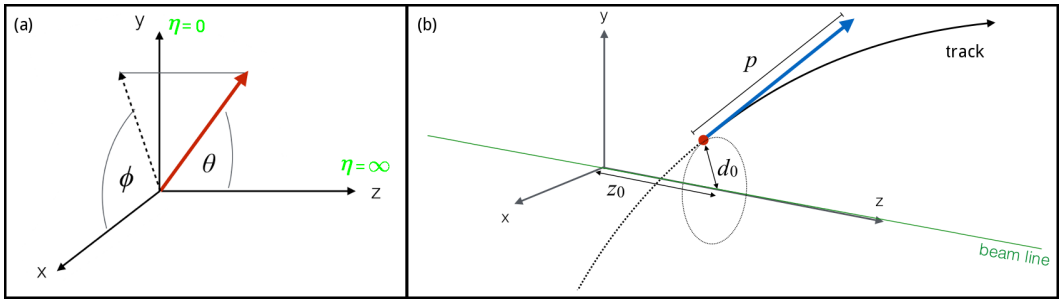

Figure 3.9: The ATLAS coordinate system (a) and the impact parameters d_0 and z_0 (b).

As protons are composite particles made of partons and the strong interaction at high energy proton-proton collisions is mainly between the partons, there is an inconvenient ambiguity on the parton c.o.m reference frame along the beam direction with respect to the hadron reference frame. Variables involving the transverse components only, are very useful as they are invariant under longitudinal boosts. The transverse momentum of a particle is defined in the transverse plane as $p_T = \sqrt{p_x^2 + p_y^2}$ and in the same way the transverse energy

[3]Pointing from the origin, to LHC's point 8.

E_T is defined. Despite the fact that the incoming protons collide with a non zero angle with respect to the z axis, the incoming $\vec{p}_T$ sum can be approximated to zero. Following momentum conservation, the $\vec{p}_T$ sum over all outgoing particles must be zero. As some particles as neutrinos can pass through the detector without being detected, the $\vec{p}_T$ sum is always different than zero. A vector of the same magnitude and pointing in the opposite direction than the $\vec{p}_T$ sum is defined as the missing transverse momentum, and its magnitude is often called missing transverse energy E_T^{miss}.

Differences in the polar angle $\Delta\theta$ are not Lorentz invariant, and as the parton system can be boosted with respect to the hadron reference frame, instead of using θ it is more convenient to define the pseudorapidity: $\eta = -\ln[\tan(\theta/2)]$. Pseudorapidity is a close approximation to rapidity[4] if $m \ll E$. Differences in rapidity Δy are Lorentz invariant. If a vector lies in the XY plane with no component in the z direction then $\theta = \pi/2$ and $\eta = 0$. If a vector lies in the z axis with no component in the transverse plane then $\theta = 0$ and $\eta = \infty$. The angular distances between two points is defined in the rapidity-azimuthal space as $\Delta R = \sqrt{(\Delta\phi)^2 + (\Delta\eta)^2}$. Besides the regular space coordinates, the impact parameters d_0 and z_0 are defined with the closest approach parametrization. In the trajectory of any particle inside the detector the point of closest approach as is the point closest to the interaction point. The longitudinal impact parameter z_0 is defined as the distance along the z axis between the point of closest approach and the transverse plane. The transverse impact parameter d_0 is defined as the distance between the same point and the z axis. The definition for d_0 and z_0 are represented in figure 3.9b.

3.2.2 The Inner Detector

The component closest to the interaction point is the inner detector that can be divided in three main parts: The pixel detector [74, 75], the semi-conducting tracker (SCT) [76–78] and the transition radiation tracker (TRT) [79–82]. The inner Detector is fully contained inside the solenoid magnet [83] that bends charged particles inside it. It is used mainly to find the

[4]For a massive particle, the rapidity y is defined as $y = \frac{1}{2}\ln\frac{E+p_z}{E-p_z}$ where E is the particle energy and p_z is the projection of its momentum on the z axis. For a massless particle both definitions agree

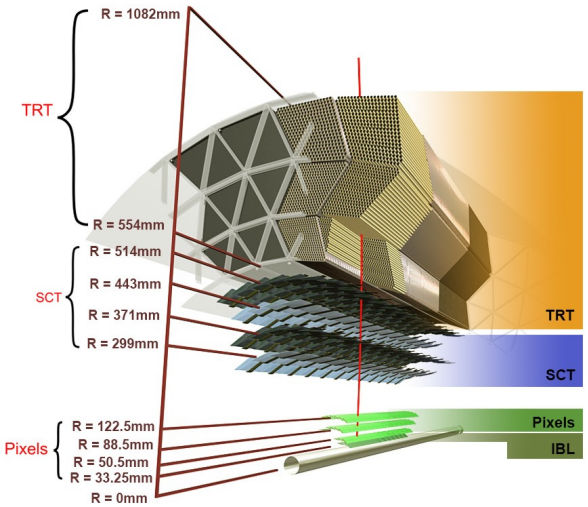

Figure 3.10: The inner detector array: The insertable B layer, the pixel detector, the semi-conducting tracker and the transition radiation tracker [84].

tracks of charged particles as they travel outwards the detector, calculating its momentum and finding the vertex from where they might have been produced. The layout of the inner detector is shown in figure 3.10

The Pixel Detector

The pixel detector [74, 75], represented in figure 3.11, was[5] the innermost part of the inner detector. It consists of three concentric cylindrical layers in the barrel region plus 3 circular layers on each side, covering the region of $|\eta| < 2.5$ with three hits. The three layers are built with 1744 pixel modules fixed to carbon fiber staves that include an integrated cooling system. As shown in figure 3.12(a), each pixel module consists of a 250 µm thick, 2 cm width and 6.3 cm long, silicon sensor with its area divided in 47232 pixels. Each sensor is connected to 16 front-end (FE) chips with a solder bump bonding technique. The chips are connected to a module-control circuit (MCC), an integrated chip that communicates with the external read-out drivers. Being so close to the beam it must be highly radiation resistant. Given the shape

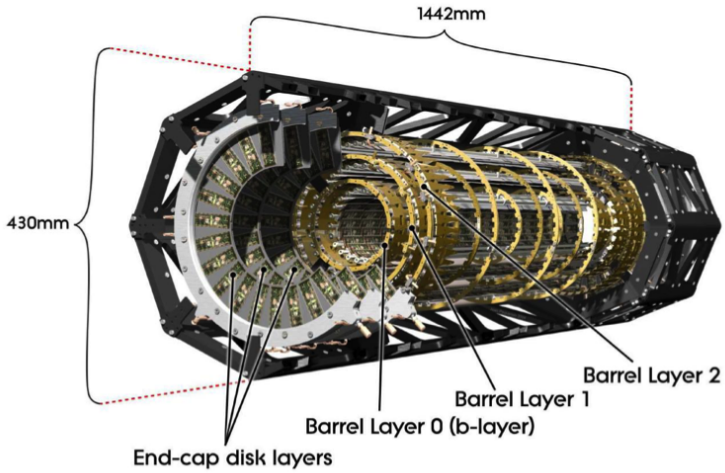

`Figure 3.11:` A sketch of the 3 layer design of the pixel detector with the barrel and end cap regions [74].

of the FE chips, there are 2880 solder bumps per chip, adding for a total of 46080 read-out channels per pixel module. Many of the sensor sensor pixels lie above the gap between chips. The space between the eight adjacent FE chips on each row is covered by *long pixels* which are longer than others. The gap between the two 8 FE chips rows, has eight pixels above with no solder bump below. These pixels are connected to four read-out channels already connected to other pixels on each side. An sketch of the two types of gaps between chips is presented in figure 3.12(b). With 46080 read-out channels per module and a total of 1744 modules, there are more than 80 million readout channels providing a spatial resolution of 8 µm in $r\phi$ and 75 µm in the z direction. Such an enormous granularity is needed to accurately find primary vertices. This is essential to define objects and select events under high luminosity conditions, where many interactions per bunch crossing are occurring almost simultaneously[6]. With the

[5] Before the introduction of the Insertable B-Layer (IBL) during LS1

[6] Often the term *pileup* is used to define these conditions. There is the *in-time* pileup referring to multiple interactions in one event, and *out-of-time* pileup referring to interactions from previous or succeeding bunch crossings. Pileup makes a non negligible impact on the objects reconstruction, and corrections need to be done by dedicated algorithms to mitigate its contribution.

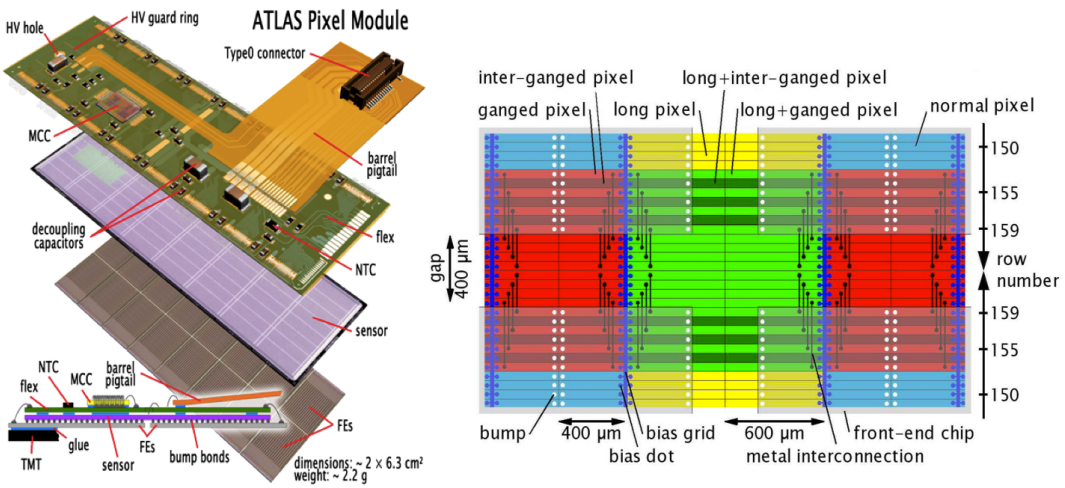

Figure 3.12: (a) Body and cross-section of a Pixel Detector module with the sixteen front-end chips aligned in two rows [74]. (b) Pixel types and connections to get full coverage despite the gaps between the chips. (Colored areas represent the different pixel types while the four transparent gray areas represent the chips [75].

high Luminosity of the LHC, each time two bunches collide at the interaction point, many proton-proton interactions take placee. The average number of interactions per bunch crossing is shown in figure 3.13 for the 2015 data taking period, showing a mean value of 13.7 with a maximum of 28. The exceptional granularity of the pixel detector is also crucial to find secondary vertices to identify heavy jets.

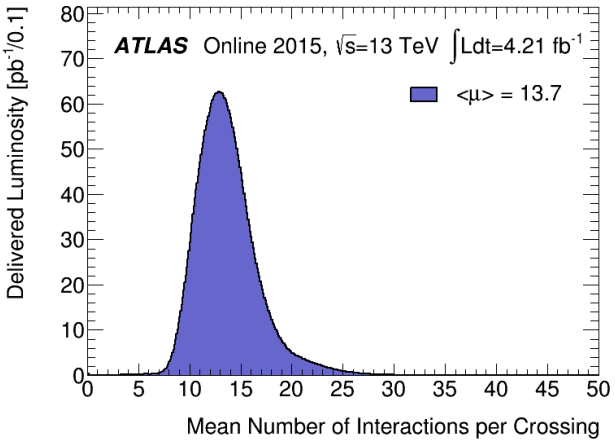

Figure 3.13: Average number of interactions per bunch crossing for the 2015 data taking period [71].

The Insertable B Layer

The insertable B layer (IBL) [72, 73] is now the closest layer to the thiner Beryllium beam pipe. During LS1 the Pixel detector was extracted from the experiment to prepare it for

higher luminosities. The changes included the replacement of damaged modules, and the installation of the IBL aiming for excellent vertex detector performance and to minimize reconstruction inefficiencies in case of failures in any of the other layers. As observed in figure 3.14a, the IBL consists of cylinder with 14 carbon foam staves shifted 14 inducing a $\Delta\phi = 0,18°$ overlap providing full coverage. Figure 3.14c shows that each stave is divided in 12 central planar silicon modules plus four novel 3D silicon sensor modules in each border [86]. The central modules are similar to pixel detector modules, consisting of n-on-n silicon sensors bump bonded to two read-out chips. Each normal pixel measures 50*250 µm^2, the long pixels used in the borders and above the gap between the two chips have the same width but are 500 µm long. Each central chip has 40 double columns of 366 solder bump rows for a total of 26880 read-out channels. These dimensions refine the granularity of the previous pixel detector, improving the resolution. Figure 3.14b shows that the spatial resolution on z_0 is improved roughly by 40% for tracks with $p_T < 200$GeV

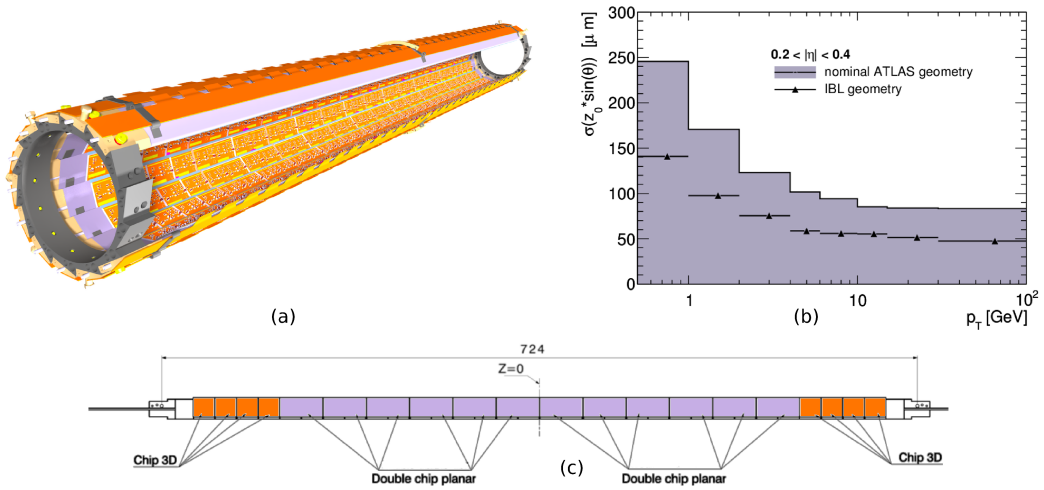

Figure 3.14: (a) The IBL module design mounted in the 14 staves. (b) The improved spatial resolution on the z-axis impact parameters z_0 vs track p_T. (c) Each stave with the 20 double chip planar sensor modules at the center plus four single chip 3D sensor modules at the ends. [85]

During cosmic ray data commissioning, it was found that the shape of the IBL staves was distorted because of temperature, causing them to bow. The main reasons for the bowing were a mismatch between the thermal expansion coefficient between the flex services and the carbon foam and the mechanics of the fixed points of the staves. The effect of the bowing on b-tagging efficiency and on the impact parameters was studied. Physical recommendations plus off-line run by run corrections were made to correct for the distortion resulting in a negligible impact on b-tagging performance [87].

The Semiconductor Tracker

The semiconductor tracker (SCT) [76–78] is the middle part of the inner detector. With four cylindrical layers in the barrel and nine disks at each end cap, it provides four space points per track. The layout of the SCT layers inside the inner detector is presented in figure 3.15. The semiconductor tracker uses thin silicon strip sensors instead of pixels to cover a wider area. The four barrel layers are built with 2112 rectangular modules, each built with four 63.56×63.96 cm^2 area and 285 μm thick p-in-n silicon strip sensors. In the barrel two sensor

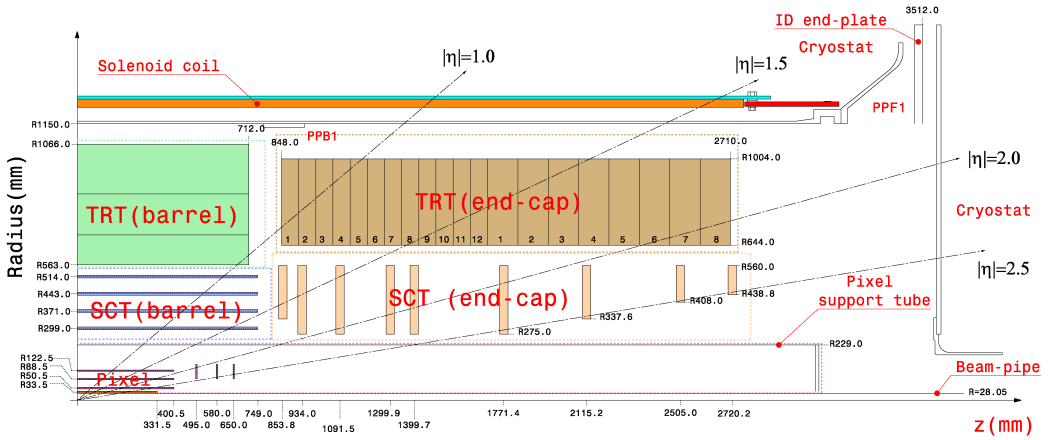

Figure 3.15: The diagram of the inner detector as it was for Run 1 including the SCT system in the middle. The four barrel layers plus the four different type end cap layers are designed to deliver 4 hits per track. [76].

are plates wire-bonded to each other to form longer strips of 126 mm which are aligned with the beam axis. A second pair of sensor plates is placed back-to-back against the first pair. The strips in the second layer form an angle of 40 mrad with respect to the firsts, improving the resolution for a 2D measurement. The end cap discs are built with 1976 trapezoidal modules of 4 different types, also with two back to back layers. Each module is built with a distinct combination from five different wedge-shaped sensor plates adding 6944 sensor plates. The end cap sensors are similar to the barrel ones, both contain 768 strips each, but the end cap strips are cones instead of cylinders to fit the trapezoidal shape. While the barrel strips have a constant pitch of 80 μm, in the end cap the pitch goes from 56.9 to 90.4 μm. The strips the modules are read by 6 FE chips with 128 channels each, providing the amplification, shaping and digitalization of the signals. The SCT modules are shown in figure 3.16. In Run 1 the performance of the SCT was outstanding and during LS1 no big changes were made. The SCT was although prepared for Run 2 to sustain higher trigger rates.

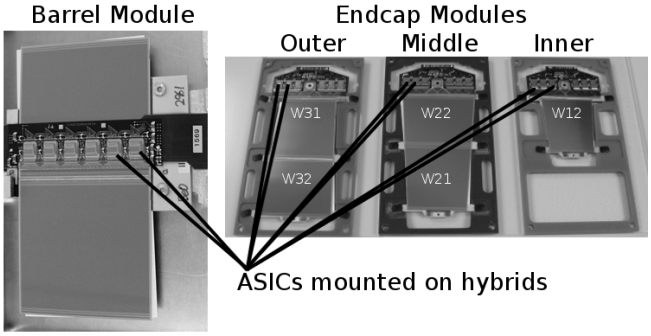

Figure 3.16: Different types of SCT modules. Left: The barrel module with two adjacent sensors on top (gray) plus two in the bottom slightly rotated (white). Right: Three of the four end cap modules built with the five different sensor plates W12, W21, W22, W31 and W32. The fourth module is only built with two back-to-back W22 sensor plates [78].

The Transition Radiation Tracker

The transition radiation tracker (TRT) [79–82] is the outer most part of the inner detector covering the region of $\eta < 2.0$. It is a straw-tube detector based on transition radiation, that combines tracking reconstruction with particle identification, providing more than 30 straw hits per track. It consist in 52,544 carbon-fiber reinforced kapton[7] tubes with 4 mm diameter and 144 cm length in the barrel, and 122,880 tubes of 4 mm diameter and 37 cm length in each end cap. Each tube has a 31 μm diameter gold-plated tungsten wire at the center connected to a voltage of 1530 V with respect to the tubes. The tubes are filled with a mixture of 70% Xenon (Xe) or Argon (Ar)[8], 27% Carbon dioxide (CO_2) and 3% Ozone (O_2). The tubes are separated by polypropylene fibers or foils to produce transition radiation when

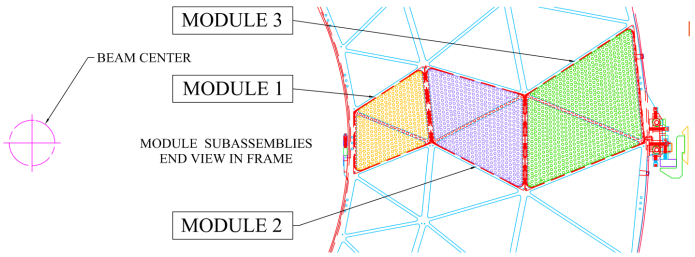

Figure 3.17: The three different types of TRT barrel modules [81].

charged particles pass trough. In the barrel [81] the straws are aligned parallel to the beam axis, arranged in 96 modules on three cylinders of 32 modules each. The number of straws per module depend on the module type as illustrated in figure 3.17. Module 1 has 329 straws arranged in 19 layers, module 2 has 520 straws in 24 layers and module 3 has 793 straws in 30 layers, for a total of 73 layers. In the end cap region [82] the straws are aligned perpendicular to the beam axis. The main unit is an eight layers wheel, consisting of two back-to-back four layer wheels. There are two types of wheels, both with eight layers. The spacing between the layers in the z-axis depends in the type of wheel. In type A wheels the distance is 4 mm, while for type B wheels it is 11 mm, such that tracks at different η hit approximately the same number of straws. As shown in figure 3.15, in each end cap there are 12 consecutive type A wheels followed by 8 consecutive type B wheels. In all wheels there are 768 straws per plane so each wheel has 6,144 straws for a total of 73,728 straws in type A wheels and 49,152 straws in type B wheels on each end cap.

The TRT has not only tracking capabilities, it can also discriminate between electrons and charged hadrons. The transition radiation emitted by charged particles passing trough, depends on its Lorentz factor γ. Ultra relativistic light particles as electors produce higher radiation levels than slower heavier particles like hadrons. The emitted photons ionize the gas in the tubes and the applied voltage separates ions from electrons producing a current through the central wire of the tubes. Depending on the intensity of the current, particle discrimination can be done. The spatial resolution of TRT goes from 100 to 200 µm.

As the way of measuring the p_T consists measure the curved tracks of charged particles bent by the magnetic fields, higher momentum means smaller curvatures and momentum resolution also increases with p_T, this means having worse reolution for higher momentum tracks. The overall p_T resolution of the ID was measured after calibration tests with cosmic

[7] A polyimide film which remains stable over a wide range of temperatures

[8] Finishing Run 1 near 10 l/h of Xe leaked from the tubes. Reparable leaks were fixed during LS1 but there were still irreparable leaks. Due to the high cost of Xenon, during 2015 some layers of the TRT worked with Ar instead of Xe.

muons [88]:

$$\frac{\sigma_{p_T}}{p_T} \cong \frac{0.05\% \cdot p_T}{\text{GeV}} \oplus 1\%$$

The p_T resolution was found to be nearly constant for low p_T tracks (∼1.6% for $p_T \sim 1$ GeV) while for higher p_T tracks it grows with p_T (∼50% for $p_T \sim 1$ TeV).

3.2.3 The Central Solenoid Magnet

The ATLAS central solenoid (CS) magnet [83] bends the trajectories of charged particles along the transverse plane to find its momentum. Is consists of a 5.5 ton, 2.5 m diameter, 5.3 m long and 4.5 cm thick cylinder, with 1,173 turns of Ni-Ti superconducting cable in a single layer coil. An electric current of 7,730 A is passes trough the cable, inducing a 2 T magnetic field along center of the z axis that can raise up to 2.6 T at the coil itself. To achieve the desired calorimeter performance, the CS was designed to be as thin as possible. This is achieved sharing a common vacuum vessel with the EM calorimeter, which cools it down to the required 4.5 K. A picture of the coil can be seen in figure 3.18.

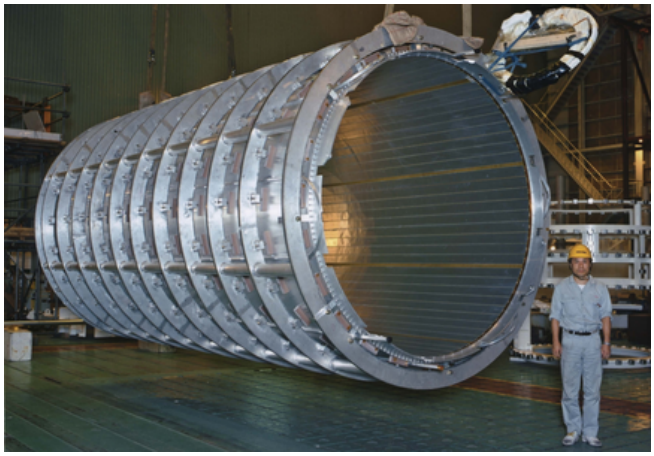

Figure 3.18: The ATLAS solenoid magnet [61].

3.2.4 The Calorimeter

The ATLAS calorimeter system [89] measures the energy of outgoing particles. It is divided in two main parts: The electromagnetic calorimeter (EM-Cal) [90] that measures the energy of photons and electrons, and the hadronic calorimeter [91] designed to measure jet energy. Figure 3.19 shows the spatial distribution of the calorimeter, which is divided in the barrel, end caps and two forward forward calorimeters [92] on the sides, covering large η regions. The calorimeter system provides precision measurements of electrons, photons, jets, and missing transverse energy and its granularity is good enough to identify photon vertices. It also plays a crucial role for triggering. The calorimeters combining the barrel, end-caps and forward parts cover a region of $|\eta| \leq 4.9$

The Electromagnetic Calorimeter.

The electromagnetic calorimeter (EM-Cal) [90] is a sampling calorimeter that uses lead and stainless-steel plates as absorbers. The space between the plates is filled with liquid Argon (LAr) as the active medium. Immersed in the LAr there is a copper grid that works as an

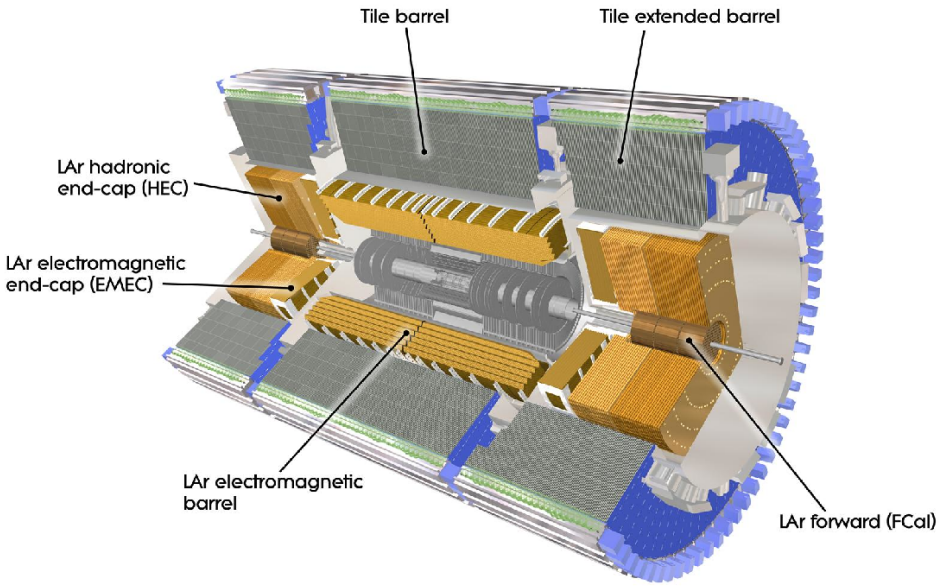

Figure 3.19: The calorimeter system of the ATLAS detector [93].

electrode to measure the particles passing through. When an high energy electron from a collision hits an absorber plate, it interacts with it producing an EM shower of low energy electrons, positrons and photons. After hitting several layers, it finally stops, leaving only a shower of EM particles inside the EM-Cal. The lower energy particles from the shower interact with the liquid argon, ionizing is atoms. The electrons from the ionization are pulled to the copper plates by a high voltage, where they are measured. The energy of the incoming high energy electron (or photon) will depend on the amount of low energy electrons deposited in the copper electrodes.

Figure 3.19 shows the geometric distribution of the EM-Cal which is divided in three regions: The barrel, covering the range of $|\eta| < 1.475$; two end-caps covering a range of $1.375 < |\eta| < 3.2$ and two forward calorimeters covering the $3.1 < |\eta| < 4.9$ region. For the barrel and the end cap wheels, the absorber plates and the electrodes are radially bent in an accordion shape, to cover the whole ϕ region avoiding cracks. The barrel region is divided in two identical half-barrels separated by a 6 mm gap at $|\eta| = 0$. Each half-barrel is built with 1024 accordion-shaped absorbers alternated with 1024 copper-polymide multilayer read-out boards. The half-barrels are divided in 32 ϕ regions connected by pairs to 16 modules. Each module covers a region of $\Delta\phi$=22.5°. Radially it is divided in three layers or samplings plus a fourth layer or pre-sampler:

- The pre-sampler: It consists of only a thin 1.1 cm (0.5 cm) LAr layer in the barrel (end-caps), located after the solenoid magnet and before the first layer of the calorimeter itself. Its function is to compensate for energy loss due to dead material before it.

- Layer 1: It is located after the pre-sampler and consists of thin strip towers with a granularity in the $|\eta| < 1.8$ region of 0.003×0.1 in the $\eta - \phi$ plane. The granularity on η increases with η, to a value of 0.004 in the $1.8 < |\eta| < 2.0$ region, 0.006 in the $2.0 < |\eta| < 2.5$ region, reaching its coarser value of 0.1 in the $2.5 < |\eta| < 3.2$ region. The finer granularity for low $|\eta|$ values is crucial to distinct neutral mesons such as pions

(π^0) from photons. At $\eta = 0$ this sampling has a depth of 4.3 radiation lengths X_0 which increases slightly with η.

- Layer 2: It consists in square cells ranging from 0.025×0.025 granularity in the $|\eta| < 2.5$ region to 0.1×0.1 in the $2.5 < |\eta| < 3.2$ region. Together with the first sampling it has the capability to identify vertices associated to photons leaving no track in the inner detector. With a depth 16 X_0 for η=0, it is the deepest layer and collects the largest energy fraction of EM showers.

- Layer 3: It is the last layer of the EM-Cal and has a coarser granularity 0.025×0.05 in the $|\eta| < 2.5$ region where it ends. Its depth is only 2 X_0, and it is designed to collect the remaining part of the EM showers not absorbed by the previous layers. It is also used to discriminate between hadronic and electromagnetic showers.

The total depth of the EM-Cal is more than 22 X_0 in the barrel and more than 24 X_0 in the end-caps, designed for a minimal EM energy leakage. The accordion shape, layers, depth, and granularity in the barrel is presented in figure 3.20. The desired granularity is accomplished

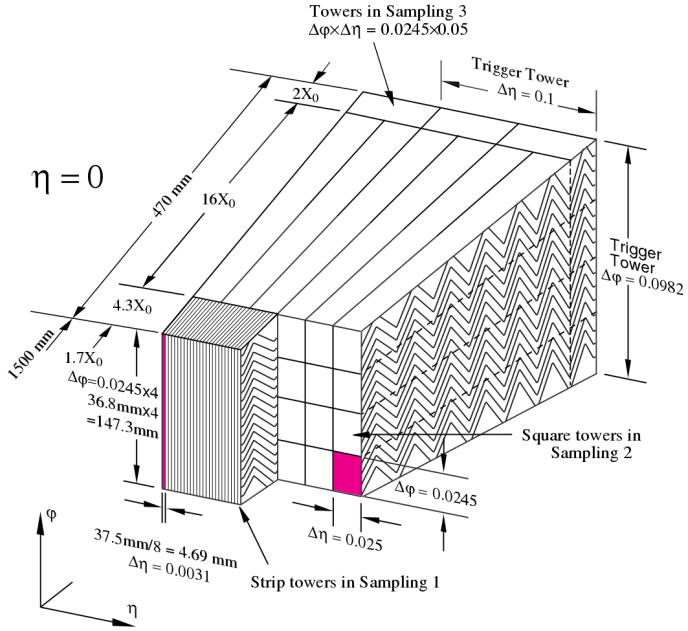

Figure 3.20: The accordion shape, depth and granularity of EM-Cal towers [93].

in ϕ by grouping together four adjacent read-out boards, while for η the boards are divided into cells, etching the copper surface. For production and handling convenience, the read-out boards are separated in two parts at $|\eta| = 0.8$ denominated type A and B. The flat (before accordion shaping) read-out board electrode design in η is shown in figure 3.21. Including the pre-sampler, each module provides 3,424 read-out channels and a total of 109,568 channels in both half-barrels.

The end caps are built with two concentric wheels which are also accordion shaped. The inner (outer) wheel covers the $2.5 < |\eta| < 3.2$ ($1.4 < |\eta| < 2.5$) region. Each wheel is segmented in eight wedge shaped modules, called C and D for the inner and outer wheel respectively. Their relative η positions requires for the D type modules to have a finer granularity than the coarser C modules. Together, one wheel pre-sampler module, one inner and one outer module add up to a total of 3,984 readout channels and total of 63,744 channels in both end caps.

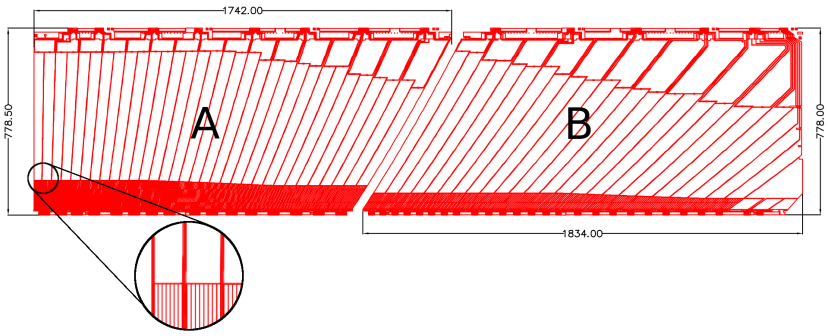

Figure 3.21: The ATLAS calorimeter type A and B read-out boards flattened [94].

The Hadronic Calorimeter.

The hadronic calorimeter (HAD-Cal) [91] is located after the EM-Cal. It is divided in four parts: The long central barrel covering the $|\eta| < 1.0$ region, one extended barrel on each side covering the $0.8 < |\eta| < 1.7$ region, two end-cap regions covering the $1.5 < |\eta| < 3.2$ region and two parts in the forward detector covering the $3.1 < |\eta| < 4.9$ region. Both the barrel and extended barrels are also sampling calorimeters with steel as an absorber and scintillating plastic tiles or plates as the active medium. Between the barrel and each of the extended barrels there is a gap of about 60 cm used for cables and services. In a region in these gaps there are intermediate tile calorimeters to maximize the active material. Each of the three barrels is divided in ϕ in 64 wedge shaped modules, each of which is built with 11 parts in depth, alternating between the absorbers and the scintillating tiles perpendicular to the beam axis. Each module has 11 types of tiles with the same thickness of 3 mm, the lengths and widths vary roughly from 200 mm to 400 mm and from 100 to 200 mm respectively depending on the tile type. Roughly 450,000 tiles are used in the whole TILE-Calorimeter. When a high energy hadron passes through the absorber, it interacts with the steel nuclei generating a shower of particles. When the particles from the shower enters the scintillator it radiates light, that is carried by wavelength shifting fibers to two photomultiplier tubes (PMTs) located in the outermost part of the modules, transforming it into electric currents. The intensity measured can be used a measurement of the incoming hadron. To calibrate the scintillator response, a ^{127}Cs γ source can be moved through small tubes across each tile. In figure 3.22 the layout of the 64 modules in a barrel is shown in the left while the design of one module is shown in the right. Similar to the LAr EM-Cal, the TILE-Cal modules are divided in three layers or samplings. For η=0 the thicknesses the first second and third layer are roughly 1.5, 4.1 and 1.8 hadronic interaction lengths λ. In the extended barrels the lengths are 1.5, 2.6 and 3.3 λ respectively. The granularity of the TILE-Cal is $2\pi/64 \approx 0.1$ rad. in the ϕ direction, while the η segmentation by grouping fibers into PMTs is 0.1 in the first two samplings and 0.2 in the third one. Each barrel module has 45 PMs, plus 32 in each extended barrel module for a total of 9856 read out channels.

The hadronic end-cap calorimeter (HEC) is also a sampling calorimeter, with copper as a passive absorber and LAr as the active material. Each end-cap is built with two wheels HEC1 and HEC2. Each wheel is built with 32 identical wedge shaped modules divided in 2 segments in depth. In the HEC1 there are 25 copper plates, the first one is 12.5 mm thick and the remaining 24 are 25 mm thick. In the HEC2 there are 17 copper plates, the first one is 25 mm thick and the remaining are 50 mm thick. In both wheels the copper plates are separated from each other by 8.5 mm gap filled with liquid argon. Each LAr gap has three boards dividing the gap in four. The middle board contains all the readout electronics, while the other two

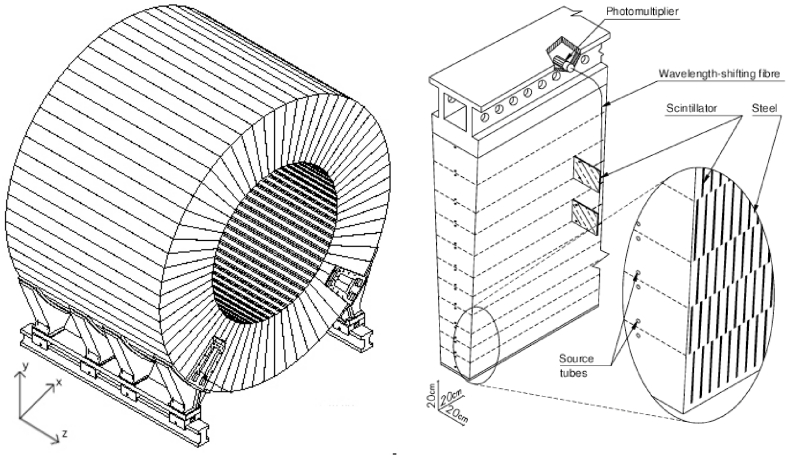

Figure 3.22: The ATLAS tile calorimeter modules. [95]

are needed for technical reasons as signal-noise optimization and high voltage reduction. The granularity in the $1.5 < |\eta| < 2.5$ region is 0.1×0.1 and 0.2×0.2 in the $2.5 < |\eta| < 3.2$ region for a total of 5632 readout channels.

The Forward Calorimeter.

The last piece of the calorimeter system is the forward calorimeter (FCal) [92]. It is built to measure the energy of particles in the forward region delimited by $3.1 < |\eta| < 4.9$. It consists of three blocks, the first one designed for EM energy and the remaining for hadronic energy. Due to the extreme conditions in forward region of the detector with high energy particle flux, the material used must be radiation hard. The active medium in all blocks is LAr and the absorbers are made of copper for the first layer (EM) and tungsten for the next two (Had). The copper layer was chosen mainly because of its high thermal conductivity, making it easier to cool down. For the hadron layers, cooling is less important and the tungsten is chosen mainly because its short λ helps it stopping hadronic showers in a short range. The first layer consists of many copper tubes parallel to the beam axis embedded in a copper matrix, both ground connected. Each tube has inside a copper electrode rod connected to positive high voltage. The gap between the tubes and the rods is filled with the liquid argon, and it is preserved by a helically coiled insulating PEEK plastic of 250 mm diameter. The right picture in figure 3.23 shows the structure of a tube for the first layer where the LAr gap is 0.250 mm. The second and third layers also use copper tubes but with tungsten rods electrodes. The matrix between the tubes is filled with several small tungsten slugs. The LAr gap in the second and third layer is roughly 0.375 and 0.5 mm respectively. The nearly 60,000 electrodes from the three blocks in both sides of the detector are readout by 3524 channels.

As the calorimeter measures the energy of the objets based on energy deposits in the calorimeter cells, the resolution is energy dependent, and in general is reduced for hich energy showers. The resolution of of a sampling calorimete can be parametrized by the resolution function given by:

$$\frac{\sigma_E}{E} = \frac{N}{E} \oplus \frac{S}{\sqrt{E}} \oplus C$$

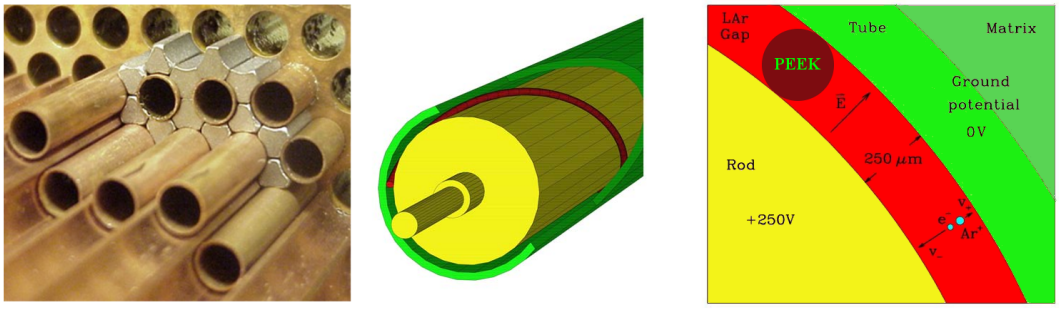

Figure 3.23: The ATLAS forward calorimeter array. Left: Matrix with tungsten slugs surrounding the copper tubes. Middle: Tube with electrode rod and readout pin surrounded by the PEEK plastic. Right: Cross section of an electrode showing the matrix, tube, LAr gap and the rod [92].

where N represents the noise term, S the stochastic term and C a constant term [61]. This parametrization is a way to separate the different contributions to the total resolution. The Noise term includes noise coming from electronic, detector and pileup activity. The nature of the noise term makes it the dominant term for energies below ~ 30 GeV, and depending on η, N spreads from ~ 0.5 GeV in the central region to ~ 1.5 GeV in the forward regions. The Stochastic term parametrizes statistical fluctuations in the energy measurement dominating for intermediate energies reaching $\sim 60\%\sqrt{\text{GeV}}$. For higher energies above ~ 400 GeV the constant term is the dominanting one. It parametrizes the fluctuations which grow linearly with the particle energy, such as losses due to inactive materials it was also tested and found to be $\sim 3\%$ [125]. Additional information of the ATLAS calorimeter resolution is presented in the last chapter when parametrizing the systematic uncertainties of the objects.

3.2.5 The Muon Spectrometer

The muon spectrometer [96] is the outermost part of the ATLAS detector. It consists of four different types of detectors: The monitored drift tube chambers (MDT), the cathode strips chambers (CSC), the resistive plate chambers (RPC) and the thin gap chambers (TGC). These sub-detectors are distributed in the barrel and two end caps with three layers each. The main task of the muon system is to measure the momentum and tracks of muons passing trough, which are bent by the superconducting toroidal magnet. The MS plays a main role for the triggering system containing two types of trigger chambers: The RPC and TGC that provide a fast signal output. It covers the $|\eta| < 2.7$ region. The overall layout of the different chambers is presented in figure 3.24.

The Monitored Drift Tube Chambers

Used in the barrel and end caps the MDTs are the basic components of the muon spectrometer for precise position measurements. MDTs contain many 30 mm diameter and 400 µm thick aluminum drift tubes filled with an $ArCO_2$ gas mixture with 93% Argon (Ar). In the center of each tube there is a tungsten (W) rhenium (Re) wire held at 3270 V. When a muon passes trough a tube, it ionizes the gas liberating electrons from the atoms, leaving a trail of electrons and ions that drift towards the center wire or to the walls on each case. Measuring the time that takes for the electrons to reach the wire at the center of the tube, it is possible to calculate traveled distance. With this information the trajectory of the muon passing trough can be inferred. The drift times are near 400 ns, higher as the bunch crossing rate. There are different

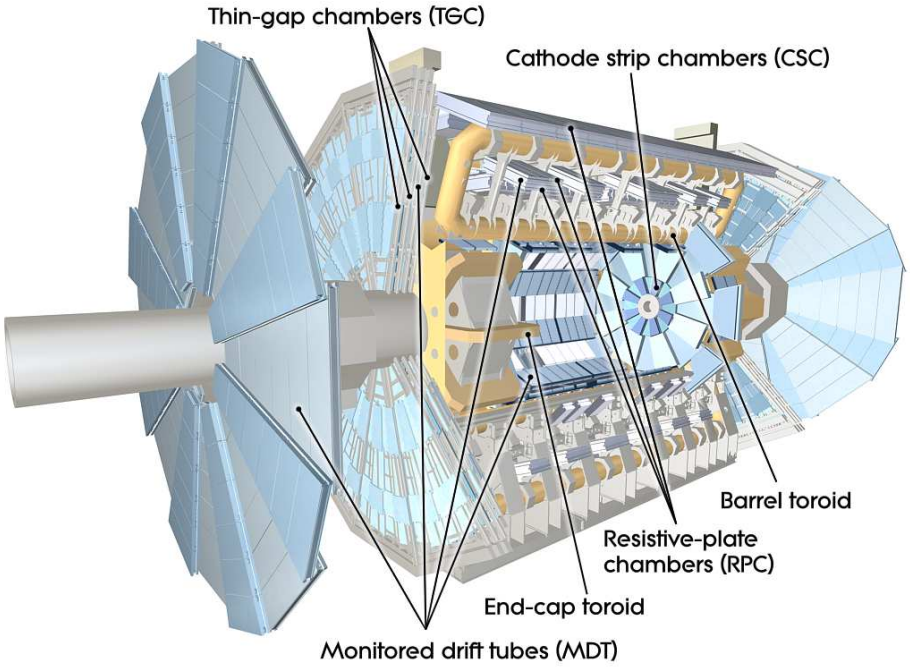

Figure 3.24: The muon detector array including its sub-detectors: MDTs, CSCs, RPCs and TGCs [61].

MDT chamber types depending on the location on the detector, each with different number of tubes, but most of them share a basic principle layout: Six or eight layers of parallel tubes, arranged in two groups of three or four layers on each side of the chamber, separated by 0, 8, 121, 170, or 317 mm depending on the chamber. The tubes in the MDTs are perpendicular to the beam axis and follow approximately the magnetic field lines. As a result each camber provides six to eight coordinates of a typical track resulting in one coordinate measurement with 40 μm precision per chamber and 30 μm using the three layers of MDTs in the whole detector. In total there are 1,194 chambers with 372,000 tubes, providing excellent track reconstruction plus a high reduction of random associations. A model of a standard MDT chamber is presented in the left picture of figure 3.25.

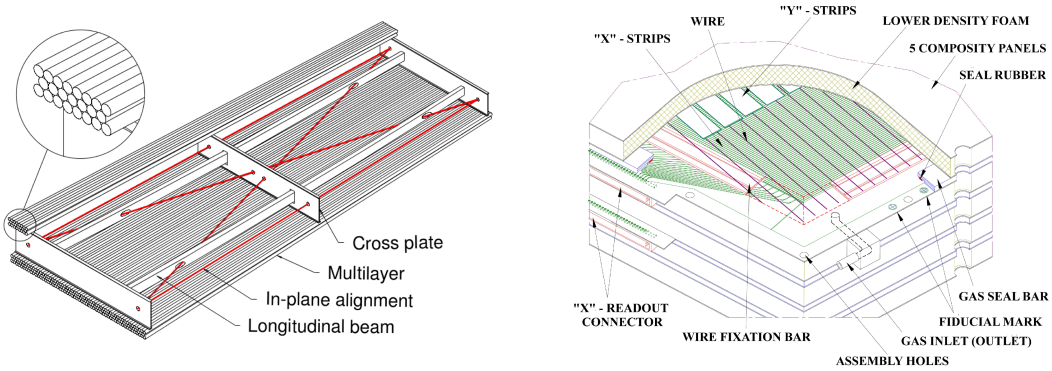

Figure 3.25: Left: A standard MDT chamber. Right: A cut view of a CSC layer [61].

The Cathode Strip Chambers

The CSC are only used in the innermost layer of the muon end caps in the $2.0 < |\eta| < 2.7$ region, where the extreme radiation conditions exceeds the rate limitations of the drift tubes. The CSCs are multi-wire proportional chambers with the following detecting principle: An array of anode wires is located between two conductive cathode plates with a mixture of Ar (80%) and CO_2 (20%) filling the gap. One cathode plate is divided in strips perpendicular to the wires providing the precision coordinate, the second is divided in strips parallel to the wires providing the transverse coordinate and a 2D coordinate measurement. The precision coordinate is obtained by the charge measurement induced on the cathode strips by the avalanche on the wires. When a muon passes trough, ionizing the gas atoms, the electrons and ions from the ionization process are accelerated by the electric field between anodes and cathodes generating a localized ionization cascade. The chambers are built with light construction materials to minimize multiple scattering and detector weight. Each end cap is built with 16 chambers: Eight in the *large-wheels* and eight in the *small-wheels* alternated and with a small ϕ overlap to avoid gaps. The space between the anode wires and the cathode plates is 2.5 mm, same as the anode wire pitch. In large-wheels (small-wheels) the precision cathode strips pitch is 5.308 mm (5.567 mm) while the transverse cathode strips coarser pitch is roughly 21.004 mm (12.922 mm). In total there are 61,440 cathode strips. A cut view of a standard CSC layer is presented in the right picture of figure 3.25.

To accurately reconstruct tracks and measure muon momentum, the precise alignment of the muon chambers is essential. The shape the chambers can be deformed by heat, gravity or torsion and it is controlled by an in-plane alignment (left picture in figure 3.25). The relative positions between chambers and within the detector is controlled in the barrel by a projective alignment scheme. Both methods need sophisticated optical system, consisting in one set (or a combination of 4 sets) of a coded mask illuminated by an infrared source, a lens and a ccd positioned in different points. For the end caps, a combination of optical and mechanical systems as reference bars, made of stable material is needed. At high background rates, the drift tube chambers operate at high occupancy levels. Independent and dedicated fast low-occupancy readout chambers covering the $|\eta| < 2.4$ region are used for the muon triggering system for which resolution loss is accepted to enhance fast readout.

The Resistive Plate Chambers

The RPC system provides trigger signals in the barrel region. They are gaseous parallel plate detectors consisting in two resistive plates made of Bakelite plastic kept parallel by 12 mm diameter and 2 mm thick insulating polycarbonate spacers, and creating the 2 mm gap that is filled with the gas mixture. The plates are orthogonally segmented into 30 to 40 mm width strips to provide two-dimensional measurements with a 1 cm space resolution and operated with a 4.9 kV/mm electric field. The main difference with the wire chambers is that while wire chambers have strong electric fields near the wires to create the avalanches, the RPCs have strong electric fields across the whole gas gap. This difference makes the drift velocities of electrons higher and the avalanches develop much faster, providing a time resolution of few nanoseconds. The chambers are mounted also in three layers in the barrel, one layer before and a second after the middle MDT layer. The third layer is located after the outermost MDT layer. Each chamber is made of two or four detector layers and four or eight readout strip panels. The MS uses 596 RPCs summing 355,000 readout channels.

The Thin Gap Chambers

The TGCs conform the muon trigger system used in the end caps. They are also multi wire proportional chambers but in contrast with the CSCs, the wire-cathode distance (1.4 mm) is

smaller than the distance between wires (1.8 mm) which is also smaller as the wire pitch in the CSCs. This reduces the readout time. Each chamber has two or three layers, that combined into one triplet plus two doublets, adds up to 7 layers in depth. For a trigger signal, depending on the granularity required per region, groups of anode wires are grouped together to only one readout channel. The number of grouped wires varies between 4 and 20 depending on $|\eta|$ for a total of 320,000 wire readout channels and 120,000 strip readout channels.

A total muon p_T resolution of $\sim 3\%$ is obtained in most of the detector with a reduced resolution of $\sim 5\%$ in specific regions of the detector due to the structure of the magnet coils and to in transition between the barrel and end-cap regions.

3.2.6 The Toroidal Magnets

The toroidal magnets are a distinct signature of the ATLAS detector, bending particles in the longitudinal plane. As shown in figure 3.26, it is built with three air-core superconducting toroid magnets, one in the barrel and two on each end cap. For the barrel, 8 superconducting coils are used, each ow which have its own cooling system. For each end cap, 8 superconducting coils are used, all of which share one cooling system. The end cap coils are rotated in ϕ by 22.5° with respect to the barrel coils, providing a radial overlap and optimizing the bending power in the transition region. Each coil is a flat racetrack coil with two double pancake windings, with 120 (116) turns in the barrel (endcap) providing a maximum magnetic field of 4 T.

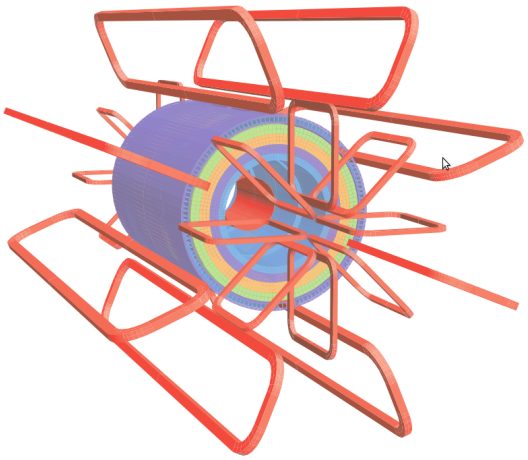

`Figure 3.26:` The ATLAS Toroidal Magnets: The barrel and the two end cap toroidal magnets [61].

3.2.7 Luminosity forward detectors

ATLAS is equipped with additional forward detectors, mainly for luminosity measurements.

The LUminosity measurement using a Cherenkov Integrating Detector (LUCID) [97] is the main luminosity detector of ATLAS. It is located beyond the end caps, 17 m apart from the interaction point along the $z-$axis on both sides of the detector. Due to the extreme conditions in the forward regions for Run 2, the LUCID detector was redesigned and rebuilt during LS1. It uses photomultipliers (PMT) with 7 and 10 mm diameter quartz windows which are used as a Cherenkov radiators. On each side of the detector, a module consists of 16 PMTs, grouped by 4 with ^{207}Bi source for calibration purpose. There are 4 additional groups of quartz fibers readout by PMTs located in a lower radiation area 1.5 m away. At the end

of the 2015 data-taking period, the total systematic uncertainty of the integrated luminosity was 2.1% [98]

The Absolute Luminosity For ATLAS (ALFA) detector [99] is located 240 m away from the interaction point on each side of the detector to cover the small angles in the forward region. The ALFA detectors, designed to measure inelastic forward proton scattering are contained in Roman Pots to approach the beam axis as close as 1 mm. It is build up from 500 µm squared scintillating fibers readout by multi-anode photomultiplier tubes.

During LS1 new Diamond Beam Monitors (DBM) [100] were designed to upgrade the existing Beam Conditions Monitor (BCM) [101] The BCM detector consists of eight diamond pad detectors that perform accurate time of flight measurements. The DBM inclusion complements the BCM's functionality implementing tracking capability. Thanks to its projective geometry, pointing towards the interaction region, the DBM also distinguishes particle tracks from the interaction point from background hits. When a particle passes through the sensor, it creates electron-hole pairs in the sensor that drift due to an electric field inducing a current trough the electrodes on the diamond's surface [102].

3.2.8 Trigger and Data Acquisition

During Run1 data taking period the LHC worked with a bunch crossing rate of 20 MHz, i.e. 50 ns bunch spacing. For Run 2 the bunch space was reduced to 25 ns increasing the rate to 40 MHz. At such rates, is impossible to save the information from all readout channels for all events. To tackle this problem the ATLAS has a dedicated trigger system [61, 103] to quickly filter only a small fraction of events containing relevant physics information. It first waits for all sub detectors to finish reading out the signals of each event. Then, additional time is needed to gather this information and create a rough picture of the interesting objects. Based on this information, a decicion is made whether the event contains relevant physics information or not. As this process takes longer than the bunch crossing rate, storage buffers are needed to temporarily save all read out information During Run1 The trigger system consisted in three

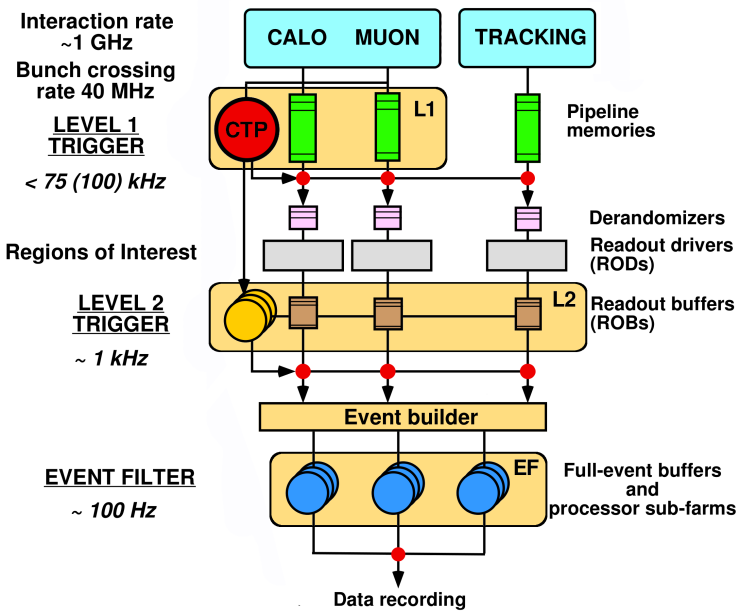

Figure 3.27: The ATLAS trigger system during Run1. Based on [62].

decision steps or levels as shown on figure 3.27. The first trigger level (L1) is hardware based.

L1 algorithms uses only energy depositions in the calorimeters (L1Calo) and hits in the muon system (L1Muon).

L1Calo uses a sliding window algorithm [104] on trigger towers[9] searching for local maxima of energy depositions called Regions of Interest (RoIs). L1Calo is divided in two different subprocessors: The Cluster Processor (CP) and the the Jet/Energy Sum Processor (JEP).

- The CP is used to identify e/γ[10] and τ candidates. To identify leptons and photons and to suppress QCD background, isolation criteria and a veto on hadron showers are applied. Isolation is achieved identifying the ROIs core only in the EM calorimeter in a region of 2×2 trigger towers, if the energy sum of the 12 towers around the core is above a certain threshold, the ROI is vetoed as an isolated e/γ object. If the energy in a 4×4 hadronic tower around the same core center is significant, the region is vetoed as an e/γ candidate. To identify hadronically decaying tau leptons, the energy in the surrounding 12 hadronic towers is added for a similar isolation criteria, with no veto on the hadronic energy.

- The JEP is used to identify jet candidates and to sum the total transverse energy in each event. JEP algorithms use coarser regions built of 2×2 trigger towers in both calorimeters called jet elements. To identify jet candidates, the JEP searches for ROIs of 2×2, 3×3 or 4×4 jet elements. The transverse energy sum for each ROI must be above a defined threshold to be considered as a jet candidate. To evaluate the total transverse energy, the energy depositions in each jet element is projected into the transverse plane and added up. L1 missing energy is calculated by evaluating the vectorial sum of all jet elements energy pointing in the opposite direction.

Jet triggers are used only within $|\eta| < 3.2$. For total and missing transverse energy triggers, it is also crucial to include the forward region with $|\eta| < 4.9$. A sketch of the L1Calo geometry and algorithms is presented in figure 3.28.

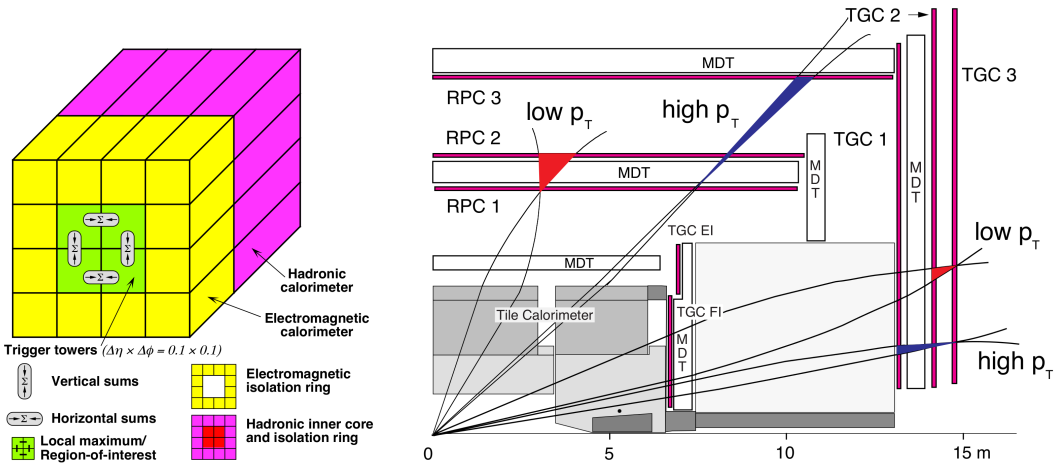

Figure 3.28: Visualization of the ATLAS L1Calo and L1Muon algorithms [61].

L1Muon uses the hits in the muon trigger chambers. The algorithms are based on finding coincidences between the different chambers (layers), tracking muons coming from

[9] Trigger towers are 0,1×0,1 regions in the $\eta - \phi$ plane projected radially in the whole EM and Had calorimeter. In forward regions the granularity of the trigger towers is coarser.

[10] As no tracks are used in L1, electrons and photons can not yet be distinguished.

the interaction point. Whenever a hit is measured in the first layer, a search for a hit in the second layer begins. The second hit must be centered within a coincidence window around the expected impact point of a track originated at the center of the detector. The area of such windows depends on the momentum threshold of each trigger item, as it depends on the bending of the track due to the toroidal magnet. A sketch of the L1Muon geometry and algorithm is shown in figure 3.28.

The output from L1Calo and L1Muon triggers is carried to the Central Trigger Processor (CTP) where it is combined and used to make decisions based on logical expressions or Trigger Items. Trigger Items are a combination of the different requirements of the input data defined in the trigger menu and stored in look-up tables. Only a limited number of items are available for the trigger menu. The CTP reduces the readout rate to less than 100 kHz. If an event satisfies the criteria of a trigger menu the object types, energy deposition, muon hits and coarse spatial information are passed to the next trigger.

L2 is a software based trigger that process finer information and includes track information within few milliseconds reducing the output rate to few kHz. If an event passes the L2 trigger, the event building is done to finally proceed to the third level called Event Filter (EF). The EF is also software based, it runs full reconstruction algorithms similar to the off-line analysis including calibrations, corrections, and advanced algorithms within seconds, reducing the rate to the order of 100 Hz. If an event finally passed the EF it was recorded in disks as RAW data, including information of the full ATLAS detector

With LHC Run2 conditions the trigger rates should roughly increase by a factor of fife; a factor of two coming from increasing the collision energy from 8 to 13 TeV, and an additional 2.5 factor from the peak-luminosity increase. The bunch spacing reduction from 50 to 25 ns can help controlling the in-time pile-up but it could increase the out-of-time pile-up. It may also increase beam-induced fake trigger rates. After Run1 during LS1 important upgrades to the ATLAS trigger system [105–108] were implemented to work under higher rates, maintaining or improving the selection efficiencies of relevant physics processes. Among the upgrades there are changes in L1Calo, the introduction of a new L1 topological trigger (L1Topo), improvements in L1Muon and the merging of L2 and EF into a single event filter farm. For Run2, the new

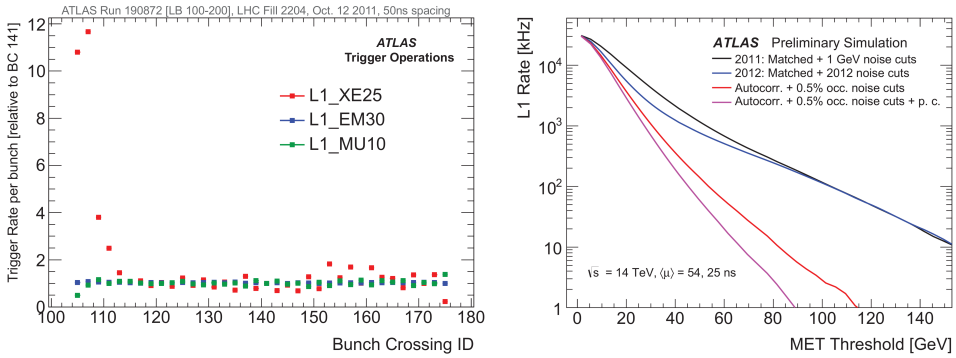

`Figure 3.29:` Left: E_T^{miss} trigger rates afected by pileup. Right: Pedestal substraction rate reduction [109].

two-stage system should reduce the rates of 40 MHz to a recording rate of 1 kHz at the High Level Trigger (HLT). L1 consists now of the L1Calo, L1Muon, the new L1Topo and the CTP. For the HLT, fast algorithms running on L1 ROIs and off-line-like algorithms running over the full-event information can run on a unique PC farm with a processing time of 0.2 s. The main problem of the L1Calo was the high rates of E_T^{miss} triggers affected by pile-up close to the start of a bunch train, this clearly presented in the left plot of fig 3.29 where the rates for three

different L1 triggers for a Run 1 event are plotted as a function of the bunch crossing identifier (BCID) for a typical bunch train. For Run 2, the signal processing is more flexible thanks to the new Multi-Chip Modules (nMCM) built with FPGAs instead of ASICs. The ASICs allowed for a dynamical pedestal subtraction based on a global cell occupancy and bunch position in each bunch train. With this correction, the rate for a 70 GeV threshold E_T^{miss} trigger, was reduced by a factor of 50 as it is hown in the right plot of figure 3.29. Another improvement of the L1 system, is that the number of thresholds available for the different L1 trigger objects are increased from 12 to 25 for jets and from 8 to 16 for both EM and tau clusters. In addition to the nMCM modules, new L1 Topological trigger modules (L1Topo) [110] were added. L1Topo modules are capable of calculating event topological quantities between L1 objects and make decisions based on these quantities within 2 µs. Typical example of these variables are angular separation between L1 objects, invariant mass reconstruction for pairs of objects, sum of jets' E_T, transverse energy and $\Delta\phi$ between L1 E_T^{miss} and other L1 objects. The inclusion of these variables improves the signal to background separation, isolation and overlap removal, they are also helpful for B-physics di-muon events with low p_T, fat jets identification, final states with E_T^{miss}, jets, τ jets and taus.

Improvements in the L1Muon were made to improve the main issue during Run 1: Fake rates coming from low p_T protons in the forward regions. With a 25 ns bunch crossing, this rate was expected to increase. The solution was to introduce a requirement for extra coincidences between the end cap TGC and the new inner muon chambers in the small wheel with the extended barrel of the tile calorimeter. With these extra coincidences a 50 % rate reduction was obtained for background L1 muons with a $p_T > 20$ GeV in the $1.0 < |\eta| < 1.9$ region.

Chapter 4

Objects Definition and Reconstruction

The search for SUSY with leptons, jets and E_T^{miss} uses all detector components to identify the interesting objects. A proper object definition is crucial for any analysis. The analysis has two selection steps. First candidate objects are identified using a pre-selection with loose criteria. After the pre-selection, some objects need to pass tighter criteria. The final objects are then used for the event selection, and to define the different analysis regions.

4.1 Tracks

The ATLAS track reconstruction [111], uses partial and full track pattern recognition algorithms to search for hits triggered by the same charged particle. All relevant track parameters are estimated from a track fit with the hits found. The ID track reconstruction is limited to $|\eta| < 2.5$, and only tracks with $p_T > 400$ MeV are considered. The main sequence chain is the *inside-out* algorithm, that first finds clusters of connected cells in the silicon detectors, and transforms them in 3D space points. TRT tubes are also included building drift circles around the wires. With the three dimensional space points, track seeds are created combining three space points. To reduce the number of possible seeds, a set of initial cuts are applied. Track seeds passing the cuts are used as an input by a track finding algorithm, which uses a Kalman filter to build *loose* track candidates. Shared track candidates from close-by particles and fake tracks are managed by the ambiguity solver, that assigns and compares scores between individual tracks. The scores are based on several variables such as number of clusters per track, number of holes and number of shared points per track. For shared tracks, a Neural Network (NN) is used to judge if they can be split into two tracks. If the tracks are indistinguishable, the candidates are discarded, leading to inefficiencies. If two tracks are separated by a distance of one single pixel, the efficiency to split a multi-particle cluster into two tracks is above 80% for the IBL layer, and above 90% for the second layer of the ID [112].

From tracks passing the previous requirements, the ones pointing to a region covered by the TRT, are extended to it, adding TRT hits to the track. A successful TRT extension extends the track length, significantly improving momentum resolution. This effect is enhanced for high p_T tracks as shown on figure 4.1 during a cosmic ray data taking period in 2008.

Increasing from 8 to 13 TeV, leads to more particles per collision and the average pile-up μ was foreseen to increase from 20 to 40, doubling the high level trigger rate to an expected value of 1 kHz. Under these assumptions plus budget limitations for computing

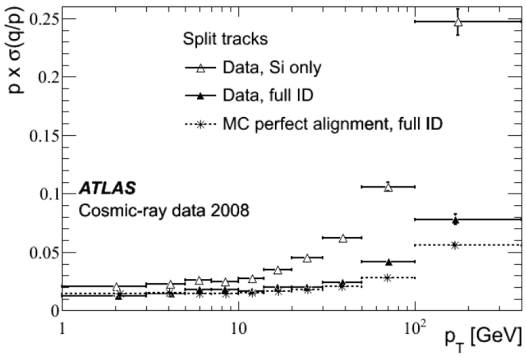

Figure 4.1: p_T resolution improvement using the TRT vs silicon sensors only [113].

resources, there was a requirement to decrease the event processing rate by at least a factor of three [111]. The main changes to track reconstruction started in the final phase of the

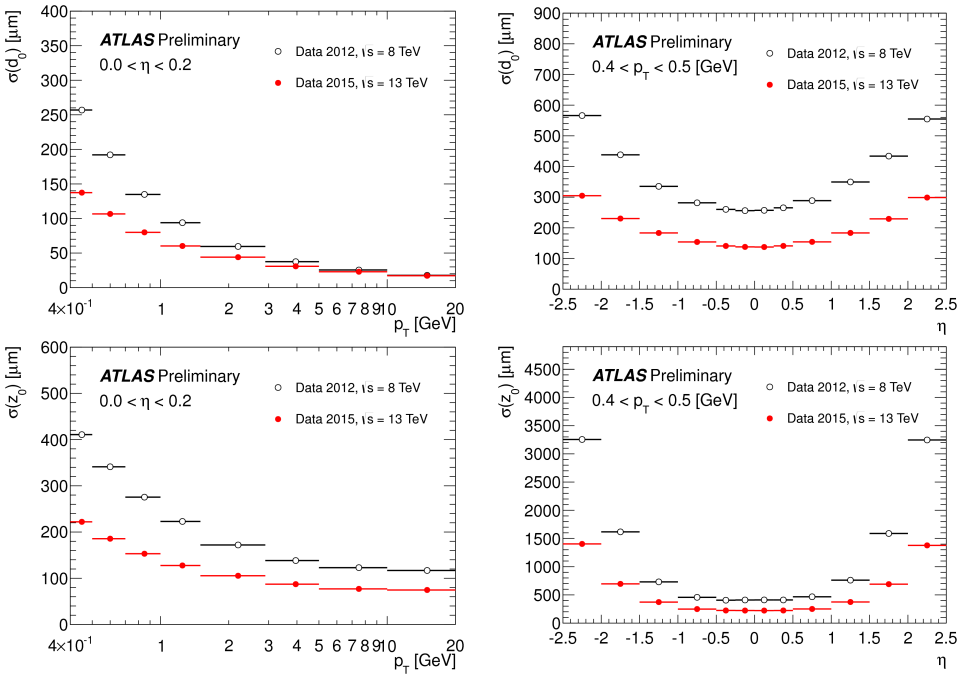

Figure 4.2: Impact parameter resolution improvement with the IBL. Up/Down: d_0/z_0. Left: As a function of p_T for $0.0 < |\eta| < 0.2$ range. Right: As a function of η for $0.4 < p_T < 0.5$ range [114].

2012 data taking period, where the high pileup μ values required larger CPU time. To reduce the reconstruction time, infrastructure and event data updates plus algorithm changes were made. The infrastructure changes included math libraries, the cleanup of the tracking event data model and the optimization of the access to the magnetic field map. Algorithms changes included track seeding updates, tracking in dense environments (TIDE) [115, 116] and task optimization. The TIDE improvements reduced the ID reconstruction time by 10% and also increased the efficiency to find tracks in dense environments. The processing time after all these changes was reduced by a factor of four. Tracking resolution also improved with the the installation of the IBL. The resolution improvement on the impact parameter reconstruction

is presented in figure 4.2.

4.2 Vertices

Vertex reconstruction [117] searches for seeds obtained from the z position of reconstructed tracks. The seeds are used iteratively in a χ^2 fit including the seed, tracks nearby and the beam spot as a constraint. Tracks beyond 7σ from the fitted vertex are used to seed the next vertex until no more vertices can be found. The primary vertex needs to be consistent with the interaction point ($d_0 < 1.5$ cm and $z_0 < 1.5$ cm) and must have at least two tracks with $p_T > 400$ MeV associated to it. If more than one of these vertices are found, the one with highest p_T^2 sum of the associated tracks is kept. Not only the reconstruction of the primary vertex is important, but also the reconstruction of additional vertices. A proper reconstruction of additional vertices plays a key role in the treatment of pileup, allowing to perform corrections to objects and to distinguish jets originating in the hard scattering from softer jets originating from pileup. In figure 4.3, the number of reconstructed vertices as a function of the average interactions per bunch crossing μ is shown for a ttbar simulation with the 2015 reconstruction algorithm. The reconstruction of secondary vertices is also crucial to differentiate for example jets coming from heavy hadrons or electrons coming from converted photons.

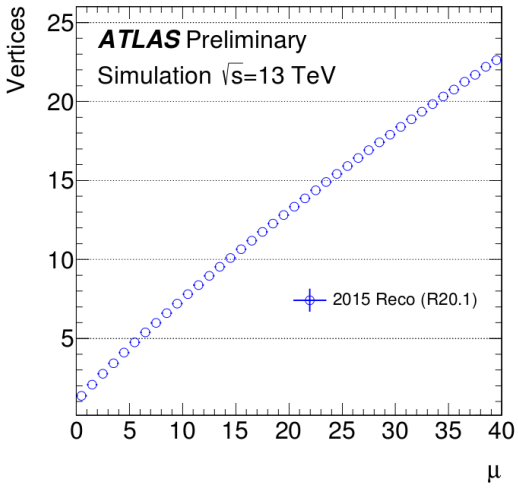

Figure 4.3: Number of reconstructed vertices vs pileup for 2015 reconstruction algorithms [118].

4.3 Jets

A detailed description of the jet reconstruction and calibration procedure is outside the scope of this thesis. In this chapter, only a brief explanation of the different steps involved are presented. To reconstruct Jets [119, 120], energy deposits in the hadronic calorimeter are used. First, three dimensional topological clusters are built selecting *seed* cells with energy depositions significantly above the noise level. Then, neighboring cells are added to the cluster if their energy is at least twice the noise level. Finally all neighboring cells are added without any threshold requirement. The noise per cell can be estimated by adding in quadrature the electronic noise and the expected pileup noise. As showed in figure 4.4 the noise levels for

different configurations is highly η dependent. In the η region relevant for this work, the noise level per cell is always less than 1 GeV.

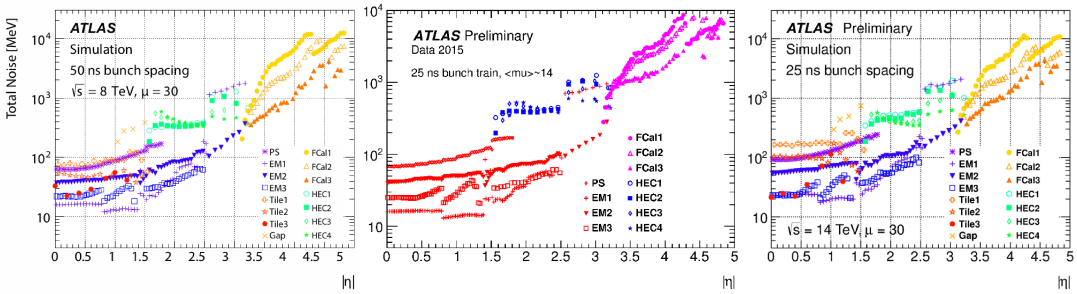

Figure 4.4: Total noise including electronics and pileup at cell level as a function of pseudo-rapidity. Left: Simulated noise for the 2012 configuration with $\mu = 30$ [119]. Middle: RMS total noise measured per LAr cell for 2015 data with $\mu = 14$, and 25 ns run [121]. Right: Simulated noise for $\sqrt{s} = 14$ TeV, $\mu = 30$, 25 ns and $L = 1.09 \times 10^{34} cm^{-2} s^{-1}$ [122]

To obtain the jet energy from the calorimeter cells, topological clusters have to be properly calibrated before jet reconstruction. Jets leave energy in the hadronic calorimeter but also in the electromagnetic calorimeter. As the response from both calorimeters is different, clusters can be calibrated with the EM calibration (which correctly measures the EM energy depositions), or with the local cluster weighting (LCW) calibration (where local cluster weights are assigned to compensate lost energy in hadronic clusters). In this work, clusters are calibrated with the EM calibration. More details on jet calibration can be found in [124,125]. The cluster reconstruction algorithm was modified for run 2. The main difference with respect to run 1, is that clusters are now forbidden from growing in the calorimeter pre-sampler. This prevents the formation of large clusters dominated by pileup noise generated from low pileup energy depositions only reaching the pre-sampler [123].

After calibrating its energy, topological clusters are re-clustered to form jet clusters using the anti-k_t algorithm [126] with $R = 0.4$. Once the jet clustering is done, an origin correction is performed: As the interaction point can be different from the detector center, correction in η to jets is done. After the origin correction, an area based pileup correction is made: Jets arising from pileup vertices could be reconstructed, leading to additional jets in an event. Pileup energy may also add up to hard jets, affecting their energy. Both effects must be considered to properly analyze any physics process. To correct for pileup energy in top of hard jets, two different corrections steps are applied one after another [128, 129]. The first step consists in an event by event correction which uses the jet area A and the median p_T density ρ (that accounts for the pileup activity per event). The jet area is obtained using an active area algorithm [130], which uniformly adds infinitesimal momentum ghost particles to the event before jet clustering. The number of ghosts clustered to one jet is a measure of its area. To obtain the pileup energy density ρ of the event, a k_t algorithm [131] with $R = 0.4$ is used. The energy density of each jet is defined as p_T/A. Pileup energy density ρ is obtained by the median energy density of all jets: $\rho = median(p_T^i/A_T^i)$, where A_T, represents the transverse component of the jet area A. Figure 4.5 shows the ρ distribution for a 13 TeV MC di-jet simulation with different numbers of primary vertices. With the definition of A and ρ, the corrected jet p_T can be written as:

$$p_T^{corr} = p_T^{uncorr} - \rho \cdot A_T \tag{4.1}$$

After the area correction, there is still a pile-up dependence of the jet p_T. This is why a

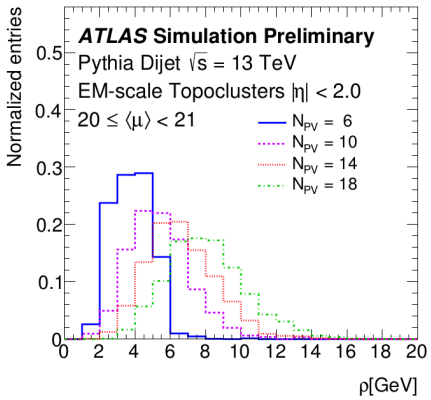

Figure 4.5: ρ distribution for 2015, 25 ns, 13 TeV MC dijet simulation for 6 to 18 N_{PV} is shown, for EM jets with $|\eta| < 2.0$, for events with an average interactions per bunch crossing μ between 20 and 21 [123].

second step for pileup correction is performed. The second step, normally referred as residual

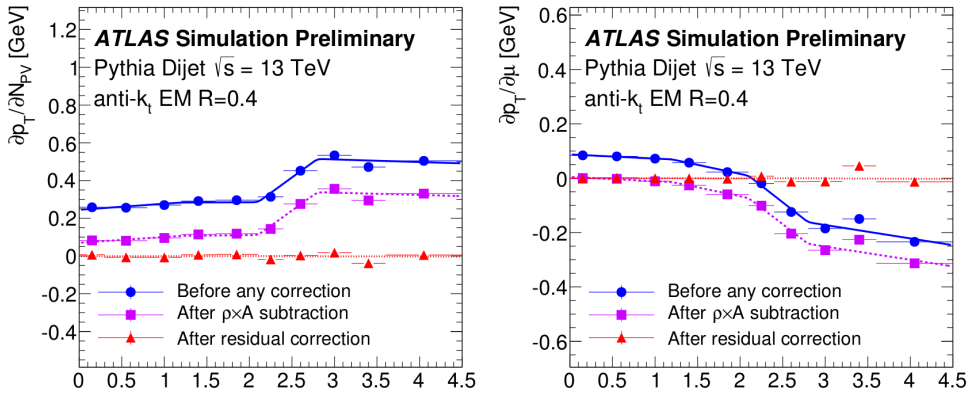

Figure 4.6: Pileup correction including the area and residual correction. Left: p_T dependence on N_{PV}. Right: p_T dependence on μ [123].

pileup correction, is applied as a function of N_{PV} and μ. The residual pileup correction takes care of the residual in-time and out-of-time effects. The full pileup correction can be expressed as:

$$p_T^{corr} = p_T^{uncorr} - \rho \cdot A_T - \alpha \cdot (N_{PV} - 1) - \beta \cdot < \mu > \tag{4.2}$$

where α and β are obtained from a fit using the residual pileup dependence in a nominal MC sample. The fit to obtain α and β is shown in figure 4.6. In the figure, the full pileup correction effect is also presented as a function of η.

To obtain the parton energy from the jet energy, the jet energy scale (JES) has to be calibrated. This calibration is done after the vertex and pileup corrections, and it is based on the reconstructed jet energy and truth jet energy relation from a dedicated di-jet MC simulation. Given the nature of the method, the correction factor is p_T and η dependent. Figure 4.7 shows the average energy response $R = E^{reco}/E^{truth}$ as a function of η for different truth energies, showing a clear drop for lower energies and in the gaps between sub detectors. The jet calibration factor corresponds to the inverse of the average energy response.

The calibrations and corrections applied, are related to the longitudinal and transverse

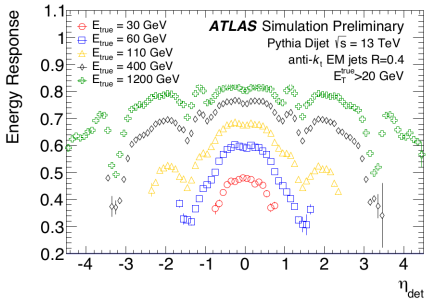

Figure 4.7: Energy response for a di-jet simulation shows a clear p_T and η dependence [123].

characteristics of the jets. Being uncorrelated, the corrections can be applied sequentially. After the p_T and η-based energy calibration, five global sequential corrections [124, 132] are applied sequentially, to reduce possible tails in the response distributions caused by highly energetic jets not fully contained by the calorimeter. These are also a MC based corrections that use data from the calorimeter, inner detector and muon chambers to improve the jet energy resolution (JER), leaving the energy unaltered. After the global sequential corrections, there are *In Situ* calibrations, used to correct differences in the jet p_T between data and MC simulation. Despite the previous corrections, MC modeling will never provide the perfect representation of data. Differences can be attributed to the simulation of the underlying events, jet formation, pileup, electromagnetic or hadronic interactions within the detector and the modeling of the detector material between others. Finally, jets in data are corrected to change their calibration based on *In Situ* studies performed in Run-1 [125, 135]. Such calibration is based on balancing well measured objects from well understood γZ+jets and multi-jets processes using a *tag and probe* method [133, 134]. The *In Situ* calibration modifies both the energy and direction of jets. In figure 4.8 the individual and combined jet response ratio of data to MC as a function of p_T is shown. This calibration can be used with 2015 data if the changes from 2012 to 2015 are modeled in the MC simulations, and if the uncertainties in such modeling is included as a systematic uncertainty.

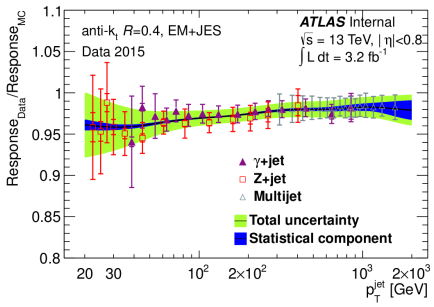

Figure 4.8: Jet response ratio of data to MC as a function of p_T for anti-k_t jets with $R = 0.4$ calibrated with the EM+JES scheme. The dark line shows the result of the combination of the three *In Situ* analyses, the outer band represents the total uncertainty resulting from the combination including systematic uncertainties, and the inner band represents the pure statistical uncertainties [135].

After correcting the jet energy from pileup, additional jets coming from pileup vertices are taken into account using a likelihood method called jet-vertex tagger (JVT) [127]. JVT is an upgrade of the jet-vertex fraction (JVF) [268] used for previous similar analysis. The JVF measures the probability for a jet to come from a primary vertex. It is defined as the ratio of the scalar sum of transverse momenta from all jet tracks coming from the primary vertex, over

the scalar sum of the transverse momenta of all tracks associated to the jet without vertex matching. A graphic explanation of JVF is presented in the left picture of figure 4.9. JVF may take values between 0 and 1. A value of -1 is assigned to jets with no associated tracks. In the plot on the right of figure 4.9 a typical distribution of JVF for a primary vertex is shown.

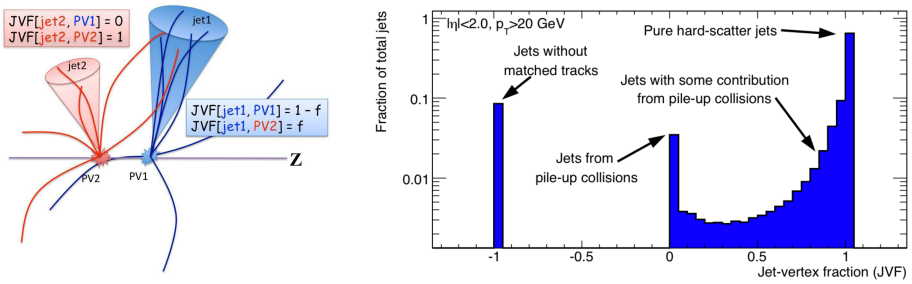

`Figure 4.9:` Left: Graphic representation of the the JVF variable. Right: Typical JVF distribution of a selected primary vertex for simulated di-jet events [268].

JVF provided an excellent separation power between hard scattered jets and jets originating from additional interactions. Nevertheless, as JVF definition depends heavily on N_{Vtx}, when a JFV cut is applied to reject pileup jets, a jet efficiency dependence on N_{Vtx} is induced. This effect is shown in the right plot on figure 4.10. To suppress pileup jets without introducing a N_{Vtx} dependence on hard-scatter jet efficiency, two new variables were developed and combined. The first variable ($corrJVF$) is defined similar to JVF with a small correction on the denominator, where the p_T sum of all tracks associated to the jet coming from non primary vertices is divided by a factor proportional to the total number of pileup tracks per event. The shape of JVT and the effect of this correction comparing JVFcorr and JVF for simulated di-jet events is presented in figure 4.10. The second variable used for the JVT

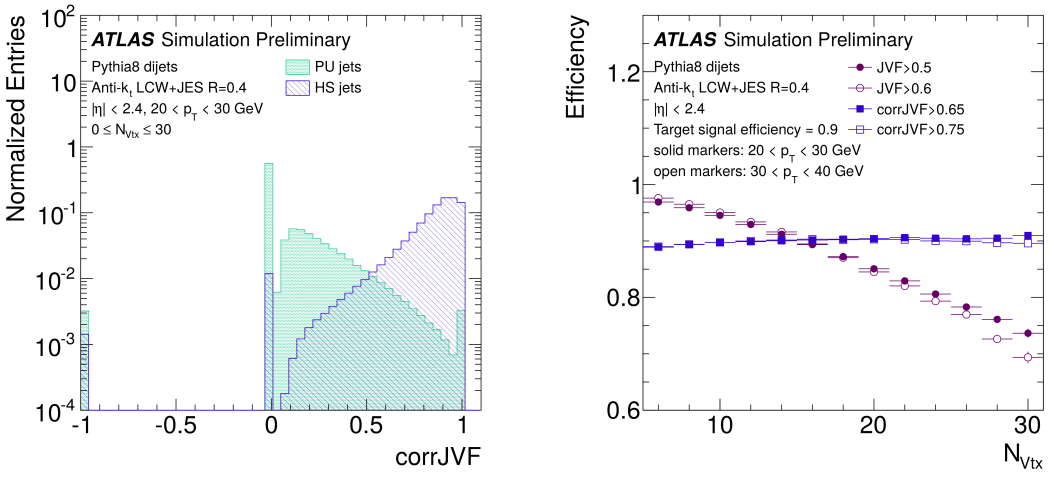

`Figure 4.10:` Left: corrJVF distribution for pileup and hard jets with 20 GeV $< p_T <$ 30 GeV. Right: Effect of the correction for corrJVF compared to JVF. The dependence of the hard jet efficiency for 20 GeV $< p_T <$ 30 GeV (filled markers) and 30 GeV $< p_T <$ 40 GeV (empty markers) jets for fixed corrJVF and JVF, keeping the inclusive efficiency at 90% [127].

calculation is R_{pT} which also uses the scalar p_T sum of all jet tracks coming from the primary vertex, this time divided by the fully calibrated jet p_T after pileup jet energy corrections. For pileup jets, R_{pT} peaks at zero and falls steeply, as only a small amount of p_T comes from the primary vertex. For hard jets, the mean value is higher and the distribution spreads over a wider range. Using only hard tracks from the primary vertex, R_{pT} does not depend directly on N_{Vtx}. In figure 4.11 (left) the shape of R_{pT} for hard and pileup jets is presented, while in the right plot the N_{Vtx} dependance is shown for a simulated di-jet sample.

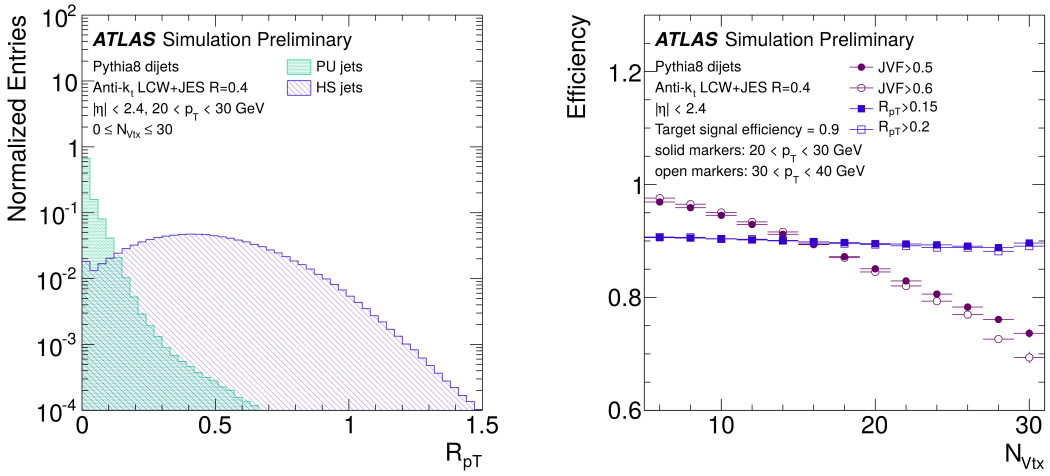

Figure 4.11: Left: R_{pT} distribution for pileup and hard jets with 20 GeV $< p_T <$ 30 GeV. Right: N_{Vtx} dependence of the hard jet efficiency for 20 $GeV < p_T <$ 30 GeV (filled markers) and 30 GeV $< p_T <$ 40 GeV (empty markers) jets, for fixed R_{pT} requirements such that the inclusive efficiency is 90%. JVF efficiency is also shown for comparison. [127]

Using these two variables, the JVT discriminant is built as a 2 dimensional likelihood. More details on how JVT is built can be found in [127]. JVT also ranges from 0 to 1 values with a value of -0.1 assigned to jets with no associated tracks. In the left plot of Figure 4.12 a distribution of JVT for di-jet simulated samples is shown, where the separation power is explicit. On the right plot in figure 4.12, the pileup jet fake rate as a function of the number of reconstructed primary vertices is shown, where the minimal JVT and JVF requirements are made such that the inclusive hard jet efficiency is 90%.

After jet calibration, the analysis specific jet requirements are imposed. For the 13 TeV analysis presented here, preselected jets are required to have $p_T > 20$ GeV and to be in the $|\eta|$ <4.5 region[1]. To define signal jets with tighter cuts, the definition of other objects is needed. Signal objects definitions will be given in section 7.2 after defining the pre-selection requirements of other objects.

4.3.1 Heavy flavor jets

To identify jets coming from $b-$quarks, a the MV2c20 $b-$tagging algorithm is used [136]. With the introduction of the IBL, plus all tracking algorithm enhancements, $b-$tagging has had significant improvements with respect to Run-1[2] MV1 method [136]. These algorithms rely

[1] For the 8 TeV analysis, there is a smaller window covering only $|\eta| < 2.5$

[2] The details concerning Run-1 $b-$tagging algorithms and performance, relevant for the 8 TeV analysis can be found in [136, 137]

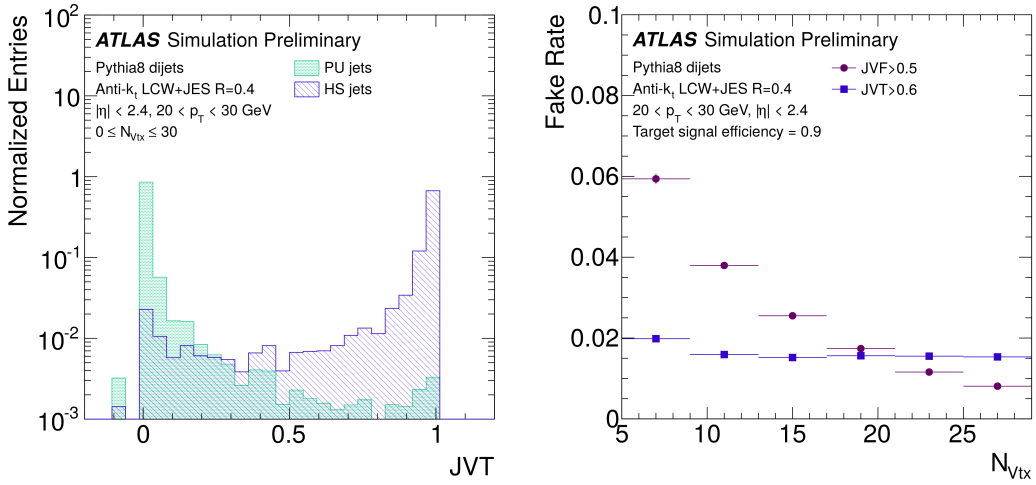

Figure 4.12: Left: Distribution of JVT for pileup and hard jets with $20 < p_T < 30$ GeV. Right: N_{Vtx} dependence of the pileup jet fake rate for the JVT and JVF requirements that keeps an inclusive hard jet efficiency at 90%. [127]

heavily on charged particle tracks reconstructed in the ID with an acceptance up to $|\eta| < 2.5$. With the ID tracks, the algorithms evaluate a set of variables used to discriminate jet flavor. Tracks are first associated to a jet and then are required to pass a variety of quality criteria depending on the algorithm. ATLAS uses three basic and complementary algorithms: The impact parameter based algorithm, the inclusive secondary vertex reconstruction algorithm and the decay chain multi-vertex reconstruction algorithm. The output obtained from these algorithms is used as the input for a boosted decision tree (BDT), trained to discriminates between b, c or light jets. The MV2c20 output distribution and the performance of MV2c20 (compared to the MV2c00 algorithm) are presented in the left and right plots of figure 4.13 respectively. The operating point chosen, corresponding to a fixed MV2c20 value provides an

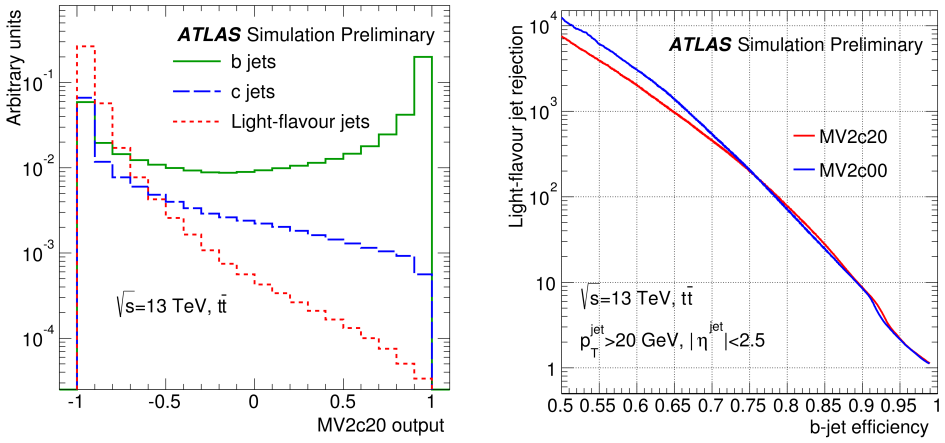

Figure 4.13: Left: MV2c20 distribution for b, c and light-flavor jets. Right: Light-flavor rejection versus $b-$jet efficiency for the MV2c20 (red) and MV2c00 (blue) algorithms [136].

inclusive b-tagging efficiency of 77% for simulated $t\bar{t}$ events, with a rejection factor of 140 for light jets and 4.5 for charm jets.

4.4 Electrons

Electrons can be identified with great detail, and their properties can be measured with high precision. This is achieved by combining energy clusters in the calorimeter cells with tracks from the inner detector. Electron recognition is divided in reconstruction and identification. The combination of calorimeter information with ID tracks limit electron positions to $|\eta| < 2.47$. The one lepton analysis presented combines two independent analysis, one with a *Soft* lepton and the second with a *Hard* lepton. The work presented has an emphasis on the *Hard* lepton analysis, but the soft lepton definitions will also be included.

4.4.1 Electron Reconstruction

Electron reconstruction is performed in few steps [138]:

- **Seed-cluster reconstruction:** Energy deposits in the EM calorimeter are clustered using a sliding window clustering algorithm [120]. First, the $\eta - \phi$ space is divided in $N_\eta \times N\phi = 200 \times 256$ cells of $\Delta_\eta \times \Delta_\phi = 0.025 \times 0.025$. Calorimeter towers are defined by summing the energy of the cells in depth for all longitudinal calorimeter layers. Then, EM clusters are seeded from such towers using a fixed size window of 2×5 cells (0.075×0.125). This fixed size window is moved across the calorimeter and if the total E_T of the towers contained by the window is a local maximum above a 2.5 GeV threshold, a pre-cluster is defined. Duplicate pre-clusters may result from real physics processes as the emission of bremsstrahlung for electrons or photon conversions. Fake pre-clusters can can be built just from EM noise. In case of duplicate clusters from physical processes, the secondary particle will cluster very close to the main particle. If the distance between both clusters is less than 0.3, the clusters are considered to be duplicated, and the cluster with highest E_T is kept. For larger ΔR, one of the two clusters is considered to be a fake. The final size of the cluster depends on how many cells are added with the clustering algorithm, depending on a *loose* shower shape criteria applied to the energy fractions across the calorimeter layers.

- **Track candidate reconstruction:** Electron track reconstruction is done in two steps: First the energy pattern is recognized, by studying the energy loss due to interactions with the detector material. The tracking algorithm defines a track seed as three hits in the silicon detector, and tries to reconstruct the track under a charged pion hypothesis. If a track seed with $p_T > 1$ GeV matching one of the EM clusters can not be extended to a full track with a minimum of seven hits using the pion hypothesis, an electron hypothesis is tested allowing additional energy loss. The second step consists to fit track candidates using the same hypothesis as for pattern recognition with the Global χ^2 Track Fitter [139]. If the track candidate fails the pion hypothesis track fit[3], the track is refitted using the electron hypothesis. Finally an electron specific track fit is performed, where the tracks found by the previous step are loosely matched to EM clusters. Tracks with more than three precision hits loosely associated to electron clusters are refitted using an optimized Gaussian Sum Filter (GSF) [140] which takes into account non standard bremsstrahlung effects.

- **Electron candidate reconstruction:** It consists of similar matching as the latter to refit track with tighter GSF requirements. Matching the track candidate to the

[3]High energy loss due to bremsstrahlung may result in high χ^2 value

cluster seed completes the electron reconstruction. If more than one track fulfills the final matching conditions, the track is chosen based on the ΔR distance between the cluster and the track, the number of pixel hits, and the presence of a hit in the IBL. Electron candidates with no associated track are removed and considered to be photons. An electron clustering is re-done using 3×7 EM towers. The energy of the clusters is calibrated to the electron energy using different techniques including inter-layer calibration to correct for non-uniformities; energy corrections based on a multivariate analysis of the candidate properties; η dependent energy scale correction based on $Z \rightarrow ee$ events and an additional smearing to MC to account for data-MC differences.

The final electron kinematics is computed using both the calibrated energy cluster and the best track matched to it. The energy is taken from the calibrated cluster, while the spatial positions are taken from the corresponding track parameters. In an attempt to reduce background from conversions and secondary particles, electron tracks are also required to be consistent with the interaction point, thus a requirements on $\sin\theta$, z_0, d_0, and its uncertainty σ_{d_0} is applied:

$$z_0 \sin\theta < 0.5 \text{ mm} \qquad \& \qquad d_0/\sigma_{d_0} < 5 \tag{4.3}$$

4.4.2 Electron Identification

Electron identification [138] determines if the reconstructed electron candidates are signal electrons or background objects as jets or converted photons. With this purpose, a set variables are defined to account for hadronic leakage, calorimeter shower shape, pileup, bremsstrahlung effects, track conditions and track-cluster matching. Some of these variables changed accordingly to the detector changes during LS1. As an example, to discriminate between electrons and converted photons a hit in the IBL is now required. For Run1 a hit in the first silicon layer was required, this is now the second pixel layer. Another example is the discrimination between electrons and hadrons in the TRT. During Run1 only the fraction of high threshold hits in the TRT was considered to distinguish electrons from hadrons. In Run2 some tubes are filled with Ar instead of Xe, and due to the lower transition radiation absorption probability of Ar with respect to Xe, a more sophisticated algorithm is used to compensate for this. The new algorithm depends on a variety factors such as gas type, tube type, location, γ-factor and track-to-wire distance. These variables are combined with a likelihood method (LH) that simultaneously evaluates the electron candidate variables to make the decision and selection. The LH method evaluates the probability for the object to be signal or background using the signal and background PDF‘s of the discriminating variables. Three operating points: *Loose*, *Medium* & *Tight* are defined for electron ID depending on how stringent is the selection. These points are defined using the same variables but different cuts such that the *Tight* set of cuts is a subset of the *Medium* set which is a subset of the *Loose* set. The combined reconstruction and identification efficiencies are presented in figure 4.14 for the full 2015, 25 ns data taking period. For this work, preselected electrons are required to be identified with the likelihood-based *Loose* criteria. The exact object definition used in the analysis is presented in the analysis section.

4.5 Muons

Muons pass through the detector without being contained or stopped loosing only a small amount of energy in the calorimeter. Muon momentum is calculated using their bent by the magnets. These trajectories are not simple, the magnetic field and the muon detectors wrapping the detector, depend on *eta* in a non trivial manner, complicating the analytic calculation of muon paths.

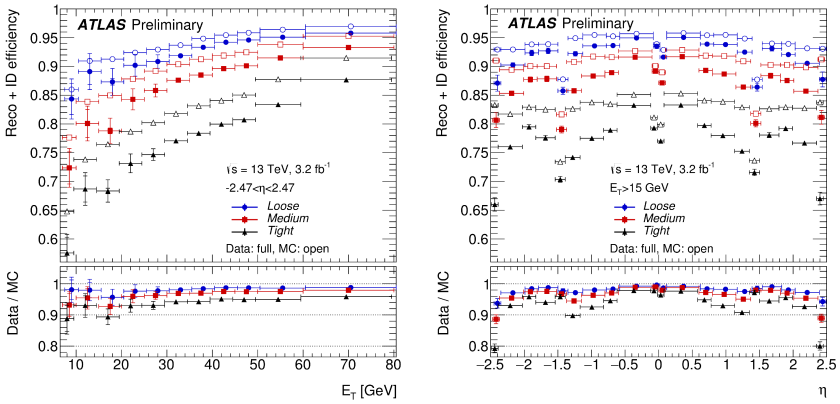

Figure 4.14: Combined electron efficiencies in $Z \to ee$ events as a function of E_T, integrated over η (left), and as a function of η, integrated over E_T (right). Data efficiencies are obtained from the data-MC efficiency ratios using J/Ψ and Z tag and probe, multiplied by the MC prediction from $Z \to ee$. The uncertainties are calculated with pseudo-experiments, treating the all statistical uncertainties from the different E_T and η bins as uncorrelated. The inner error bars show the statistical only uncertainty, while the outer error bars the combined statistical and systematic uncertainties [138].

4.5.1 Muon Reconstruction

Muon selection [141, 142] uses track information from the ID and the MS. Calorimeter information is used to estimate the energy loss. Using a variety of reconstruction criteria with the information available, four muon types can be defined: Combined (CB) muons, where an MS track is combined with an ID track; Segment-Tagged (ST) muons, where the ID tracks are combined with at least one track segment in the MDT or CSC chambers; Stand-Alone (SA) muons, where the muon trajectory is reconstructed only in the MS; and Calorimeter-Tagged (CT) muons, where tracks in the ID are matched to compatible energy deposits in the calorimeter. CB muons have the highest acceptance and the best p_T resolution, most muon candidates are CB muons. In this work, muons are defined from CB muons[4]. CB muon reconstruction is carried out independently in the ID and in the MS. The information from both sub-detectors is then combined to build muon tracks. In the ID, muons are reconstructed like any charged particles as described in chapter 4.1. The track reconstruction in the MS is briefly described below.

First, track segments are built searching for hit patterns in each muon chamber. Track segments in MDT chambers are reconstructed by a straight line fit per layer. In the CSCs the segments are built using a combinatorial search in η and ϕ, including a loose matching between tracks and calorimeter ROIs. The RPC and TGC hits, provide information of the the positions orthogonal to the bending plane. In a second step, track segment hits in different layers are combined to build muon track candidates. This algorithm starts with segment seeds in the middle layers where more trigger hits are available, and then performs a combinatorial search to find segments seeds in the inner and outer layers. These segments are defined using hit multiplicities and fit quality, and are matched based on their spatial positions. To build a track, at least two matching segments are required[5]

Due to the combinatorial nature of the algorithm, one segment could be used to build several track candidates. This ambiguity is addressed later using overlap removal algorithms that selects the best track assigned for the segment, or allows for the segment to be shared

[4]For the 8 TeV analysis, muons are defined from either CB or ST muons
[5]In the barrel-end cap transition, only a single high-quality segment can be used to build tracks.

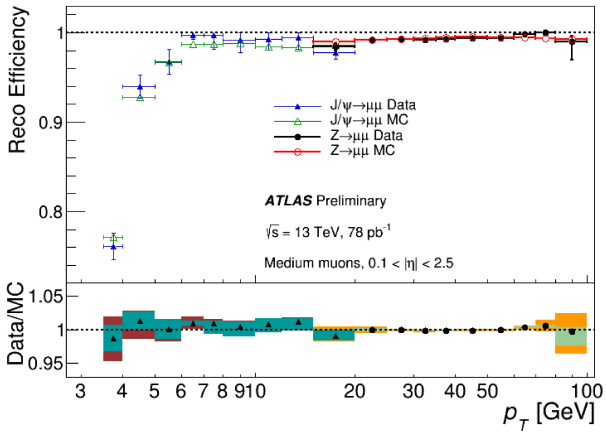

Figure 4.15: *Medium* muons reconstruction efficiency as a function of p_T. Green/cyan error bands in the ratio plot indicate statistical uncertainties, and orange/red bands correspond to the statistical and systematic uncertainty added in quadrature [142].

between two tracks. The latter might lead to efficiency loss for muons tracks close to each other, thus all tracks with three segments in three sub-regions are kept if they share two inner segments and no extra shared hit in the outer layer. Finally, hits belonging to a track candidate are fitted using a global χ^2 fit. When a hit contributes largely to the χ^2, it can be removed and the track fit is repeated. If additional hits consistent with the candidate trajectory are found, a recovery algorithm is carried out and the track candidate is refitted including the additional hits. The MS tracks built, are now matched with ID tracks. Most of the CB muons are reconstructed with an outside-in pattern recognition, extrapolating MS tracks to match with ID tracks. Inside-out reconstruction is used in a complementary approach.

Muon reconstruction efficiency is measured using a tag-and-probe method with $Z \to \mu^+\mu^-$ and $J/\Psi \to \mu^+\mu^-$ decays. The first is used for muon transverse momentum above 20 GeV while the second for low p_T muons. Muon reconstruction efficiency as a function of p_T for *Medium* muons is shown in figure 4.15 for an early 13 TeV run.

4.5.2 Muon Identification

Muon identification is performed to distinguish and suppress background muons. Background muons come mostly from charged hadrons as kaons and pions that leave a distinctive track with a 'kink' inside the inner detector, where the decay to a neutral hadron plus a muon takes place. These muons provide poor quality fits and momentum incompatibility between the ID and MS tracks.

The identification is done by applying quality cuts to the previously defined muon types. With these requisites, three inclusive muon selections are defined: *Loose*, *Medium* and *Tight*. There is one additional selection: *High-p_T* muon. In this work, preselected muons are required to pass the *Medium* selection, which uses only SA and CB muons, and minimizes the muon reconstruction and calibration systematic uncertainties. *Medium* CB muons requirements include at least three hits on at least two MDT layers, or at least three hits in one MDT layer in the $|\eta| < 0.1$ region. In addition, a very loose matching between ID and MS p_T is required to suppress hadron miss-identification. In figure 4.16 the expected probability for muons and fakes satisfying the *Medium* criteria is shown. The exact definition of the muons used in the analysis is presented in the analysis section.

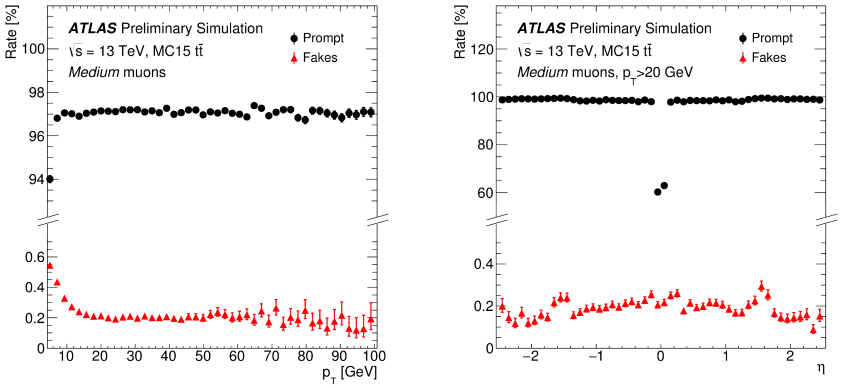

Figure 4.16: Expected efficiency as a function of p_T (left) and η (right) for *Medium* muons in simulated $t\bar{t}$ events, for signal muons (black dots) and fakes (red triangles) [141].

4.5.3 MET

In hadron colliders, four-momentum conservation is not well suited for event reconstruction, due to the ambiguity on the initial momenta of the partons taking part in the hard scattering. In the LHC the transverse momenta of the interacting partons can be neglected, thus and the initial transverse momentum of the system can also be approximated to zero. The E_T^{miss} defined as the magnitude of the p_T vector needed to balance the total transverse momentum to zero. Events with E_T^{miss} above a certain threshold, is a clear indication that particles such as neutrinos are present in the final state, that were not detected due to their weak interaction with matter. These events are of great interest as other beyond SM particles such as neutralinos or other DM candidate could leave similar distinctive measurements. To reconstruct the missing transverse energy [143, 144], information from all the previously defined objects is used. The missing transverse energy is defined as the magnitude of the vector equivalent to the inverse of the vector sum of the the p_T of calibrated hard objects as muons, electrons, photons and jets in addition to the track soft term (TST). The TST corresponds to the vector sum of the transverse momenta of all reconstructed tracks associated to the primary vertex that are not matched to any of the previous hard objects. To select these tracks, they must satisfy an overlap removal procedure consisting on removing tracks close to hard objects or with large momentum uncertainties as detailed in [144]. In addition, $Z \to \mu\mu$ events are used, to test the reconstruction resolution. These events have small background plus a small amount of real E_T^{miss}, making the resolution width of the E_T^{miss} distribution a

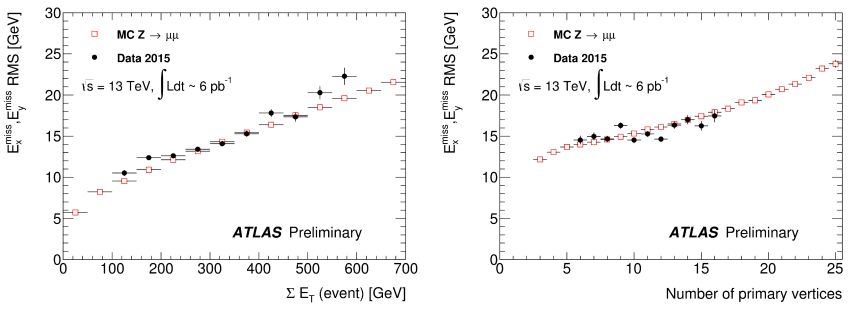

Figure 4.17: TST MET Resolution [144].

good indicator for reconstruction quality. Additionally, $W \to \mu\nu$ events with neutrinos from the hard scatter interaction, are used to validate the scale and direction of the reconstructed missing transverse energy. Figure 4.17 shows the E_T^{miss} resolution as a function of the number of primary vertices and a function of E_T^{miss} sum in the event, calculated with the calorimeter based soft term. The resolution in each bin is estimated from the RMS of the combined E_x^{miss} and E_y^{miss}. Each bin must have at least 200 events to be considered. A reasonable agreement is found between data and MC, even for low statistics available in early 2015 data.

Chapter 5

One lepton phenomenology and Analysis overview

This chapter presents a brief description of the search for squarks and gluinos production with hadron colliders, decaying into final states with one lepton, jets and missing transverse energy.

5.1 Strong production of sparticles conserving R parity

In R parity conserving models, supersimmetric particles must be produced in pairs. In a hadron collider, if the center of mass energy is high enough, the dominant SUSY production occurs via strong interactions. The main production channels for strongly interacting particles, would be gluino pair production, squark pair production and gluino-squark production. These diagrams are presented in Figure 5.1, where the gray circles represent $s-$, $t-$ and $u-$channels including quarks, gluons, squarks and gluinos as intermediate particles. For squark or gluino

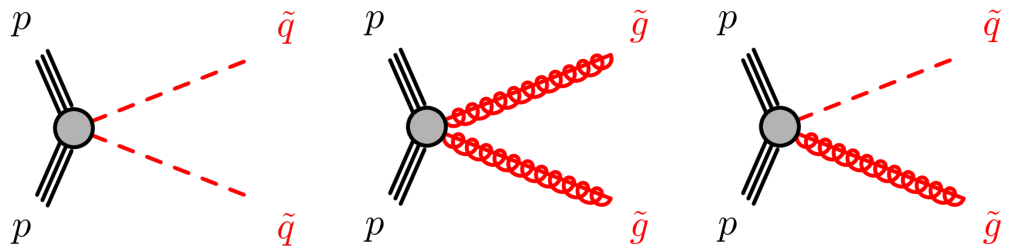

Figure 5.1: Three main channels for SUSY strong production at the LHC. Left: Squark pair production. Center: Gluino pair production. Right: Squark-Gluino production [145].

pair production, initial states may include quark and gluon pairs, while the squark-gluino channel may only be obtained in initial states with one quark and one gluon. The production cross section depends on sparticle masses and on the energy of the relevant partons. Sparticle masses are calculated from model parameters while the parton energy can be estimated using parton distribution functions (PDFs) [146–148] as the energy fraction taken by the parton from the incoming proton. For the analysis of the first 3.2 fb^{-1} of 13 TeV collision data, the sensitivity was tested and the SRs were optimized only for gluino pair production, as this is the channel with the highest production cross section (see Figure 5.2).

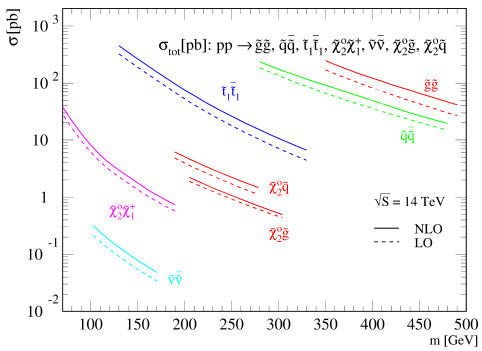

Figure 5.2: Production cross section for different SUSY production channels calculated with PROSPINO2 for 14 TeV c.o.m. energy [149].

5.2 Decay of SUSY particles

In this section the main channels for gluino and squark decay at tree level for R parity conserving susy models is presented. The decay of other susy particles as sleptons and electroweakinos is also briefly mentioned to explain the full decay chain from strong production to final states including one lepton.

5.2.1 Gluino decays

Gluinos can only decay to a squark-quark pair via strong coupling. If kinematically allowed, in the two body decay to a squark-quark pair, the squark can be produced on-shell, and will dominate over other decays. In a large region of the phase space, the lightest squarks can be stops or sbottoms, and $\tilde{g} \to t\tilde{t}_1$ or $\tilde{g} \to b\tilde{b}_1$ will usually be the only two body decays available, dominating over other gluino decays. If the mass spectrum does not allow for the squark to be produced on-shell, the only possible tree level decay will be a three body decay via virtual squarks into two quarks plus an electroweakino ($\tilde{g} \to qq'\widetilde{\chi}_i^{\pm}$ or $\tilde{g} \to qq\widetilde{\chi}_i^0$)

5.2.2 Squark decays

Squarks, can decay either into a gluino-quark pair or into a electroweakino-quark pair, depending on the mass hierarchy between the squarks and gluinos. If kinematically allowed, the two body decay to gluino-quark pair is favored due to the coupling strength. If not allowed, the two body decays to electroweakino-quark pair ($\tilde{q} \to q'\widetilde{\chi}_i^{\pm}$ or $\tilde{q} \to q\widetilde{\chi}_i^0$) are next in importance, where the direct $\tilde{q} \to q\widetilde{\chi}_1^0$ decay is kinematically favored. For right-handed squarks this channel dominates when the LSP is mostly Bino. For left-handed squarks the decay into heavier electroweakinos dominates, as the relevant $\tilde{q}q\widetilde{W}$ couplings are stronger than the $\tilde{q}q\widetilde{B}$ couplings. In the case of stops and sbottoms the decay to higgsino-like electroweakinos is also important as third generation squarks have a stronger Yukawa couplings. The specific third generation squark decays will not be detailed as this work focus in lighter squark and gluino production.

5.2.3 Slepton decays

Sleptons main decay channel is a two body decay into a lepton plus an electroweakino. If the lightest neutralino $\widetilde{\chi}_1^0$ is the LSP, the dominant channels are $\tilde{\ell} \to \ell\widetilde{\chi}_1^0$ and $\tilde{\nu} \to \nu\widetilde{\chi}_1^0$. In case of heavier sleptons, heavier electroweakinos could be present in the middle steps of the decay

chain. Squark decay via intermediate sleptons does not contribute to one lepton final states, as in the decay of a squark to a slepton a lepton is produced, the subsequent decay of the slepton contributes with an additional lepton to the final state.

5.2.4 Electroweakino decays

Electroweakino decays, together with gluino or squark decays, are the most important decays for strong SUSY production in final states with one lepton. If the sleptons or squarks are light enough, a neutralino or chargino two body decay into lepton-slepton or quark-squark pair is possible. Electroweakinos may also decay into lighter electroweakinos, sleptons or sneutrinos with their SM partners. The dominant two body decays for neutralinos are then: $\widetilde{\chi}_i^0 \to Z\widetilde{\chi}_j^0$, $\widetilde{\chi}_i^0 \to h_0\widetilde{\chi}_j^0$, $\widetilde{\chi}_i^0 \to W\widetilde{\chi}_i^{\pm}$, $\tilde{\ell}\ell$ and $\tilde{\nu}\nu$. For charginos the dominant two body decay channels are: $\widetilde{\chi}_i^{\pm} \to Z\widetilde{\chi}_j^{\pm}$, $\widetilde{\chi}_i^{\pm} \to h_0\widetilde{\chi}_j^{\pm}$, $\widetilde{\chi}_i^{\pm} \to W\widetilde{\chi}_i^0$, $\tilde{\ell}\nu$ and $\tilde{\nu}\ell$. Other type of two body decays include decays into electroweakinos and heavier higgs bosons and quark-squark pairs. If the decaying electroweakino is dominantly higgsino, and the decay to a third-family quark-squark pair is kinematically allowed, this channel is enhanced by Yukawa couplings. If two body decays are forbidden, three-body decays via virtual gauge bosons into two fermions and a lighter electroweakino is the next dominant tree level decay channel.

5.3 Final states with one lepton, jets and E_T^{miss}

One example for each of the three production processes decaying to the interesting final state are presented in figure 5.3 one example. The final state of the squark pair production contains

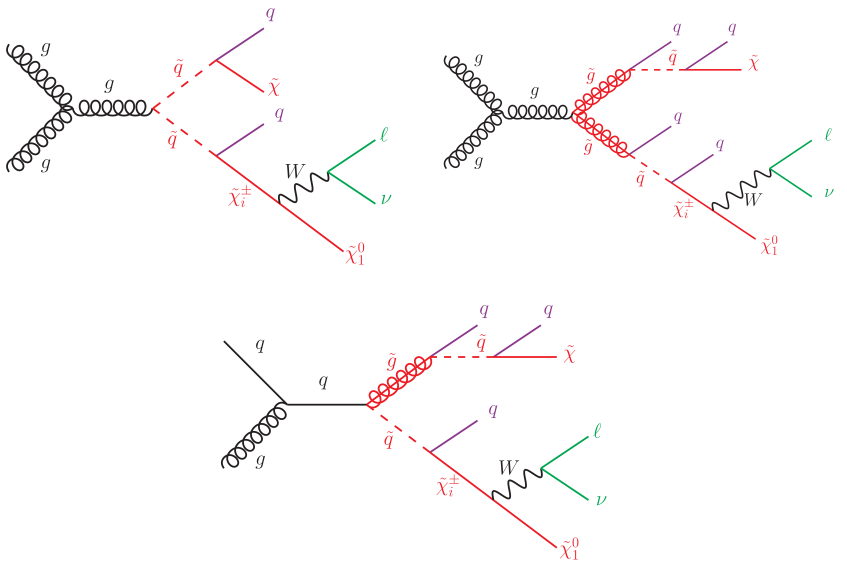

Figure 5.3: Example of the three strong production channels at the LHC decaying to final states containing one lepton, jets and E_T^{miss}. Top Left: Squark pair production via gluon fusion. Top Right: Gluino pair production via gluon fusion. Bottom Center: Squark-Gluino production via s-channel quark.

at least two jets, and the number can grow depending if the additional gaugino in the diagram is other than the LSP. If it is a chargino decaying via W to the LSP, two more jets would be expected from the hadronic W decay plus additional jets that might appear from initial

state radiation (ISR). The presence of neutrinos and neutralinos in the final state shows the the need for a E_T^{miss} requirement. For gluino pair production, the minimum jet content in the final state is four. Again the number of jets might increase depending on the type of the additional gaugino in the diagram and on ISR. For squark-gluino production, the minimum jet multiplicity is three with the same possibilities of additional jets.

If the mass difference between the produced sparticle and the LSP is large, it is possible for the outgoing lepton to have large p_T, but if the difference is small the leptons p_T is restricted to lower values. This is why the 1 lepton analysis is divided into two complementary analyses: The *hard-lepton* and the *soft-lepton* analysis covering different regions of the SUSY parameter phase space.

With such a phenomenology, for the 8 TeV data analysis, the optimized *hard-lepton* SRs had either three, five or six jets. In the case of the *soft-lepton* analysis only two SR were defined with either three or five jets. For the first 3.2 fb^{-1} of 13 TeV data SRs were optimized only for gluino production with at least four five or six jets in the hard lepton analysis. In the soft lepton analysis two SRs were defined including at least 2 or 5 jets.

5.4 Background processes

Background (BG) processes in this context refers to regular SM processes that share the same final states as the signal channel. In this case, the two main background processes are the semileptonic $t\bar{t}$ and the $W + jets$ processes. Both diagrams are presented in Figure 5.4

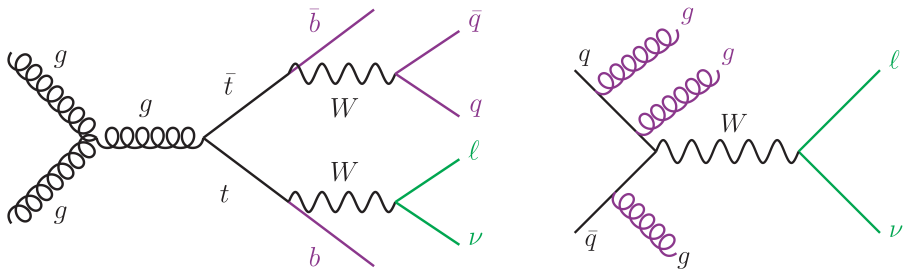

Figure 5.4: Main background processes. Left: $t\bar{t}$ production. Right: $W + jets$ production

The left diagram in Figure 5.4 shows a typical semileptonic decay of a $t\bar{t}$ pair production containing at least to $b-$jets, two additional jets from the hadronic decay of one of the W bosons, a lepton from the leptonic decay of the other W boson and E_T^{miss} from the neutrino associated to the lepton in the W decay. In the right diagram an event with a W boson production is depicted. The only source of jets letting this events into the final state is ISR.

Other background processes not as important as $t\bar{t}$ and $W+jets$, are single top production, diboson production, $Z + jets$ production and and $t\bar{t}$ production in association with a W or a Z boson.

- **Single Top** dominant diagrams are produced via W boson in the $s-$ and $t-$channel with electroweack strength. In these channels the outgoing particles are the top and an extra jet, and if the t decays leptonically another jet ($b-$jet) plus a lepton and a neutrino (E_T^{miss}) ending up in the same final state of the signal channel. There are also diagrams of assosiated $W - t$ production in both $s-$ and $t-$channels with b and g as incoming particles and a b or t are intermediate particles for each channel respectively. The total cross section is then smaller as the strong $t\bar{t}$ production. For these diagrams the final

state can be reproduced if the top quark decays leptonically contributing with one $b-$jet one lepton and E_T^{miss} and a W hadronic decay contributing with two extra jets. One lepton final state can also be reproduced if the t decays hadronically, contributing with the jets, while W contributes with a lepton and E_T^{miss} if decaying leptonically.

- **Diboson** processes include the production of a pair of EW gauge bosons. The channel with higher cross section is the production of two W bosons, with one decaying fully hadronically and the other to a lepton and a neutrino, the final state is the same as the final states of the signal searched. The next channel in importance with a fraction of the WW cross section is the WZ channel, with a W decaying leptonically contributes with the lepton and the E_T^{miss} from the neutrino, and a hadronically decaying Z contributing with the jets. The process with smaller cross section is the ZZ channel. It can only lead to one lepton if each Z decays to a τ pair, with only one τ decaying leptonically and the other three hadronically; or if one Z decays to two neutrinos while the other decays to a τ pair with one τ decaying leptonically and the other hadronically.

- $\boldsymbol{Z + jets}$ processes do not yield to one lepton final states unless again the Z decays into a τ pair with one τ decaying leptonically and the other hadronically, leading to a very small cross section.

- $\boldsymbol{t\bar{t}V}$ processes may easily yield one lepton final states. If the $t\bar{t}$ system decays semi-leptonically, the W might decay fully leptonically to reach a one lepton final state. In the other hand if the $t\bar{t}$ system decays fully hadronically, the lepton and E_T^{miss} required must come from the leptonic decay of the W boson. Decays via τ lepton are also probable. This background is nevertheless quite suppressed as the total production cross section is already much smaller than the others.

5.5 Signal and background simulation

Signal and usual SM events are normally simulated using Monte Carlo generators. This task needs time and resources to produce every day larger and robuster simulations. Simulations are built with a variety of algorithms combined to produce precise and large amount of events with the available resources. The Initial algorithms calculate the transition amplitude from the initial to the desired final states. This work can easily become impossible to calculate. Depending on the complexity of the initial and final states, the matrix elements are computed only up to a limited order in perturbation theory. The only initial states used to calculate the matrix elements are the incoming partons. Thus a second algorithm is used to simulate the proton substructure and energy by summing over all the relevant PDFs. The fragmentation and hadronization of the final state partons into the final stable particles, appears at lower energies, where QCD becomes non-pertubative. Therefore additional algorithms based on low energy models are used to simulate low energy QCD. Some of the inputs for these models are experimentally calculated, and are tuned to match soft QCD data.

5.6 Statistical procedure overview

The statistical procedure used in the 8 TeV analysis and in the 13 TeV analysis are much alike. This section presents an overview of the method, introducing the concepts and definitions used to explain the reinterpretation of 8 TeV results within pMSSM models and as a first glimpse to the 13 TeV procedure presented in the final chapter.

To check all background estimates and to verify that the data taking and reconstruction procedures were under control, BG estimates are compared with data in dedicated control

regions (CRs). CRs are designed to enrich BG like events and high background expectation. On the other hand, signal regions (SRs) are designed to enrich signal events keeping low background expectations. For both 8 and 13 TeV analyses, two types of CRs were defined in association to each SR. One Top CR built to enhance $t\bar{t}$ events and one W CR where $W+jets$ events are enhanced. Validation regions VRs are a third type of region used to validate the model that estimates the number of background events in the SRs. VRs lie kinematically between CRs and SRs. All regions are built applying specific selection criteria to different observed variables

This procedure starts by adding all the background events and then fitting it to data in the CRs. This produces normalized BG estimates in all regions. To constrain BG in the SRs, the normalization factors found by the fit to data in the CRs are used to extrapolate BG estimates to the VRs and SRs. The fit consists of a profile likelihood method [150–152] implemented within the HistFitter framework [153] introducing systematic uncertainties as nuisance parameters.

5.6.1 Likelihood function

If set of measured quantities $x = (x_1, ..., x_N)$ is described by a joint PDF[1] $P(x;\lambda)$, where $\lambda = (\lambda_1, ..., \lambda_n)$ is a set of unknown parameters. The likelihood function $\mathcal{L}$ is defined as a function of λ given by the PDF evaluated for the observed data x. If the measurements are independent, the joint PDF for x will be the multiplication of the independent $P(x;\lambda_i)$. In a toy example with only one SR with two associated CRs, the likelihood function could be expressed as the product of Poisson distribution functions P for SRs (P_S), CRs (P_W and P_t) and systematic uncertainty distributions P_{Syst}:

$$\mathcal{L}(N, \theta^0|\mu, b, \theta) = P_S \cdot P_W \cdot P_t \cdot P_{Syst} = P(N_S|\lambda_S) \cdot P(N_W|\lambda_W) \cdot P(N_t|\lambda_t) \cdot P_{Syst}(\theta^0, \theta) \quad (5.1)$$

where N_S, N_W and N_t represent the number of observed events in the signal, W and top regions respectively. The λ_S, λ_W and λ_t are the associated Poisson expectation values on each region which depend on three parameters: The signal strength μ: Set to zero for a background only hypothesis and set to one for a signal model hypothesis[2]; the normalized background b and the nuisance parameters θ parameterizing systematic uncertainties.

$$\lambda_i = \lambda_i(\mu, b, \theta) \qquad i=S,W,t \qquad (5.2)$$

Systematic uncertainties are introduced with the $P_{Syst}(\theta^0, \theta)$ distribution, where θ^0 is the nominal value of the nuisance parameter θ. In a profile likelihood fit, the λ_i are functions of θ and any variation in the nuisance parameters will affect the expectation values of λ_i. For uncorrelated systematic uncertainties P_{Syst} is just the product of the individual distributions. For correlated systematic uncertainties, the correlations are described by the combined distribution P_{Syst} and the combined impact of the nuisance parameters may be amplified or attenuated.

5.6.2 Parametrization of the expectation values

The expectation values λ_S, λ_W and λ_t can be parametrized as functions of the transfer functions c:

$$\lambda_i(\mu, b, \theta) = \mu \cdot c_{S,i} \cdot s + \sum_j c_{j,i} \cdot b_j \qquad j \in bkgd. \qquad (5.3)$$

[1] Probability Density Function

[2] $\mu = 0$ or BG only hypothesis represents the H_0 or Null Hypothesis. $\mu = 1$ or signal+background (S+B) hypothesis represents the H_1 or Test Hypothesis.

The c functions take the background normalization factors from the CRs and use them to estimate background expectations in the different regions:

$$c_{j,i} = \frac{MC_{j,i}}{MC_{j,j}} \left(1 + \sum_k \Delta_{i,j;k}\theta_k\right) \tag{5.4}$$

where a small abuse in the subindex notation was allowed: In equation 5.3, j represents the BG process while i is related to the regions. With this definitions, the term $MC_{j,i}$ represents the number of MC events of process j in region i, while for $MC_{j,j}$ the j used as a region makes reference to the dedicated CR region associated to the same j process if available. $\Delta_{i,j;k}$ characterizes the effect on the transfer factor of the systematic uncertainty k for process j in region i. Looking at the expression for $c_{j,i}$ in equation 5.4 ignoring the uncertainties for a moment, it is easy to notice that the second expression of λ_i in equation 5.3 has the form:

$$\sum_j c_{j,i} \cdot b_j = \sum_j \frac{MC_{j,i}}{MC_{j,j}} \cdot b_j = \sum_j MC_{j,i} \cdot \frac{b_j}{MC_{j,j}} = \sum_j MC_{j,i} \cdot \mu_j \tag{5.5}$$

where the ratio $b_j/MC_{j,j}$ is by definition the normalization parameter μ_j of process j in its own CR. Replacing this expression in equation 5.3 shows explicitly how the normalization of background process j is used to to find BG estimates in the SR and other CRs.

In both analysis presented in this work, there are more than one SR, each with its own associated CRs. The method is similar, but the distribution functions for the additional regions must be included in equation 5.1. To do this, all regions where the PDFs parameters are fitted to data are built statistically independent so they can be modeled by separate PDFs. If this is the case the regions can be easily combined in a simultaneous fit. In a combined fit, the globally fitted normalization parameters are shared and extrapolated between SRs and CRs. Systematic uncertainties on expected values can correlate between processes and/or regions, and even further between analyses and/or experiments via the transfer functions.

5.6.3 Fit setup

The three different fit setups used are briefly explained:

- The **Background Only Fit** is used to maximize the agreement between data and MC simulations of standard model events in the CRs. The fit is performed only in the control regions where no signal contamination is assumed. The main goal of the background only fit is to estimate the background in the control, validation[3] and signal regions before testing any signal model.

- The **Discovery Fit** is normally used to set model-independent upper limits on the number of events beyond expectation in each SR given the observed data. Once a model independent upper limit is calculated, any signal model can be tested and the number of signal events estimated in the SR is used to check if the model could be excluded by data or not. For the discovery fit setup signal and control regions are used to constrain the background. Any possible signal contamination in the CRs is still neglected. The latter makes the background estimate in the SRs rather conservative, as any additional signal event in the CRs would lower the background prediction. With this setup the null hypothesis is tested in the SRs, and the number of signal events in the SRs is fitted introducing an additional parameter to the fit.

- The **Exclusion Fit** tests specific models to check if they can be excluded with the available data or not. The fit tests the expected BG plus signal simulated events against

[3] As VRs are used only to validate the extrapolation procedure, no constrains are imposed in these regions.

data in both control and signal regions. Possible signal events in CRs are now taken into account, including the predicted signal yields in all regions. The nuisance parameters for signal such as cross section and MC statistical uncertainty are turned on. This fit setup is used to test which signal models (sampled usually from a 2 dimensional grid of points of the parameter space) could be excluded and which not, generally resulting in exclusion limits plots in the relevant two dimensional parameter space.

5.7 Interpretation of results and limit setting

Depending on the observed data, the fit results are interpreted using hypothesis tests based on the profile log likelihood ratio (LLR) [150–152] resulting until today into exclusion limits for specific SUSY models or model independent upper limits. When using a likelihood function $\mathcal{L}(N, \theta^0|\mu, b, \theta)$ to perform a hypothesis test between two models, it is proven [154] that the most powerful test to discriminate between them is the likelihood ratio test:

$$\Lambda(\mu, n, \theta^0) = \frac{\mathcal{L}(N, \theta^0|\mu, \hat{\hat{b}}, \hat{\hat{\theta}})}{\mathcal{L}(N, \theta^0|\hat{\mu}, \hat{b}, \hat{\theta})} \tag{5.6}$$

where $\hat{\mu}, \hat{b}, \hat{\theta}$ maximize $\mathcal{L}$, and $\hat{\hat{b}}$ and $\hat{\hat{\theta}}$ are the estimators which maximize $\mathcal{L}$ for a fixed value of the signal strength μ. If this ratio is large, there is a big disagreement between data and the signal prediction for a given μ. It is then of interest to test, for which parameter values the ratio has its maximum value. To maximize, the derivative of Λ with respect to λ evaluated for $\lambda = \hat{\lambda}$ must be set to zero, but this is often to complicated. Luckily, as the logarithm of a function peaks at the same point as the function itself, the log-likelihood ratio (LLR) method is the test statistic (t_μ) used instead:

$$t_\mu = -2 \cdot \ln(\Lambda(\mu, n, \theta^0)) = -2 \left[\ln \mathcal{L}(N, \theta^0|\mu, \hat{\hat{b}}, \hat{\hat{\theta}}) - \ln \mathcal{L}(N, \theta^0|\hat{\mu}, \hat{b}, \hat{\theta})\right] \tag{5.7}$$

where the -2 factor is conveniently included to link this interpretation with the minimization of a χ^2 distribution. To differentiate the LLR is much easier for two reasons: First, each likelihood is a multiplication of PDFs, and the logarithm transforms multiplications into sums, which are much easier to differentiate. Second, the PDFs are usually Poisson distributions containing exponential functions, which are simplified after applying the logarithmic operator. The signal strength estimator $\hat{\mu}$ is constrained within zero and μ ($0 < \hat{\mu} < \mu$), as $\hat{\mu} < 0$ would be non physical enabling negative number of expected signal events; while $\hat{\mu} > \mu$ would represent data fluctuation increase, which should not be treated against the signal model with strength μ [152].

To test if an observed number of events is more background like (b) or more signal plus background like ($s + b$), the corresponding $p-$value [150, 155, 156] can be calculated. The $p-$value for the $s + b$ hypothesis is defined as:

$$p_\mu = \int_{t_{\mu,obs}}^{\infty} f(t_\mu|\mu) dt_\mu \tag{5.8}$$

where $t_{\mu,obs}$ is the value of the test statistic t_μ observed from the data. $f(t_\mu|\mu)$ is the corresponding PDF of t_μ given a signal strength μ, which can be calculated using approximate analytical functions or with Monte Carlo methods as explained in [150]. The above formula can be interpreted as the probability that given μ the test statistics value is larger than the observed value using the same μ. In figure 5.5 a representation of the above is depicted. For the background only hypothesis, the $p-$value can be obtained from the probability that the

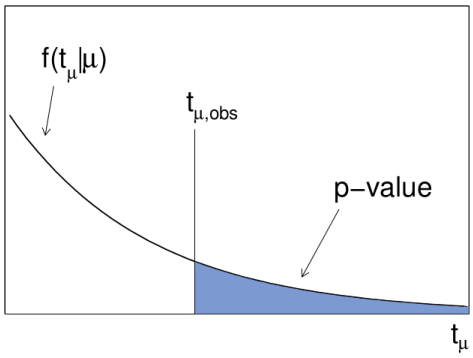

Figure 5.5: Diagram of the p-value obtained from an observed value of the test statistic t_μ [150].

background expectation, yields a larger value of the test statistics, compared to the observed value with $\mu = 0$:

$$1 - p_b = \int_{t_{\mu=0,obs}}^{\infty} f(t_\mu|\mu)dt_\mu \tag{5.9}$$

In case of having an excess of data compared to background, the above method can be used to probe new models and to statistically compare them to the null hypothesis in what is usually called a *discovery* fit. In such a case p_b is used to quantify such excess of events over the background expectation. In a single counting experiment where only the number of events in one SR is counted, a discovery can be simplified in a single plot as seen in figure 5.6.

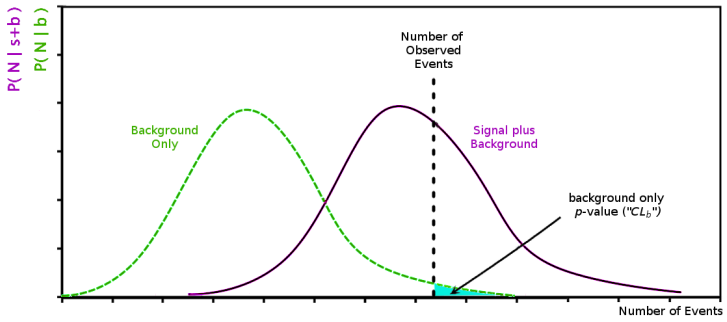

Figure 5.6: Diagram of the $p-$value used for a discovery. It must be noticed that the distribution including signal is drawn only for comparison, to visualize that data is more likely under the $s + b$ hypothesis than under the $b-$only hypothesis, but only the p_b value is used. Diagram based on [157].

Sometimes $p-$values are hard to interpret, and what is usually done in particle physics is to convert the obtained $p-$value and express it as an equivalent significance or $z-$value. This is done using a Gaussian distribution such that a variable found z standard deviations σ above its mean value, has an upper tail probability of p. With this interpretation, if there is an excess of data over background, before physicists may claim for a discovery the z-value must be over 5σ, meaning that there is a probability of less than 3×10^{-7} to obtain the observed data or higher in future identical experiments given that the null hypothesis is correct. In the opposite case, if the background is consistent with data, the specific models can be tested in what is usually called the *exclusion* fit. In this case, the $p-value$ of the $s+b$ hypothesis is used to test if the signal model could be excluded or not given the data. The convention typically

adopted is to express the result as an upper limit value of s for which $p_{s+b} = 0.05$ (5%) or below. Models with $p_{s+b} \leq 0.05$ are said to be excluded at 95% confidence level (95% C.L.). In figure 5.7 a diagram of the exclusion limit is presented in the same simplified counting experiment.

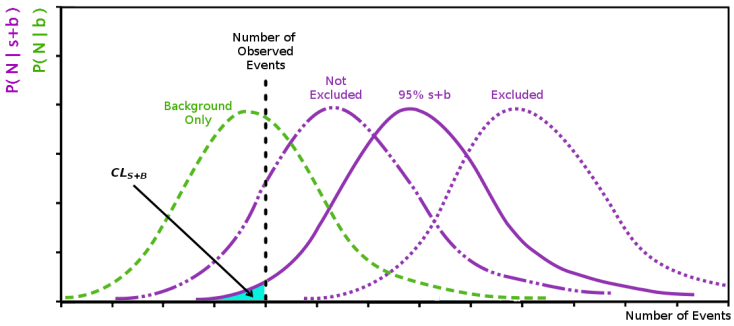

Figure 5.7: Diagram of the $p-$value used for excluding signal models. Diagram based on [157]

The previous convention is not always the best alternative. As p_{s+b} quantifies the consistency of s+b with data, there is a problem if the observed data fluctuates down with respect to the background expectation. There might be cases where using this convention might arbitrarily exclude small values of s. The usual LHC convention is to define the Confidence Levels CL_s to quantify a *Modified upper limit*:

$$CL_s = \frac{p_{s+b}}{1 - p_b} \tag{5.10}$$

This convention produces proper frequentist 95% confidence intervals. If the number of observed events is large, then p_b should be small, and $CL_s \rightarrow p_{s+b}$. The case of a small N_{obs} is shown in the left image in figure 5.8. The relation between $z-$values and $p-$values is presented in the right plot.

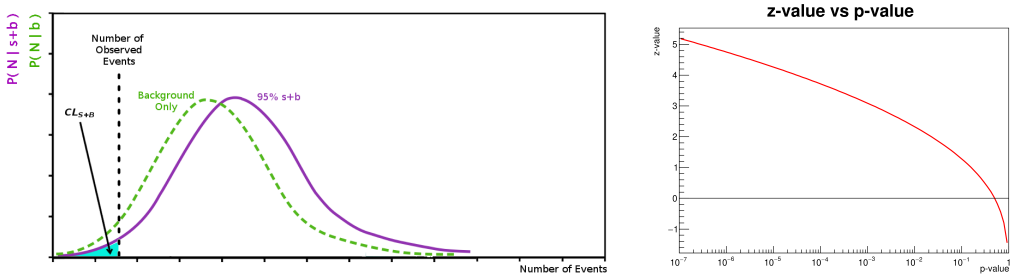

Figure 5.8: Left: Diagram of the p_{s+b} problem when N_{obs} is too small. Diagram based on [157]. Right: Relation between $z-$value and $p-$value.

In real analyses, there are more than one region and there are a variety of systematic uncertainties affecting signal and background distributions. Nevertheless, all the additional information can be used and be converted into a single number, constructing a test statistic such as the likelihood ratio.

Chapter 6

Analysis part I: Interpretation of $\sqrt{s} = 8$ TeV data in the pMSSM

In this chapter a summary of the constraints coming from the ATLAS experiment data on pMSSM models with R parity conservation is presented [158]. The results from 22 separate ATLAS analyses are used with emphasis on the interpretation of final states with one lepton plus jets and missing transverse energy. The studies are based mainly in the analysis of the 8 TeV full dataset, and also the 7 TeV dataset. The results were interpreted previously in the context of different SUSY scenarios. In this study all results are re-interpreted within the 19 parameter pMSSM and the results are also compared with simplified models. The phenomenology of models that cannot be excluded is studied.

6.1 SUSY searches with the ATLAS detector

The 22 different searches considered, cover a wide range of possible final states, and combined have more than 200 signal regions[1]. The searches can be divided in three main groups depending on the topology of the production processes:

- **Inclusive searches** targeting the direct production of light squarks or gluinos, that may decay directly to the LSP, via $\tilde{q} \rightarrow q + \tilde{\chi}_1^0$ decay and via $\tilde{g} \rightarrow q + \overline{q} + \tilde{\chi}_1^0$. The decay to the LSP may also occur in a cascade, including one or more sparticles in the intermediate steps, contributing with additional objects to the final state.
- **Third generation searches** targeting the direct production of third generation squarks or gluinos, namely stop and sbottom squarks, decaying to very distinctive signatures normally including top or bottom quarks plus large E_T^{miss}.
- **Electroweak searches** targeting gaugino and slepton direct production typically decaying into final states containing several high-p_T leptons and significant E_T^{miss}.

Besides these three groups, searches of **heavy long lived particles** and **heavy higgs bosons** are also considered. In tables 6.1, 6.2, 6.3 & 6.4 the searches considered for this study including the references, plus a small description of the final states and signal regions are presented.

The main goals of this work is to test the complementarity of the ATLAS searches and to search for possible blind spots. This is why it is so important to include all the above analyses and SRs. Another goal is to check how low can the SUSY masses be, without using simplified

[1] For few analysis some specially designed signal regions and few complex combined fits had to be dismissed, slightly underestimating the full reach of the search

Inclusive searches	
0-lepton + 2-6 jets + E_T^{miss} [159]	Wide sensitivity to sparticle production. Lepton veto suppress W and $t\bar{t}$ background. SRs with 2 to 6 high p_T Jets plus large MET: Low N-Jet SR are sensitive to squark production. High N-Jet SR are sensitive to gluino production plus cascade decays.
0-lepton + 7-10 jets + E_T^{miss} [160]	Targets gluino pair production with $\tilde{g} \to \bar{t} + t + \tilde{\chi}_1^0$ decay with an intermediate stop where the outgoing tops usually decay into many jets. Also sensitive to cascade decays. Looser MET requirement than the previous 2-6 jet analysis.
1-lepton + jets + E_T^{miss} [161]	Sensitive to decay chains of squarks and gluinos. High(low) lepton p_T makes the analysis sensitive to SUSY scenarios with large(small) mass splittings between the produced sparticle and the LSP. Two types of SRs: Hard lepton SRs with high lepton p_T and Soft lepton SRs with low lepton p_T. Both types of SR also require several jets and high MET in the final states.
τ (τ/ℓ) + jets + E_T^{miss} [162]	Targeting final states from cascades producing hadronically decaying τ leptons. Also sensitive to models with light staus ($\tilde{\tau}$) and long decay chains. SRs with either one or two τ's plus large E_T^{miss} plus jets and in addition, zero or one extra light lepton.
SS/3-leptons + jets + E_T^{miss} [163]	Sensitive to cascade decays of squark and gluino pairs leading to final states with multiple leptons, or with two same-sign (SS) leptons. SRs with multiple jets in the final state, and either two SS leptons or at least three leptons.
0/1-lepton + 3b-jets + E_T^{miss} [164]	Sensitive to models with many b-jets coming from two classes of models: Class 1: $\tilde{t}_1$ and $\tilde{b}_1$ are lighter than $\tilde{g}$, so they are produced either in pairs, or via gluino pair production decaying by $\tilde{g} \to \tilde{t}_1 t$ or $\tilde{g} \to \tilde{b}_1 b$. Class 2: All sparticles masses are above the TeV scale, except for $\tilde{g}$ and $\tilde{\chi}_0$. Then $\tilde{t}_1$ and $\tilde{b}_1$ are only produced off-shell via prompt decay of the gluinos and $\tilde{t}$ and $\tilde{b}$ masses have little impact on the kinematics. Both types yield different amount of b-jets and may or not have leptons in the final states.
Monojet [165]	Sensitive to models with no observed products from sparticle decays. It targets either direct LSP pair production, or models with tiny mass differences between the the produced sparticles and the LSP, leading to SM particles not hard enough to be detected by other searches. SRs selects events with large E_T^{miss}, no leptons, and one hard jet with p_T as large as 50% of the E_T^{miss} originating from initial state radiation (ISR)

Table 6.1: Inclusive searches included.

Third generation searches	
0-lepton stop [166]	Sensitive to models with direct production of stop pair decaying directly to a top quark and neutralino. Hadronic final states with at least two $b-$jets and large E_T^{miss}. SRs are built using variables related to the reconstructed top quarks in the final states. Dedicated SRs target the $\tilde{t} + \tilde{t} \to t\tilde{\chi}^0 + b\tilde{\chi}^{\pm}$ decay.
1-lepton stop [167]	Also sensitive to direct stop pair production buth with a lepton coming from the top decay. All SRs require one isolated lepton, at least two jets and large E_T^{miss}.
2-lepton stop [168]	Targeting stop decay through an intermediate chargino. SRs containing two isolated leptons and large E_T^{miss} Only SR targeting chargino decay through on-shell W boson is included for this study.
Monojet stop [169]	Sensitive to stop production decaying into a neutralino and an undetected charm when the LSP mass is similar to the stop mass. The SRs are built to search for signature with large E_T^{miss}, at least one high-p_T jet, no leptons and no more than two jets.
Stop with Z boson [170]	Sensitive to $\tilde{t}_2$ production decaying via $\tilde{t}_2 \to \tilde{t}_1 Z$. Typical signatures with many leptons in the final state. The SRs require to have at least two leptons consistent with the Z mass, at least one b-jet and large E_T^{miss}
2b-jets + E_T^{miss} [171]	Sensitive to SUSY scenarios where the produced $\tilde{b}$ or $\tilde{t}$ decay to a third generation quark and a gaugino: $\tilde{b} \to b\tilde{\chi}^0$ or $\tilde{t} \to b\tilde{\chi}^{\pm}$ Final states containing exactly two b-jets, significant E_T^{miss} and no isolated lepton
tb + E_T^{miss},stop [172]	Targets the direct production of $\tilde{t}$ or $\tilde{b}$ pairs each decaying to different number of $\tilde{\chi}^0$ or $\tilde{\chi}^{\pm}$ The final states consist in t-, b-quarks and large E_T^{miss}. Depending on the decay chain of the t- and b-quarks several SR are used to cover a wide range of topologies including extra jets, leptons, c-jets, higgs bosons, Z bosons or extra t- or b-quarks

Table 6.2: Third generation searches included.

Electroweak searches	
lepton plus higgs (ℓh) [173]	Targeting the direct production of a chargino and a neutralino decaying to final states with large E_T^{miss}, an isolated lepton, and a higgs boson. For the SR used in this study, the higgs is identified by requiring two $b-$jets.
2-leptons [174]	Sensitive to electroweak production of charginos, neutralinos, or sleptons with two leptons in the final state. SRs with exactly two leptons and large E_T^{miss}. Depending on the SR, zero, two or more jets can be required.
$2-\tau$ [175]	Targeting the 2 τ production, complementing third generation searches. SRs built for at least two hadronically decaying τ leptons, large E_T^{miss} and no extra jets.
3-leptons [176]	Sensitive to the direct production of charginos and neutralinos decaying to final states with three leptons. One or two of the leptons may be hadronically decaying τ leptons. SRs require three leptons plus large E_T^{miss}.
4-leptons [177]	Sensitive to electroweak production with final states containing four or more leptons. At least two of the leptons must be either e or μ. They may also be hadronically decaying τ leptons. The high lepton multiplicity in the final states can occur if a degenerate pair or heavier neutralinos decay to the lightest neuttralino via sleptons ($\tilde{\ell}$), staus ($\tilde{\tau}$) or Z bosons.
Disappearing Track [178]	Looking for specific scenarios where the LSP is Wino-like, an the $\tilde{W}^{\pm}$ is only $\sim$ 160 MeV heavier than the LSP. Within this spectra, the $\tilde{\chi}_1^{\pm} \rightarrow \pi^{\pm}\tilde{\chi}_1^0$ decay occurs in few tenths of a cm and the soft pion track cannot be reconstructed. Such a distinctive signature presents a high-p_T chargino track disappearing within the detector.

Table 6.3: Electroweak searches included

Other searches	
Long lived particle [179, 180]	Designed to detect heavy long-lived particles. Only the direct production of pairs of long lived $\tilde{t}$ or $\tilde{b}$, $\tilde{g}$, $\tilde{\tau}$ or $\tilde{\chi}^{\pm}$ are considered. For 7 TeV 2011 data, sparticles were as light as 200 GeV. In the later analysis sparticles masses were above 400 GeV. Both searches are included in the study for maximal sensitivity.
$H/A \to \tau^+\tau^-$ [181]	Designed to detect the neutral MSSM higgs bosons decaying to τ-pairs.

Table 6.4: Additional searches included.

models and to test the sensitivity of the combination of the SUSY searches performed by the ATLAS collaboration.

6.2 Data and background samples

6.2.1 Data samples

Most of the analyses mentioned, are based on the full 2012 data taking period of proton-proton collisions with 8 TeV center of mass energy. Only in few exceptions the results include 7 TeV data. The peak luminosity during 2012 reached 7.73×10^{33} cm^{-2}s^{-1} for a total integrated luminosity recorded by ATLAS of 21.7 fb^{-1}. The average number of interactions per bunch crossing spread from 6 to 40, with a mean value of 21.

Data taking is organized in ATLAS by Runs which consists of time periods during which the data acquisition system is working. The runs are divided in luminosity blocks (*lumi-blocks*) used as data units. Every lumi-block contains similar data loads, so their time intervals are luminosity dependent. To ensure data quality the, groups of lumi-blocks per run that may be used for physics analysis are summarized in Good Run Lists (GRL) [182]. Some of this lists include all sub-systems while others are more specific. For the 1-Lepton SUSY search and for most of SUSY searches the whole detector is needed and the GRLs including the "ALL_GOOD" tag are used. After the GRL requirement[2] the total integrated luminosity used for the one lepton analysis is 20.3 fb^{-1}. As each analysis has its own needs some analyses might use different GRLs yielding slightly different integrated luminosities.

Due to the variety of final states, each group has chosen their own trigger menus. For example: The one lepton analysis used different triggers. For the hard single electron channel a combined electron+E_T^{miss} trigger was used, with 24 GeV threshold for the electron p_T and 35 GeV for E_T^{miss}. The electron trigger is 70% efficient for electrons with $p_T > 24$ GeV and fully efficient for electrons above 30 GeV. The E_T^{miss} trigger is fully efficient for $E_T^{miss} > 80$ GeV. For the hard single muon channel a combined muon+jet+E_T^{miss} trigger is used with 24 GeV threshold for the muon, 65 GeV for jets and 40 GeV for E_T^{miss}. The combined efficiency reaches its maximum value of 70% for muons in the barrel and 90% in the EC for muons with $p_T > 25$ GeV, $E_T^{miss} > 100$ GeV and fully calibrated jets with $p_T > 80$ GeV. The previous lepton thresholds are too high for soft lepton selections. This channel uses only one $E_T^{miss} > 80$ GeV trigger which is fully efficient for events with $E_T^{miss} > 150$ GeV and jets

[2]The GRL used for the One lepton analysis is:
data12_8TeV.periodAllYear_DetStatus-v61-pro14-02_DQDefects-00-01-00_PHYS_StandardGRL_All_Good.xml

with $p_T^{miss} > 80$ GeV. The integrated luminosity after trigger requirements is 20.3 fb^{-1} for the hard lepton channel. Additional trigger information can be found in the paper [161].

6.2.2 Background samples

In the original analyses, the groups used different BG samples to cover their own variety of relevant BG processes. In most cases the prediction were estimated using Monte Carlo simulation though in other cases data driven techniques were used to simulate specific BG processes. In the one lepton analysis, the main BG processes $t\bar{t}$ and $W + jets$ were predicted using different MC generators. For $t\bar{t}$ samples the generator used was POWHEG-BOX r2129 [183] connected to PYTHIA 6.426 [184] for the parton shower simulation. The cross section is calculated at NNLO+NNLL. For $W + jets$ samples the SHERPA 1.4.1 [185] generator was used with its own parton shower simulation. Cross section is calculated at NNLO. For the rest of the background processes: $Z + jets$ generator and parton shower simulation is the same that for $W + jets$ for hard lepton samples. Soft lepton samples[3] are generated with ALPGEN 2.14 [186] while HERWIG 6.520 [187] is used to simulate the parton showering. Diboson samples are also generated with SHERPA 1.4.1. Single-top *t-channel* samples were generated with ACERMC 3.8 [188] while *s-channel* and Wt samples were generated with POWHEG-BOX r1556. For all Single-top samples, PYTHIA 6.426 was used to simulate the parton shower. $t + Z$ and $t\bar{t}+W/WW/Z$ samples were generated with MADGRAPH5 1.3.28 [189] where parton showering is also simulated with PYTHIA 6.426. The PDF set used, underlying event tunes, cross section accuracy for secondary backgrounds is found in the original paper [161].

6.3 Signal samples

Te generation of signal samples was far from trivial, to reinterpret 8 TeV data within the pMSSM, more than 300,000 model points were to studied. The algorithms used to generate all the model points is based on the algorithms used in [190] and the samples were generated in collaboration with the authors. The differences with the previous simulations arise from new experimental results such as the Plank results [191], tool updates, the knowledge gained with the previous model set and the higher power of the ATLAS simulation resources between others. A description of the procedure used to generate the models, pick the parameters, the constraints used and further information about the used tools is presented below.

6.3.1 Generation of model points parameters

The guiding principles when choosing the parameters for each model are the five constraints found at the beginning of section 2.4. Combining the first with last of these effectively reduces the number of MSSM parameters to the 19 pMSSM parameter subspace. The remaining parameters and their possible values are presented in table 6.5. The lower limits are imposed to agree with previous experimental results while the higher are imposed to limit the particle spectrum to the masses accessible by the 8 TeV LHC collisions. It is clear that many of the limits are the same in different rows, the table is displayed to explicitly show which parameters are degenerated and also to present the remaining 19 independent parameters.

With this amount of parameters and their possible values, a regular interval sampling for each variable is not possible and was not performed. Instead each parameter was chosen randomly from a flat probability distribution within the boundaries in table 6.5. Once each of parameters has a numerical value, the properties of each model point are calculated using different software packages. To calculate the particle spectrum SOFTSUSY 3.4.0 [192] is used

[3] SHERPA generated samples had a $p_T^{\ell_1} > 9$ GeV filter, making it unsuitable for soft lepton searches

Parameter	Minumum	Maximum
$m_{\tilde{L}_{1,2}}$	90 GeV	4 TeV
$m_{\tilde{L}_3}$	90 GeV	4 TeV
$m_{\tilde{E}_{1,2}}$	90 GeV	4 TeV
$m_{\tilde{E}_3}$	90 GeV	4 TeV
$m_{\tilde{Q}_{1,2}}$	200 GeV	4 TeV
$m_{\tilde{Q}_3}$	100 GeV	4 TeV
$m_{\tilde{U}_{1,2}}$	200 GeV	4 TeV
$m_{\tilde{U}_3}$	100 GeV	4 TeV
$m_{\tilde{D}_{1,2}}$	200 GeV	4 TeV
$m_{\tilde{D}_3}$	100 GeV	4 TeV
$\lvert M_1 \rvert$	0 GeV	4 TeV
$\lvert M_2 \rvert$	70 GeV	4 TeV
M_3	200 GeV	4 TeV
$\lvert \mu \rvert$	80 GeV	4 TeV
$\lvert A_t \rvert$	0 GeV	8 TeV
$\lvert A_b \rvert$	0 GeV	4 TeV
$\lvert A_\tau \rvert$	0 GeV	4 TeV
M_A	100 GeV	4 TeV
$\tan\beta$	1	60

Table 6.5: Scan ranges for the 19 pMSSM parameters

and run within MicrOMEGAs 3.5.5 [193,194], a tool used to calculate DM relic density which contains external tools suitable to calculate SUSY particle spectrum such as IsaJet [195], Spheno [196], SuSpect [197] and SoftSUSY between others[4]. The particle spectrum was then passed as an input to FeynHiggs 2.10.0 [198, 199] that calculated light CP-even higgs masses at 3-loop level. For decay rates SUSY-HIT 1.3 [200] was used with some modifications needed to fix, add and improve the following features : First light quark and lepton masses were included to get more precise Branching Ratios (BR) and decay widths. Also the mass of the lightest meson was included to account for hadronization effects. Another important change was the addition of the correct analytic chargino decay expressions found in the addendum [201], which was needed for case when the mass splitting between the chargino and the neutralino is smaller than 1 GeV. Further changes included the removal of QCD corrections from stop and sbottom decays as they often gave negative decay rates and the separation of higgs decays to τ-sneutrinos from e- and μ-sneutrinos.

In some cases is has been shown that SUSY-HIT misses important decay channels or predicts wrong values for some decay widths. For such cases extra work was done to get more precise values. As an example, for the decay of right handed sfermions, SUSY-HIT only calculates the leading two-body decays of the type $\tilde{f}_R \to f\tilde{\chi}^0$ or $\tilde{q}_R \to q\tilde{\chi}^0$. Nevertheless there is a non negligible part of the space phase where the $\tilde{\chi}^0$ has a negligible bino component, strongly suppressing this channels. For such cases additional three-body and four-body decays are included using MadGraph5_aMC@NLO 2.1.1 [202]. As the two body decays include include the on-shell component of intermediate particles in three body decays redundant decays are selected and removed to avoid double counting. Similar adjustments were done to neutralino decays to sfermions and to four-body stop decays.

[4] MicrOMEGAs was also used to calculate the relevant parameters for applying the experimental constrains detailed in the next section.

6.3.2 Selection of points

For a model point to be considered as acceptable, its spectrum must be calculable without errors and it must be consistent with theoretical and experimental limits as electroweak and flavor precision measurements, dark matter relic density and additional collider results.

The first step was to ensure that the model spectrum was properly calculated, and all models with pathological errors in the SoftSUSY output were dismissed. The particle spectrum was also tested recalculating it with SuSpect. Any model for which SuSpect either gave a fatal error or predicted any particle mass with more than 50% difference with respect to SoftSUSY was dismissed. For higgs bosons, there is a requirement that the mass cannot be 5 GeV apart from the SoftSUSY prediction. This was done because there was a small set of models for which a larger deviation existed, insinuating that for those cases the results were not to trust. Another sanity check was done with the FeynHiggs estimate for the higgs mass uncertainty. If it is larger than 5 GeV the model is dismissed. Finally SUSY-HIT decays are checked, discarding any model that included one or more particles above 1 TeV, larger widths or with negative BRs.

Additionally, theoretical constrains required removing any point for which SoftSUSY output included tachyons or a wrong shape for the Higgs potential. It was also tested that the scalar potential did not break color or charge [203].

Parameter	**Minumum**	**Maximum**
$\Delta\rho$	-0.0005	0.0017
$\Delta(g_\mu - 2)$	-17.7×10^{-10}	43.8×10^{-10}
$BR(b \to s\gamma)$	2.69×10^{-4}	3.87×10^{-4}
$BR(B_s \to \mu^+\mu^-)$	1.6×10^{-9}	4.2×10^{-9}
$BR(B^+ \to \tau^+\nu_\tau)$	66×10^{-6}	161×10^{-6}
$\Omega_{\tilde{\chi}_1^0} h^2$	—	0.1208
$\Gamma_{invisible}(Z)$	—	2 MeV
Charged sparticle masses	100 GeV	—
$m_{\tilde{\chi}_1^\pm}$	103 GeV	—
$m_{\tilde{u}_{1,2}}, m_{\tilde{d}_{1,2}}, m_{\tilde{c}_{1,2}}, m_{\tilde{s}_{1,2}}$	200 GeV	—
m_h	124 GeV	128 GeV

Table 6.6: Experimental constraints on pMSSM model points form precision measurements, DM relic density and other collider limits

Finally, experimental constraints were imposed to satisfy results from flavor physics, precision electro-weak measurements, the higgs mass, previous collider experiments and cosmological observations. These limits are presented in table 6.6. References to the publications and a brief description of each of the requirements is presented below.

- The limits for the EW parameter $\Delta\rho$ are taken from a global SM fit to electroweak precision data [204].
- The muon anomalous moment $\mu_g - 2$ range is quite loose. It is built from the union of the 3σ region from the SM mean value of $(0.0 \pm 5.9) \times 10^{-10}$ found in equation 18 of [205] and the experimental value $(24.9 \pm 6.3) \times 10^{-10}$ found in equations 1 and 19 of the same publication.
- Flavor constraints come from three decays involving $b-$quarks: The decay of the $b-$quark to an $s-$quark plus a photon, The decay of the B_s meson to a di-muon pair and the

decay of the B^+ meson to a τ plus its corresponding neutrino. The limits are set by the union of the 2σ region from the SM mean value and the experimental value.

For $b \to s\gamma$ the experimental value is taken from world averages that can be found in [206] where the theoretical value is also available.

For $B_s \to \mu^+\mu^-$ the experimental value is taken from the combined LHCb and CMS results [207] and the SM value is obtained with MICROMEGAS and scaled by 1/(1-0.088) as proposed in [208].

The $B^+ \to \tau^+\nu_\tau$ decay is calculated using SUPERISO [213] including $\tan\beta$ corrections. In this case the experimental result is taken from [209–212] and its 2σ range is united with the 2σ SM prediction [214].

- DM constrains come from the fact that pMSSM assumes R-parity conservation. In this case, the LSP is stable and thus must have a cosmological abundance. The total dark matter abundance is used as an upper limit on LSP abundance. The value given in table 6.6 represents the central value given the Plank collaboration [191] plus two times its experimental uncertainty.

- The last five collider constraints displayed on table 6.6 come from LEP and from the higgs mass at the LHC.

  The first parameter $\Gamma_{invisible}(Z)$ is used to dismiss models that contribute to the invisible width of the Z boson, that according to LEP results [215] must lie below 2 MeV.

  The second and third constraints come from the combined LEP searches [216] where it was found that charged sparticle masses below 100 GeV are forbidden. For charginos, this limit is slightly extended to 103 GeV if all sneutrinos are heavier than 160 GeV and if the chargino-LSP mass splitting is at least 2 GeV. Both results are presented in figure 6.1.

  The next limit on light squark masses is rather loose, forbidding masses below 200 GeV. Given the scan ranges in table 6.5 and the negligible mixing for the first two squark generations, this constraint does not entail additional requirements.

  The final constraint comes from the ATLAS higgs mass. At the moment of generating the pMSSM points the ATLAS higgs mass central value was 126 GeV [15] instead of the 125.10 ± 0.14 GeV [217] at the moment of writing this document. Within the pMSSM, the lightest higgs mass was calculated with FEYNHIGGS and it was required to be within 2 GeV window from the experimental value, which is the regular theoretical uncertainty found to be given by FEYNHIGGS.

6.3.3 Undersampling of models with Bino-like LSP

The nature of the LSP depends largely on the values of M_1, M_2 and μ which are present in the neutralino mass matrix shown in A.30 in Appendix A. Depending on these values, some components of the diagonalizing matrix N_{ij} will dominate over the others making the neutralino to be either Bino-like, Wino-like or Higgsino-like. Using equation A.31 the LSP can be written as:

$$\widetilde{\chi}_1^0 = N_{11}\widetilde{B} + N_{12}\widetilde{W}^3 + N_{13}\widetilde{H}_d^0 + N_{14}\widetilde{H}_u^0. \tag{6.1}$$

If $N_{11}^2 > N_{1j}^2$, it is said that the neutralino is of bino type. If $N_{12}^2 > N_{1j}^2$, then the neutralino is of the wino type. Finally, if $N_{13}^2 + N_{14}^2 > N_{1j}^2$ the neutralino is of the higgsino type.

To be in agreement with the DM abundance, neutralino annihilation is a key process to keep neutralino relic density below the limit in table 6.6. There are two main annihilation

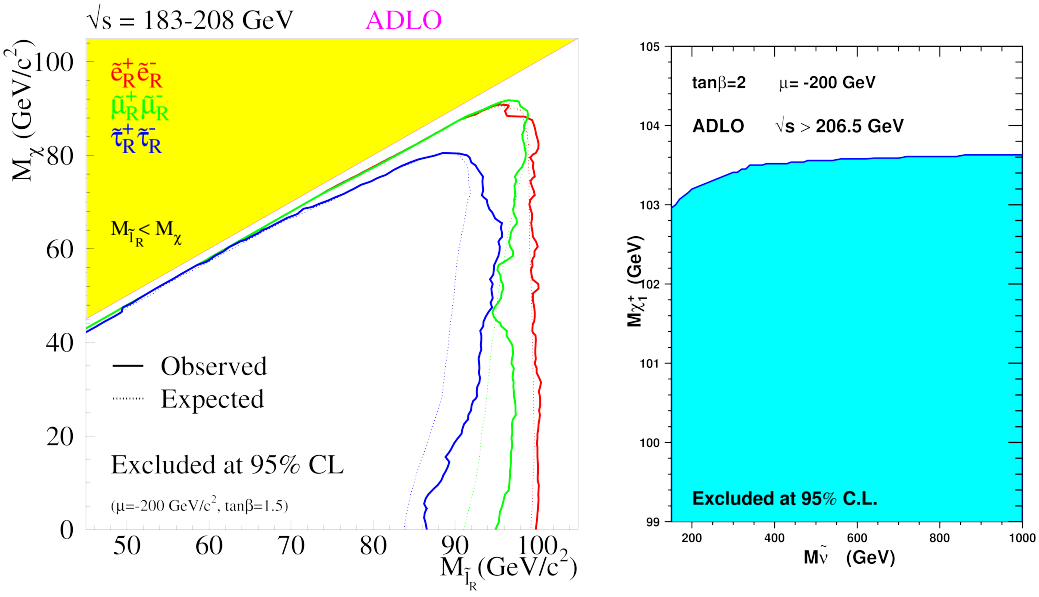

Figure 6.1: Left: Slepton mass exclusion plane. Right: Chargino mass exclusion plane. Both from LEP collaboration combined search ADLO [216]

processes. The first is via a higgs or a Z boson in the s-channel, or via a chargino or slepton in the t-channel. A second possibility is the co-annihilation when another particle is nearly mass degenerate with the neutralino LSP. If the model has a Wino- or a Higgsino-like LSP (large values of M_2 or μ), it is clear by looking at the chargino mass matrix in A.21 in Appendix A, that a chargino with a very similar mass as the LSP would exist. This translates into high rates of annihilation via a chargino in the t-channel, and in co-annihilation processes. In this cases, the DM relic abundance limit is easily satisfied as long as the wino mass lies below 2.7 TeV or the higgsino mass below 1 TeV [219–221]. In models with a Bino-like LSP, the mechanisms for annihilation are not confirmed, and would strongly depend on very specific combination of the parameters. This leads to a very low percentage of models satisfying the DM requirement and therefore to an under-sampling of models with Bino-like LSP. The generation of points is thus divided in two: The first 20×10^6 points are required to have a Wino- or Higgsino-like LSP, from which 206,917 models fulfill the criteria required in table 6.6. From these models 80,233 have Wino-like LSP and the remaining 126,684 have a Higgsino-like LSP. For the Bino-like LSP models, 480×10^6 point were sampled, from which 103,410 passed the requirements in table 6.6. In these categories more than 87% of the points have a defined LSP type with at least 90% purity.

6.3.4 Set of model points

Once all the constraints in table 6.6 have been applied, a total of 310,327 models survived from the 500×10^6 initially sampled model points. Figure 6.2 shows the normalized distributions of sparticle spectra. The mass distributions in the plots are shown separately depending on the LSP type of each model. As observed in the left plot, there is a preference for lighter gluinos in Bino-like LSP models, enabling the co-annihilation process to fulfill the DM constraint. On the right plot, there is a spike for the Bino-like LSP models at very low neutralino masses. These points keep the LSP abundance below the CDM limits thanks to annihilation via higgs

or Z bosons in the s-channel in the so called h or Z *funnels*. The peak is composed of two individual peaks (zoomed in to on the upper right corner of the plot) right at the values of the Z and the lightest higgs masses.

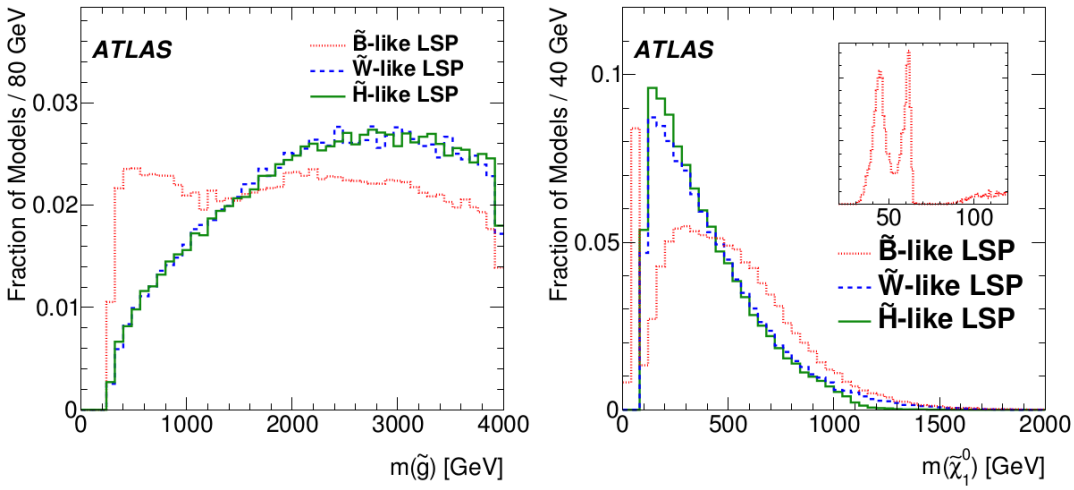

Figure 6.2: Normalized distributions of the gluino (Left), LSP (right) masses once the constraints in table 6.6 have been applied [158]

The next to lightest supersymmetric particle (NLSP) plays a crucial role on the phenomenology of a model, and will be usually determined by the LSP type. For Wino-like and Higgsino-like LSP models, the NLSP is either the lightest chargino or the next to lightest neutralino, as for these models there is only a small splitting between their masses as already explained. In Wino-like LSP models more than $99,9\%$ of the models have a chargino NLSP, while for Higgsino-like LSP models roughly 89% of the models have a chargino NLSP and in $10,7\%$ of the models the NLSP is the next to lightest neutralino. The small mass difference $\Delta m(\widetilde{\chi}_1^0, \widetilde{\chi}_1^\pm)$ increases the lifetime of $\widetilde{\chi}_1^\pm$ that could even decay inside the tracker leaving the distinctive disappearing track signature searched in [178]. In Bino-like LSP models there is a wider variety NLSP types. Most of the models $\sim 32\%$ still have a $\widetilde{\chi}_1^\pm$ LSP. Nearly 12% of the models have a $\widetilde{\chi}_2^0$ NLSP and another 12% of the models have a $\tilde{g}$ NLSP. The remaining models have light squarks as NLSPs.

6.3.5 Event generation of signal samples

After all the points and its parameters have been set, sensitivities of the searches must be tested to check the model could be excluded or not. Simulating events for more than 300k models, including detector simulation and reconstruction to run the analysis including all their SRs over this huge set, is rather unpractical and would require a enormous amount of effort, time and resources. Instead, a categorization and evaluation of the model is previously done to test for which points makes sense to run a full event generation and if a full detector simulation is needed.

Cross section requirement

If the cross section of a process is too low, none or very few events will be produced in a collision. For this reason a minimum cross section requirement is applied[5]. In each model

[5]The cross sections were calculated using Prospino 2.1 [222–226]

SUSY particles are produced in different processes that can be classified in four groups: Strong production including squark or gluino pair production and squark-gluino production. Electroweak production includes electroweakino pair production and slepton pair production[6]. Finally the mixed production which includes electroweakino-squark and electroweakino-gluino pair production.

For the first round, only MC events at particle level were generated[7] for points satisfying a minimal cross section threshold and an upper LSP limit. Then the analyses tested their sensitivities to these models using the method that will be explained below. After these tests, the limits for the cross section and LSP requirements were changed a few times, allowing the event generation of more models, that despite of a small cross section were in a sensitive region. After a few rounds, the final limits were chosen and are displayed on table 6.7. The final upper limit for the neutralino mass was fixed at 1000 GeV

Production channel	**Cross section threshold (fb)**	**Percentage of models with event generation**		
		Bino LSP	**Wino LSP**	**Higgsino LSP**
Strong	0.25	82.5	74.9	76.7
Mixed	0.25	52.6	42.1	13.9
Electroweak	7.50	38.3	72.5	75.5
Slepton pair	0.75	9.6	7.9	9.5

Table 6.7: Cross sections thresholds required for particle-level event generation divided by LSP and production type. Any models may exhibit one or more production channels. For each production channel the fraction of models passing the cross section requirement is shown.

Event production at particle level

For the models satisfying the cross section and LSP mass requirements, an event generation at particle level is performed using MADGRAPH5 1.5.12 [189] with the CTEQ 6L1 PDF to generate sparticle pair production plus one additional parton in the matrix element and PYTHIA 6.427 [184] with the AUET2B parameter set for the decays and parton showering. Additional information can be found on reference [158]. Before generating any event using detector simulation and reconstruction efficiencies, the groups performing *inclusive*, *third generation* and *electroweak* searches, implemented a simplified version of each analysis using only particle or *truth* level information and run it over the samples. A brief summary of the truth analysis implemented for the one lepton analysis is given below.

One lepton analysis: Truth object definition

The object pre-selection, event selection and signal region definitions are as close as possible to the definition of the objects used for the full analysis [161]. For electrons muons and jets, a pre-selection is applied before performing the overlap removal between objects which are tightened in the event selection. As a first step the hard(soft) electrons must have $p_T > 10(7)$ GeV and $\eta < 2.47$. For the hard(soft) muons, $p_T > 10(6)$ GeV and $\eta < 2.4$. Jets are preselected with $p_T > 20$ GeV and an $\eta < 2.8$ and an isolation requirement of $\Delta R(jet, e) > 0.2$ for which the used electrons are the ones previously defined. These jets are used in the lepton-jet overlap removal requirement of $\Delta R(\ell, jet) > 0.4$ for leptons. Additionally, electrons must lie within $|\eta| < 2.47$ region, hard(soft) signal electrons are required to have $p_T > 25(10)$ GeV with an

[6]Slepton processes are considered as an independent group, as the ATLAS acceptance for slepton pairs can be much higher as for with EW production.

[7]Without including detector simulation or reconstruction efficiencies

upper limit on soft electrons of $p_T < 25$ GeV All events with an electron in the crack region ($1.37 < \eta < 1.52$) are vetoed. For muons $|\eta| < 2.4$, hard(soft) signal muons have a similar requirement of $p_T > 25(6)$ GeV with an upper limit on soft muons of $p_T < 25$ GeV. For signal jets an additional cut of $p_T > 30(25)$ GeV is used in both analysis, plus the $\Delta R(jet, e) > 0.2$ with preselected electrons already discussed. These requirements are summarized in tables 6.8 , 6.9 and 6.10. No special requirements are used for truth missing transverse energy.

Cut	Value/description	
	Hard Analysis	Soft Analysis
	Preselected jet	
Acceptance	$p_T > 20$ GeV	
	$\|\eta\| < 2.8$	
Overlap	$\Delta R(\text{jet}, e) > 0.2$	
	Signal jet	
Acceptance	$p_T > 30$ GeV	$p_T > 25$ GeV
	$\|\eta\| < 2.5$	

Table 6.8: Jet selection criteria. Signal selection requirements are applied on top of the pre-selection.

Cut	Value/description	
	Hard	Soft
	Preselected Electron	
Acceptance	$p_T > 10$ GeV	$p_T > 7$ GeV
	$\|\eta\| < 2.47$	
	Signal Electron	
Acceptance	$p_T > 25$ GeV	10 GeV $< p_T <$ 25 GeV
Overlap	$\Delta R(e, jet) > 0.4$	
	Crack Electron	
Acceptance	$1.37 < \|\eta\| < 1.52$	

Table 6.9: Electron selection criteria. Signal selection requirements are applied on top of the pre-selection.

Cut	Value/description	
	Hard	Soft
	Preselected Muon	
Acceptance	$p_T > 10$ GeV	$p_T > 6$ GeV
	$\|\eta\| < 2.4$	
	Signal Muon	
Acceptance	$p_T > 25$ GeV	6 $GeV < p_T <$ 25 GeV
Overlap	$\Delta R(\mu, jet) > 0.4$	

Table 6.10: Muon selection criteria. Signal selection requirements are applied on top of the pre-selection.

One lepton analysis: Global variables

Several global variables are defined with the use of the previously defined objects to help isolating specific background processes or enhance the signal over background ratio in the signal regions.

- the transverse mass, $m_T = \sqrt{2 \cdot p_T^{\ell} \cdot E_T^{miss} \cdot (1 - cos(\Delta\phi(\ell, E_T^{miss})))}$,
- the effective mass, m_{eff} :

$$m_{eff} = p_T^{\ell} + \sum_{j=1}^{N_{jet}} p_T^{jet_j} + E_T^{miss} \tag{6.2}$$

  where p_T^{ℓ} is the transverse momentum of the signal lepton and $p_T^{jet_j}$ are the transverse momenta of all good jets with $p_T > 40$ GeV to be less sensitive to softer jets coming from increased pile-up conditions.

Two different versions of the effective mass are considered. The first one is based on all good jets with $p_T > 40$ GeV in an event, defined as:

$$m_{eff}^{incl} = p_T^{\ell} + \sum_{j=1}^{N_{jet}} p_T^{jet_j} + E_T^{miss} \tag{6.3}$$

This effective mass m_{eff}^{incl} is used as the final discriminating variable in the signal region. Including all jets gives the effective mass a better separation power between signal and backgrounds as usual signal models exhibit more jets than the backgrounds in the final states.

The second definition uses only the first three jets that are required as a minimum in the three jets signal region and it is used in the ratio cut $E_T^{miss}/m_{eff}^{excl}$.

$$m_{eff}^{excl} = p_T^{\ell} + \sum_{j=1}^{3} p_T^{jet_j} + E_T^{miss} \tag{6.4}$$

The reason of using just the leading 3 jets for $E_T^{miss}/m_{eff}^{excl}$ comes from the fact that the variable is originally introduced to remove events with large E_T^{miss} from missing objects in the reconstruction.

One lepton analysis: Truth signal regions definition

In the original analysis there were 6 SRs for the hard lepton channel. Three looser SR, labeled with an *exlusion* tag, which are binned in $E_T^{miss}/$ and m_{eff}^{incl}. The binning is used to exploit the expected signal shape when placing model-dependent limits making them sensitive to a large variety of models not originally optimized for. For the truth simplified analysis these regions are not binned and the *exclusion* tag is kept only to maintain consistency with the original analysis. The next three tighter SR labeled with a *discovery* tag were optimized for the best discovery reach. Besides the six hard lepton signal regions, 2 SR for the soft lepton channel are defined. The main differences with respect to the original SRs are: The requirements of no $b-$jets for the soft SR, the binning in m_{eff} and E_T^{miss} for the herd *exclusion* SRs and the absence of any pileup jet correction or requirement. The definition of these 8 simplified SRs is summarized in table 6.11

	discovery (exclusion) hard single lepton			soft single lepton	
	3-jet	**5-jet**	**6-jet**	**3-jet**	**5-jet**
N_ℓ	1 (electron or muon)				
p_T^ℓ (GeV)	> 25			[10,25] (ele) , [6,25] (mu)	
$p_T^{add.\ell}$ (GeV)	< 10			< 7 (ele), < 6 (mu)	
N_{jet}	≥ 3	≥ 5	≥ 6	[3,4]	≥ 5
p_T^{jet} (GeV)	$> 80, 80, 30$	$> 80, 50, 40, 40, 40$	$> 80, 50, 40, 40, 40, 40$	$> 180, 25$	
$p_T^{add.\ jets}$ (GeV)	– (< 40)	– (< 40)	–	–	
E_T^{miss} (GeV)	> 500 (300)	> 300	> 350 (250)	> 400	> 300
m_T (GeV)	> 150	> 200 (150)	> 150	> 100	
$E_T^{miss}/m_{eff}^{excl}$	> 0.3	–	–	–	
$E_T^{miss}/m_{eff}^{incl}$	–			> 0.3	
m_{eff}^{incl} (GeV)	> 1400 (800)		> 600	–	
$\Delta R_{min}(jet, \ell)$	–			> 1.0	–

Table 6.11: Overview of the selection criteria for the hard and soft single lepton signal regions. The requirements of the exclusion signal region are shown in parentheses when they differ from those of the discovery signal region.

Evaluation of models produced at particle level

With the simplified version of the analyses, each group evaluated their sensitivity to the models produced at particle level. Inefficiencies from detector reconstruction were usually parametrized using efficiency factors in each SR. These efficiencies were calculated using previously simulated samples. For some analyses, there are more sophisticated methods to calculate these efficiencies such as p_T or angular dependent efficiencies. In the case of the one lepton analysis, based on previous non pMSSM signal samples, only one efficiency was fixed over all SRs. The one lepton analysis efficiency is defined as number of expected events using detector reconstruction (N_{reco}^{exp}) for a given number of events with only particle or *truth* level information over the number of *truth* events (N_{truth}) and it is set to 0.5:

$$\epsilon = \frac{N_{reco}^{exp}}{N_{truth}} = 0.5 \tag{6.5}$$

The number of *truth* events (N_{truth}) in the SRs are now compared to the model-independent 95% confidence level (CL) upper limit (UL) on the number of signal events (N_{max}^{95}) in each signal region. The N_{max}^{95} in all the one-lepton SRs are presented on table 6.12. This values and the procedure to calculate them are found in the original 8 TeV one lepton analysis paper [161]. The limits are shown for the soft signal regions and for both hard lepton

Signal Channel	N_{max}^{95}
Hard SR3J (exclusion)	18.7
Hard SR5J (exclusion)	11.1
Hard SR6J (exclusion)	8.1
Hard SR3J (discovery)	8.2
Hard SR5J (discovery)	5.7
Hard SR6J (discovery)	4.5
Soft SR3J	8.1
Soft SR5J	7.1

Table 6.12: 95% CL upper limits on the number of signal events (N_{max}^{95}).

discovery and *exclusion* SRs. Only the combined electron-muon limits are shown as these

channels are not divided in the simplified *truth* analysis. For the hard lepton analysis, the *discovery* SRs place more stringent limits than the *exclusion* SRs. This behavior is expected due to the tighter requirements and because the binning in $m_{\text{eff}}^{\text{incl}}$ and E_T^{miss} is not exploited here.

After comparing N_{truth} with N_{max}^{95} and taking into account the reconstruction efficiency factor ϵ the pMSSM models were categorized in three categories, using different criteria convenient for each analysis. The first category is models that can very likely not be excluded, the second category is models that can possibly be excluded and finally the third category for models that can almost certainly be excluded. The exact lower and upper limits to define such regions are analysis and signal region dependent. The initial one-lepton categorization of the models was:

- Cat. 1 (Not Excluded): $\epsilon \cdot N_{truth} < N_{max}^{95}$ in all SR.
- Cat. 2 (Uncertain): $N_{max}^{95} < \epsilon \cdot N_{truth} < 2.5 \cdot N_{max}^{95}$ in at least one SR.
- Cat. 3 (Excluded): $2.5 \cdot N_{max}^{95} < \epsilon \cdot N_{truth}$ in at least one SR.

After this first categorization, and with the first round of reconstructed production where only 73 models in category 2 for the 1 lep analysis were produced, a first truth to reconstructed (Reco) comparison was done for these 73 pMSSM samples.

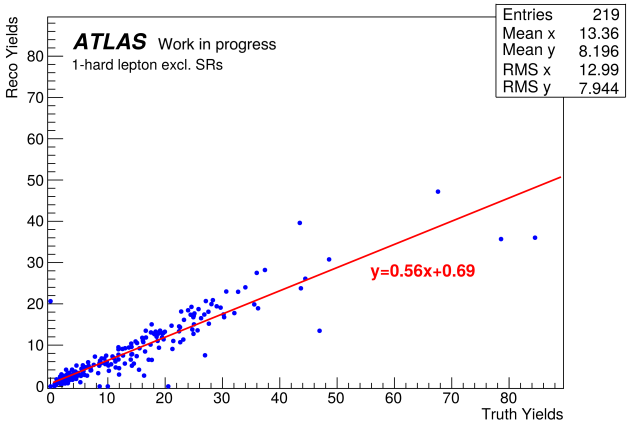

`Figure 6.3:` First Truth to Reco comparison for 73 pMSSM points. For each point, the yields in the three 1 hard lepton exclusion SRs (SR3J_excl, SR5J_excl and SR6J_excl) are shown

As seen in Figure 6.3 a good agreement between the truth level and simulation level (Reco) yields can be observed for the displayed signal regions. With this correlation, the assumption that $N_{truth} = 2 \cdot N_{reco}$ ($\epsilon = 0.5$) was tested to be accurate. This tests were also performed by other groups also showing good agreement using their assumptions. In cases where a good agreement was not found, a redefinition of category 2 was done, and the models for which the truth level evaluation was not reliable, have been simulated. Despite the good agreement for the one lepton analysis, after the first rounds of simulation of pMSSM models, the limits were slightly adjusted to ensure that no non-excluded model was being assigned to Cat. 3. The one-lepton lower limit was shifted to a less tighter limit, also more consistent with the limits chosen by the other groups. The new set of limits is given by:

- Cat. 1 (Not Excluded): $\epsilon \cdot N_{truth} < 0.5 \cdot N_{max}^{95}$ in all SR.

- Cat. 2 (Uncertain): $0.5 \cdot N^{95}_{max} < \epsilon \cdot N_{truth} < 2.5 \cdot N^{95}_{max}$ in at least one SR.

- Cat. 3 (Excluded): $2.5 \cdot N^{95}_{max} < \epsilon \cdot N_{truth}$ in at least one SR.

With this final categorization, for Bino-like LSP models for which strong production was run, the 1 lepton analysis can certainly exclude $\sim 2k$ models $\sim 2.5\%$ and cannot exclude $\sim 80k$ models $\sim 91,8\%$ leaving $\sim 5k$ models $\sim 5.6\%$ in the second category. For strong produced in Wino-like and Higgsino-like LSP models combined, the 1 lepton analysis can exclude $\sim 7k$ models $\sim 4.9\%$ and cannot exclude $\sim 128k$ models $\sim 85.2\%$ leaving $\sim 15k$ $\sim 9,9\%$ uncertain in category 2. A quick examination of these numbers shows that the one lepton analysis has rather low sensitivity to a large set of pMSSM points, as the bulk ends up in the first category. Additional insights on this matter will be given later when studying the set non excluded points.

For the most sensitive analysis (inclusive 0-lepton analysis) a huge set of models would be in Cat.2 unless the upper and lower limits are chosen close to each other. This was shown to be possible for most of the SRs, but in some cases this causes miss-categorizations. The inclusive 0-lepton analysis created another set of subcategories to deal with this issue allowing to capture the most models with uncertain exclusion while keeping low miss-categorization rates. More details on this can be found on [158].

Having the set of models in each category for each analysis, an overall categorization is done, by taking the results from the most sensitive SR from all searches. This shows that 35.9% of the models can be excluded, while 44.7% end up in the first category and thus cannot be excluded at the 95% CL. The latter leaves roughly a 20% ($\sim 45k$) of the models in category 2, for which a more detailed investigation is done as explained in the next section.

Event production: Simulation and reconstruction

For the $\sim 45k$ remaining models in category 2, a complete simulation was performed where GEANT4 [227] is used to simulate events combined with ATLFAST II [228], using a *fast* parametrization of EM and HAD calorimeters performance [229] and full event reconstruction. Additionally to test truth level categorization, 5% of the models in Cat.3 were also fully simulated. The simulation included a description of pileup events and corrections based on identification efficiencies and resolution effects. For these points signal events are generated with four times the integrated luminosity recorded ($4 \cdot 20.3$ fb$^{-1} = 81.2$ fb^{-1}). The processes simulated were only the ones contributing to the analyses of interest. The full cross section calculation is based on [230] which includes NLL corrections [231–235] and enveloping of the PDFs, factorization and normalization scale. The envelope also defines the theoretical uncertainty on the cross section. A diagram showing the main procedure for the signal model generation, selection and evaluation can be seen in figure 6.4

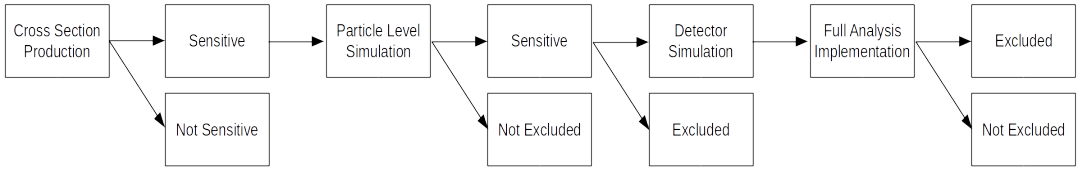

Figure 6.4: Diagram of the pMSSM generation and evaluation chain.

6.4 Evaluation of models

To test if the inconclusive model points can be either excluded or not, each of the analyses tested their sensitivity to these models, using the full procedure used in the original analyses. Most of the analysis use the HistFitter [153] software to perform this evaluation. Once the SR with the best expected sensitivity is found, the "CL_s method" [155] is used to determine if the model point can be tagged as excluded or not at 95% CL for that analysis. For some analyses, including the one lepton analysis, a multi-bin fit is performed to obtain an enhanced exclusion power. In such cases the multi-bin fit provides the expected and observed CL_s values. The observed CL_s value finally establishes if a model is excluded or not. For most of the exclusion fits, only nominal signal cross sections are used, without any theoretical uncertainties on the signal. The Mono-jet and Mono-jet stop analyses which are sensitive to high p_T ISR jet modeling apply an additional 25% ISR signal uncertainty. In other analyses, to apply the fully combined original fit procedure was not possible, and only the individual SRs are used, resulting in a lower exclusion power. Truth level and simulated analysis were combined to perform a full and wide evaluation of the complete model set including overlapping results from all analysis. If a model was fully simulated, only these results are used. If two or more analyses are sensitive for a model, the decision is based in the analysis with the best expected CL_s value, and the model is categorized as excluded if the observed CL_s value is below 0.05. With this approach there is the possibility for some models to be categorized as not excluded even when another analysis was found to exclude it. If the model had only particle level production, it is tagged as excluded if at least for one analysis it was considered to be excluded, and not excluded if it was found to be not excluded by all analyses. No model should be in the second category as these were all simulated, but there is an exception for models tagged as excluded for one type of production process but ended in category 2 for another production channel. In such a case, the model will be tagged as excluded independent of the second result.

For the *Other Searches* found in table 6.4 there are a few details in the model evaluation. For the case of long lived particle searches most of the long lived particles are χ_1^+ and χ_2^0. Model points with these long lived electroweakinos, are evaluated using the same procedure already described. Model points where the long lived particles are squarks, gluinos and sleptons with $c\tau > 1$ mm have not been simulated, thus only long lived searches are used to constrain them. Long lived particle searches have limits on the production cross section of squarks, gluinos and sleptons when their lifetime is long enough to leave the detector before decaying. Model points with $\tilde{b}$, $\tilde{t}$, $\tilde{g}$, $\tilde{\tau}$ or χ^+ with lifetimes greater than 85 ns and production cross section above the limits from the 7 or 8 TeV result, are to be excluded. If the lifetimes are shorter or the cross sections smaller, the point is considered not to be excluded.

The *Heavy higgs boson search* evaluation is done only for models for which no other search is expected to exclude them at 95% CL. The relevant higgs production for this search is gluon fusion and associated production with $b-$quark(s). The former is dominant for low $\tan\beta$ values while the latter dominates for large $\tan\beta$ values. Both gluon fusion and $b-$associated production cross sections receive large radiative corrections, which are in general not known to a good accuracy for arbitrary masses of the super-partners. The cross sections and BRs to $\tau\tau$ pair are calculated as described in [236–238]. For the pMSSM analysis a simplified version of the original analysis is performed, using only the high m_A category ($m_A > 200$ GeV) as due to the pMSSM constraints this is true for all model points. For this phase space $b-$associated production dominates and it is calculated for each model point using SusHi 1.3.0 [239]. Within this models A and H masses are very close to each other ($m_A \sim m_h$) and both are simulated. The production cross section times BRs ($\sigma(bbH) \times BR(H \to \tau\tau) + \sigma(bbA) \times BR(A \to \tau\tau)$ is calculated and compared to the upper limits found on the original paper.

6.5 Results: ATLAS limits to pMSSM models from LHC Run 1 results

The results and reach from all searches probing the pMSSM spectrum with Run 1 results, constitute a vast group of very interesting plots and tables. In this document only some of the most important results are presented. In Appendix B a few complementary plots are available. An extended list with plots, parameters, observables and a breakdown of the analysis excluding every model, are available in the ATLAS Collaboration public results [240]. Most of the results will be presented as projections into 2-dimensional subspaces of the full 19 parameter pMSSM space. It is clear that the interpretation of these plots must be taken with care as much of the observables depend on the distribution of the generated model points in the parameters that have been projected, and on experimental constraints on parameters other than those plotted. However, common aspects of the impact of the ATLAS Run 1 searches are clear.

6.5.1 Impact on light squarks and gluino masses

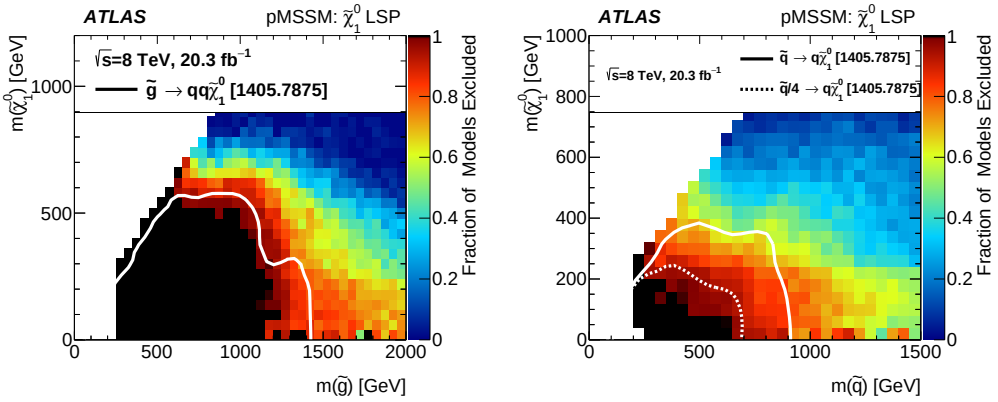

Figure 6.5: Fraction of pMSSM points excluded by the combination of ATLAS searches in the $m_{\tilde{\chi}_1^0} - m_{\tilde{g}}$ plane in the left, and in the $m_{\tilde{\chi}_1^0} - m_{\tilde{q}}$ plane [158].

The left plot in figure 6.5 shows the fraction of excluded models in each mass bin[8] after imposing ATLAS Run 1 limits, presented in a 2-D plot of the LSP and gluino masses. The fraction of excluded models is depicted with a color code where black means 100% of the models excluded and blue the opposite. White represent regions where no model has been generated. As expected from previous studies, light gluino masses are largely constrained, while for increasing gluino masses the fraction of model points excluded is reduced. Additionally, a white reference line is superimposed on top of the plot showing the previous limit in the same plane for one of the most sensitive analysis (0 lepton + 2-6 jets + E_T^{miss} [159]). This limit corresponds to the observed simplified model limit at 95% CL where only the gluino and the LSP are kinematically accessible and where the gluino decay occurs via one virtual squark to 2 quarks and a neutralino $\tilde{g} \rightarrow q\bar{q}\tilde{\chi}_1^0$. There is in general a good agreement between the solid line and the fraction of excluded pMSSM models on this plot, and the simplified model successfully grasps the pMSSM phenomenology. However it is clear that pMSSM sensitivity differs from the simplified model in certain regions of the phase space. Near the diagonal where $m_{\tilde{g}}$ is almost degenerate with $m_{\tilde{\chi}_1^0}$ the simplified model is less sensitive than the combined pMSSM search, underestimating the ATLAS sensitivity due to its simplified nature. Possible sources

[8] Each mass bin usually includes large number of pMSSM model points

of these differences include the fact that multiple analyses were considered and probably more important, the residual dependence of the sensitivity on other sparticles masses which are absent in a simplified model. The plot also shows that all models with gluino masses below 600 GeV can be excluded. This limit extends to $\sim 1\ TeV$ for $m_{\tilde{\chi}_1^0} \lesssim 500$ GeV.

In the right plot in figure 6.5 the same results are shown but projected in the lightest squark mass versus the LSP mass plane. For low squark masses there is good sensitivity and models with a $m_{\tilde{q}}$ below 250 GeV can be excluded by the ATLAS analyses. The white line shows the 95% CL exclusion obtained by the same search than the plot in the left, but for a simplified model where the only accessible particles are the LSP and the eight lighter squark assumed to be mass degenerate and where the produced squark decays directly to a quark and a neutralino ($\tilde{q} \to q\tilde{\chi}_1^0$). There is no agreement between the simplified model limit and the pMSSM fraction of excluded models in this case. Within the the pMSSM only a small fraction of the points excluded by the simplified model can be excluded. This is in principle because in the pMSSM not all eight lighter squarks are be degenerate in mass but only two. The dashed line superimposed represents an alternative simplified model for which the cross section is divided by four, just to mimic the effect of having only 2 degenerate squarks. Comparing the pMSSM exclusion fraction with the dashed line shows a much better agreement.

Another feature seen in both plots in figure 6.5 is that for light LSP mass ($m_{\chi_1^0} \lesssim 200$ GeV) region, there is a high fraction of excluded models penetrating beyond the simplified model reference line reaching high gluino or squark masses. The production cross section for these heavy sparticles is small, and direct direct searches are not so sensitive in this region. Therefore, the channels excluding these models cant̀ be one of the inclusive searches looking for direct squark or gluino production. In fact searches looking for disappearing tracks from long lived charginos are responsible to constrain this region. Additional information on how these searches are constraining this region is found in section B.1 of Appendix B.

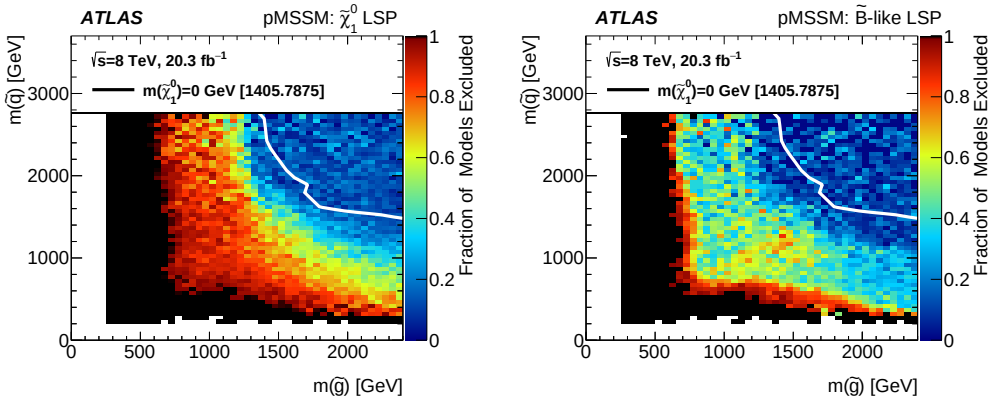

Figure 6.6: Left: Fraction of pMSSM points excluded by the combination of ATLAS searches in the $m_{\tilde{q}} - m_{\tilde{g}}$. Right: The same plot as in the left but only for Bino-like LSP [158].

Other interesting 2-D plot to present the effects of ATLAS searches is the $m_{\tilde{g}} - m_{\tilde{q}}$ plane where $\tilde{q}$ represents the lightest squark from the first two generations. Figure 6.6 shows the fraction of excluded models projected in this plane, for any LSP mass. As seen in the left plot there is almost a full exclusion of gluinos masses below 700 GeV plus a high exclusion fraction up to $\sim 1.2\ TeV$ for all $m_{\tilde{q}}$ values. On the other hand light squarks are also constrained, but only for low $m_{\tilde{g}}$. At higher gluino masses both direct squark pair production via gluino exchange on the t-channel and the associated squark-gluino production are suppressed. In this plane, the simplified model line on top assumes all eight light squarks to be degenerate and a massless LSP. The comparison with the pMSSM sensitivity is unfair since the pMSSM allows

for different squarks masses (reducing the signal cross section), and an LSP mass (reducing the acceptance) reducing the total sensitivity. The right plot in figure 6.6 shows the same plot but only for Bino-like LSP models. It is clear that the sensitivity is reduced even more by the existence of a massive LSP. As said in section 6.3.4 these models have usually small $\Delta(m_{\tilde{\chi}_1^0}, m_{\tilde{q}})$ to fulfill the dark matter relic constraint via co-annihilation processes. This is explicitly shown in the upper right plot in figure B.4 in appendix B where the number of models is shown for Bino-like LSP models projected in the $m_{\tilde{q}} - m_{\tilde{\chi}_1^0}$ plane.

Besides looking only at the lightest squark, having four different light squark masses gives the pMSSM a much wider phenomenology than any of the simplified models, making the direct squark production dependent on the flavor of the lightest squark. Figure B.5 in section B.1 of Appendix B shows again two dimensional plots with the number of excluded models on the $z-$axis for u_L, u_R, d_L and d_R masses on the $x-$axis and $m_{\tilde{\chi}_1^0}$ on the $y-$axis followed by a complementary discussion.

The impact on pMSSM model parameters from LHC Run 1 results for other than light squarks and gluinos are left in Appendix B. The impact on third generation squarks is presented in B.2, the impact on electroweakinos and sleptons are comented in B.3 and a brief description on the impact on long lived particles is presented in B.4. Additionally the impact on heavy neutral higgs bosons, the impact on dark matter and on precision measurements are briefly presented at the end of Appendix B. Additional results and discussions can be found in the original documents [158, 241] and in the ATLAS Collaboration public results [240].

6.6 Categorization of non excluded models

The results have been so far used to test the sensitivity of the ATLAS searches to 8 TeV data, and to establish exclusion limits for pMSSM parameters whenever possible. However this does not bring the discovery of SUSY any closer. If SUSY exists and if ATLAS were sensitive to it, all the reachable parameter space should be covered looking for all possible signal scenarios. The models that could not be excluded by any of the ATLAS searches, were further analyzed within the 1 lepton analysis. As no simulations of detector reconstruction was carried for non excluded models, this study was done only at particle level.

Initially, a categorization of the models for which the one lepton analysis was not sensitive was performed. As mentioned in section 6.3.5 in models with strong production, the one lepton analysis was not able to exclude 91, 8% of the Bino-like LSP models neither 85.2% of the combined Wino- Higgsino-like LSP models. To understand what is leaving these events outside the one lepton SRs, the efficiencies of each cut were tested. It was found that the main discriminator was the one lepton cut requirement, which pointed to low lepton content on the models. In Figure 6.7 the efficiency of the 1 hard (top) and 1 soft (bottom) lepton cuts is presented for Bino-like (left) and Wino-Higgsino-like (right) LSP models divided by category.

The plots shows that most models that could not be excluded (Cat.1), have rather low one lepton cut efficiencies. This means that only few events of these models have at least one lepton on the final state. The plots also shows low efficiencies for some of the models in categories 2 and 3, pointing to the low lepton content of these models as well.

Only studying Hard 1 lepton cut efficiencies it was proven that from the nearly $80k$ Bino-like LSP models in Cat. 1, $\sim 52k$ had a 1 lepton cut efficiency less than 0.5% while only $\sim 28k$ had higher efficiencies. Wino-Higgsino-like LSP models usually have higher lepton content and it was found that from the $\sim 128k$ models in Cat. 1 $\sim 43k$ had the same poor 1 lepton cut efficiency while $85k$ had efficiencies larger than 0.5%

This is one of the main reasons why the 0 lepton + 2-6 jets + E_T^{miss} analysis presented higher sensitivities than the 1 lepton analysis to pMSSM models. Studying the hard or soft 1

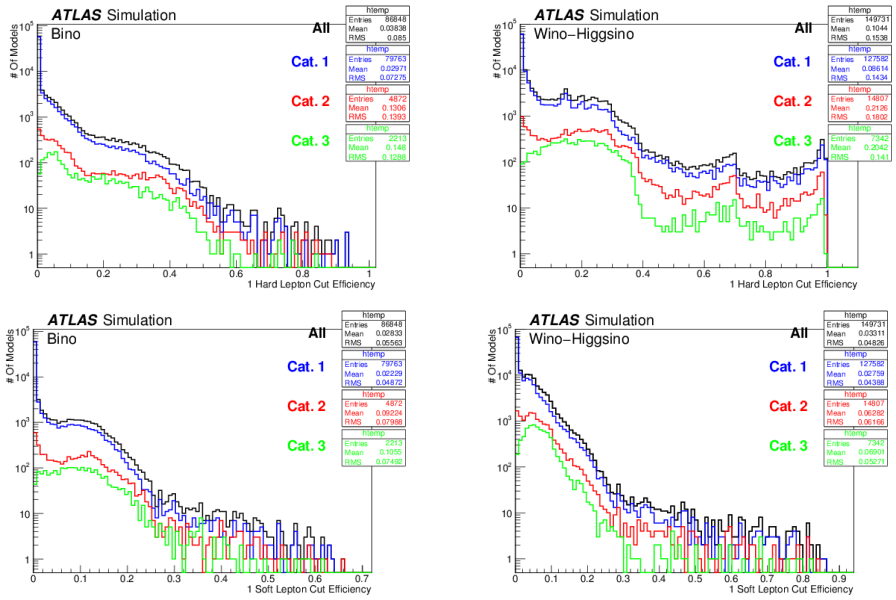

Figure 6.7: 1 hard lepton (top) and 1 soft lepton (bottom) cut efficiencies to Bino-like LSP (left) and Wino-Higgsino-like LSP (right) models dived by category.

lepton cut efficiencies separately is not highly effective, as many models might have extremely low hard 1 lepton cut efficiencies with large soft 1 lepton efficiencies. Figure 6.8 presents a two dimensional plot, where the expected events after the one lepton hard and soft cuts is plotted for each model.

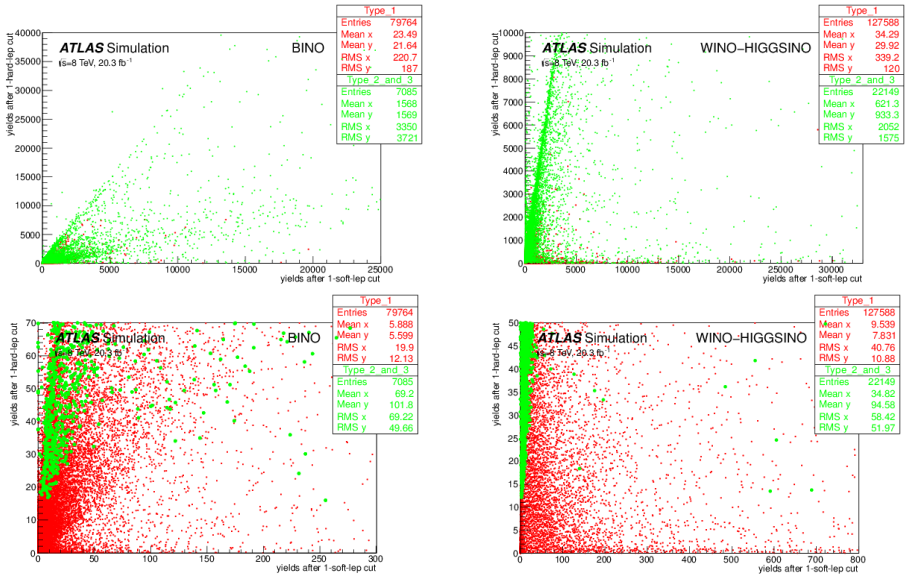

Figure 6.8: Bino-LSP (left) and Wino-Higgsino-LSP (right) model yields displayed on the 1 lepton yields plane. Cat. 1 points are red, while Cat. 2 and 3 are combined in green. On top all the models are shown. In the bottom a zoom to the lower yield region is presented.

It is clear by looking at the top plots in figure 6.8, that models that could be excluded

(green points) usually have more leptons compared to excluded (red points). Only a few amount of non excluded models reach to high event yields after the 1 lepton requirement. In fact, looking at the bottom plots where a zoom has been made, models with poor 1 hard lepton content could not be excluded by the 1 lepton analysis. Due to the lack of lepton content, these models are not of great interest for the one lepton analysis and are better suited for searches without lepton requirements in the final states.

The important question for the one lepton searches is: Why do the models with higher 1 lepton content could not be excluded? It could be because of low cross section, or maybe is it because a specific cut in the SR selection is rejecting them. This must be a detailed study, that requires many properties of the interesting models such as the kinematic variables, mass differences between the LSP and the produced sparticles, possible decay chains, all cut efficiencies, cross sections and more. It is rather complicated to perform such a detailed analysis for all the non excluded models. Instead, a very restricted selection is done to reduce the number of interesting models suited for 1 lepton searches. Firs, only models that could not be excluded by any other search are selected. Similar plots as the ones presented in Figure 6.8 are presented in Figure 6.9 for all models which including strong production. The red points now represent the models that cannot be excluded by any of the ATLAS searches, clearly reducing the number of red points. A blue rectangle has been overlaid to show a region where the lepton content is too low to be interesting for the one lepton analyses. The number of interesting red points outside this region is reduced to 2759 for Bino-like LSP models and 10850 for Wino-Higgsino-like LSP models.

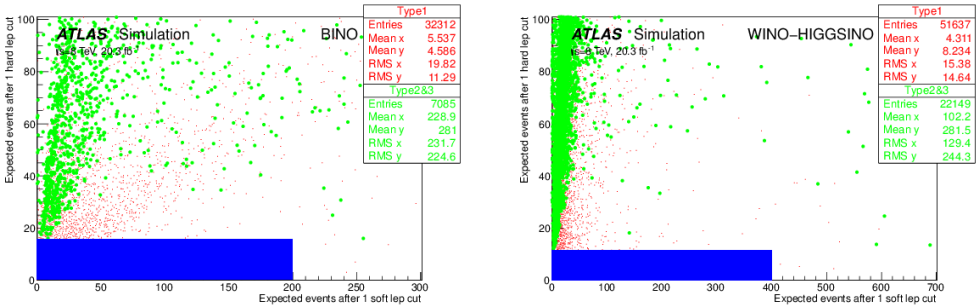

`Figure 6.9:` Bino-LSP (left) and Wino-Higgsino-LSP (right) models that could be excluded by the 1 lepton analysis in green and models that cannot be excluded by any analysis in red. The points are presented on the 1 lepton cut yields plane zoomed in to lower yields area. The blue region is considered not interesting for 1 lepton analyses

With the reduced set of points, the next step was to categorize them and to discard models that could easily move from category 1 to categories 2 or 3 by just a small luminosity increase. With this idea behind, the yields in each SR ($N^{SR}_{truth}[i]$) are compared to the model independent 95% CL upper limit for each SR ($N^{95}_{max}[i]$) by a simple ratio. The maximum value of this ratio is used to pick the best ratio between both quantities as figure of merit:

$$max\left(\frac{N^{SR}_{truth}[i]}{N^{95}_{max}[i]}\right), \qquad \text{with } i = 1, 2, ..., 8. \tag{6.6}$$

In Figure 6.10 the distribution of this variable is presented for all the remaining points in category 1 after removing the models with low lepton content as explained above.

For Bino-like LSP models the distribution is found in the left plot while for Wino-Higgsino-like LSP models in the right. The concept behind this variable is to discriminate models that could be easily excluded in future runs with increased luminosity, by choosing high values of

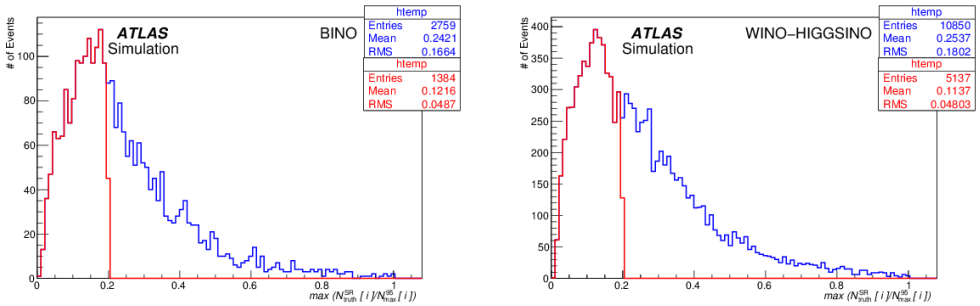

Figure 6.10: $max(N^{SR}_{truth}[i]/N^{95}_{max}[i])$ for Bino-like LSP (left) and for Wino-Higgsino-like LSP (right). The red histogram indicates the cut below 0.2

the variable. Nevertheless it can be seen in both plots, that most of the models have low yields in the best SRs, far from the model independent upper limit of that region. However trying reduce the amount of conflictive models for a better understanding, a selection is performed based on the distributions by requiring a maximum value for this variable of 0.2. The cut is included in figure 6.10 a a reference. After this cut, 1,384 Bino- and 5,137 Wino-Higgsino-like LSP models survive as interesting models, which are studied deeply to check what is the major production channel for each. The remaining models are categorized by choosing the dominant production channel. This information is summarized in table 6.13 showing in each cell the number of models for each dominant production type.

Production channel	**Number of models with preferred production channel**	
	Bino LSP	**Wino+Higgsino LSP**
$\tilde{q}\tilde{g}$	11	28
$\tilde{g}\tilde{g}$	14	49
$\tilde{q}\tilde{q}$	337	1928
$\tilde{q}\bar{\tilde{q}}$	354	995
$\tilde{b}_1\bar{\tilde{b}}_1$	463	1715
$\tilde{t}_1\bar{\tilde{t}}_1$	205	422
Total	1384	5137

Table 6.13: Number of models categorized according to the principal production process.

The same points are also presented in the 1 lepton yields plane in figure 6.11 categorized by a color code: Cyan stands for models where is $\tilde{q}\tilde{g}$ is the dominant production process, black is for $\tilde{g}\tilde{g}$, blue $\tilde{q}\tilde{q}$, red $\tilde{q}\bar{\tilde{q}}$, green $\tilde{b}_1\bar{\tilde{b}}_1$ and magenta for $\tilde{t}_1\bar{\tilde{t}}_1$. As the models with third generation production ($\tilde{b}_1\bar{\tilde{b}}_1$ and $\tilde{t}_1\bar{\tilde{t}}_1$) are better suited for specialized third generation searches, only a closer look is given to the models where $\tilde{q}\tilde{g}$, $\tilde{g}\tilde{g}$, $\tilde{q}\tilde{q}$ and $\tilde{q}\bar{\tilde{q}}$ are the major production channels. Reducing the interesting group of models to 716 Bino-and 3000 Wino-Higgsino-like LSP models. From the surviving models, only the ones with the highest number of events after the 1 soft or 1 hard lepton cuts are taken a closer look. This means leaving for a moment the bulk on the plots and concentrating explicitly only on models presenting hard lepton yields above 150 or soft lepton yields above 200. These points are studied in detail analyzing the mass spectrum, decay chains and cross sections. The selected models are dominated by squark pair production (red and blue points in figure 6.11).

For most of these models the LSP mass and the $\tilde{\chi}^{\pm}_1$ mass are nearly degenerate and in

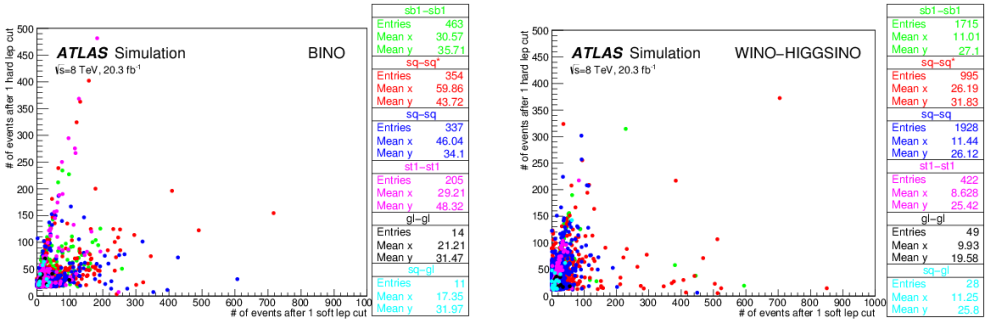

Figure 6.11: Non excluded models with *high* lepton content, far from the the model independent 95% CL upper limits, presented in the 1 lepton yields plane categorized with colors for each production process.

many of the models, the mass of the produced squark is just slightly higher than the LSP mass. Additionally, for most of the models close to the x-axis (with non negligible amount of soft lepton events) the mass difference between the produced squark and the LSP is not greater than ~ 50 GeV. For Wino-Higgsino-like LSP models with non negligible hard leptons yields (near the y-axis) this is not always the case, reaching values as high as ~ 250 GeV. In the case of Bino-like LSP models with hard leptons the dominant light squark decay will lead to no leptons, as the lightest squark can only decay directly into the LSP with an additional low energy jet. Looking at the masses of the predominantly produced squark, for models with enough soft lepton events the squarks are generally light ($\lesssim 400$ GeV) while for hard lepton models the squark mases are medium to large ($\lesssim 800$ GeV). For all the surviving models, the hardest cuts leaving them out of the SRs is either the number of hard jets and E_T^{miss}.

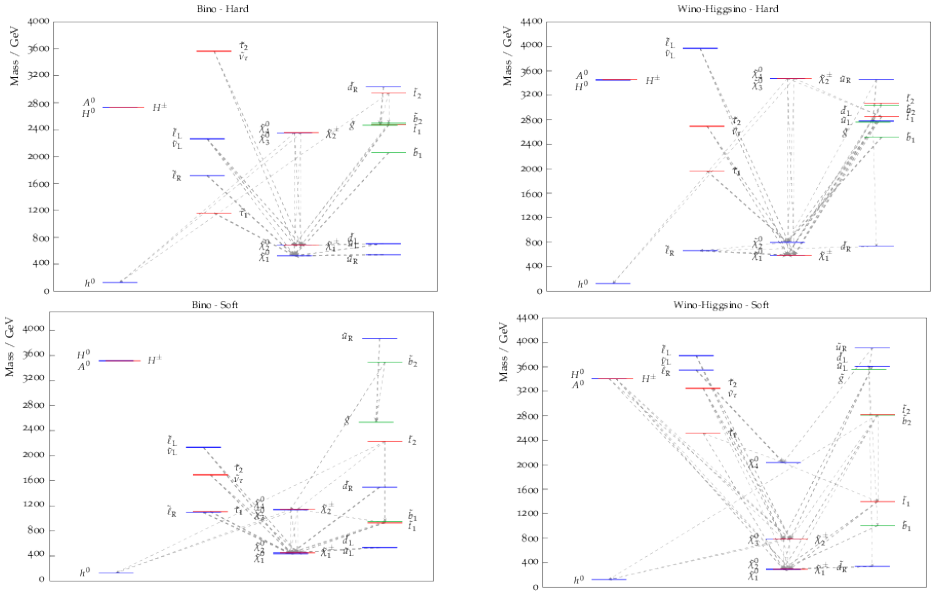

Figure 6.12: Typical sparticle mass spectrum for the models found.

In figure 6.12, the sparticle mass spectrum for usual surviving models is presented. The plots on the left are for the usual Bino-like LSP surviving models while the plots on the right represent the usual Wino-Higgsino-LSP surviving models. Both plots on top represent models

with hard lepton events while the bottom plots represent models with soft lepton content. In all the plots it can be seen that the lightest squark masses are very similar as the LSP masses as already mentioned.

In figure 6.13 the mass spectrum for the same four exemplary models is presented, zooming into the important region where the dominantly produced squark, the LSP and possible intermediate particles are present. In almost all cases, the squark decays via slepton, or $\tilde{\chi}_1^{\pm}$ to the LSP. In Bino-like LSP models with hard lepton events (top-right), the squark decays directly to the LSP with no leptons involved so the leptons found might come from additional non-dominant processes.

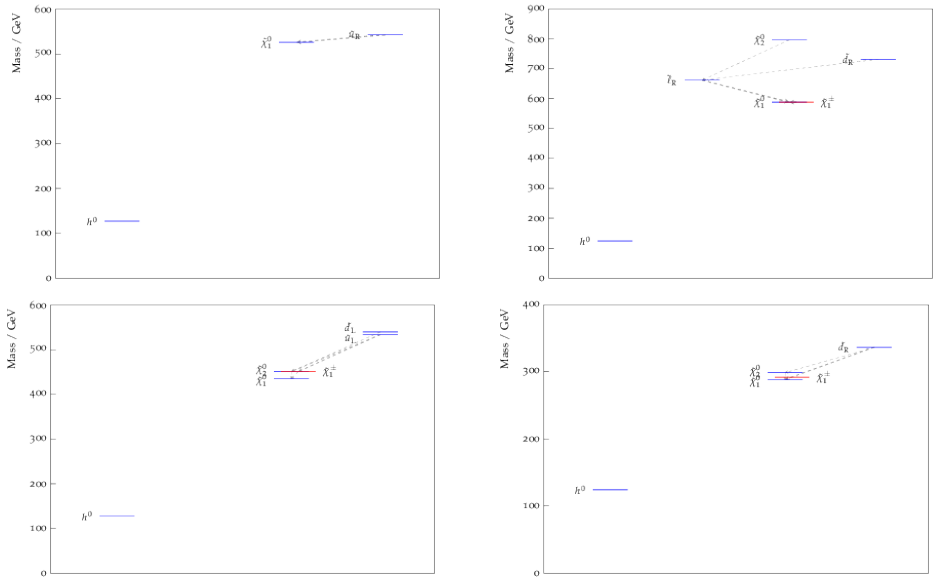

Figure 6.13: Zoom to the important part of the typical sparticle mass spectrum for the models found.

After searching for non excluded models with enough lepton content that could be suited for the one lepton analysis, it was found that the usual signatures for the surviving models is much better suited for analyses that do not explicitly require leptons in the final state.

6.7 Summary

With the previous LHC runs at 7 and 8 TeV c.o.m energy, the ATLAS SUSY collaboration has analyzed up to 20.3 fb^{-1} of data. The interpretation of the results within different analyses, specially the model independent upper limits, were reinterpreted to probe a much general supersymmetric framework as the pMSSM.

An initial sample of 5×10^8 models with 19 parameters randomly chosen within pMSSM limits, was reduced to $\sim 300k$ pMSSM models satisfying previous experimental constraints from detector physics, dark matter searches and precision measurements. For models satisfying a minimal cross section criteria ($\sim 215k$) more than $\sim 3{\times}10^{10}$ events were generated at particle level. After a categorization of the models, for $\sim 45 \times 10^3$ models a fast detector simulation and full reconstruction was performed to determine if the model could be excluded at 95%CL.

The impact of the ATLAS Run 1 searches was presented mainly as the fraction of model points surviving, projected into two-dimensional spaces of SUSY parameters. In general, the complementarity of the different ATLAS searches was evidenced, where some searches showed

exclusive sensitivities to certain regions of the phase space. The most sensitive ATLAS analyses were found to be the 0-lepton + 2-6 jets + E_T^{miss} and the Disappearing Track analysis, which showed to be the most constraining search for model points with a light Wino-like LSP.

The ATLAS analyses constraints to strong pMSSM production showed that all models with gluino masses below ~ 700 GeV can be excluded. For models with $m_{\chi_1^0} < 500$ GeV, the limit extends to ~ 1 TeV. On the other hands models with light squarks below 250 GeV can always be excluded. Constraints on the masses of third generation squarks, electroweakinos, sleptons and heavy neutral Higgs bosons were also presented together with the impact on dark matter and precision measurements.

It was also observed that the ATLAS searches are more powerful to constraint strongly interacting sparticles than for electroweakinos and sleptons. In most of the cases there was accordance between the previously simplified model limits and the the pMSSM points excluded. However there were important discrepancies found due to the richer phenomenology of the pMSSM compared to the simplified models.

The models that were not excluded by any analysis were studied within the 1-lepton + jets + E_T^{miss} analysis. It was found that most of the non excluded models had a low one lepton cut efficiency. After a detailed selection of non excluded models that could be fit to the one lepton analysis, it was found that the signatures for the most suitable models included leptons from non-dominant processes, making them much better suited for analyses with no lepton requirements in the final state.

Chapter 7

Analysis Part II: SUSY search in the one lepton final state with $\sqrt{s} = 13$ TeV.

This chapter presents the results of the SUSY search with final states including one isolated lepton, multiple jets and missing transverse energy using the ATLAS detector for 13 TeV c. o. m. energy collisions. The results are interpreted in the context of a simplified model where a pair of strongly produced gluinos decay via lightest chargino to the lightest neutralino with an an emphasis in the hard lepton channel. The results of this study was published and can be found in [244][1].

The result presented extends similar ATLAS searches [48] performed previously with data collected during LHC Run 1, expanding the sensitivity and excluding higher gluino masses for similar phenomenologies. Previous ATLAS searches targeting squark and gluino pair production and other SUSY searches were cited in the previous chapter. Similar searches performed by the CMS collaboration show similar results [245,246] for 8 TeV and in [247–249] the preliminary 2015 13 TeV results are presented for comparison.

7.1 Data and simulation samples

7.1.1 Data samples

The dataset is taken from the full 2015 data taking period, with a center of mass energy of $\sqrt{s} = 13\ TeV$, 25 ns bunch spacing and an integrated luminosity up to 3.3 fb^{-1}, with an associated uncertainty of 9%. As said in chapter 3 the peak instantaneous luminosity reached 5×10^{33} cm^{-2}s^{-1}, with a mean number of interactions per bunch crossing of ~ 14.

The events are first selected using a missing transverse energy high level trigger with a 70 GeV threshold. As it can be seen in figure 7.1 the turn on curve reaches an efficiency plateau above 95% for values over 185 GeV. The offline E_T^{miss} minimum requirement for the analysis is above 200 GeV in the loosest E_T^{miss} region making this a valid trigger choice. This is one of the differences between this analysis and previous one lepton analyses as for the latter usually lepton or lepton-jet or lepton-met-jet combined triggers were used. The E_T^{miss} trigger was chosen after testing the efficiencies for different un-prescaled triggers. It was found that the best alternative for a single muon trigger showed an efficiency of only 90% in the plateau, which was not efficient enough. To choose between different E_T^{miss} triggers, triggers with low

[1] The results presented in the paper use an updated GRL with only 3.2 fb^{-1}

thresholds were tested using two methods. For the first method the idea was to find a trigger that suits the one lepton specific analysis, therefore a pre-selection was defined consisting of one lepton with $p_T > 35$ GeV plus at least three jets with p_T above 25 GeV and $p_T > 50$ GeV for the hardest jet. For the second method the idea was to ensure the selection of events containing real E_T^{miss}, thus the pre-selection was 1 tight lepton with $p_T > 35$ GeV including the firing of a single lepton trigger, at least 3 jets with p_T above 25 GeV, $m_T > 20$ GeV and $E_T^{miss} > 25$ GeV. For both methods both data and background simulation were tested analyzing the different trigger efficiencies and rates. The lowest un-prescaled trigger that best suited our need was the HLT_xe70_tc_lcw trigger. Furthermore a 2% difference between data and simulation efficiencies was found, but it had a negligible impact on the final results of the analysis, thus no extra trigger weight is applied.

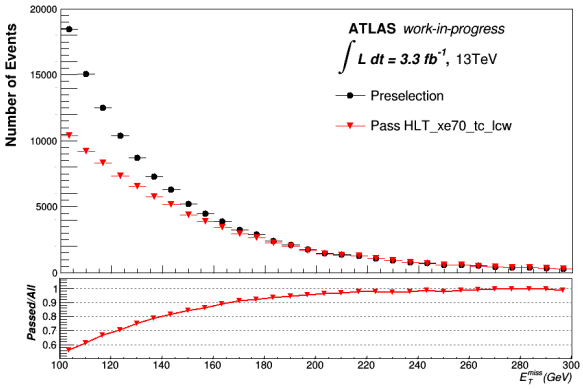

Figure 7.1: Zoom into the HLT_xe70_tc_lcw trigger turn on plot. For values over 180 GeV the trigger is almost fully efficient, with an efficiency above 95%

7.1.2 Background samples

The simulation of background samples is performed using a variety of generators, with different PDFs and tunes. A summary of all simualted SM samples used for this analysis is presented below.

- $t\bar{t}$ samples are generated using the Powheg-Box v2 [183] generator. The matrix elements are calculated at NLO with the CT10 [250] PDF set used for proton substructure. The additional parton showering is simulated with Pythia 6.428 [184] and the CTEQ6L1 PDF set [251] using the Perugia2012 tune [252]. The events are normalized to a NNLO+NNLL cross section calculated with Top++2.0 [253].

- $W + jets$ events are generated with Sherpa 2.1.1 [185]. The matrix elements are calculated at NLO with two partons and at LO for four partons. The matrix elements are calculated using Comix [254] and OpenLoops [255] generators merged with the Sherpa parton shower algorithm [256], using the ME+PS NLO method [257]. The CT10 PDF set is used with the default Sherpa parton shower tune. The events are normalized to NNLO cross section, and are simulated with massive b/c-quarks for a more accurate description of W bosons production with associated heavy flavor quarks.

- For Single-top background the Powheg-Box v1 generator is used for electroweak t-channel and with Powheg-Box v2 generator for Wt- and s-channels. For the t-channel

the PDF set used is CT10f4 while for Wt- and s-channels the usual CT10 PDF set is used. The additional parton showering is also calculated with PYTHIA 6.428 and the CTEQ6L1 PDF using the PERUGIA2012, same as for $t\bar{t}$ samples, but the cross sections are calculated only to NLO level.

- Diboson samples are also generated with SHERPA 2.1.1, same as for $W + jets$ samples. The PDFs sets used, fragmentation and tune setup is also the same that for $W + jets$ samples. As the possible diboson combinations are WW, WZ and ZZ, the final states include four leptons, three leptons plus a neutrino, two leptons with two neutinos or one lepton plus three neutrinos. For final states containing four leptons or two leptons plus two neutrinos, the matrix element can be calculated at NLO with a maximum of one additional parton. For processes containing three leptons plus a neutrino or one lepton plus three neutrinos in the final states, the matrix element is calculated at NLO with no additional partons. Processes with up to three additional partons can only be calculated at LO. The cross sections are calculated at NLO level.

- The production for $Z + jets$ events, including matrix elements, proton structure, fragmentation, tuning and merging is calculated using the same procedure than for $W + jets$ events. Also the events are normalized to cross sections calculated at NNLO.

- The associated production of $t\bar{t}$ pairs with vector bosons ($t\bar{t} + W$, $t\bar{t} + Z$ or $t\bar{t} + WW$) is calculated using MADGRAPH 5 V2.2.2. [189]. The matrix elements are calculated at LO and may include up to 2 partons for the $t\bar{t} + W$ case, 1 for the $t\bar{t} + Z$ case and no extra parton for the $t\bar{t} + WW$ case. The showering is calculated using PYTHIA 8.186 and the ATLAS A14 tune [258] is used with the NNPDF2.3 LO PDF set [259]. The cross sections are calculated at NLO level.

Besides the process specific event generation, all samples also include an amount of minimum-bias interaction events to account for in-time pileup which are added to the harder events. This interactions are simulated using the PYTHIA 8 generator with the MSTW2008LO PDF set [260] plus the ATLAS A2 tune [262]. Out-of-time pileup is treated as explained in section 4.3. For all background samples, the response of the detector is modeled with the full ATLAS simulation [229] using GEANT4 [227].

7.1.3 Signal samples

The signal samples are generated with MADGRAPH 5 V2.2.2. The matrix elements are calculated with up to two extra partons. The hadronization and parton showering is done using PYTHIA 8.186 generator using the CKKW-L matching scheme [261]. For the underlying events, the ATLAS A14 tune [258] is used with the NNPDF2.3 LO PDF set. The signal cross sections are calculated at NLO+NLL, the nominal values and uncertainties are taken from an envelope of different PDF sets, factorization and renormalization scales [263, 264]. For all signal samples the response of the detector is modeled with the ATLAS fast simulation [229] using ATLFAST 2 [265, 266] which reduces computing time by using a simplified detector geometry for the inner detector and the calorimeter.

The first 13 TeV events recorded during 2015, were interpreted within a simplified model SUSY scenario. The signal model considered is the exclusive gluino pair production. The gluinos decay via lightest chargino $\widetilde{\chi}_1^{\pm}$ into the LSP, which is assumed to be the lightest neutralino $\widetilde{\chi}_1^0$. This choice was made as this was the channel with the best sensitivity for the one lepton analysis during the 2015 data taking period. Being a simplified model, the branching ratios of each decay are assumed to be 100%. The only allowed gluino decay are via first and second generation squarks and no b- nor t-squarks are produced in the model. The

parameters of the model are the gluino mass $m_{\tilde{g}}$, the chargino mass $m_{\widetilde{\chi}_1^\pm}$, and the neutralino mass $m_{\widetilde{\chi}_1^0}$.

For these parameters, two scenarios are considered: One having a fixed LSP mass at 60 GeV where the gluino mass, and a mass ratio parameter $x = (m_{\widetilde{\chi}_1^\pm} - m_{\widetilde{\chi}_1^0})/(m_{\tilde{g}} - m_{\widetilde{\chi}_1^0})$ are varied. For the second scenario $m_{\tilde{g}}$ and $m_{\widetilde{\chi}_1^0}$ are free parameters, while $m_{\widetilde{\chi}_1^0}$ is set as a function of the chargino and gluino masses such that $m_{\widetilde{\chi}_1^\pm} = (m_{\tilde{g}} + m_{\widetilde{\chi}_1^0})/2$ making the chargino mass to be exactly between the gluino and the neutralino mass. For an easy reference, the first scenario will be referred as the $x - free$ scenario while the second will be called the $x = 1/2$ scenario. The diagram for the model is presented in figure 7.2

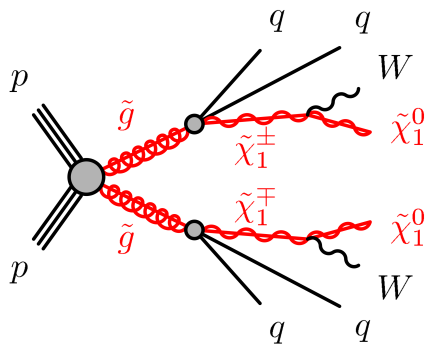

Figure 7.2: One step simplified model: Gluino pair production decaying via lightest chargino to the lightest neutralino [45].

7.2 Object selection

A general definition of the objects including reconstruction and identification has been introduced in sections 4 and 5, however the analysis specific object selection is detailed and summarized below. As explained before, there are two steps in the selection. First, the pre-selection, in which the objects must pass a looser set of requirements, these are the objects that are used for the E_T^{miss} computation. Second, the signal selection, where reconstructed objects must pass tighter criteria. These are the objects used in the various control, validation and signal regions.

7.2.1 Preselection

The jet selection requires jets to be reconstructed from topological clusters in the calorimeter using the anti-k_t algorithm with a distance parameter $R = 0.4$. To account for the calorimeter responses to the various jet constituent and to mitigate the expected contributions from pileup, additional corrections are applied as explained in section 4.3. Preselected jets must have $p_T > 20$ GeV and $|\eta| < 4.5$. Contamination from cosmic rays and other sources besides collisions including detector noise is suppressed to improve jet quality as explained in [267].

For electrons candidates, the reconstruction uses ID tracks matched to EM clusters in the calorimeter and for identification the likelihood-based *Loose* criteria[2] is used. Preselected electrons must have $|\eta| < 2.47$ and $p_T > 10$ GeV for hard electrons and $p_T > 7$ GeV for soft electrons. To avoid double counting, regular overlap removal requirements are applied. If an

[2] As defined in [138]

electron candidate and a preselected jet lie between $0.2 < \Delta R(e, jet) < 0.4$, only the jet is retained removing electrons from b decays. If $\Delta R(e, jet) < 0.2$ only the electron is kept, as this should have also been reconstructed as a jets by the jet algorithms. If $\Delta R(e, \mu)$ between the electron candidate and a preselected muon is less than 0.01 only the muon is preserved, avoiding electron candidates coming from muon bremsstrahlung.

The reconstruction of Muon candidates uses a combination of ID and MS tracks and for the identification, the *Medium* criteria[3] is used. Preselected muons must have $|\eta| < 2.4$ and $p_T > 10$ GeV for hard muons and $p_T > 6$ GeV for soft muons. After the electron-jet overlap removal is done, when the distance between a muon candidate and the closest preselected jet is $\Delta R(\mu, jet) < 0.4$, the jet is retained avoiding muons from b decays, only if the preselected jet is associated to two or less tracks, the muon is retained and the jet dismissed.

Before defining the signal objects, M_T^{miss} is calculated using the previously selected objects. Its magnitude corresponds to the sum of the transverse momenta of all identified and calibrated objects (electrons, photons, muons and jets) plus the track soft term (TST). The direction of the M_T^{miss} points exactly in the opposite direction of the p_T sum.

7.2.2 Signal selection

A signal jet must pass harder cuts. It must be inside the $|\eta| < 2.8$ region and its p_T higher than 25 GeV. To remove pileup energy from signal jets the Jet area correction has been applied, and to remove extra jets coming from pileup, an additional JVT cut is applied: Any jet with $p_T < 50$ GeV inside the $|\eta| < 2.4$ region with $JVT < 0.64$ will be rejected. This JVT working point provides 92% efficiency in selecting hard-scatter jets.

To identify jets from b-quarks, signal jets containing b-hadrons are identified using the MV2c20 algorithm with a cut value for MV2c20 of -0.4434 providing 77% b-tagging efficiency with a rejection factor of 140 for light jets and of 4.5 for c-jets.

Signal electrons are required to pass the likelihood-based *Tight* criteria. Electron p_T must satisfy $p_T \geq 35$ GeV for hard electrons while $p_T < 35$ GeV for soft electrons.

Signal muons are also required to have $p_T \geq 35$ *GeV* for hard muons and $p_T < 35$ *GeV* for soft muons.

Both electrons and muons must satisfy the *GradientLoose* isolation requirement as defined in [138]. This criteria rely on tracking-based and calorimeter-based variables, implementing a set of η and p_T dependent criteria. The efficiency for GradientLoose leptons from a $Z \to \ell\ell$ sample with $p_T > 25$ GeV is measured to be 95% [141]

Finally signal leptons are also required to pass the $|z_0 \cdot \sin(\theta)| < 0.5$ cut, to make the compatibility with the primary vertex tighter. Also, the distance of closest approach of the lepton track to the beam line (d_0) divided by its corresponding uncertainty must be less than three in case of muons and less than five in case of electrons.

A summary of the pre-selection and signal selection criteria for the objects used is presented in tables 7.1, 7.2 and 7.3.

7.3 Event selection

After having all preselected and signal objects ready, each triggered event is selected after passing specific criteria. The first and simplest criteria is for the event to contain one reconstructed primary vertex. Also an event is dismissed if it is found to contain a preselected jet which does not pass the jet quality criteria to suppress detector noise, cosmic jets and non-collision background jets as defined in [267]. To select only with one lepton final states, events are required to have exactly one signal lepton in both channels. An event is vetoed if it

[3] As defined in [141]

Cut	Value/description
Preselected jet	
Algorithm	AntiKt4Topo
Acceptance	$p_T > 20$ GeV $\|\eta\| < 4.5$
Overlap	$0.2 < \Delta R(jet, e) < 0.4$
Signal jet	
Acceptance	$p_T > 25$ GeV $\|\eta\| < 2.8$
JVT	92% working point for $p_T < 50$ GeV and $\|\eta\| < 2.4$
Signal b-jet	
Acceptance	$p_T > 25$ GeV $\|\eta\| < 2.5$
b-tagging Algorithm	MV2c20 at 77% working point

Table 7.1: Summary of the jet selection criteria. Signal selection requirements are applied on top of the pre-selection.

Cut	Value/description	
	Hard	Soft
Preselected Electron		
Algorithm	AuthorElectron	
Acceptance	$p_T > 10$ GeV	$p_T > 7$ GeV
	$\|\eta\| < 2.47$	
Quality	LooseLLH	
Overlap	$\Delta R(jet, e) < 0.2$ $\Delta R(\mu, e) > 0.01$	
Signal Electron		
Acceptance	$p_T \geq 35$ GeV	7 GeV $< p_T <$ 35 GeV
Quality	TightLLH	
Isolation	GradientLoose	
Interaction Point	$\|z_0 \cdot \sin\theta\|$<0.5 mm $\|d_0^{PV}\|/\sigma(d_0^{PV})$<5	

Table 7.2: Summary of the electron selection criteria. Signal selection requirements are applied on top of the pre-selection.

contains additional preselected leptons, suppressing di-lepton $t\bar{t}$, single top (Wt-channel) and di-boson backgrounds. Besides these general requirements, each dedicated region will have specific event selection to cover the specific defined phase space.

7.3.1 Global variables

Similar global variables that the ones defined in section 6.3.5 are defined to isolate specific backgrounds or enhance signal over background ratio. Some differences with the previous 8 TeV analysis is that the jets entering the effective mass m_{eff} and the m_T calculation must have $p_T > 30$ GeV instead of the former 40 GeV requirement. Also, only the inclusive effective

Cut	Value/description	
	Hard	Soft
Preselected Muon		
Algorithm	AuthorElectron	
Acceptance	$p_T > 10$ GeV	$p_T > 6$ GeV
	$\|\eta\| < 2.4$	
Quality	Medium	
Overlap	$\Delta R(\text{jet}, \mu) > 0.4$ After $jet - e$ OR $\Delta R(\mu, e) < 0.01$	
Signal Muon		
Acceptance	$p_T \geq 35$ GeV	6 GeV $< p_T <$ 35 GeV
Isolation	GradientLoose	
Interaction Point	$\|z_0 \cdot \sin\theta\|$<0.5 mm $\|d_0^{PV}\|/\sigma(d_0^{PV})$<3	

Table 7.3: Summary of the muon selection criteria. Signal selection requirements are applied on top of the pre-selection.

mass m_{eff}^{incl} is used as a discrimination variable to select events in the different regions and m_{eff}^{excl} is not longer used. The ratio $E_T^{miss}/m_{eff}^{incl}$ is now used in both channels, providing good discrimination power between signal and background with fake E_T^{miss} coming from detector effects.

Another variable used for the soft lepton analysis not present in the 8 TeV analysis is the transverse scalar sum (H_T), defined as:

$$H_T = p_T^{\ell} + \sum_{j=1}^{N_{jet}} p_T^{jet_j} \tag{7.1}$$

H_T is useful in the soft-lepton 5-jet SR, where many hard jets in the signal events make it useful to separate signal from background.

Another discrimination variable used in this analysis to distinguish between signal and background events is aplanarity $\mathcal{A}$. Aplanarity is a topological based variable which gives more information about the global momentum distribution in an event. It helps to test if the momentum distribution is isotropic or if it is rather concentrated in one plane. The momentum distribution can be studied using the full momentum tensor M_{xyz} and its eigenvalues λ_1, λ_2 and λ_3:

$$M_{xyz} = \sum_i \begin{pmatrix} p_{xi}^2 & p_{xi}p_{yi} & p_{xi}p_{zi} \\ p_{yi}p_{xi} & p_{yi}^2 & p_{yi}p_{zi} \\ p_{zi}p_{xi} & p_{zi}p_{yi} & p_{zi}^2 \end{pmatrix}, \tag{7.2}$$

where the sum over label i runs over all jets used in the measurement[4]. The eigenvalues of M_{xyz}; λ_1, λ_2 and λ_3 are normalized such that $\lambda_1 \geq \lambda_2 \geq \lambda_3$ and $\lambda_1 + \lambda_2 + \lambda_3 = 1$. Using this values, aplanarity $\mathcal{A}$ is built using only the lightest eigenvalue λ_3 such that:

$$\mathcal{A} = \frac{3}{2}\lambda_3 \tag{7.3}$$

[4]This is the definition for the Jet Aplanarity which is used in this analysis. It must be said that there is also a lepton version of aplanarity which was tested as a discriminating variable, but after comparing the sensitivity gain with the efficiency of the cuts made, it was decided to include only the jet aplanarity for the signal region selection.

Defined like this, $\mathcal{A}$ quantifies the p_T distribution in the plane formed by the two leading jets, it can take values between 0 and 0.5, with measured values usually within 0 and 0.3. Events with small $\mathcal{A}$ are shown to be fairly planar events. For this analysis $\mathcal{A}$ was shown to be useful to discriminate signal from background, specially for $t\bar{t}$ events which tend to appear as rather planar events, peaking at low $\mathcal{A}$.

7.3.2 Common event pre-selection

After all the object definitions, before defining any of the control, validation or signal regions, events are required to pass a common pre-selection criteria aimed to remove events that are not part of the GRL, or events for which some part of the detector indicated a malfunction, or also to remove events with physics which is not interesting for this analysis trying to clean the dataset, reducing its size while keeping all interesting physics. Theses requisites include vetoing all events not listed in the latest recommended GRL, vetoing any event with a LArError, TileError or incomplete eventInfo flag, also veto events with no primary vertex with at least two track associated to it and any event with a bad jet. The pre-selection also includes the requirement of exactly one preselected hard lepton with $p_T > 10$ GeV or one preselected soft lepton with $p_T > 6(7)$ GeV for muons (electrons) additionally, exactly one signal lepton with $p_T > 35$ GeV in case of hard leptons or with 6(7) GeV $< pT < 35$ GeV in case of soft muons (electrons) is required. The next pre-selection requirement is at least three (two) signal jets with $p_T > 25$ GeV for the hard (soft) lepton analysis. The last pre-requisite is that all events must pass a $E_T^{miss} > 100$ GeV cut with the HLT_xe70_tc_lcw trigger fired. After pre-selection, the nearly 748 million events in the full 25 ns with 3.3 fb^{-1} integrated luminosity, are reduced nearly to 0.02% of the total amount.

7.3.3 Kinematic distributions

With the full 3.3 fb^{-1} 2015 dataset, there are not many events left after the pre-selection stage. With limited statistics, it is not quite useful to compare kinematic distributions between data and MC in all the specific regions with rather tight cuts. To check for consistency the kinematic distributions were studied using looser selections. The shapes of the relevant variables for data and MC are compared after a rather loose background-like selection given by the following cuts after pre-selection and before fit: One signal lepton with $p_T > 35$ GeV, at least four jets with $p_T > 30$ GeV with the first jet $p_T > 125$ GeV, $E_T^{miss} > 200$ GeV to work at full trigger efficiency, and 60 GeV $< m_T <$ 125 GeV keeping SR-like regions blind. Additionally, a b-jet veto is required for a loose W_CR, and at least one b-jet is required for a loose T_CR. In figures 7.3 and 7.4, the kinematic distributions for *top*-like loose CR are presented. The same plots for W-like loose CR are presented in figures 7.5 and 7.6. As no fit is performed yet, MC is normalized to the total number of events just to compare the shapes of the distributions. Overall a good agreement is found between data and MC simulation in both regions for all distributions. In most of the plots, the object and region selection criteria are explicitly shown by leaving empty bins before and after the distributions. For the p_T of the fifth and sixth jet, events with no fifth or sixth jet are included in the first bin corresponding to jet $p_T = 0$ GeV. Kinematic distributions in the CRs (after background fit) are included in Appendix C in figures C.3 -C.14.

7.4 Hard lepton signal region optimization

In figure 2.5 the Run 1 limits for ATLAS are presented. LHC searches reached sensitivities to gluinos up to the TeV scale, and to third generation squarks up to hundreds of GeV. The discovery reach in Run-2 was expected be enhanced due to the boost in the LHC c.o.m

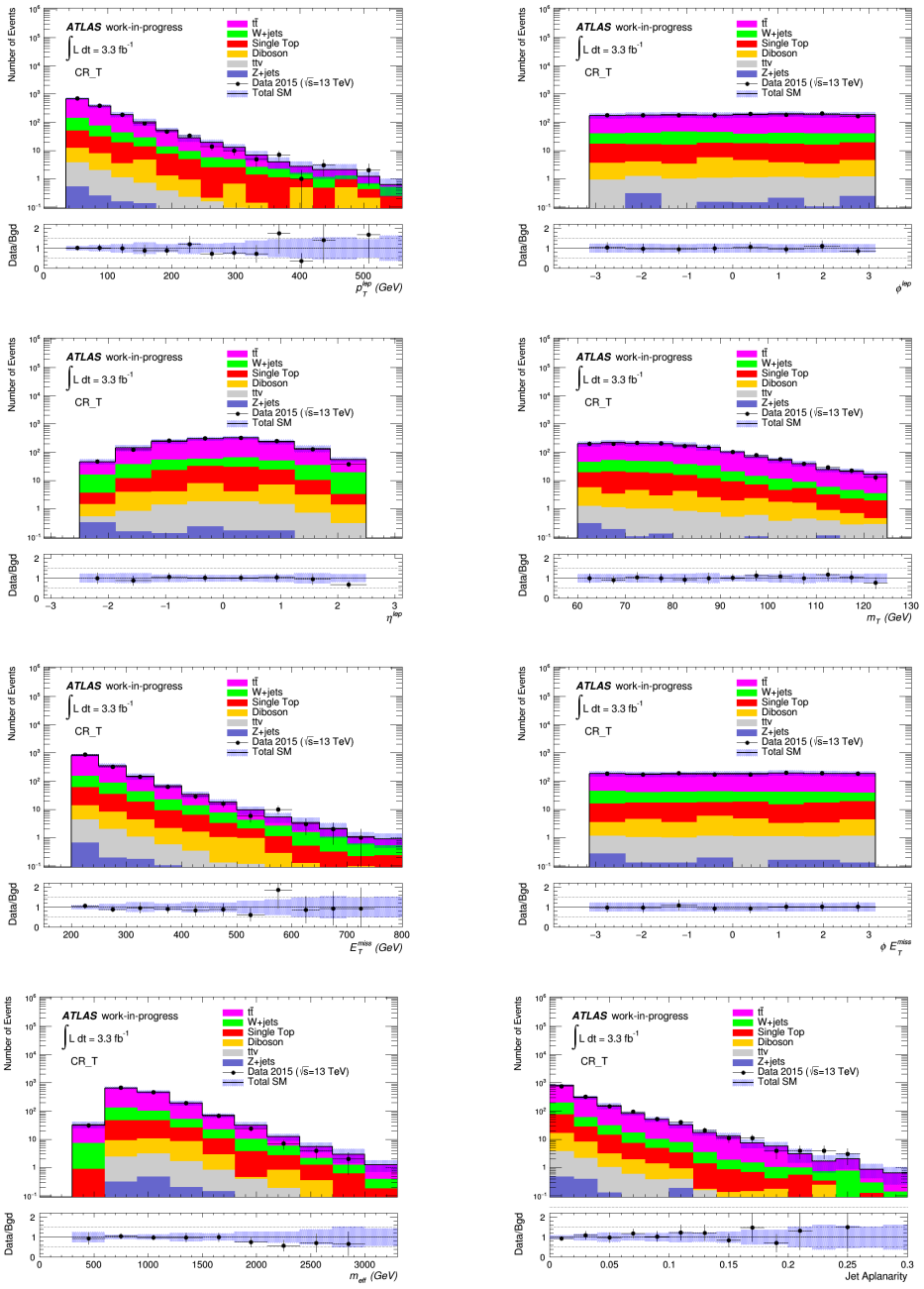

Figure 7.3: Kinematic distributions of variables in a loose *top* region.

collision energy from 8 TeV to 13 TeV. The 1-lepton analysis proved to be sensitive even at low integrated luminosity [269], making it a good candidate for early 2015 data analysis.

Prior to data analysis, a sensitivity projection study [269] targeting squark and gluino production was performed. These specific channels were chosen because of its cross section increment with respect to the cross section increment of typical background processes. As an example, the 13 TeV/8 TeV cross section ratio for 1.5 TeV gluino pair production is of the order of 49 while typical $t\bar{t}$ production cross section ratio is near 3.3 [270].

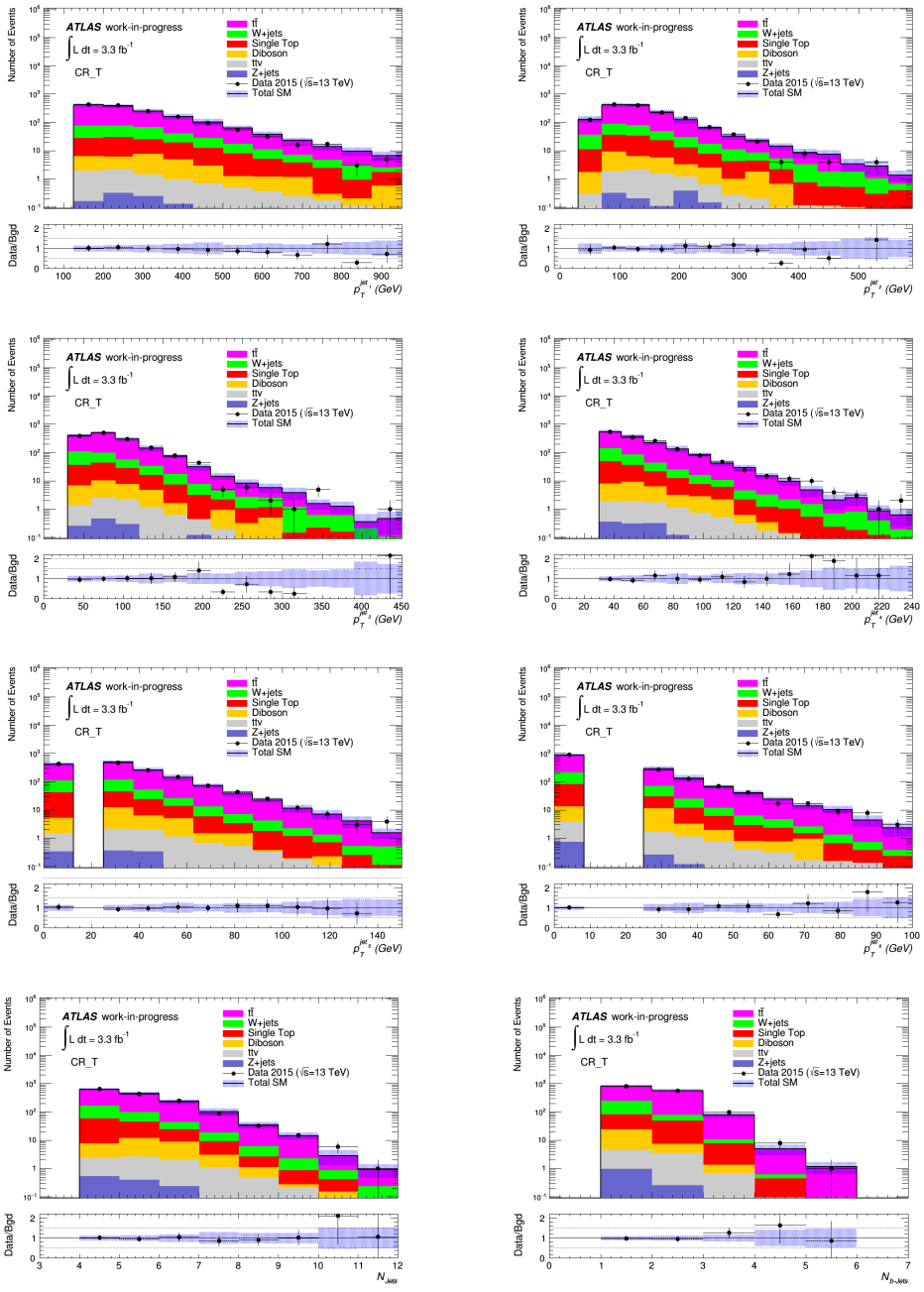

Figure 7.4: Kinematic distributions of variables in a loose *top* region.

The aim of [269] was to provide the expected sensitivities for early Run-2 data based on simulations. The outcome relies on the corresponding 8 TeV analyses, but all signal regions were re-optimized for the 13 TeV collision, relying only on MC for signal and background yields. The study showed that already with 2 fb^{-1} of integrated luminosity, the one lepton analysis reached a 3σ discovery sensitivity for gluino masses above the Run-1 limit, for a simplified gluino pair production model. This is presented in figure 7.7, where the discovery p-value (p_0) and the equivalent z-value are displayed vs the gluino mass for four possible

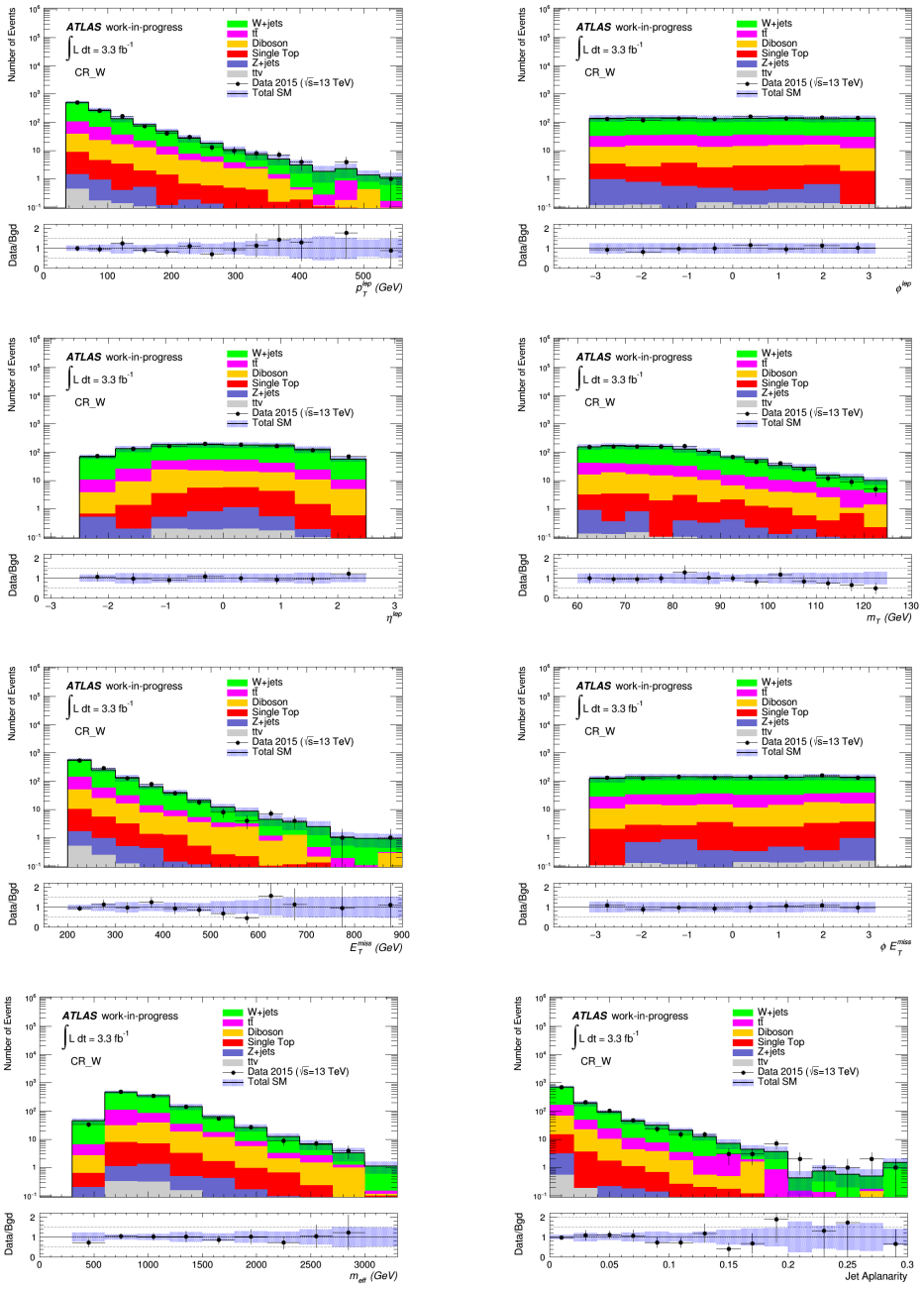

Figure 7.5: Kinematic distributions of variables in a loose W region.

integrated luminosities. The gray area represents the Run-1 limit for gluino masses. It can be seen that the black 2 fb^{-1} line shows a 3σ discovery sensitivity for gluino masses right above the Run-1 limit. After proving that the 1-lepton analysis was sensitive to early 13 TeV data, and after the first data started to come, a new prediction on the total integrated luminosity was calculated and a specialized one-lepton signal region optimization was performed

As already discussed in previous chapters, the event topology of SUSY scenarios strongly depends on sparticle masses and the relative differences between them. To exploit this

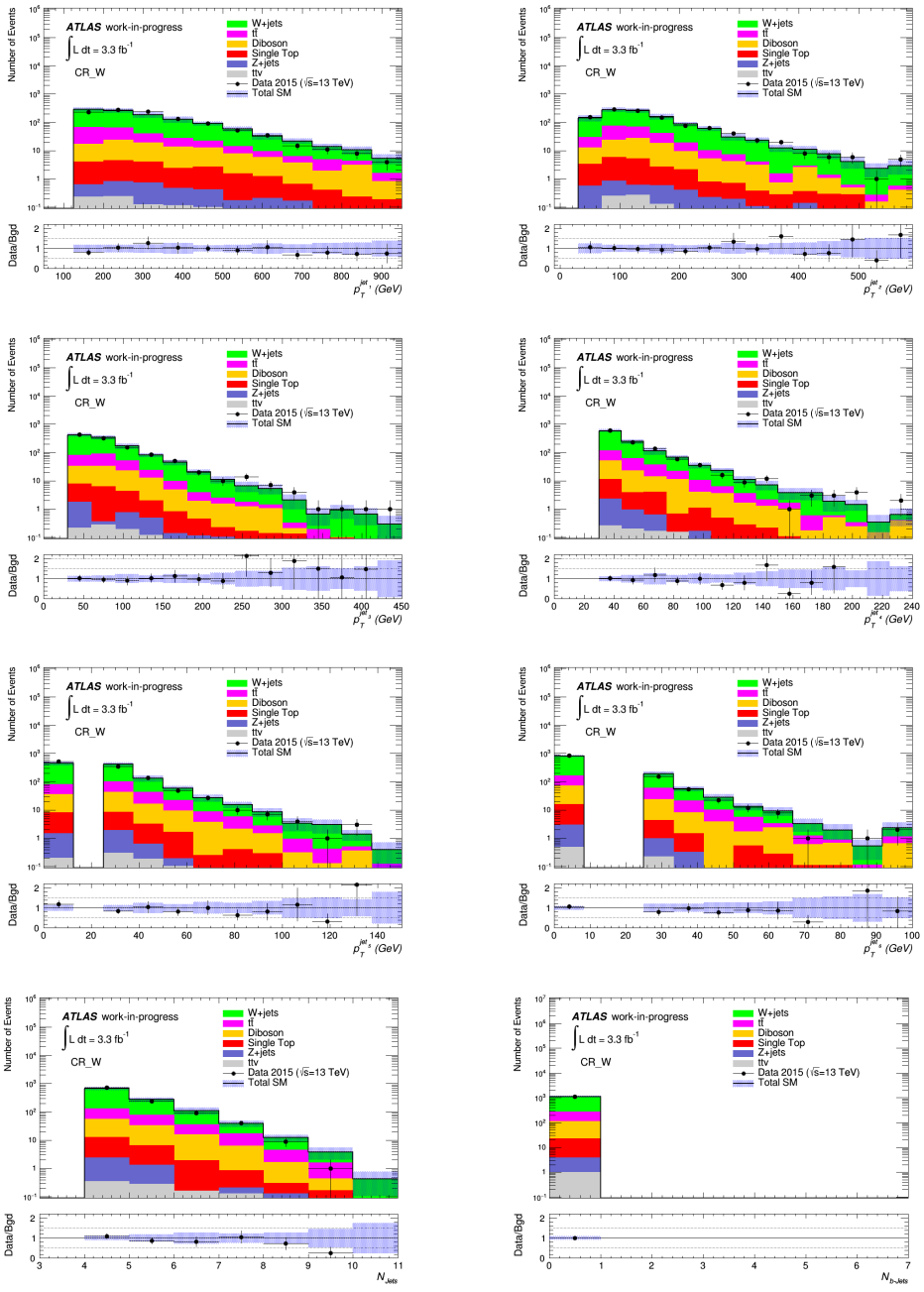

Figure 7.6: Kinematic distributions of variables in a loose W region.

kinematic features, four hard lepton signal regions are defined, each of them optimized for the highest discovery potential in four different benchmark points within gluino pair production simplified models. The points are chosen in characteristic kinematic scenarios beyond Run-1 limits. For the soft lepton analysis two SR were defined. In figure 7.8 the four points chosen for the high p_T lepton analysis are shown next to the Run-1 exclusion limits.

From the four points chosen, two are chosen in the $X = 1/2$ fixed grid, while the other two are chosen in the free X grid with a fixed neutralino LSP mass of 60 GeV. From the first

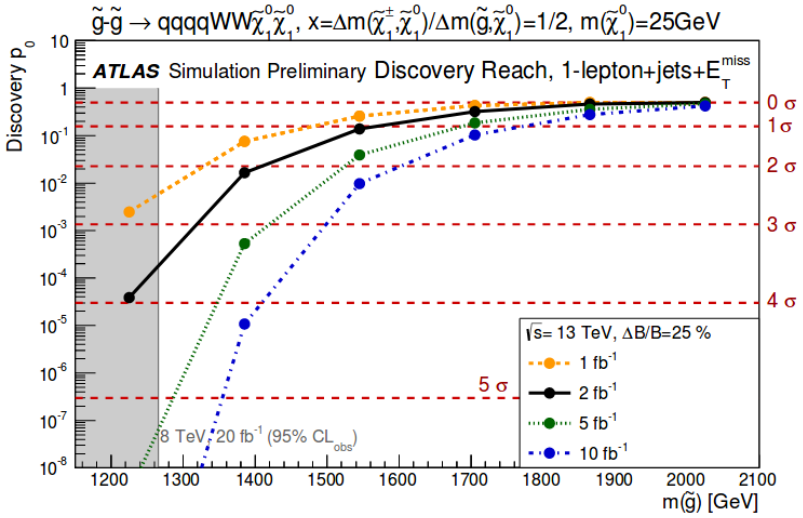

Figure 7.7: Best p_0 value after optimization for different luminosities for simplified gluino pair production models decaying via chargino to the LSP with mass ratio parameter of $x = 0.5$ and an LSP mass set to 25 GeV and assuming a total uncertainty of 25% on the background yields [269]

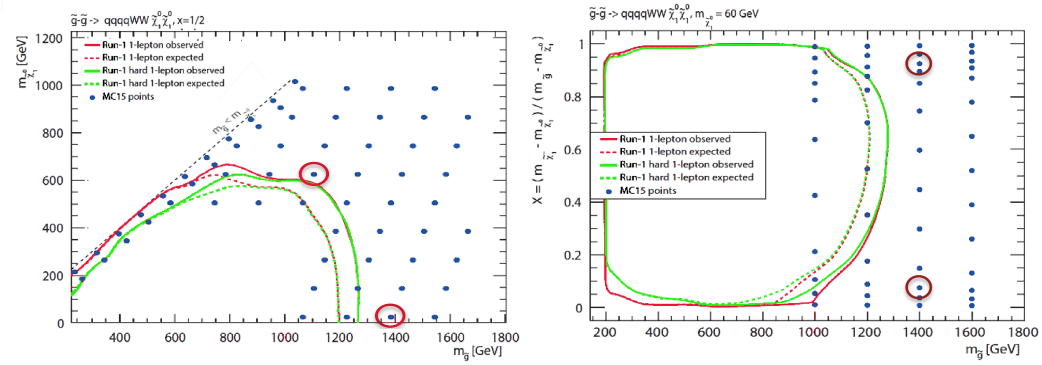

Figure 7.8: Left: One lepton Run-1 limits in the $m_{\tilde{\chi}_1^0} - m_{\tilde{g}}$ plane. Right: One lepton Run-1 limits in the $X - m_{\tilde{g}}$ plane. In both plots, blue points represent available simulated gluino pair production points. The red circles represent the four chosen benchmark points

two points, one targets moderate gluino and LSP mass while the second targets high gluino mass with low LSP mass scenarios. From the las two points, one aims at high X values while the last one is designed for low X values. The points chosen have the following spectrum:

- $m_{\tilde{g}} = 1105$ GeV, $m_{\tilde{\chi}_1^0} = 625$ GeV, $m_{\tilde{\chi}_1^\pm} = 865$ GeV and $X = 1/2$
- $m_{\tilde{g}} = 1385$ GeV, $m_{\tilde{\chi}_1^0} = 25$ GeV, $m_{\tilde{\chi}_1^\pm} = 705$ GeV and $X = 1/2$
- $m_{\tilde{g}} = 1400$ GeV, $m_{\tilde{\chi}_1^0} = 60$ GeV, $m_{\tilde{\chi}_1^\pm} = 1300$ GeV and $X = high$
- $m_{\tilde{g}} = 1400$ GeV, $m_{\tilde{\chi}_1^0} = 60$ GeV, $m_{\tilde{\chi}_1^\pm} = 160$ GeV and $X = low$

The guiding principle to build the four hard lepton signal regions, is to find the best cut combination for each of the four benchmark points. The best cut combination is defined and explained in the following subsections. The SR definition was initially performed using two

methods. The first method consisted in a robust yet time consuming n-dimensional scan, over a grid of cut combinations within a fixed range. The second method makes some reasonable assumptions to reduce the number of cut combinations and hence reducing computing time. Both methods use the discovery significance as the figure of merit to quantify the best cut combination. The discovery significance is given by:

$$Sig = \frac{S}{\sqrt{B}} \tag{7.4}$$

where S and B represent the expected number of signal and background events. Defined like this, the significance quantifies the difference between the $S + B$ and the B hypothesis compared the 1σ uncertainty of the background expectation B. Large significances will mean high probabilities of a deviation from the b-only model. To calculate the significances, also two methods are used. The first one is the full calculations using the HistFitter [153] software including all systematics, the second method which is faster uses RooStats [271] functions to evaluate an approximate value of the significances assuming a flat 25% systematic uncertainty based on previous analyses.

7.4.1 N-dimensional scan method

To perform the scan, first the sensitive variables must be chosen. Usually this variables include lepton and harder jets kinematic variables, missing transverse energy, transverse and effective mass, and any variable with separation power between signal and background could be included. With the chosen variables a scan range is defined. Initially, for some variables and based on previous knowledge of their shapes, the ranges were somehow easily chosen, while for other variables previous tests and plots were needed in order to choose sensitive ranges. After the ranges are chosen, a small discrete step, dividing the range in integer parts is defined. Starting from the lower boundary of the range and increasing the variable value in one step, a second cut value for the variable is fixed. Iterating this procedure reaching the top value, a group of equidistant values within the range are chosen. As an example, the variable E_T^{miss} could be chosen to run between 150 GeV and 450 GeV in steps of 25 GeV. This means that the possible E_T^{miss} cut values to test are in GeV: $\{150, 175, 200, 225, 250, 275, 300, 325, 350, 375, 400, 425, 450\}$. The largest the range and the smaller the step, means sharper sensitivity but higher computing time, no arbitrarily small steps are not ideal. With all possible cut values for all variables, an N-dimensional grid is built, looping for each cut of each variable, resulting in all the possible cut combinations. Having all the potential SRs defined by all the previous cut combinations, the significances are calculated to search for the optimal SR. This was done using two algorithms, the first algorithm used RooStats approximation with flat background systematic uncertainties of 25%[5]. This algorithm was found to be too restrictive, yielding sometimes too low background MC statistics in the SR. This problem was addressed with different approaches. One of the possible solutions was the introduction of the the second algorithm, for which HistFitter was used to compute the significances of all cut combinations for each of the benchmark points, using all signal and background systematic uncertainties instead of fixing flat systematics. This second algorithm was proven to be much more precise and gave sometimes better SR candidates with higher significances. Nevertheless, the statistics problem was only partially solved. Depending on the point for which the optimization procedure was being performed, different scan ranges and step sizes can be defined. Usually an initial rough scan and optimization was performed and depending on the results, finer steps or different limits for some of variables were defined. Even though the second algorithm provided more accurate signal significances, if the scan range

[5]The functions used are $RooStats :: NumberCountingUtils :: BinomialExP(N_S, N_B, syst_B)$ and $RooStats :: NumberCountingUtils :: BinomialExZ(N_S, N_B, syst_B)$

was to fine, or if too many variables are used, if some extra variables needed to be tested or if new scans were to be performed after looking at the results, the process became a burden to the computing clusters, and quick results were harder to obtain. This is why a second method was introduced.

7.4.2 Fast optimization procedure

This method reduces the number of cut combinations for which the full HistFitter significance calculation is performed, reducing drastically computing time. To do this, for each cut combination the signal and background efficiencies ($1 - \epsilon_B$ and ϵ_S) are calculated. With these efficiencies a $1 - \epsilon_B$ vs ϵ_S plot is built for each cut combination, binned in 100 ϵ_S bins. For each ϵ_S bin, it is assumed that the cut combination with the best background suppression has the higher significances. Only these 100 possible SRs with the best background suppression power are kept for a full HistFitter significance calculation. Figure 7.9 shows an example of the $1 - \epsilon_B$ vs ϵ_S plot, where each point represents a possible cut combination and were the red points represent the cut combinations with higher background rejection per bin. Only for the latter the signal significances are fully calculated.

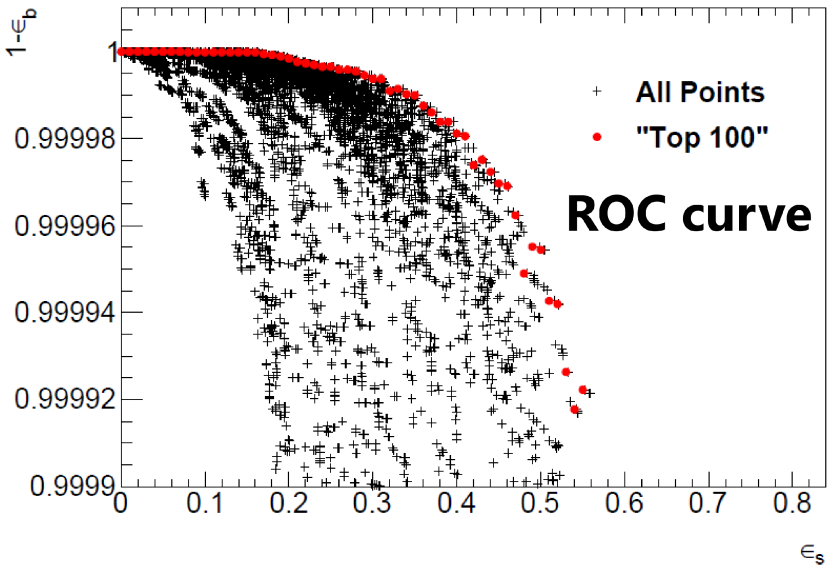

Figure 7.9: Example of a $1 - \epsilon_B$ vs ϵ_S ROC curve for one benchmark point. The full HistFitter significance is only computed for the red points with higher background rejection per bin [272].

Ideally the best cut combination for each benchmark point is the one with highest significance, but this is not always the case. It was found by all methods, that selections with the highest significances presented too low MC statistics making almost impossible to extract a reliable background estimation. For the high gluino and low neutralino mass benchmark point with $x = 1/2$ this was the case. The optimal solution for such a problem is to produce more MC events, or to develop a different method to infer the background yields in the SRs, correctly extrapolating the background distributions to higher values of the discriminating variables. For $t\bar{t}$, an additional sample was produced with a filter based on true $E_T^{miss} > 200$ GeV. The sample was merged with the inclusive sample to cover a larger phase space. To avoid double counting an overlap removal procedure was implemented to merge them. The merging improved the $t\bar{t}$ statistics in potential signal regions by factor

of 10. Nevertheless, producing additional events is budget and time consuming and under the tight schedule to process the first ATLAS results with 13 Tev it was rather unpractical. Instead, to balance high sensitivity keeping reasonable background statistics, different options were tested. Some of these options included fixing thresholds on MC statistics restricting the discovery reach, requiring an arbitrary amount of raw or weighted MC event of different backgrounds allowing tighter cuts and re-optimizing for another benchmark point. Some of this options had no real physics motivation, the final decision should not rely on this arbitrary values only. Instead the decision must be based in a combination of components: Significances, the reach in parameter space, the outcome of some the options given above, and by looking at $N-1$ plots[6]. The reach in parameter space was studied by choosing a small set of possible SRs defined by some of the options given above. Then the significances for all simulated points in the parameter space was computed, and an interpolation to evaluate significances for regions of the parameters between the simulated points was done. A 3σ significance contour is drawn over the parameter space plot. The SR candidate, giving a contour which includes a larger fraction of the parameter space outside the Run-1 current limit, is preferred over smaller contour reach. The study of $N-1$ plots was done in parallel to ensure that the optimization is not done based on MC fluctuations, as some times the best cut combination, was chosen just after a MC spike coming from MC fluctuations, or before entering into a low statistics region. The final four hard lepton signal regions optimized for each of the four benchmark point are defined in table 7.4

Benchmark Points	1400_1300_60	1400_160_60	1385_705_25	1105_865_625
SR Name	4-jet high-x SR	4-jet low-x	5-jet SR	6-jet SR
N_{lep}	==1			
p_T^{lep}(GeV)	> 35			
N_{jets}	≥ 4		≥ 5	≥ 6
p_T^{jet}(GeV)	$> 325, 30, ..., 30$	$> 325, 150, ..., 150$	$> 225, 50, ..., 50$	$> 125, 30, ..., 30$
E_T^{miss}(GeV)	> 200		> 250	
m_T(GeV)	> 425	> 125	> 275	> 225
m_{eff}^{incl}(GeV)	> 1800	> 2000	> 1800	> 1000
$E_T^{miss}/m_{eff}^{incl}$	> 0.3	-	> 0.1	> 0.2
Jet Aplanarity	-	> 0.04		

Table 7.4: Summary of the selection criteria for the hard lepton signal regions.

In the high-x point, $m_{\tilde{g}} = 1400$ GeV, $m_{\tilde{\chi}_1^\pm} = 1300$ GeV and $m_{\tilde{\chi}_1^0} = 60$ GeV, so the mass difference between the chargino and the neutralino is large. In this scenario the W boson produced in the chargino decay is boosted, leading to a one high p_T jet from the W decay and high lepton p_T. With this topology, signal events in regions alike should have large m_T values. On the other hand due to the small difference between gluino and chargino masses, jets produced in the gluino decays must be relatively soft. The SR targeting this scenarios (4-jet high-x SR) shows kinematic requirements aiming exactly at the described phenomenology such as high m_T, one hard jet plus soft trailing jets.

For the low x point, $m_{\tilde{g}} = 1400$ GeV, $m_{\tilde{\chi}_1^\pm} = 160$ GeV and $m_{\tilde{\chi}_1^0} = 60$ GeV. Unlike the previous point, here the mass different between the chargino and the neutralino is small, leading to a usually virtual W boson from the chargino decay and therefore to softer lepton and jets from the W decay. However the large difference between the gluino and chargino masses gives a large phase space for higher jet p_T from the gluino decays. This is reflected

[6] $N-1$ plots are built using the selection of events passing all but one of the possible SR cuts. The plot shows the distribution of the exact same variable for which the cut has not been applied

in the 4-jet low-x SR where a looser m_T requirement is seen while stringent p_T^{jet} cuts are required.

In the case of the points with fixed $x = 1/2$, the point with high gluino and low neutralino masses with the chargino mass just between ($m_{\tilde{g}} = 1385$ GeV, $m_{\tilde{\chi}_1^\pm} = 705$ GeV and $m_{\tilde{\chi}_1^0} = 25$ GeV), has relatively large mass differences between the gluino and the chargino, and the same mass difference between chargino and neutralino masses. This allows for relatively hard jets from the gluino decays plus relatively hard jet and lepton from the W decay. The cuts aiming this scenario can be seen in the 5-jet SR where tight p_T^{jet}, m_T and m_{eff}^{incl} requirements are imposed.

The last benchmark point with fixed $x = 1/2$, with $m_{\tilde{g}} = 1105$ GeV, $m_{\tilde{\chi}_1^\pm} = 865$ GeV and $m_{\tilde{\chi}_1^0} = 625$ GeV has smaller mass separations. This is reflected in the 6-jet SR requirements which are optimized for such phenomenology with less stringent p_T^{jet}, m_T and m_{eff}^{incl} cuts.

7.5 Soft lepton signal region optimization

For the soft lepton analysis, the signal region optimization targets 2 types of compressed scenarios. In one scenario the entire mass spectrum is compressed, with a relatively heavy neutralino LSP, and an almost degenerate chargino. The gluino is also only slightly heavier than the chargino, making most of the decay objects soft. With this kinematics a heavy ISR recoiling jet is required to enhance signal events over background. The second targeted scenario consists in a large mass difference between the gluino and the chargino, with only a small mass difference between the chargino and the neutralino. With such spectrum, hard jets are expected from the gluino decays while the virtual W boson from the chargino decay can only decay into low p_T lepton and jets. To easily reference these regions, the first will be labeled as *Compressed-ISR* region and the second as *Gaugino-compressed* region.

To keep the soft and hard lepton analysis orthogonal for the final statistical combination, an upper cut of 35 GeV on the lepton is imposed. The optimization procedure, contrary to what was done for the hard lepton analysis is not only fixed to benchmark points. Instead, the significances are calculated using RooStats approximation with flat 25% background systematics for few points within each of the two main scenarios. Then, two dimensional significance plots are studied for each of the points. In the plots two of the main discriminating variables are varied while the remaining variables are fixed to the values that maximized the significance. $N - 1$ plots were also studied, and after analyzing the best coverage, two SRs were defined aiming both distinctive spectra. The summary of the final two soft lepton signal regions requirements are presented in table table 7.5

The kinematics of the Compressed-ISR region has soft final state leptons and jets. The number of jets depends heavily on the mass splittings, and the p_T distribution of the leading jet is much harder than for the trailing jets p_T indicating the presence of a hard (ISR) jet. This kinematics is reflected 2-jet soft-lepton SR which requires at least two jets, with the hardest jet p_T above 180 GeV. Jet aplanarity was proven to be not a good discriminant for such scenario, because a hard ISR jet recoiling against the rest of the event, makes the distribution for signal to be also quite planar.

In Gaugino-compressed scenarios the average lepton p_T increases as the chargino-neutralino mass difference increases slightly. Also as the gluino-chargino mass difference is high, many energetic jets are present in the final states. These features are covered by the 5-jet soft-lepton SR targeting such regions, mainly with the p_T of the three leading jets required to be higher the 200 GeV.

In figure 7.10 the expected 3σ discovery significance contours for 3 fb^{-1} of all SRs is presented in the x-free and in the $x = 1/2$ phase space plane, where the Run-1 upper limits are superimposed. The plots show that with an intregrated luminosity of 3.0 fb^{-1} the 3σ

Scenario SR Name	Compressed-ISR 2-jet soft-lepton SR	Gaugino-compressed 5-jet soft-lepton SR
N_{lep}	==1	
p_T^{lep}(GeV)	$7(6) - 35$	
N_{jets}	≥ 2	≥ 5
p_T^{jet}(GeV)	$> 180, 30$	$> 200, 200, 200, 30, 30$
E_T^{miss}(GeV)	> 530	> 375
m_T(GeV)	> 100	-
H_T(GeV)	-	> 1100
$E_T^{miss}/m_{eff}^{incl}$	> 0.38	-
Jet Aplanarity	-	> 0.2

`Table 7.5:` Summary of the selection criteria for the soft lepton signal regions.

discovery significance contours extend already outside the previous 8 TeV limits.

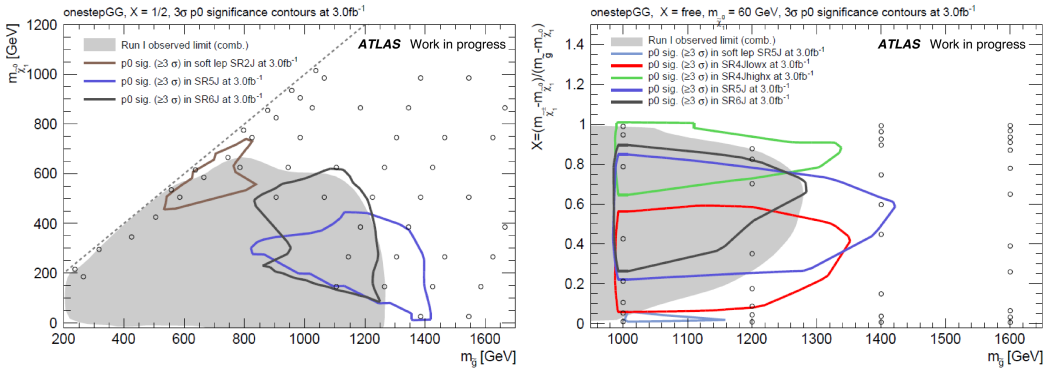

`Figure 7.10:` Discovery significance (3σ) contours for 3 fb^{-1} for the gluino one step simplified model with $x = 1/2$ grid (left) and x-free grid (right). Contours are shown for the 6-jet, 5-jet, 4-jet high-x and 4-jet low-x hard lepton signal regions and for the 2-jet and 5-jet soft lepton signal regions. The combined hard-soft Run-1 observed exclusion limit is shown as a gray area as a reference.

7.6 Background estimation

The two main background processes ($t\bar{t}$ & $W + jets$) are predicted by simulation, which is normalized to data in dedicated control regions. The smaller backgrounds are also taken from simulation but remain fixed when performing the fit normalized to the most accurate cross section available. Multi-jet background from QCD processes, was proven to be negligible using the same matrix method used for the 8 TeV analysis [48]. This contribution is now negligible mainly due to the harder E_T^{miss} requirement together with the improved lepton reconstruction and identification. The CRs must include large number of events and high purity of the process of interest, where only a small amount of signal contamination is allowed. Both criteria are required to give a robust background prediction with a small statistical uncertainty. Additionally, as the background prediction is going to be extrapolated to validation and signal regions, any miss-modeling might have a big impact when extrapolated. To accurately model the kinematics of the background processes in the SRs, it is crucial that the kinematic

properties of the CRs to be as similar as possible to those on the SR, keeping the discriminating power.

The normalization of the background events to data is performed simultaneously in a background only fit, in which the simulation is fitted to the observed data in the control regions. For each SR there are two CRs, one dedicated to $W + jets$ and the second to $t\bar{t}$ processes. The two normalization factors obtained are then used to extrapolate both background rates to the associated SR. The small statistical uncertainties on the background prediction in the CR, extrapolated to the stringent SR phase space, narrows the influence of possibly large systematic uncertainties in such extreme scenarios. To differentiate between $W + jets$ and $t\bar{t}$ regions b-tagging is used. As it can be seen in the $N_{b\text{-jets}}$ plots in figures 7.4 and 7.6 there is a strong discriminating power between $t\bar{t}$ and $W + jets$ events when looking at events with or without b-tagged jets. To select events in the $t\bar{t}$ CR, there is the requirement that at least one signal jet is a b-jet, while events in the $W + jets$ CR are selected by vetoing any event containing b-tagged signal jets. To simplify notation, $W + jets$ CR will be labeled as WCR while $t\bar{t}$ CR is labeled as TCR.

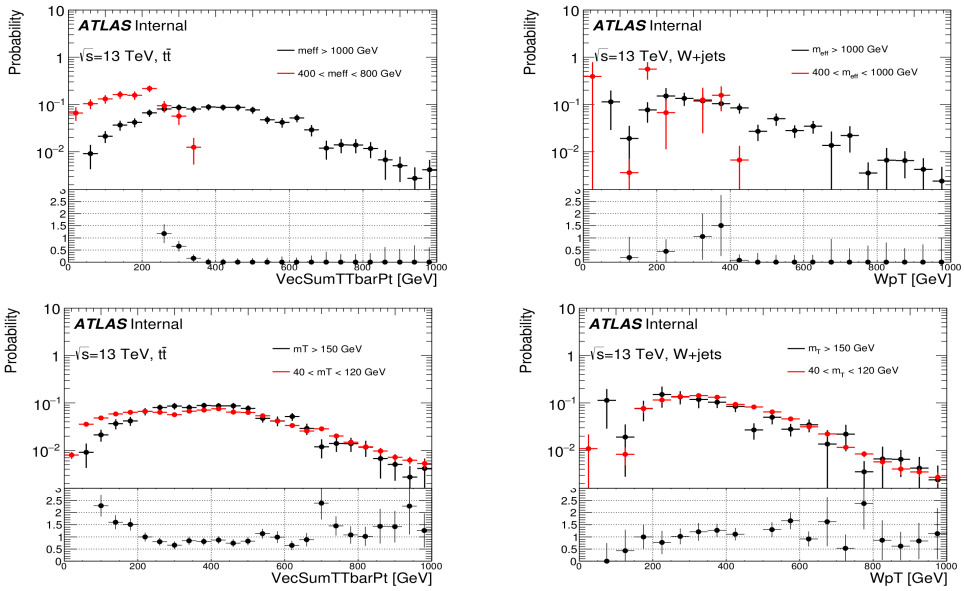

Figure 7.11: Extrapolation impact on truth W p_T shapes and on truth p_T shapes of the $t\bar{t}$ system in the looser region defined by $p_T^{lep} > 35$ GeV, $N_{jet} > 4$ with $p_T > 50$ GeV, $E_T^{miss} > 150$ GeV, $m_T > 150$ GeV and $m_{eff} > 1000$ GeV. All the cuts are applied except for the corresponding extrapolating variable [272].

To keep kinematics of the $t\bar{t}$ & $W + jets$ processes similar between control and validation regions, the truth p_T sum of the $t\bar{t}$ system and the truth W p_T distributions are studied in a rather looser selection given by at least four jets with $p_T > 50$ GeV, $E_T^{miss} > 150$ GeV, $m_T > 150$ GeV and $m_{eff} > 1000$ GeV . The distributions are compared for low and high values of one the potential discriminating variables. As an example, to test m_{eff} as an extrapolating variable, the m_{eff} cut is removed from the previous requirements, and truth p_T of the W-boson and of the $t\bar{t}$ system are plotted for both low and high m_{eff} regions. If the distributions look very different, it means that the variable is not ideal to extrapolate from CR to SR, as the kinematics of the processes close to signal region is different than in the control regions. To illustrate this, the truth p_T sum of the $t\bar{t}$ system and the truth W p_T distributions are shown in the top two plots in figure 7.11 for a SR-like selection with $m_{eff} > 1000\ GeV$ and

for a lower m_{eff} CR-like selection given by 400 GeV $< m_{eff} <$ 800 GeV. As it can bee seen in both plots there are large shape differences between low and high m_{eff} selections, this means that the kinematics in the CR-like selection is not close to the kinematics in the SR. This result is expected, as m_{eff} correlates strongly with the p_T of the $t\bar{t}$ system and with W p_T making it not the best variable to extrapolate from control to signal regions. In the bottom plots of figure 7.11, the same variables are plotted for $m_T > 150$ GeV and 40 GeV $< m_{eff} <$ 120 GeV cuts. As it can be seen, the distributions are much closer than the ones with m_{eff}. The small difference on the shapes especially for low p_T values were proven to improve by slightly relaxing the jet p_T and/or m_{eff} cuts in the CRs. Similar analysis has been performed for the other possible discriminating variables, proving that m_T and aplanarity are good candidates for extrapolation variables, if loosening jet p_T and m_{eff} cuts in the CRs. E_T^{miss}/m_{eff} was also proven to be a good extrapolation variable. The extrapolating variables used for the hard lepton analysis are m_T, aplanarity and E_T^{miss}/m_{eff}. For the soft lepton analysis, the extrapolating variables are m_T, E_T^{miss} and H_T. The summary with all control regions definition is presented on tables 7.6, 7.7 and 7.8

Associated SR	4-jet high-x SR		4-jet low-x SR	
CR Name	4-jet high-x TCR	4-jet high-x WCR	4-jet low-x TCR	4-jet low-x WCR
N_{b-jets}	≥ 1	$== 0$	≥ 1	$== 0$
$p_T^{4th\ jet}$(GeV)	Same as SR		> 30	
m_T(GeV)	60 - 125		95 - 125	60 - 125
m_{eff}^{incl}(GeV)	Same as SR		> 1500	> 1900
$E_T^{miss}/m_{eff}^{incl}$	<0.3		Same as SR	
Jet Aplanarity	Same as SR		< 0.04	

Table 7.6: Summary of the selection criteria for the 4-jet hard lepton control regions. Only the requirements that are different than the SR requirements are presented.

Associated SR	5-jet SR		6-jet SR	
CR Name	5-jet TCR	5-jet WCR	6-jet TCR	6-jet WCR
N_{b-jets}	≥ 1	$== 0$	≥ 1	$== 0$
$p_T^{5th\ jet}$(GeV)	> 30		Same as SR	
m_T(GeV)	60 - 125			
m_{eff}^{incl}(GeV)	> 1500		Same as SR	
Jet Aplanarity	< 0.04			

Table 7.7: Summary of the selection criteria for the 5- and 6-jet hard lepton control regions. Only the requirements that are different than the SR requirements are presented.

Besides control and signal regions, validation regions (VR) are built to confirm or *validate* the extrapolation from control to signal regions. These regions are at the same time orthogonal to both control and signal regions and are also designed to be kinematically close to the signal regions with only a small expected signal contamination. The VRs are not used to constrain any parameter in the fit and are intended to provide an independent quality check of the extrapolation to the SRs. For each SR there are two independent validation regions, one for each of the extrapolating variables. For all hard lepton SRs, one of the two VRs verifies the extrapolation from low to high m_T values, and the second validates the extrapolation along E_T^{miss}/m_{eff} for the 4-jet high-x SR and aplanarity for the remaining three SRs. Each of the two soft SRs also have two VRs associated to test the extrapolation using E_T^{miss}, m_T and

Associated SR	2-jet soft-lepton SR		5-jet soft-lepton SR	
CR Name	2-jet soft TCR	2-jet soft WCR	5-jet soft TCR	5-jet soft WCR
N_{b-jets}	≥ 1	$== 0$	≥ 1	$== 0$
$p_T^{1st\ jet}$(GeV)	Same as SR		> 150	
$p_T^{2nd\ jet}$(GeV)	Same as SR		> 100	
$p_T^{3rd\ jet}$(GeV)	Same as SR		> 30	
m_T(GeV)	40 - 80		Same as SR	
E_T^{miss}(GeV)	250 - 500		250 - 375	
H_T(GeV)	Same as SR		500 - 1000	

Table 7.8: Summary of the selection criteria for the 2- and 5-jet soft lepton control regions. Only the requirements that are different than the SR requirements are presented.

H_T depending on the SR. The summary with all validation regions definition is presented on tables 7.9, 7.9 and 7.11.

Associated SR	4-jet high-x SR		4-jet low-x SR	
VR Name	4-jet high-x m_T	4-jet high-x E_T^{miss}/m_{eff}	4-jet low-x m_T	4-jet low-x Aplanarity
$p_T^{4th\ jet}$(GeV)	Same as SR		> 30	
m_T(GeV)	150-475	60 - 125	125 - 350	60 - 125
m_{eff}^{incl}(GeV)	Same as SR		> 1900	
$E_T^{miss}/m_{eff}^{incl}$	< 0.3	> 0.3	Same as SR	
Jet Aplanarity	< 0.004	Same as SR	< 0.04	> 0.04

Table 7.9: Summary of the selection criteria for the 4-jet hard lepton validation regions. Only the requirements that are different than the SR requirements are presented.

Associated SR	5-jet SR		6-jet SR	
VR Name	5-jet m_T	5-jet Aplanarity	6-jet m_T	6-jet Aplanarity
$p_T^{5th\ jet}$(GeV)	> 30		Same as SR	
m_T(GeV)	125 - 350	60 - 125	125 - 350	60 - 125
m_{eff}^{incl}(GeV)	> 1500		Same as SR	
Jet Aplanarity	< 0.04	> 0.04	< 0.04	> 0.04

Table 7.10: Summary of the selection criteria for the 5- and 6-jet hard lepton validation regions. Only the requirements that are different than the SR requirements are presented.

A diagram of all control, validation and signal regions is presented in figure 7.12, where the SRs are represented as green areas, CR as red areas and VR as blue areas. Any requirement different from the SR is also presented inside each of the regions.

With the CRs defined, the simultaneous normalization fit of $t\bar{t}$ & $W + jets$ to the observed number of events can be performed. The main kinematic distributions after fit in the control regions are presented in figures C.3 - C.14 where a good data vs background agreement is found within uncertainties. It was also seen that in general MC was slightly overestimated with respect to data, so most of the normalization factors are less than one. The detailed fit configurations, systematic uncertainties and results are presented in the following sections.

Associated SR	2-jet soft-lepton SR		5-jet soft-lepton SR	
VR Name	2-jet soft m_T	2-jet soft E_T^{miss}	5-jet soft H_T	5-jet soft E_T^{miss}
$p_T^{1st\ jet}$(GeV)	Same as SR		> 150	
$p_T^{2nd\ jet}$(GeV)	Same as SR		> 100	
$p_T^{3rd\ jet}$(GeV)	Same as SR		> 30	
m_T(GeV)	> 80	40 - 100	Same as SR	
E_T^{miss}(GeV)	250 - 500	> 500	250 - 375	> 375
H_T(GeV)	Same as SR		> 1000	500 - 1000

Table 7.11: Summary of the selection criteria for the 2- and 5-jet soft lepton validation regions. Only the requirements that are different than the SR requirements are presented.

7.7 Systematic uncertainties

One of the key aspects for excluding a model or making a discovery, is the proper treatment of systematic uncertainties. In experiments like ATLAS, involving large amounts of individual channels, different calibration methods for object identification and a vast supply of theoretical calculations, systematic uncertainties arise from diverse sources and must be carefully estimated. Systematic uncertainties may come from experimental uncertainties or could arise from theoretical predictions. In this analysis, as the dominant background processes are derived in the CRs, the related systematic uncertainties will be extrapolated to the SRs only by influencing the transfer factors. Only the relevant and most dominant uncertainties for this analysis will be described below.

7.7.1 Experimental uncertainties

The dominant experimental systematic uncertainties found are the jet energy scale (JES) and jet energy resolution (JER). JES uncertainty accounts for the uncertainty on how the jet energy measured in the ATLAS calorimeter is translated into parton energy. The JER uncertainty accounts for uncertainty on the fluctuation of the measured jet energy around the central value. As mentioned in chapter 4 to calibrate jets, different corrections and calibrations are made and each of the corrections and calibrations includes an associated uncertainty. These calibrations and corrections are obtained exploiting the combination of different simulated samples together with data analysis, such as the study of jet balance in di-jet Z+jet and γ+jet events [123]. Jet calibration coefficients depend on the p_T and η of the jet, also on pileup and jet flavor composition, consequently JES and JER uncertainties also depend on these variables.

The total number of uncertainties arising from the different calibration procedures, would require for an analysis to include an amount of roughly 70 JES uncertainty parameters to accurately meet all correlations of the calibration procedure. Depending on the analysis, time and statistics, it might be inconvenient and even unnecessary for certain analyses to include such a large number of nuisance parameters. For analyses that might be blind to some of the calibration correlations, a reduced set is built which has only a reduced set 17 nuisance parameters. A further reduction is built, following the prescription in [273] to end up with four sets of minimal representations of the JES systematic uncertainties, each of which includes only three nuisance parameters. In these minimal representations an important loss of correlation from changes to the jet energy scale is observed. However, this effect is covered by the four sets, and each analysis can probe its own sensitivity to such correlations. If observables remain unchanged when using each of the four different scenarios, it means that the analysis is not

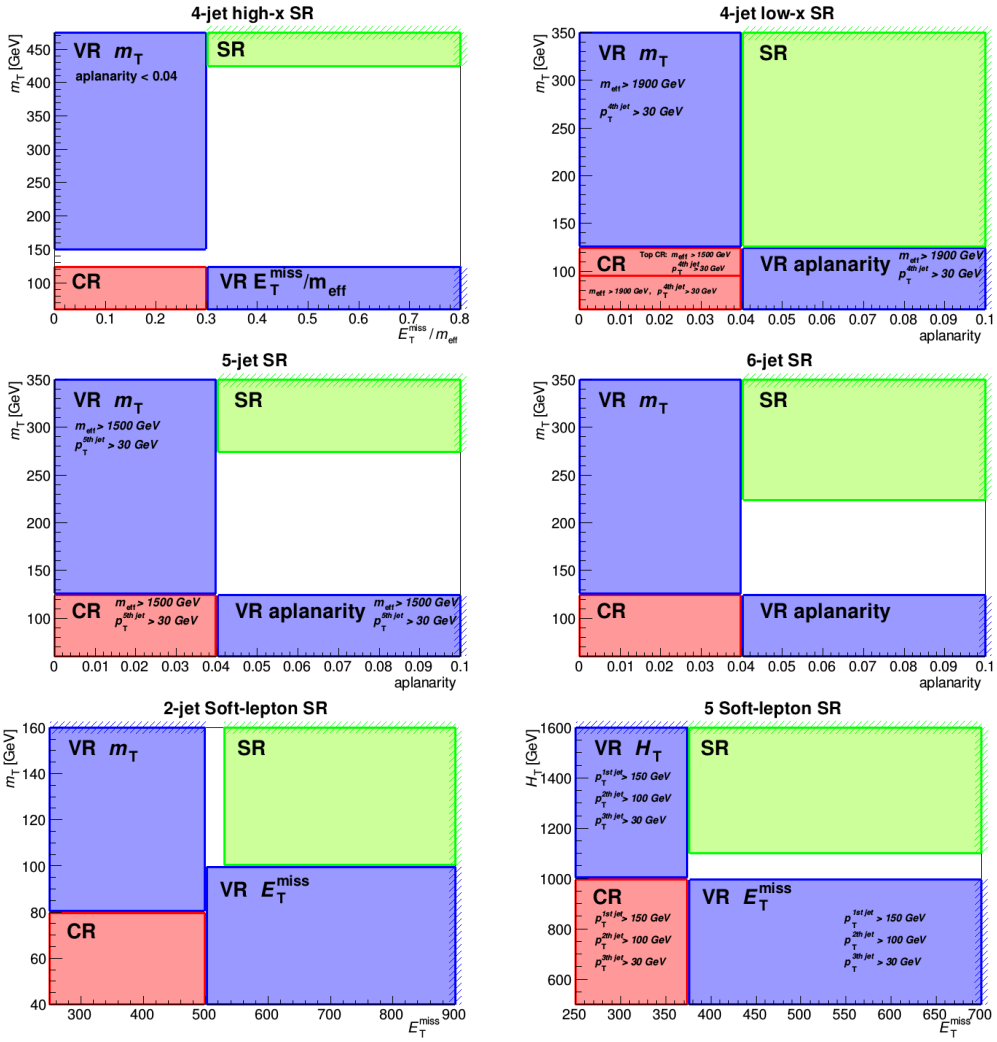

Figure 7.12: Representation of all signal, validation and control regions. The variables displayed in the x and y axes are the variables used for the extrapolation. Additional requirements other than the SR requirements and different to the exclusive cut on the extrapolating variables are included on top of each region. Also each CR represents both $W + jets$ and $t\bar{t}$ control regions, only different to each other by the requirement of at least one b-jet in the $t\bar{t}$ CR while for the $W + jet$ CR, exactly no b-tagged jets are required. In only one region, there is a difference besides the b-jet requirement between $W + jets$ and $t\bar{t}$ control regions, this is the 5-jet TCR in which there is a looser m_{eff} cut is required. All requirements are presented explicitly from table 7.6 to table 7.11.

sensitive to those correlations and could use one of the reduced sets. For the jet energy resolution, the dominant uncertainties have similar shapes, and can be combined into only one nuisance parameter without significant correlation loss.

In figure 7.13 a summary of the the total JES and JER uncertainties is presented, for transverse jets reconstructed with the anti-k_t algorithm with $R = 0.6$. The left plot in figure 7.13 shows the final 2012 JES uncertainties and the total updated JES uncertainties for 2015 data. Also the contributions from pile-up, flavor, 2012 in-situ corrections plus the contributions estimated from the quantification of the 2012 - 2015 changes affecting jet energy uncertainties as a function of jet p_T and η. For low energy jets with $p_T < 40$ GeV the resulting uncertainty

is the highest ranging between 4% and 6% decreasing with jet p_T. As the p_T increases, JES uncertainty keeps sinking to reach a minimum value of 1% for jets with $p_T = 200$ GeV. At this point the uncertainty remain almost constant with values of 1% for jets with 200 GeV $< p_T <$ 1800 GeV. For jets with $p_T >$ 1800 GeV the JES uncertainty rise again to reach values near 3%. In the right plot in figure 7.13, the final 2012 JER uncertainties and the total updated JER uncertainties for 2015 data are shown. The individual pile-up contribution, in-situ corrections and the contributions estimated from the quantification of the 2012 - 2015 changes affecting jet energy resolution are also shown. For low energy jets with $p_T < 20$ GeV the resulting uncertainty can go as high as 4% and starts decreasing with jet p_T reaching a values of 1.5% for jets with p_T close to 70 GeV. For jets with 70 GeV $< p_T <$ 200 GeV the uncertainty decreases slowly reaching a minimum of 0.5%. For jets with $p_T >$ 200 GeV the JES uncertainty stays at the lowest value of 0.5%.

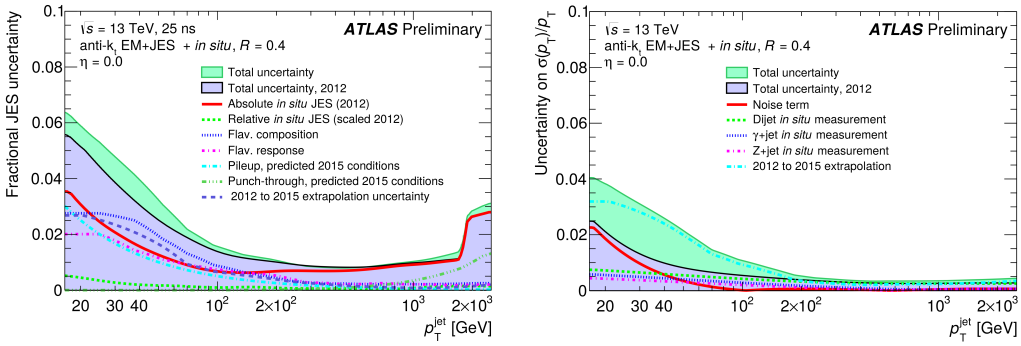

`Figure 7.13:` Left: Final JES uncertainties estimated for 2015 data with 25 ns bunch spacing as a function of jet p_T for jets with $|\eta| = 0$. Right: Final JER uncertainties estimated for 2015 data with 25 ns bunch spacing as a function of jet p_T for jets with $|\eta| = 0$ [123].

For the hard one-lepton analysis, the first test for the JES reduced set with only 3 nuisance parameters was made with $t\bar{t}$ samples. The first study tested the impact of JES uncertainties on MC yields in the 6-jet WCR, 6-jet WTR and 6-jet SR as well as in the transfer factors from control to signal regions. To compare results, a fit was performed using the JES set containing 17 nuisance parameters and the 4 reduced sets of only 3 parameters each. Due to low statistics given mainly by the samples and the stringent cuts defining the regions, the results were not conclusive. To obtain relevant and significant results, the impact of JES systematic uncertainties on an observable must be compared within statistical uncertainties. To obtain reliable statistical errors on the JES systematic uncertainties, a BootStrap Method [274] was used. The impact on the raw MC yields on the 6-jet SR using any of the four strongly reduced scenarios or using the 17 parameter reduced representation are consistent within statistical errors and thus a reduced set of only three nuisance parameters was used.

Muon momentum resolution is also among the dominant experimental systematic uncertainties. For muons, the momentum resolution and scale are determined separately for the the ID and MS and its associated uncertainties are separately assigned to each measurement. Lepton scale and resolution are calibrated from $Z \to \ell^+\ell^-$, $W \to \ell^\nu$ and $J/\Psi \to \ell\ell$ events from data and MC samples using the tag-and-probe method. The corresponding scale and resolution uncertainties plus reconstruction and isolation uncertainties are computed by varying several of the fit parameters as described in [141]. As an example, in the left plot in figure 7.14, the the peak of the invariant mass $m_{\mu\mu}$ distribution obtained from the fit to $Z \to \mu\mu$ sample is presented as a function of the leading muon η for CB pairs. Both data and the corrected simulation are shown. It can be seen that the simulation is in good agreement with data and deviations lie within the systematic uncertainty band of 0.1%. The right plot in

figure 7.14 presents the di-muon mass resolution as a function of the leading muon's η also for CB pairs. The di-muon mass resolution is close to 1.6% for small η values and increases to 1.9% in the end caps, corresponding to a relative muon p_T resolution of 2.3% in the center of the detector and 2.9% in the end caps. After applying the corrections, the simulation resolution agrees with the resolution measured in data within systematic uncertainties.

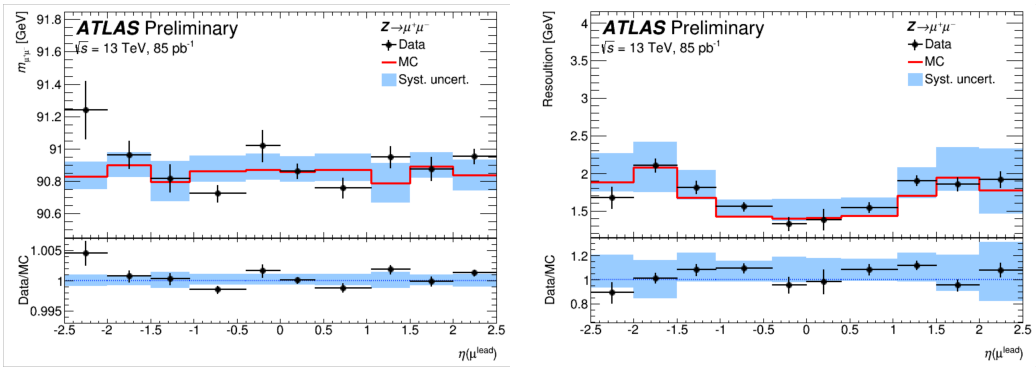

Figure 7.14: Left: Fitted mean mass of the dimuon system events for data and corrected $Z \to \mu^+\mu^-$ simulation as a function of the leading muon η. Right: Di-muon invariant mass resolution for CB muons for data and corrected $Z \to \mu^+\mu^-$ simulation as a function of the leading muon η. The shaded bands represent systematic uncertainties. [141].

E_T^{miss} systematic uncertainties are estimated by propagating the uncertainties of the energy and momentum scale of each of the objects affecting the E_T^{miss} calculation. The scale and resolution uncertainties of the soft-term components of E_T^{miss} are also included and are quantified using the balance between hard and soft contributions using different dedicated $Z \to \mu\mu$ MC samples. The uncertainty related to different detector materials affecting the E_T^{miss} soft-term distribution is found generating additional MC samples with diverse detector geometry as explained in [143].

Another experimental uncertainty that cannot be neglected comes from the re-weighting of simulations to match the average number of interactions per bunch crossing distribution observed in data. In signal regions with higher jet multiplicity, the pileup uncertainty arising from this re-weighting is more relevant than in lower jet multiplicity regions. Pile-up dependent uncertainties are determined from 2012 in-situ studies and can be applied to 2015 data using a similar method to what is done for jet p_T and η dependent uncertainties. Systematic uncertainties from the difference between 2012 and 2015 conditions are included as additional uncertainty sources and are estimated comparing MC simulations [129].

7.7.2 Theoretical uncertainties

Theory Uncertainties on the main backgrounds.

Theory uncertainties come from variety of sources, the estimation of the main sources for $t\bar{t}$ and $W + jets$ theoretical uncertainties for the hard lepton channel is described below. As the main backgrounds are normalized to data in dedicated CRs and extrapolated to the validation and signal regions, the theoretical uncertainties will affect the transfer factors affecting the final background yields.

Scale Variations: The choice of the QCD renormalization and factorization scales determines directly the MC predictions. For $t\bar{t}$ and $W + jets$ samples, the estimation of the related uncertainty is performed by generating equivalent samples, with both scales

modified up and down by a factor of two over the nominal value. For $W + jets$ samples the choice of the re-summation and the matching scale between the matrix elements and the parton shower also affects the simulations, and the uncertainty is quantified also by an up and down variation of the corresponding parameters in SHERPA by a factor of two around the nominal value [278].

Initial and final state radiation: The uncertainty related to the amount of ISR and FSR modeling in $t\bar{t}$ samples, is assessed by interfacing the RADHI and RADLOW specific PYTHIA tunes [252] to POWHEG. In these tunes, the scale at which α_S is obtained is varied by two and by half respectively inducing more and less parton radiation. The uncertainty is evaluated as half the relative difference between both transfer factors. In addition NLO radiation is varied up and down by a scale of two above the nominal value by varying the h_{damp} parameter in PYTHIA to be twice and half of m_t which is the nominal value[7].

Hadronization and fragmentation: Parton showering modeling depends on the hadronization and fragmentation schemes chosen and hence there is a systematic uncertainty related to it. Such uncertainty is obtained for $t\bar{t}$ samples by comparing the predictions using the POWHEG generator interfaced with PYTHIA and with HERWIG++ [276] showering algorithms. The absolute difference between the transfer factors evaluated with both samples is adopted as a symmetric uncertainty.

Monte Carlo generator: The simulation of the interaction of hard partons depends on the generator used, these differences can be quantified and included as an uncertainty. $t\bar{t}$ samples generated with POWHEG-BOX are compared to AMC@NLO [277]. To account for limited MC statistics, the theoretical uncertainty is added in quadrature with the statistical error. For $W + jets$ samples, the transfer factors using the nominal SERPA generator are compared to those obtained from MADGRAPH

Theory uncertainties on minor backgrounds: $Z + jets$, single-top, di-boson and $t\bar{t}V$

As the secondary backgrounds are estimated only from simulation and are normalized in all regions to the expected SM cross sections, the uncertainties are taken as the relative difference in the expected rates between the nominal and the varied samples. The estimation of the main sources of theoretical uncertainties for the secondary hard lepton backgrounds is described below.

Scale Variations: Similar to what is done for $t\bar{t}$, specialized samples are produced for single-top and for $Z + jets$ events, where the QCD renormalization and factorization scales have been varied and compared to the nominal sample. For di-boson samples, renormalization, factorization and re-summation scale uncertainties are computed varying the pertinent SERPA parameters [278].

Initial and final state radiation: For single-top background, the uncertainty related to the amount of ISR and FSR modeling is also obtained by connecting the RADHI and RADLOW PYTHIA tunes to the POWHEG generator.

Hadronization and fragmentation: Parton showering modeling is also a non negligible source of uncertainty for single-top samples and the related uncertainty is obtained using a similar approach as for $t\bar{t}$, in the context that the results using PYTHIA as the nominal showering algorithm are compared to what is obtained using HERWIG++.

[7]The h_{damp} parameter mainly regulates the $high - p_T$ emission against which the top quark pair system recoils [275]

Monte Carlo generator: For $Z+jets$ samples the uncertainty related to the choice of the hard scattering generator is obtained by comparing the predictions obtained by the nominal SHERPA generator with those obtained using MADGRAPH. In the case of Diboson samples, nominal SHERPA predictions are compared to POWHEG-BOX predictions.

Cross-section: Following the results on [279], an uncertainty of 6% is conservatively assigned for the inclusive $Z+jets$ cross-section. Similarly, for the single-top cross-section uncertainty, an uncertainty of 3.7% (4.7%) is estimated for the inclusive s-channel top (anti-top) production, for the t-channel top (anti-top) production an uncertainty of 4% (5%) is assigned while for the Wt-channel the uncertainty taken is 5.3% [280]. For diboson processes a global uncertainty of 6% on the inclusive cross-section is assigned, to account four various sources of uncertainties such as the lack of higher order corrections or the chosen PDF set. For the $t\bar{t}V$ samples an overall uncertainty on the expected rates of 30% is set.

Theory uncertainties on signal samples

The cross section uncertainty of signal models is extracted varying the factorization scale, the renormalization scale and the PDF sets [281]. ISR is also an important source of uncertainty for signal models, specially on models with compressed mass spectrum where the overall uncertainty can be as large a 25%. These uncertainties are estimated varying by a factor of two the parameters related to the renormalization scale, factorization scale, initial state radiation scale, QCD radiation scale and jet matching scale in MADGRAPH and PYTHIA.

7.8 Combined fit configuration

In Chapter 5 an overview of the profile likelihood method was presented. In this chapter, further details related to the specific 13 TeV analysis are added. All background and signal information, its uncertainties, normalization factors and observed data are included in the fit setup using the following objects:

- **Probability Density Functions:** Simulations of signal and background processes are described by PDFs in different regions, which are technically included as a collection of histograms where the bin content is taken as a counting experiment.
- **Free parameters** The contributions of the main backgrounds as well as signal components in the different regions, can be adjusted by free normalization parameters called mu_top, mu_W and mu_SIG respectively, where mu_X = 1 defines the corresponding nominal value for process X.
- **Nuisance parameters** Systematic uncertainties and statistical uncertainties related to the limited amount MC events are added to the fit as *nuisance* parameters. These parameters allow for fluctuations of the central value (changing normalization and shapes) and variations of the widths of the distributions (changing the uncertainty estimate). Systematic uncertainties are typically constrained by Gaussian PDFs and are labeled as alpha_X, where X denotes the specific uncertainty. The value alpha_X = 0 corresponds to the nominal value of the related systematic. The width of the Gaussian is given by Δalpha_X, where Δalpha_X = 1 corresponds to the 1σ shift before fit. In the same manner, the uncertainty related to limited MC statistics is constrained by Poisson functions and are labeled as gamma_X.

With these objects a likelihood function is built for every background-only fit, consisting in the product of the Poisson PDFs for every region entering the fit including systematic

uncertainties constraints. As the hard lepton SRs are not orthogonal to each other, they are not fitted together and one fit configuration is defined per SR, including its associated control and validation regions. Thus, the systematic uncertainties parameters are only correlated between regions within the same fit configuration and not between all available regions. Due to the low event yields in the diverse regions, the fit configurations are kept simple with only one bin per region. The latter translates into including one bin per signal region plus one bin for each of the two CRs plus one bin for each of the two VR associated to the SR.

The fit to data maximizes the likelihood function by adjusting simultaneously the central value and uncertainty bands of the normalization and nuisance parameters to their optimal value. If the fit is minimally constrained, usually the free parameters are adjusted, normalizing the main backgrounds to fit data, while the nuisance parameters only propagate the uncertainties. On the other hand, if the fit is over constrained, the values and widths of the nuisance parameters are also adjusted to fit data. As the main background parameters are constrained by the fit to data in CRs with enough statistics, the impact of the related uncertainties in the SRs with is reduced, despite the reduced statistics. This method of adjusting the size of systematic uncertainties is usually called profiling.

To generate model independent limits, the fit configuration is similar. Only one fit is performed for each set of regions related to one SR and the uncertainty parameters are correlated between all the regions of each set. Signal and control regions are used to constrain the background. Signal contamination in the CRs is neglected, making the background estimate in the SRs rather conservative. With this setup the null hypothesis is tested in the SRs, the number of signal events in the SRs is fitted using the mu_SIG parameter in the fit. In the case of model dependent fit, where a signal sample is added, the normalization parameter of the signal sample is the same in all regions. The expected signal plus BG events is fit to data in both control and signal regions. Signal events in CRs are taken into account, including the predicted signal yields in all regions.

The treatment of systematic uncertainties should depends on the nature of the uncertainty and its desired desired interpretation. The HistFitter framework allows to include systematics of different natures. The nuisance parameters types chosen in HistFitter including a brief description and some of the main uncertainties for each type are given below.

- **OverallSys:** Consists in a global scaling factor that only changes the normalization of the distribution without changing its shape. In the software it is built as a Gaussian constrain of mean $(1 \pm \alpha)$ and width σE, where α and σ correspond to fit parameters while the input uncertainty is E. Uncertainties on signal cross sections are taken as OverallSys only for the signal components in all regions. Also luminosity uncertainty of 9% is taken as OverallSys in all regions. Theoretical uncertainties are also taken as OverallSys.

- **overallNormHistoSys:** Uses two additional histograms for each nominal histogram containing the distributions after applying the upward and downward variation of a systematic uncertainty. For this interpretation, the up and down histograms are normalized to the nominal histogram in the control regions, allowing only for a shape variation, and transforming the uncertainty on the number of events to an uncertainty on the the transfer factor. After normalization, the global normalization uncertainty is handled with an OverallSys. Experimental uncertainties such as JES, lepton identification, lepton energy scale and resolution and some of the E_T^{miss} soft term uncertainties are treated as shape variations using overallNormHistoSys.

- **overallNormHistoSysOneSide:** The treatment is similar to overallNormHistoSys, but only one additional histogram containing the distribution obtained with a

one sided variation of the systematic. The JER uncertainty is typically treated as a shape variation induced only by an up variation of JER using the overallNormHistoSysOneSide type. Also some of the E_T^{miss} soft term uncertainties are treated as overallNormHistoSysOneSide.

- **MCStatError:** Built as a poisson error with mean γ_i and width σ_i assigned for the sum of all samples per bin. No correlations among bins are assumed. It is only used on bins where σ_i is above 5%. Monte Carlo statistical uncertainty arising from limited MC events are treated as MCStatError.

7.9 Results and interpretation

The results of the various fits and its interpretations are presented in this section. The first results presented are the background-only fit results, where the normalization factors for the main backgrounds and the background estimates in all regions are obtained. Then the discovery fit results are presented obtaining model-independent upper limits consistent with data. Finally the exclusion fit results are presented, resulting in model dependent exclusion limits that extends significantly previous searches limits obtained in LHC Run 1 [48, 49].

7.9.1 Background-only fit results

In the background-only fit, the likelihood functions are maximized by adjusting normalization and nuisance parameters. The event yields before and after the background fit in the control regions for the hard lepton analysis are presented in table 7.13. The first row in the tables displays the observed data in the respective region (represented in columns). The second row shows the sum of all estimated background yields after the fit. From the third to the eighth rows, the estimate after fit is presented for each background process. The ninth row shows for comparison the total before fit MC yields normalized to MC cross-sections while from the tenth to fifteenth rows the MC yields before fit are presented by process. Soft lepton yields are included for completion in Appendix C in tables C.9 and C.12. As it can be seen on the tables, in general the MC generators predicted higher rates in the control regions than what is observed in data. Therefore, the normalization factors of the main backgrounds are usually less than one to reduce MC rates to match data. The fitted values for the normalization factors are presented in table 7.12.

Region	mu_top	mu_W
4-jet low-x	$0.52^{+0.38}_{-0.32}$	$0.98^{+0.34}_{-0.32}$
4-jet high-x	$0.34^{+0.28}_{-0.25}$	$1.04^{+0.32}_{-0.31}$
5-jet	$0.65^{+0.23}_{-0.22}$	$0.76^{+0.29}_{-0.26}$
6-jet	$0.82^{+0.19}_{-0.16}$	$0.72^{+0.31}_{-0.33}$
2-jet soft	$0.72^{+0.29}_{-0.26}$	$1.00^{+0.04}_{-0.04}$
5-jet soft	$0.92^{+0.14}_{-0.12}$	$0.69^{+0.20}_{-0.19}$

Table 7.12: Normalization factors and their total uncertainty after the background-only fits.

Some of the transfer factors are considerably smaller than one, presenting also large uncertainties. Such behavior was already observed in the previous 8 TeV one lepton analysis

[48] in regions defined with similar tight cuts.

Regions	4-jet low-x TR	4-jet low-x WR	4-jet high-x TR	4-jet high-x WR
Observed events	15	33	32	44
Fitted bkg events	15.01 ± 3.89	32.97 ± 5.83	32.03 ± 5.63	43.94 ± 6.69
Fitted ttbar events	7.81 ± 5.09	2.12 ± 1.65	12.17 ± 9.40	1.70 ± 1.57
Fitted wjets events	3.84 ± 1.59	22.69 ± 7.19	11.22 ± 4.25	31.13 ± 8.70
Fitted zjets events	0.14 ± 0.10	0.19 ± 0.09	0.15 ± 0.07	0.23 ± 0.10
Fitted singletop events	2.82 ± 2.34	1.51 ± 1.29	6.97 ± 5.63	1.81 ± 1.55
Fitted diboson events	$0.08^{+0.49}_{-0.08}$	6.40 ± 2.79	$0.94^{+1.06}_{-0.94}$	8.99 ± 4.34
Fitted ttv events	0.31 ± 0.10	0.06 ± 0.03	0.59 ± 0.19	0.09 ± 0.04
MC exp. SM events	22.31 ± 3.24	35.30 ± 4.43	55.52 ± 6.84	46.06 ± 6.23
MC exp. ttbar events	15.05 ± 1.42	4.08 ± 0.97	36.11 ± 2.34	5.05 ± 1.74
MC exp. wjets events	3.91 ± 0.70	23.07 ± 1.69	10.78 ± 1.60	29.93 ± 2.34
MC exp. zjets events	0.14 ± 0.10	0.19 ± 0.09	0.15 ± 0.07	0.23 ± 0.10
MC exp. singletop events	2.82 ± 2.34	1.50 ± 1.29	6.95 ± 5.62	1.80 ± 1.55
MC exp. diboson events	$0.08^{+0.49}_{-0.08}$	6.40 ± 2.78	$0.95^{+1.06}_{-0.95}$	8.97 ± 4.32
MC exp. ttv events	0.31 ± 0.10	0.05 ± 0.03	0.59 ± 0.19	0.09 ± 0.04

Regions	5-jet TR	5-jet WR	6-jet TR	6-jet WR
Observed events	46	36	71	34
Fitted bkg events	46.12 ± 6.79	35.97 ± 6.07	71.06 ± 8.46	34.13 ± 5.94
Fitted ttbar events	29.81 ± 9.85	4.89 ± 2.49	54.35 ± 11.01	6.70 ± 2.67
Fitted wjets events	7.35 ± 3.02	21.89 ± 7.34	6.41 ± 3.14	18.67 ± 8.00
Fitted zjets events	0.17 ± 0.09	0.22 ± 0.07	0.06 ± 0.03	0.14 ± 0.06
Fitted singletop events	6.64 ± 5.40	1.58 ± 1.38	6.27 ± 5.24	1.28 ± 1.10
Fitted diboson events	1.51 ± 1.40	7.32 ± 1.95	3.21 ± 1.77	7.26 ± 3.46
Fitted ttv events	0.63 ± 0.21	0.06 ± 0.03	0.76 ± 0.25	0.07 ± 0.04
MC exp. SM events	64.37 ± 6.78	45.29 ± 4.83	85.54 ± 6.82	43.03 ± 5.87
MC exp. ttbar events	45.77 ± 2.57	7.43 ± 2.11	66.36 ± 3.22	8.24 ± 2.40
MC exp. wjets events	9.70 ± 1.17	28.73 ± 1.97	8.89 ± 1.17	25.97 ± 1.92
MC exp. zjets events	0.17 ± 0.09	0.22 ± 0.07	0.06 ± 0.03	0.14 ± 0.06
MC exp. singletop events	6.59 ± 5.38	1.55 ± 1.35	6.26 ± 5.24	1.28 ± 1.10
MC exp. diboson events	1.51 ± 1.40	7.29 ± 1.94	3.21 ± 1.77	7.32 ± 3.50
MC exp. ttv events	0.63 ± 0.21	0.06 ± 0.03	0.76 ± 0.25	0.07 ± 0.04

Table 7.13: Background fit combined $e + \mu$ results for the 4-jet CRs on top and for the 5 and 6 jet CRs on bottom. MC expectations normalized to MC cross-section are also shown for before/after fit comparison. Non symmetric errors appear only from truncating the negative error to zero to avoid negative yields. The error on the expected values include all systematic uncertainties.

Among the possible reasons for the higher MC rates, generator limitations in such extreme space phases and miss-modeling of kinematics distributions for $t\bar{t}$ samples are the main contributors. The miss-modeling of the hardest jet p_t in $t\bar{t}$ samples is found already in looser regions. As observed in the top left plot in figure 7.4, there is a clear slope in the $p_T^{jet_1}$ distribution where more events are simulated for higher p_T. Similar miss-modeling were found previously when analyzing the 8 TeV results where a slope was found on m_{eff}^{incl} in $t\bar{t}$

dominated regions. For the 8 TeV analysis few data driven $t\bar{t}$ re-weighting methods were tested, nevertheless as the slope fitted well within the total uncertainty band, it was decided not to apply any of the corrections. For the 13 TeV analysis the mismatch is again statistically compatible with the differential cross section measurements obtained by ATLAS for these processes [282–285]. Nevertheless, a truth based re-weighting procedure for the top p_t miss-modeling was studied and is presented in Appendix C in section C.3. This opportunity the re-weighting was not included in the official paper neither in the following results, mainly because results are statistically compatible and because it was performed during and after presenting and publishing the official one lepton 2015 results.

Besides the normalization factors, the nuisance parameters are also adjusted to find the best fit. The resulting fit parameters for the hard lepton analysis including nuisance parameters and the already shown normalization factors are presented in Appendix C from table C.1 to table C.7. The fits results for the soft lepton analysis are presented in tables C.10 and C.13.

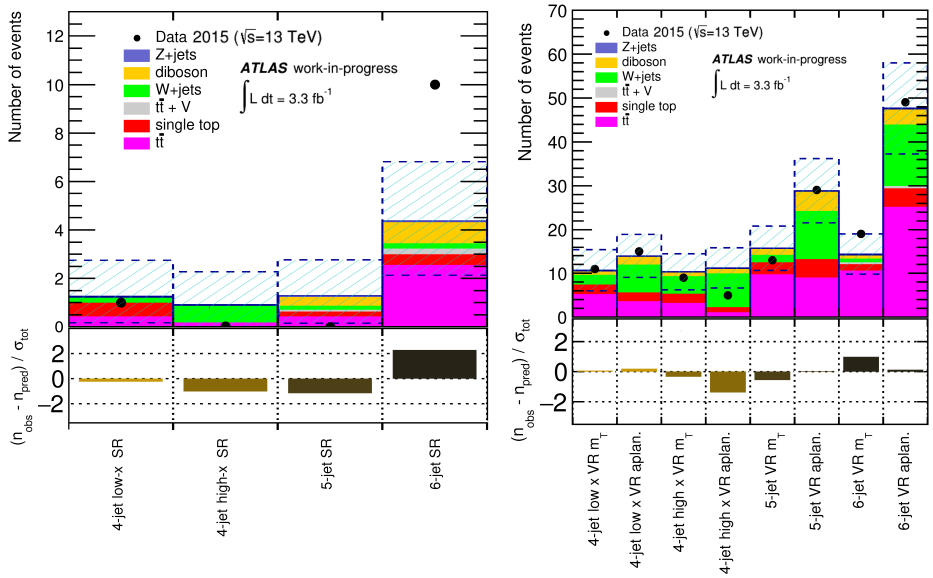

Figure 7.15: Extrapolation to Signal (left) and Validation (right) regions. The top panels shows the expected background yields obtained after the background-only fit in all hard lepton regions together with observed data. Uncertainties on the fitted background estimates include all systematic uncertainties. The bottom panels show the differences between observed and predicted event yields, divided by the total statistical and systematic uncertainty on the prediction

Each fit also introduces correlations between the normalization and nuisance parameters and thus the uncertainty in the total expected background may be smaller or larger than the individual uncertainties added in quadrature. The correlation matrices for the background-only fits are presented from figure C.17 to C.20 for the hard lepton analysis, showing healthy fits with no problematic large correlations. For the soft lepton analysis the correlation matrices are presented for completion in figures C.21 and C.22.

The background-only fit results are extrapolated using the transfer factors to validation and signal regions. The event yields before and after the background fit in all signal and validation regions for the hard lepton analysis are presented in tables 7.14 and 7.15. These results are summarized in the left plot on figure 7.15 for SRs and on the right plot for VRs.

Many of the systematic uncertainties affect the background estimates in the signal regions as already mentioned. The influence of the dominant systematic uncertainties and the final

Regions	4-jet low-x VR m_T	4-jet low-x VR aplanarity	4-jet high-x VR m_T	4-jet high x VR m_{eff}
Observed events	11	15	9	5
Fitted bkg events	10.66 ± 3.37	13.97 ± 3.13	10.33 ± 2.55	11.20 ± 3.16
Fitted ttbar events	5.10 ± 3.70	3.47 ± 2.39	3.14 ± 2.55	1.01 ± 0.82
Fitted wjets events	2.28 ± 1.08	6.27 ± 2.61	4.00 ± 1.73	7.65 ± 3.23
Fitted zjets events	0.17 ± 0.10	0.05 ± 0.03	0.19 ± 0.11	0.05 ± 0.01
Fitted singletop events	1.99 ± 1.71	1.93 ± 1.53	1.85 ± 1.46	1.05 ± 0.86
Fitted diboson events	$0.92^{+0.96}_{-0.92}$	2.10 ± 1.38	0.94 ± 0.32	1.37 ± 1.05
Fitted ttv events	0.19 ± 0.07	0.16 ± 0.05	0.21 ± 0.07	0.07 ± 0.02
MC exp. SM events	15.43 ± 3.73	17.29 ± 3.03	16.34 ± 3.50	12.89 ± 2.71
MC exp. ttbar events	9.83 ± 2.90	6.69 ± 1.12	9.31 ± 2.25	3.00 ± 0.65
MC exp. wjets events	2.32 ± 0.67	6.37 ± 1.74	3.85 ± 1.06	7.35 ± 2.21
MC exp. zjets events	0.17 ± 0.10	0.05 ± 0.03	0.19 ± 0.11	0.05 ± 0.01
MC exp. singletop events	1.99 ± 1.71	1.93 ± 1.53	1.85 ± 1.46	1.05 ± 0.86
MC exp. diboson events	$0.93^{+0.96}_{-0.93}$	2.11 ± 1.38	0.94 ± 0.32	1.37 ± 1.06
MC exp. ttv events	0.19 ± 0.07	0.16 ± 0.05	0.21 ± 0.07	0.07 ± 0.02

Regions	5-jet VR m_t	5-jet VR aplan.	6-jet VR m_t	6-jet VR aplan.
Observed events	13	29	19	49
Fitted bkg events	15.72 ± 3.14	28.79 ± 5.00	14.34 ± 2.63	47.62 ± 7.81
Fitted ttbar events	9.66 ± 3.80	8.86 ± 3.66	10.49 ± 2.86	25.02 ± 6.71
Fitted wjets events	1.70 ± 1.25	10.94 ± 4.19	0.78 ± 0.43	14.06 ± 7.14
Fitted zjets events	$0.03^{+0.03}_{-0.03}$	$0.04^{+0.05}_{-0.04}$	0.05 ± 0.02	0.07 ± 0.06
Fitted singletop events	2.34 ± 1.87	3.96 ± 3.21	1.46 ± 1.22	4.22 ± 3.44
Fitted diboson events	1.62 ± 0.42	4.67 ± 1.68	1.12 ± 0.46	3.74 ± 2.04
Fitted ttv events	0.36 ± 0.12	0.33 ± 0.11	0.44 ± 0.15	0.51 ± 0.18
MC exp. SM events	21.39 ± 3.29	36.92 ± 5.75	16.99 ± 2.55	58.69 ± 7.73
MC exp. ttbar events	14.81 ± 2.33	13.58 ± 3.22	12.82 ± 2.11	30.59 ± 4.95
MC exp. wjets events	2.24 ± 1.36	14.38 ± 1.93	1.09 ± 0.40	19.53 ± 4.18
MC exp. zjets events	$0.03^{+0.03}_{-0.03}$	$0.04^{+0.05}_{-0.04}$	0.05 ± 0.02	0.07 ± 0.06
MC exp. singletop events	2.33 ± 1.86	3.92 ± 3.19	1.46 ± 1.22	4.20 ± 3.43
MC exp. diboson events	1.62 ± 0.42	4.66 ± 1.68	1.13 ± 0.46	3.77 ± 2.06
MC exp. ttv events	0.36 ± 0.12	0.33 ± 0.11	0.44 ± 0.15	0.52 ± 0.18

`Table 7.14:` Background fit combined $e + \mu$ results extrapolated to the 4-jet VRs on top and for the 5 and 6 jet VRs on bottom. MC expectations normalized to MC cross-section are also shown for before/after fit comparison. Non symmetric errors appear only from truncating the negative error to zero to avoid negative yields. The error on the expected values include all systematic uncertainties.

statistical uncertainty on the background estimates in the hard lepton signal regions are also presented in Appendix C from tables C.2 to C.8. The dominant systematic uncertainties on background estimates in the Soft lepton signal regions is presented in tables C.11 and C.14.

As it can be seen in figure 7.15 the results of the background only fit extrapolated to the validation and signal regions show good agreement between predicted and observed event yields in all regions. In the SRs, a mild $\sim 2\sigma$ excess is seen in the 6 jet SR where 10 events are observed while the fit predicts only 4.37 ± 1.01. Similar results were found for the 6 jet m_T

Regions	4-jet low-x SR	4-jet high-x SR	5-jet SR	6-jet SR
Observed events	1	0	0	10
Fitted bkg events	1.27 ± 0.50	0.92 ± 0.50	1.27 ± 0.55	4.37 ± 1.01
Fitted ttbar events	0.40 ± 0.31	0.08 ± 0.07	0.40 ± 0.24	2.52 ± 0.86
Fitted wjets events	0.19 ± 0.12	0.75 ± 0.49	0.16 ± 0.12	0.23 ± 0.16
Fitted zjets events	0.04 ± 0.02	0.03 ± 0.03	0.07 ± 0.03	$0.08^{+0.08}_{-0.08}$
Fitted singletop events	0.52 ± 0.45	$0.04^{+0.10}_{-0.04}$	$0.21^{+0.22}_{-0.21}$	0.44 ± 0.39
Fitted diboson events	$0.06^{+0.19}_{-0.06}$	$0.00^{+0.01}_{-0.00}$	0.37 ± 0.23	0.87 ± 0.52
Fitted ttv events	0.05 ± 0.02	0.02 ± 0.01	0.06 ± 0.03	0.23 ± 0.08
MC exp. SM events	1.64 ± 0.59	1.05 ± 0.48	1.53 ± 0.68	5.02 ± 1.10
noalign MC exp. ttbar events	0.77 ± 0.33	0.25 ± 0.10	0.61 ± 0.32	3.09 ± 0.83
MC exp. wjets events	0.19 ± 0.11	0.72 ± 0.42	0.22 ± 0.15	0.31 ± 0.15
MC exp. zjets events	0.04 ± 0.02	0.03 ± 0.03	0.07 ± 0.03	$0.08^{+0.08}_{-0.08}$
MC exp. singletop events	0.52 ± 0.45	$0.04^{+0.10}_{-0.04}$	$0.21^{+0.22}_{-0.21}$	0.44 ± 0.39
MC exp. diboson events	$0.06^{+0.19}_{-0.06}$	$0.00^{+0.01}_{-0.00}$	0.37 ± 0.23	0.87 ± 0.52
MC exp. ttv events	0.05 ± 0.02	0.02 ± 0.01	0.06 ± 0.03	0.23 ± 0.08

`Table 7.15:` Background fit combined $e + \mu$ results extrapolated to the 4-jet SRs on top and for the 5 and 6 jet SRs on bottom. MC expectations normalized to MC cross-section are also shown for before/after fit comparison. Non symmetric errors appear only from truncating the negative error to zero to avoid negative yields. The error on the expected values include all systematic uncertainties.

VR. Even though this excess is not significant, it was studied carefully. The excess might be only a statistical fluctuation, an artifact created by a poor understanding of the fit, or it might even be a hint for interesting physics. Different tests were made aiming to understand better the cause of the excess. The test included looking at electron and muon channels separately, studying kinematic distributions in the different regions, including looser variations of the 6 jet validation and signal regions to increase statistics. Additional tests were included checking for possible pile up dependency on SR acceptances and background estimates and testing one additional background process (ttH) which was proven to show negligible impact in the SR to cover for the low background yields. From the tests, it was observed that 8 from the 10 events in the SR were muons while the prediction was only up to 2.48 ± 0.74 events. The kinematic distributions showed that the excess appears in low lepton p_T and low E_T^{miss} regions, with a possible correlation in events with large angle between the lepton and E_T^{miss} ($\Delta\phi(\ell, E_T^{miss}) \sim \pi$). It was also noticed that in the 6 jet SR most data excess concentrated ins events with 3 b-jets. Unfortunately the statistics was rather low to make robust statements about the nature of the excess. However it was found that the $t\bar{t}$ kinematics controlled in the 6 jet TCR is not exactly the same as in the 6 jet SR. When looking at the $t\bar{t}$ sample composition, it was found that most $t\bar{t}$ events in the 6 jet TCR correspond to the semi-leptonic decay channel. The same channel is the dominant $t\bar{t}$ decay process present in the 6 jet VR Aplanarity. But the dominant $t\bar{t}$ decay channel present in the 6 jet SR and in the 6 jet VR m_T is the hadronic τ plus lepton decay followed by di-lepton decays. Additional and more detailed information on $t\bar{t}$ modeling in the different 6 jet regions and possible re-weighting procedures can be found in Appendix C.3. Despite the excess in the 6 jet SR, the overall pull distribution in the validation and signal regions shows that the observed discrepancies are consistent with statistical fluctuations and no significant tendency is observed in the plots.

7.9.2 Discovery fit results: Model independent upper limits

The discovery fit was used to obtain model-independent upper limits in all signal regions. In this setup, both SRs and CRs are used to constrain the background estimates. In table 7.16 the 95% confidence level (CL) upper limit on the visible cross-section ($\langle\epsilon\sigma\rangle^{95}_{\text{obs}}$) is presented in the first column. The observed and expected upper limits at 95% confidence level (CL) on the number of events beyond the SM and the background-only confidence level CL_b observed for the null hypothesis are also shown.

Signal region	$\langle\epsilon\sigma\rangle^{95}_{\text{obs}}$[fb]	S^{95}_{obs}	S^{95}_{exp}	CL_B
4-jet low-x	1.23	3.9	$4.1^{+1.5}_{-0.9}$	0.46
4-jet high-x	0.87	2.8	$2.9^{+1.3}_{-0.2}$	0.27
5-jet	0.87	2.8	$3.5^{+1.4}_{-0.7}$	0.19
6-jet	3.90	12.5	$6.5^{+2.6}_{-1.6}$	0.98
2-jet soft	1.33	4.3	$5.3^{+2.2}_{-1.3}$	0.23
5-jet soft	2.87	9.2	$8.1^{+2.9}_{-2.1}$	0.68

Table 7.16: Model independent upper limits: The first two columns shows the 95% confidence level (CL) upper limits on the visible cross section ($\langle\epsilon\sigma\rangle^{95}_{\text{obs}}$) and on the number of signal events (S^{95}_{obs}). The third column shows the 95% CL upper limit on the number of signal events given the expected number of background events (S^{95}_{exp}). The $\pm1\sigma$ on S^{95}_{exp} represents the uncertainty on expected events. The last column shows the two-sided CL_B value representing the confidence level observed for the background-only hypothesis.

As it can be seen on the table, the number of excluded non standard model events agrees quite well with the expected limits on the number of non standard model events within uncertainties. The larger discrepancy is found on the hard-lepton 6-jet SR, where due to the the mild excess of data presented in table 7.15 a stringent limit on the number of non standard model events compared to the expected value is observed. Due to the low background expectation on this region, the bound on the visible cross sections is the highest, rising up to 3.9 fb.

7.9.3 Exclusion fit results: Model dependent limits

For this fit configuration, an additional signal sample is included into the fit in all regions, introducing a non negative signal normalization factor μ_{sig} as the signal strength parameter. Both SRs and CRs are used to constrain all likelihood parameters. The fits must run once for each of the SUSY points in the two (x-free and $x = 1/2$) two dimensional parameter grids defined in section 7.1.3. For each of the points, the 95% CL exclusion limits is obtained. In Figure 7.16, the nominal 95% CL expected and observed exclusion limits, is presented in both parameter planes for all the relevant signal regions. In both plots the complementary nature of the SRs is clearly observed, the SRs were designed to cover different regions of the parameter space. The mild excess presented in the 6-jet SR traduces in a reduced observed exclusion power. The previous combined observed exclusion limit found for Run-1 [48] is shown as a gray area. It can also be seen in the bottom plot representing the $x - free$ grid, that while the 4-jet lox- and high-x SRs help improving the exclusion reach in the extreme x cases, the 5-jet SR extends the exclusion reach in the middle zone.

Figure 7.17 shows the combined 95% CL exclusion limits in both planes compared to the

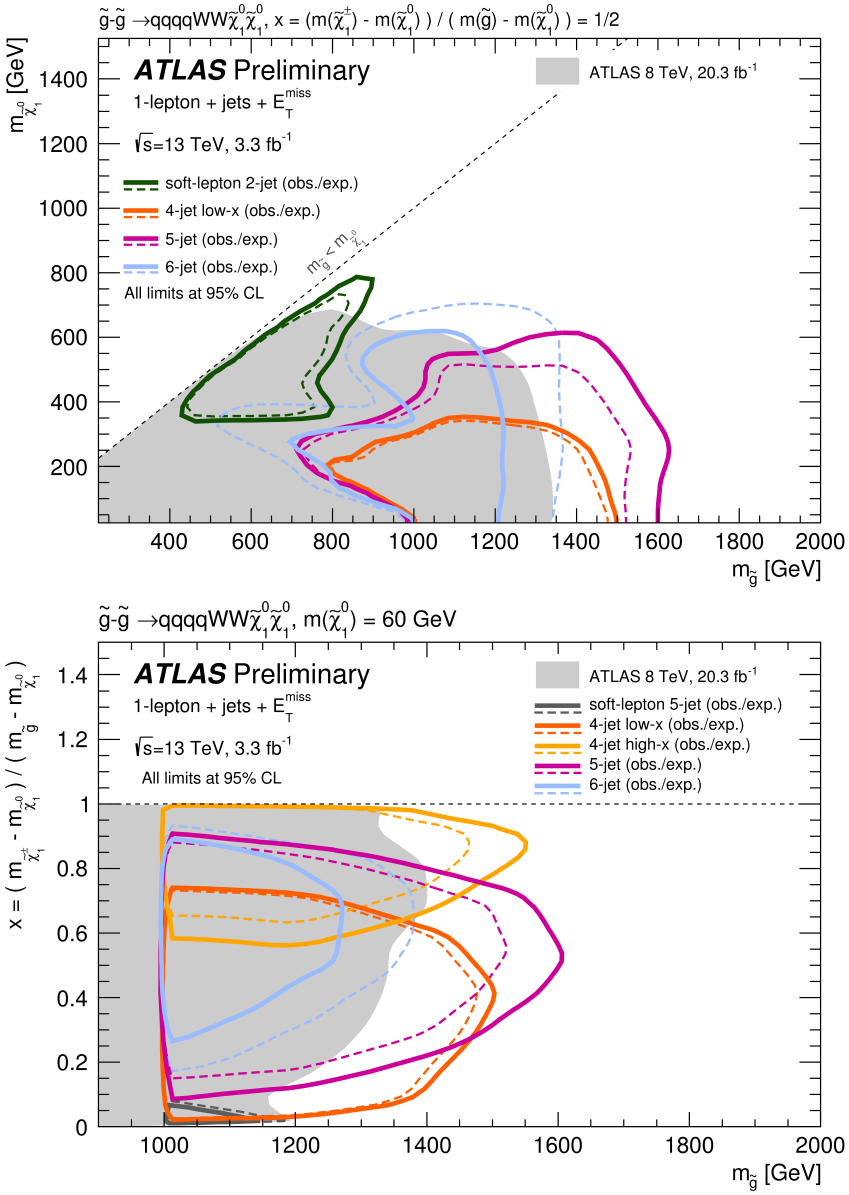

Figure 7.16: Summary exclusion limits for the signal regions in the gluino one step grids, with $x = 1/2$ on the top and free-x at the bottom [286].

previous Run-1 observed limits. For each model point the SR with the best expected sensitivity is taken. It is seen in the top plot that for large $\Delta(m_{\tilde{g}}, m_{\tilde{\chi}_1^0})$, gluino masses of up to 1.6 TeV can be excluded, while for compressed scenarios with smaller $\Delta(m_{\tilde{g}}, m_{\tilde{\chi}_1^0})$, gluino masses of up to 870 GeV can be excluded. In the bottom plot, gluino masses of up to 1.6 TeV can be excluded in the middle-x region which is consistent with the limits found in the $x = 1/2$ grid. For lox-x scenarios, gluino masses between 1.2 and 1.4 TeV can be excluded depending on the gluino-chargino mass difference, while for high-x scenarios gluino masses above 1.3 or 1.5 TeV can be excluded depending on the mass difference.

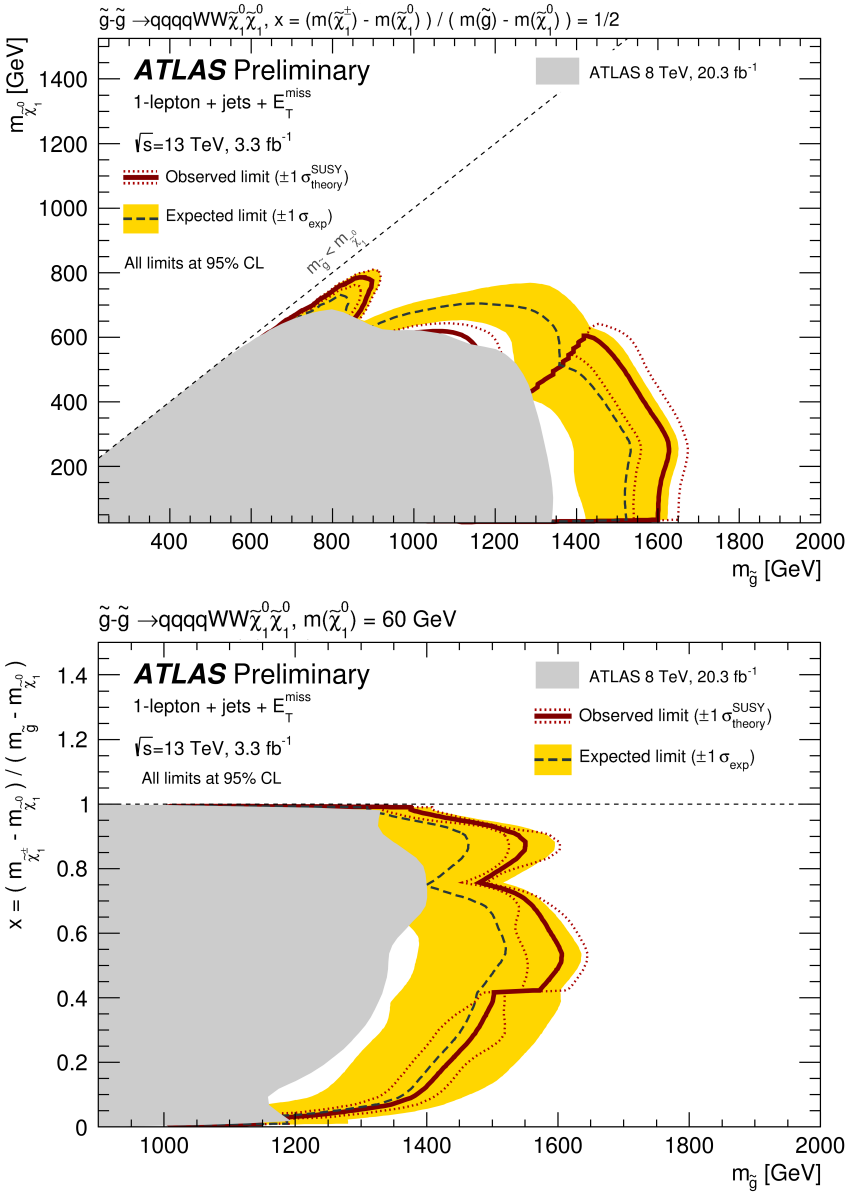

Figure 7.17: Combined exclusion limits in the simplified gluino pair production grids, with x fixed to 1/2 on the top and floating x on the bottom. The red solid line represents the observed limit where its 1σ variation from scale and PDF uncertainties in the signal cross section is represented by the red dotted lines. The gray dashed line with the yellow band represents the expected limit with a 1σ variation of the median expected limit from experimental and theoretical uncertainties. For reference the previous combined observed exclusion limit found for Run-1 [48] is shown as agray area [286].

7.10 Summary

Through this chapter a search for gluinos decaying to final states containing one electron or muon, multiple jets and large missing transverse momentum was presented. The analysis was optimized for 3 fb^{-1} of Run-II data, and ended up using the 3.3 fb^{-1} of 13 TeV data collected by ATLAS during 2015 with 25 ns bunch spacing. Four hard-lepton plus two soft-lepton signal

regions were defined by lepton p_T and jet multiplicity, ranging from two to six jets, aiming to cover a a wider parameter space region. The hard-lepton regions are built to target models with large mass differences while soft-lepton regions aim at to models with compressed mass spectrum. Additionally, the regions require rather tight cuts on the E_T^{miss}, m_T and m_{eff} to be able to suppress the main background processes ($t\bar{t}$ and $W + jets$) enhancing the discovery sensitivity to regions beyond Run-1 exclusion limits.

The two main backgrounds were estimated in the SR using a simultaneous MC fit to data in specialized control regions. For each of the SRs two CRs were defined, relaxing the E_T^{miss}, m_T and m_{eff} cuts. The extrapolation from control to signal regions was validated in validation regions defined between control and signal regions.

Overall an agreement between observed data and standard model background predictions in the signal regions was observed, with the largest deviations being up to 2 σ in the hard-lepton 6-jet SR. The excess found was studied and possible improvement for future analyses was developed and presented in Appendix C.3. Limits on the visible cross-section were derived for beyond SM models in all SRs. Exclusion limits on specific simplified SUSY models with gluino production and one step decays were evaluated. With these limits, gluino masses below 1.6 TeV can be excluded for low neutralino masses, extending significantly the limits placed by similar Run-1 previous searches [48].

Chapter 8

Summary and Outlook

This document presented the search for Supersymmetry in the one lepton plus jets plus missing transverse energy, using a total integrated luminosity of 3.3 fb^{-1} recorded with the ATLAS experiment, corresponding to the full 2015 dataset of proton-proton collisions with a center of mass energy of $\sqrt{s} = 13$ TeV. The document also presents a reinterpretation of the one lepton analysis results with the full 2012 $\sqrt{s} = 8$ TeV dataset within pMSSM signal scenarios.

Both analyses rely on the events found in statistically independent control validation and signal regions. Control regions are built to control the dominant $t\bar{t}$ and $W + jets$ Standard Model backgrounds. Signal regions are used to probe for possible supersymmetric events. For the 13 TeV analysis, the SRs were optimized to search for one step simplified models of gluino pair production decaying to the neutralino LSP via the lightest chargino. Validation regions are used for validation purposes. The analyses are based on a simultaneous fit to data, where the main backgrounds estimates are normalized in the control regions using a profile likelihood method. This estimates are extrapolated to the SRs for precise background estimates in the statistically lower signal regions.

The reinterpretation of the 8 TeV analysis tested its sensitivity to a large set of randomly distributed pMSSM points. A first fast comparison at particle (*truth*) level, showed that the one lepton analysis displays rather low sensitivities to a large set of pMSSM points, where the hardest discriminator was found to be mainly the one lepton cut requirement. This leads directly to low content of events with hard leptons in the final states of the models. The results were combined with the results of many other SUSY searches to cover a vast region of the phase space. They were presented as the fraction of excluded models after imposing ATLAS Run 1 limits in bins of two dimensional histograms of relevant SUSY parameters such as LSP and gluino masses. It was shown that exclusion limits for simplified models should be carefully interpreted, as kinematically richer models are not always constrained by the same results. Additionally, the combination of different analysis showed to be crucial to restrict more general SUSY scenarios, showing the importance of the complementarity of ATLAS searches. It was also observed that ATLAS searches are more powerful to constraint strongly interacting sparticles than for electroweakinos and sleptons. The ATLAS constraints to strong pMSSM production showed that 100% of the models with gluino masses below 700 GeV were excluded. All the models with neutralino LSP mass below 500 GeV and gluino mass below 1 TeV were able to excluded. In the squark sector, the models containing light squarks below 250 GeV were always excluded. From the models that could not be excluded by any of the ATLAS analysis, a selection of models with enough lepton content was analyzed. It was shown that the signatures for most of the models included leptons from non-dominant processes, making this models not the best target for one lepton searches. This analysis showed the importance of searching beyond simplified models, including more realistic scenarios. It also pinpointed

the impact of combining different searches to cover for wider regions of the phase space. A first reinterpretation of the early 13 TeV supersymmetry searches within the pMSSM can be found in [289], where 15.7% of the models that could not be excluded by Run-1 searches, were found to be excluded at 95% confidence level by Run-2 analyses.

The search for Supersymmetry in the one lepton plus jets plus missing transverse energy final state using the full 2015 13 TeV dataset, was optimized for gluino pair production simplified models decaying to a neutralino LSP in one step step via the lightest chargino. The hard lepton analysis was combined with an independent soft lepton analysis to cover for different kinematic regions of the phase space. The hard lepton analysis searches for events with large lepton p_T, aiming for models with large mass differences between the produced gluino and the LSP. The soft lepton analysis searches for soft leptons instead, aiming for models with compressed mass spectrum. The results showed that in all signal regions, the observed data was consistent with the Standard Model prediction. With these results, model independent and model dependent exclusion limits were set. Exclusion limits on the simplified models showed that gluino masses below 1.6 TeV can be excluded for low neutralino masses, extending the previous limits placed by previous searches. On the other hand, the largest deviation found between data and simulation was a 2σ excess in the hard 1 lepton 6-jet signal region. When normalizing the main background in the control regions it was found that the MC predictions are higher than for data, making the normalization factors for $t\bar{t}$ rather low. Besides a possible miss-modeling of $t\bar{t}$ sample was studied and it was concluded that it is crucial to have more precise way to estimate $t\bar{t}$ distributions and its uncertainties in all regions. Possible solutions include the evaluation of NNLO QCD contributions in the simulations, binning control and signal regions (if having enough data) to cover for possible distribution dependent transfer factors, or carefully performing re-weighting of the samples before normalizing. In a more recent one lepton analysis using 36.1 fb^{-1} of 13 TeV collisions [290] some of these issues were tackled dividing the signal regions in multiple m_{eff} bins. The same binning is done in the control regions, such tat every signal region bin has a corresponding control region with the same m_{eff} requirements, estimating the backgrounds independently in each bin. This can be done thanks to the increased integrated luminosity resulting in more events and less stringent statistics conditions. The new results showed also that events in the SRs are consistent with SM expectations, extending the observed exclusion limits presented in this thesis for gluino masses up to ~ 2 TeV for low neutralino LSP, reaching to gluino masses up to 2.1 TeV. The exclusion plots in the same mass plane for gluino pair production simplified model is presented in figure 8.1.

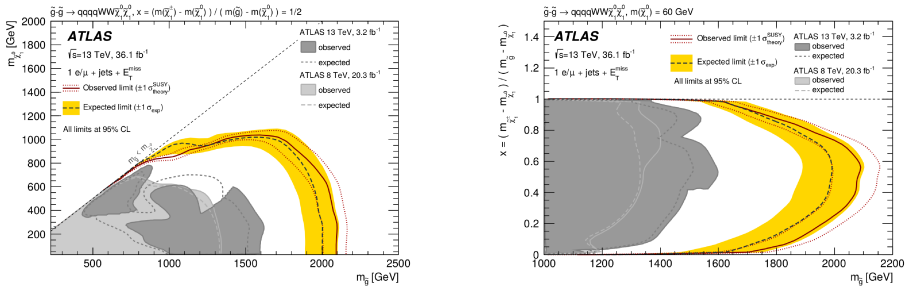

Figure 8.1: Exclusion contours for gluino one-step simplified models in the $x = 1/2$ (left) and $free - x$ (right) 2D planes. The red solid line represents the observed limit where its 1σ variation from scale and PDF uncertainties in the signal cross section is represented by the red dotted lines. The gray dashed line with the yellow band represents the expected limit with a 1σ variation from experimental and theoretical uncertainties. For reference, the exclusion limits presented in the official paper [244] for the full 2015 dataset analyzed in this thesis is presented as a dark gray area [290].

Appendix A

Supersymmetry mass eigenstates

A.1 The Higgs Sector

The Higgs potential including quartic interactions is given by:

$$\begin{aligned} V &= (m_1^2+|\mu|^2)H_1^{i\,*}H_1^i + (m_2^2+|\mu|^2)H_2^{i\,*}H_2^i - m_{12}^2(H_1^1H_2^2 - H_1^2H_2^1 + cc) \\ &+ \frac{1}{8}(g^2+g'^2)(H_1^{i\,*}H_1^i - H_2^{j\,*}H_2^j)^2 + \frac{1}{2}g^2|H_1^{1\,*}H_2^1 + H_1^{2\,*}H_2^2|^2 \end{aligned} \tag{A.1}$$

where:

$$H_1 = \begin{pmatrix} H_1^0 \\ H_1^- \end{pmatrix} \quad H_2 = \begin{pmatrix} H_2^+ \\ H_2^0 \end{pmatrix} \tag{A.2}$$

The following derivation is made in analogy to what was done for the SM case. The condition for EWSB is that the potential has the mexican hat shape so the fields acquire a vacuum expectation value. This condition is:

$$\frac{\partial V}{\partial H_1^1}\Big|_{\langle H_1\rangle} = \frac{\partial V}{\partial H_2^2}\Big|_{\langle H_2\rangle} = 0 \tag{A.3}$$

performing the derivatives in the same way it was done for the SM in eq. 1.20, the tadpole equations are found:

$$m_1^2 + |\mu|^2 - m_{12}^2\tan\beta + \left(\frac{m_Z^2}{2}\right)\cos 2\beta = 0 \tag{A.4}$$

$$m_2^2 + |\mu|^2 - m_{12}^2\cot\beta - \left(\frac{m_Z^2}{2}\right)\cos 2\beta = 0 \tag{A.5}$$

The fields can be expanded around the minimum:

$$H_1 = \begin{pmatrix} v_1 + \frac{1}{\sqrt{2}}(h_1 + i\psi_1) \\ H_1^- \end{pmatrix} \quad H_2 = \begin{pmatrix} H_2^+ \\ v_2 + \frac{1}{\sqrt{2}}(h_2 + i\psi_2) \end{pmatrix} \tag{A.6}$$

Replacing A.6 in A.1, using the tadpole equations, and looking at the quadratic terms, the potential has the form:

$$V = (h_1\ h_2)\,\mathcal{M}_{H^0}^2\begin{pmatrix} h_1 \\ h_2 \end{pmatrix} + (\psi_1\ \psi_2)\,\mathcal{M}_{\psi}^2\begin{pmatrix} \psi_1 \\ \psi_2 \end{pmatrix} + \left(H_2^{+*}\ H_1^-\right)\mathcal{M}_{H^\pm}^2\begin{pmatrix} H_2^+ \\ H_1^{-*} \end{pmatrix} \tag{A.7}$$

where:

$$\mathcal{M}_{H^0}^2 = \begin{pmatrix} \frac{m_1^2}{2} + \frac{|\mu|^2}{2} + \frac{1}{8}(g^2+g'^2)(3v_1^2 - v_2^2) & -\frac{1}{4}(g^2+g'^2)v_1v_2 - \frac{m_{12}^2}{2} \\ -\frac{1}{4}(g^2+g'^2)v_1v_2 - \frac{m_{12}^2}{2} & \frac{m_2^2}{2} + \frac{|\mu|^2}{2} + \frac{1}{8}(g^2+g'^2)(3v_2^2 - v_1^2) \end{pmatrix}$$

$$\mathcal{M}^2_\psi = \begin{pmatrix} \frac{m_1^2}{2} + \frac{|\mu|^2}{2} + \frac{1}{8}(g^2+g'^2)(v_1^2-v_2^2) & \frac{m_{12}^2}{2} \\ \frac{m_{12}^2}{2} & \frac{m_2^2}{2} + \frac{|\mu|^2}{2} + \frac{1}{8}(g^2+g'^2)(v_2^2-v_1^2) \end{pmatrix}$$

$$\mathcal{M}^2_{H^\pm} = \begin{pmatrix} m_2^2 + |\mu|^2 + \frac{1}{4}(g^2+g'^2)(v_2^2-v_1^2) + \frac{1}{2}g^2v_1^2 & \frac{1}{2}g^2v_1v_2 + m_{12}^2 \\ \frac{1}{2}g^2v_1v_2 + m_{12}^2 & m_1^2 + |\mu|^2 + \frac{1}{4}(g^2+g'^2)(v_1^2-v_2^2) + \frac{1}{2}g^2v_2^2 \end{pmatrix}$$

These matrices are clearly not diagonal. To find mass eigenstates a redefinition must be done using unitary matrices. The pseudo-scalar and the charged sector can be rotated with the same rotation matrix:

$$\mathcal{R}_{\theta_\psi}\mathcal{M}^2_\psi\mathcal{R}^T_{\theta_\psi} = \begin{pmatrix} \frac{1}{2}m^2_{G^0} & 0 \\ 0 & \frac{1}{2}m^2_{A^0} \end{pmatrix} \qquad \mathcal{R}_{\theta_{H^\pm}}\mathcal{M}^2_{H^\pm}\mathcal{R}^T_{\theta_{H^\pm}} = \begin{pmatrix} \frac{1}{2}m^2_{G^\pm} & 0 \\ 0 & \frac{1}{2}m^2_{H^\pm} \end{pmatrix}$$

Where $\theta_\psi = \theta_{H^\pm} = \beta$, and $\tan\beta \equiv v_2/v_1$. Such rotation also implies that:

$$m^2_{G^0} = 0 \tag{A.8}$$

$$m^2_{G^\pm} = 0 \tag{A.9}$$

$$m^2_{A^0} = \frac{2m_{12}^2}{\sin 2\beta} \tag{A.10}$$

$$m^2_{H^\pm} = m_A^2 + m_W^2 \tag{A.11}$$

For the case of the neutral Higgs fields another matrix is needed for diagonalization:

$$\mathcal{R}_{\theta_{H^0}}\mathcal{M}^2_{H^0}\mathcal{R}^T_{\theta_{H^0}} = \begin{pmatrix} \frac{1}{2}m^2_{h^0} & 0 \\ 0 & \frac{1}{2}m^2_{H^0} \end{pmatrix}, \tag{A.12}$$

where:

$$m^2_{h^0,H^0} = \frac{1}{2}\left(m_A^2 + m_Z^2 \pm \sqrt{(m_A^2+m_Z^2)^2 - 4m_A^2m_Z^2\cos^2 2\beta}\right) \tag{A.13}$$

and the mixing angle $\theta_{H^0} = \alpha$, that is given by:

$$\frac{\tan 2\alpha}{\tan 2\beta} = \frac{m_Z^2 + m_A^2}{m_Z^2 - m_A^2} \tag{A.14}$$

From the eight degrees of freedom, three are three Goldstone bosons that can be absorbed to give mass to the $W^\pm$ and Z boson while the remaining five will correspond to real massive particles: Two neutral higgs bosons h and H, two charged higgs bosons $H^\pm$ plus one pseudo-scalar neutral higgs boson A^0.

A.2 The squark sector

In principle 6×6 matrices corresponding to the $(\tilde{q}^i_L, \tilde{q}^i_R)$ basis should be diagonalized, where $i = 1,2,3$ labels the three families. Using only third generation notation the matrices can be written as:

$$M^2_{\tilde{t}} = \begin{bmatrix} M^2_{\tilde{Q}} + m_t^2 + m_Z^2(\frac{1}{2} - e_u s_W^2)\cos 2\beta & m_t(A_t - \mu\cot\beta) \\ m_t(A_t - \mu\cot\beta) & M^2_{\tilde{U}} + m_t^2 + m_Z^2 e_u s_W^2\cos 2\beta \end{bmatrix} \tag{A.15}$$

$$M^2_{\tilde{b}} = \begin{bmatrix} M^2_{\tilde{Q}} + m_b^2 + m_Z^2(\frac{1}{2} - e_d s_W^2)\cos 2\beta & m_b(A_b - \mu\tan\beta) \\ m_b(A_b - \mu\tan\beta) & M^2_{\tilde{D}} + m_b^2 + m_Z^2 e_d s_W^2\cos 2\beta \end{bmatrix} \tag{A.16}$$

where $e_u = 2/3, e_d = -1/3$. The terms in the diagonal are governed by the square of the squark mass parameters $M_{\tilde{Q}}$, $M_{\tilde{U}}$ and $M_{\tilde{D}}$. The off-diagonal terms are proportional to the

quark masses, making the $\tilde{q}_L - \tilde{q}_R$ mixing negligible. For the third generation, the mixing is not negligible. In such a case the mass eigenstates $\tilde{q}_1$ and $\tilde{q}_2$ can be obtained by diagonalizing the above matrices. If all generations were included, diagonalizing the 6×6 matrices would results in a $\tilde{f}_{iL} - \tilde{f}_{jR}$ mixing ($i \neq j$). As said before, the $\tilde{q}_L - \tilde{q}_R$ mixing is important mainly for the third generation only and is usually neglected in the first and second generations.

A.3 The slepton sector

For Sleptons, using the $(\tilde{f}_L, \tilde{f}_R)$ basis, the corresponding mass matrix is:

$$M_{\tilde{\tau}}^2 = \begin{bmatrix} M_{\tilde{L}}^2 + m_\tau^2 + m_Z^2(\frac{1}{2} - s_W^2)\cos 2\beta & m_\tau(A_\tau - \mu \tan\beta) \\ m_\tau(A_\tau - \mu\tan\beta) & M_{\tilde{E}}^2 + m_\tau^2 + m_Z^2 s_W^2 \cos 2\beta \end{bmatrix} \tag{A.17}$$

In this case the mixing is also only important if the masses in the non diagonal part of the matrices are comparable with the SUSY mass parameters. This is only relevant for the third generation. For the case of the sneutrinos, as no $\tilde{\nu}_R$ exist in the MSSM, the $\tilde{\nu}_L$ is a mass eigenstate given by:

$$M_{\tilde{\nu}_L}^2 = M_{\tilde{L}}^2 + \frac{1}{2} m_Z^2 \cos 2\beta \tag{A.18}$$

A.4 The chargino sector

Charginos is the name given to the mass eigenstates arising from the mixing of charged gauginos $\widetilde{W}^\pm$ with charged higgsinos $\widetilde{H}^\pm$. As both fields have the same transformation rules under the gauge group, it can be defined:

$$\psi^+ = \begin{pmatrix} \widetilde{W}^+ \\ \widetilde{H}_u^+ \end{pmatrix} \qquad \psi^- = \begin{pmatrix} \widetilde{W}^- \\ \widetilde{H}_d^- \end{pmatrix} \tag{A.19}$$

The mixing in the Lagrangian has the form:

$$\mathcal{L} = -\frac{1}{2}\left(\psi^{-T}, \psi^{+T}\right) \begin{pmatrix} 0 & M^T \\ M & 0 \end{pmatrix} \begin{pmatrix} \psi^- \\ \psi^+ \end{pmatrix} + h.c., \tag{A.20}$$

where M is a 2×2 matrix given by:

$$M = \begin{pmatrix} M_2 & m_w\sqrt{2}S_\beta \\ m_w\sqrt{2}C_\beta & \mu \end{pmatrix}, \tag{A.21}$$

As the matrix is not diagonal, charginos are defined as the mass eigenstates resulting from diagonalizing the above matrix. As M is not a real symmetric matrix, two 2×2 matrices U and V are needed to diagonalize it. In this form the diagonalized matrix will be:

$$U^* M V^{-1} = M_D \tag{A.22}$$

where U y V are given by:

$$V = \begin{pmatrix} \cos\theta_R & \sin\theta_R \\ -\sin\theta_R & \cos\theta_R \end{pmatrix}, \qquad U = \begin{pmatrix} \cos\theta_L & \sin\theta_L \\ -\sin\theta_L & \cos\theta_L \end{pmatrix} \tag{A.23}$$

And the charginos have the form:

$$\widetilde{\chi}_i^+ = V_{ij}\psi_j^+ \qquad \widetilde{\chi}_i^- = U_{ij}\psi_j^- . \tag{A.24}$$

In order to find U y V the eigenstates of M^2 must be found. Thus, chargino masses can be found imposing the condition that M_D^2 must be diagonal and obtaining θ_R y θ_L:

$$U^* M M^\dagger U^{*-1} = V M^\dagger M V^{-1} = M_D^2, \tag{A.25}$$

resulting in the following chargino masses m_χ:

$$2m_\chi^{\pm 2} = M_2^2 + \mu^2 + 2m_W^2 \pm \sqrt{(M_2^2 - \mu^2)^2 + 4m_W^4 \cos^2 2\beta + 4m_W^2 \,(M_2^2 + \mu^2 + 2M_2 \mu \sin 2\beta)},$$

where the values of θ_R and θ_L are given by:

$$\tan 2\theta_R = 2\sqrt{2} m_W \left(\frac{\mu \sin\beta + M_2 cos\beta}{M_2^2 - \mu^2 - 2m_W^2 cos2\beta} \right) \tag{A.26}$$

$$\tan 2\theta_L = 2\sqrt{2} m_W \left(\frac{\mu \sin\beta + M_2 cos\beta}{M_2^2 - \mu^2 + 2m_W^2 cos2\beta} \right). \tag{A.27}$$

A.5 The neutralino sector

Neutralinos is the name given to the mass eigenstates arising from the mixing of neutral gauginos $\widetilde{W}^3$ and $\widetilde{B}$, and the neutral higgsinos $\widetilde{H}_d^0$ and $\widetilde{H}_u^0$:

$$\psi^0 = \left(\widetilde{B}, \widetilde{W}^3, \widetilde{H}_d^0, \widetilde{H}_u^0 \right) \tag{A.28}$$

The interaction Lagrangian then has the form:

$$\mathcal{L} = -\frac{1}{2} \psi^{0T} Y \psi^0 + h.c., \tag{A.29}$$

where Y is a 4×4 matrix given by:

$$Y = \begin{pmatrix} M_1 & 0 & -m_Z C_\beta S_W & m_Z S_\beta S_W \\ 0 & M_2 & m_Z C_\beta C_W & -m_Z S_\beta C_W \\ -m_Z C_\beta S_W & m_Z C_\beta C_W & 0 & -\mu \\ m_Z S_\beta S_W & -m_Z S_\beta C_W & -\mu & 0 \end{pmatrix}, \tag{A.30}$$

Neither $\widetilde{B}$, $\widetilde{W}^3$, $\widetilde{H}_u^0$ nor $\widetilde{H}_d^0$ are mass eigenstates but interaction eigenstates. Mass eigenstates comes from the mixing of these fields and are called neutralinos:

$$\widetilde{\chi}_i^0 = N_{ij} \psi_j, \qquad i = 1, \ldots, 4 \tag{A.31}$$

where N is an unitary diagonalization matrix:

$$N^* Y N^{-1} = N_D \tag{A.32}$$

Both Charginos and Neutralinos are usualy called gauginos or electroweakinos.

Appendix B

Additional pMSSM material

B.1 Additional information on the impact on light squarks and gluino massess

This section complements the discussion presented in section 6.5.1 for strong production, and presents additional results on the impact of ATLAS searches to pMSSM models and additional parameters.

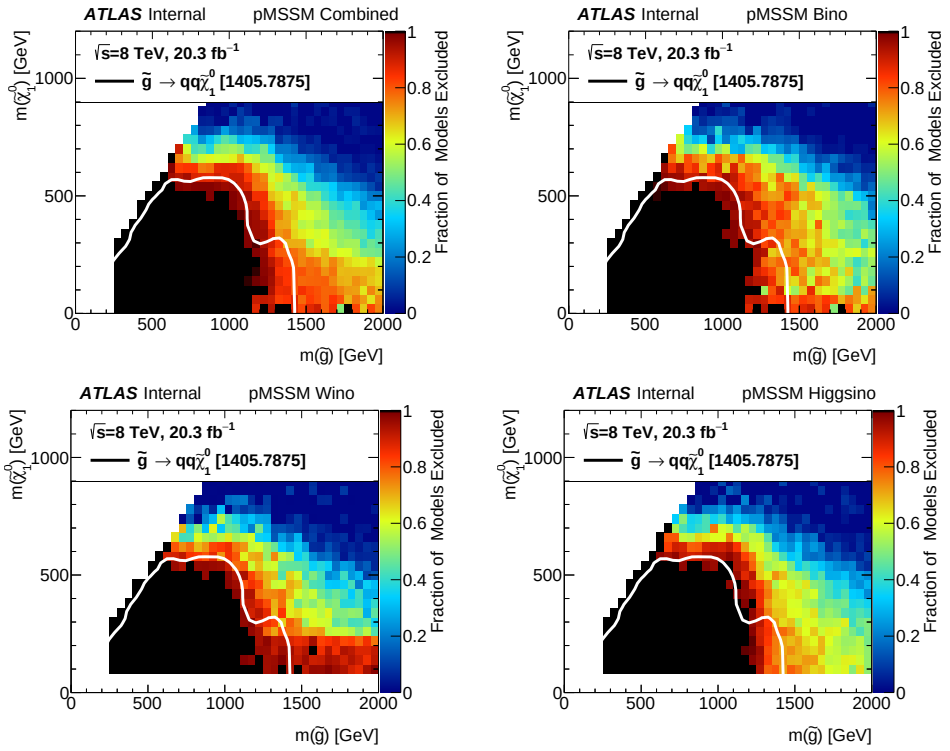

`Figure B.1:` Breakdown of the fraction of pMSSM points excluded by the combination of ATLAS searches in the $m_{\tilde{\chi}_1^0} - m_{\tilde{g}}$ plane: Top-left: Inclusive LSP type. Top-right: Bino-like LSP: Bottom-left: Wino-like LSP. Bottom-right: Higgsino-like LSP [241].

Long lived charginos appear in models with Wino-like LSP and a chargino NLSP with

mass differences $\Delta(m_{NLSP}, m_{LSP}) \lesssim 200$ GeV. In this cases the NLSP would decay inside the detector to an invisible LSP and a $\pi^{\pm}$ with energy low enough not to be detected leading to a disappearing track signature. Such phenomenology for pMSSM models depends on all SUSY masses and the search is sensitive even in the absence of direct squark or gluino production.

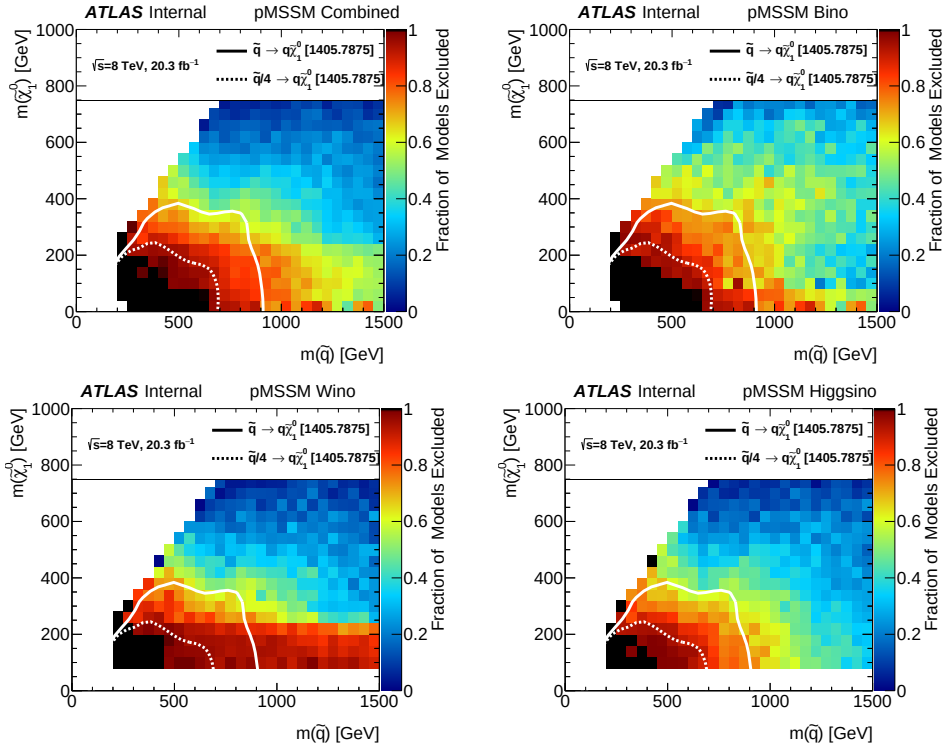

Figure B.2: Breakdown of the fraction of pMSSM points excluded by the combination of ATLAS searches in the $m_{\chi_1^0} - m_{\tilde{q}}$ plane: Top-left: Inclusive LSP type. Top-right: Bino-like LSP: Bottom-left: Wino-like LSP. Bottom-right: Higgsino-like LSP [241].

Figures B.1 and B.2 present three complementary plots, for each of the two plots presented in figure 6.5 in section 6.5.1. The exact same plots are displayed in the upper left corner for inclusive LSP types. The three remaining plots are categorized by LSP type. It is clear in both images that the horizontal arm reaching towards higher sensitivities for low LSP masses comes mainly from the Wino-like LSP models.

The fact that the disappearing track search has an impact on strongly produced sparticles is a key example of this analysis. As all parameters are connected, all searches must be combined showing complementarity of ATLAS SUSY searches. In figure B.3 similar plots are presented but showing only the impact of the 0 lepton + 2-6 jets + E_T^{miss} analysis [159]. In this plot instead of showing the fraction of excluded points, the maximum value of the best expected CL_s of the analysis is shown projected in the $m_{\tilde{g}} - m_{\tilde{\chi}_1^0}$ plane. The white line is again the limit obtained for simplified models with the very same analysis, allowing a direct comparison of exclusion reaches in both cases. The upper left plot for inclusive in LSP types shows points inside the simplified model excluded region with unexpectedly high CL_s values. This shows the dependence on other sparticles besides the ones accessible for the simplified model. It also also points to the importance of the complementarity of the searches when studying non simplified models. Looking at all plots, it is clear that the points with high CL_s in the low mass region come mostly from Wino-like LSP models. In these models many leptons may appear

in the final state, reducing the 0 lepton analysis sensitivity. This stress the key importance of including all ATLAS analyses to efficiently cover the final mass planes. Having four different

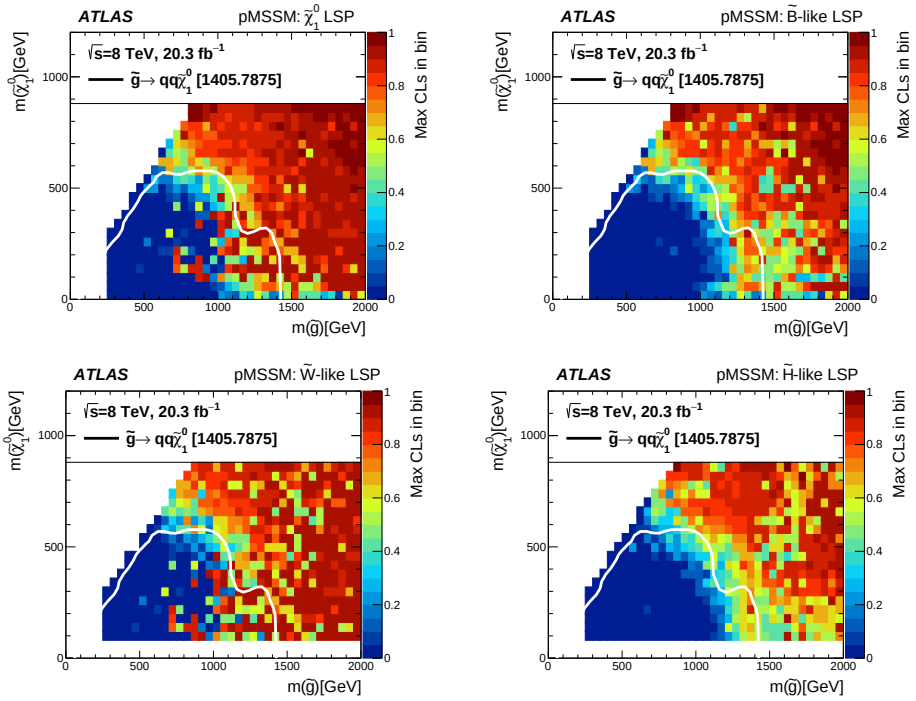

Figure B.3: Impact of ATLAS searches complementarity [240]

light squark masses the pMSSM richer in phenomenology than any of the simplified models. This makes direct squark production dependent on the flavor of the lightest squark. Figure B.5 shows two dimensional plots with the number of excluded models with u_L, u_R, d_L and d_R masses on the $x-$axis and $m_{\tilde{\chi}_1^0}$ on the $y-$axis. Superimposed on top of the plots in figure B.5 reference simplified model limits are drawn. This limits come again from the 0 lepton + 2-6 jets + E_T^{miss} analysis but for the left (right) handed squarks the production cross section is divided by two (four) in an attempt to mimic the four (two) degenerate squarks of pMSSM models. From the plots it can be seen that the exclusion power depends largely on whether the squark is left- or right-handed. The $\tilde{u}_L$ and $\tilde{d}_L$ squarks form a SU(2) doublet and are nearly degenerate in mass, as shown in the squark mass matrix presented in equations A.15 and A.16 in Appendix A. Being almost degenerate, a higher production cross section would be expected in relation with their right counterparts. Besides a smaller cross section, right handed squarks couplings to Wino-like or Higgsino-like LSP are highly suppressed and the right handed squarks must cascade decay resulting in events with smaller E_T^{miss}, additional less energetic jets and usually smaller sensitivity. The small differences between up and down squarks should come from production cross section as there are more valence up quarks than down in the proton (bigger $u-$quark PDF). These same plots divided by LSP type can be found in [241]

B.2 Impact on third generation squarks

In the left plot in figure B.6 the fraction of excluded models is shown in the $m_{\tilde{t}_1} - m_{\tilde{\chi}_1^0}$ plane where $\tilde{t}_1$ represents the lighter of the two stops. Few model points have light stops, in order to

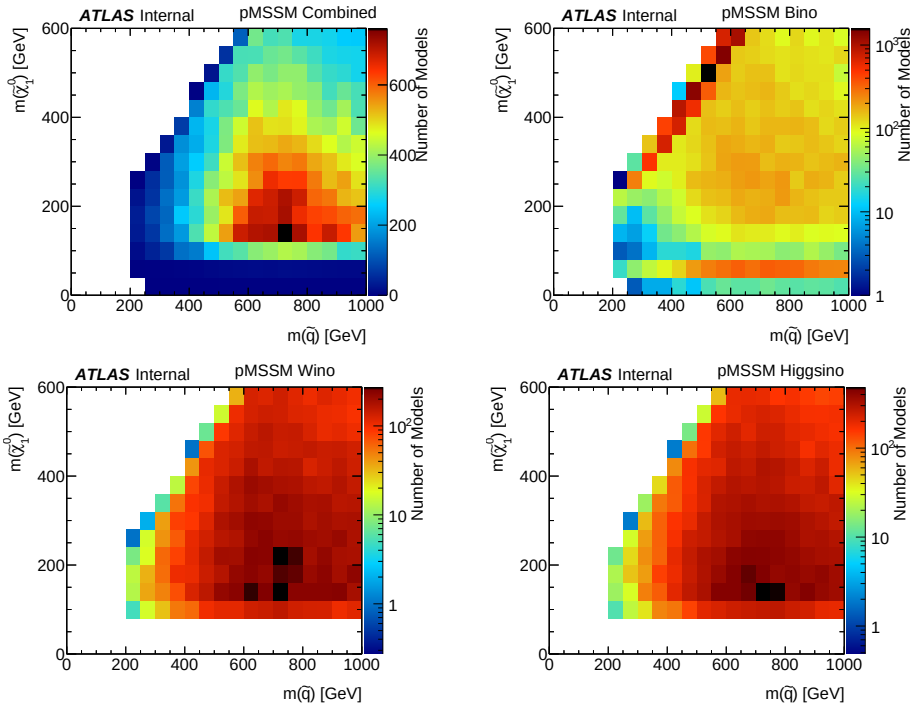

Figure B.4: Number of models in the $m_{\tilde{q}} - m_{\chi_1^0}$ plane for combined (top-left), bino (top-right), wino (bottom-left) and higgsino (bottom-right) LSP types. [241]

fulfill the higgs boson mass requirement. Despite the small number of points with light stops, for $m_{\tilde{\chi}_1^0} < 300$ GeV, most of the points can be excluded for stop masses below ~ 600 GeV. In this plot the reference line is taken from direct stop production for simplified models where the stop decays only to a top plus the LSP [172]. This line reaches higher values near 700 GeV for lighter LSP. This is expected as within the pMSSM the stop might decay to the LSP in a chain via other intermediate spartcles. In [172], it was shown that for a two step decay like $\tilde{t} \to b\tilde{\chi}_1^{\pm}$ followed by the chargino decay $\tilde{\chi}_1^{\pm} \to W^{\pm}\tilde{\chi}_1^0$ assuming mass degeneration between the chargino and the LSP, the exclusion recoiled to values near 540 GeV. In the region close to the diagonal for low masses, there are many mass bins for which all the points are excluded, but lying outside the simplified model exclusion region. This again shows the power of the complementarity of ATLAS SUSY searches, as most of these points are excluded by the $2b$-jets + E_T^{miss} analysis [171]. In figure B.7 the fraction of excluded models is presented only for third generation searches. The shows that outside the simplified model limit, there is a gain in sensitivity if more searches are included.

In the right plot in figure B.6 a similar plot is presented for the lightest sbottom $\tilde{b}_1$. For $m_{\tilde{\chi}_1^0} < 300$ GeV sbottom masses are very likely to be excluded below ~ 600 GeV. In this case the reference lines for simplified models come from $2b$-jets + E_T^{miss} analysis [171] assuming direct $\tilde{b}_1$ production decaying solely to a $b-$quark plus LSP. In figure B.7 the same 2-D plot is shown only for third generation searches, presenting similar features than for the lightest stop case.

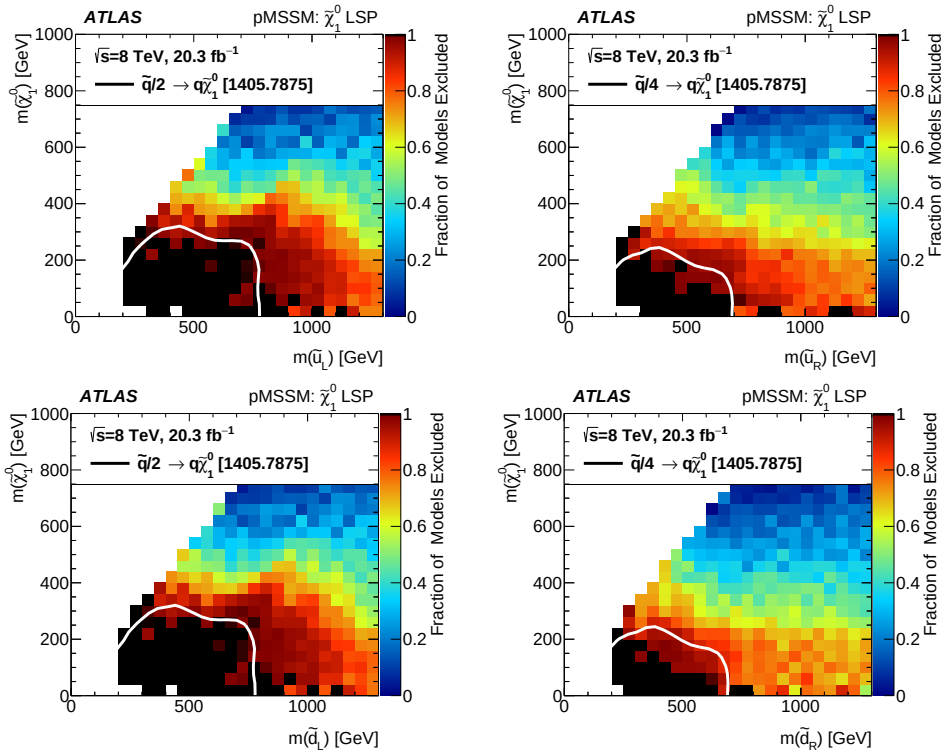

Figure B.5: Fraction of pMSSM points excluded by the combination of ATLAS searches in the $m_{\tilde{u}_L} - m_{\tilde{\chi}_1^0}$ plane (top-left), in the $m_{\tilde{u}_R} - m_{\tilde{\chi}_1^0}$ plane (top-right), in the $m_{\tilde{d}_L} - m_{\tilde{\chi}_1^0}$ plane (bottom-left) and in the $m_{\tilde{d}_R} - m_{\tilde{\chi}_1^0}$ plane (bottom-right) [158].

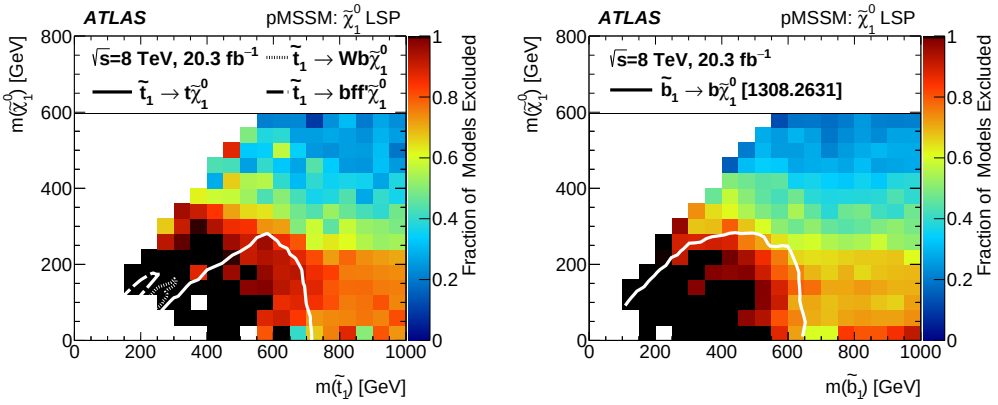

Figure B.6: Fraction of pMSSM points excluded by the combination of ATLAS searches in the $m_{\tilde{t}_1} - m_{\tilde{\chi}_1^0}$ plane (left) and in the $m_{\tilde{b}_1} - m_{\tilde{\chi}_1^0}$ plane (right) [158].

B.3 Impact on electroweakinos and sleptons

In the left plot in figure B.8 the fraction of excluded models by all ATLAS electroweak searches presented in table 6.3 is projected into the $m_{\tilde{\ell}} - m_{\tilde{\chi}_1^0}$ plane. $\tilde{\ell}$ represents the lightest slepton including sneutrinos and excluding staus. The white reference line comes from the 2-leptons EW search [174] and represents the limit to a simplified model consisting in direct slepton pair

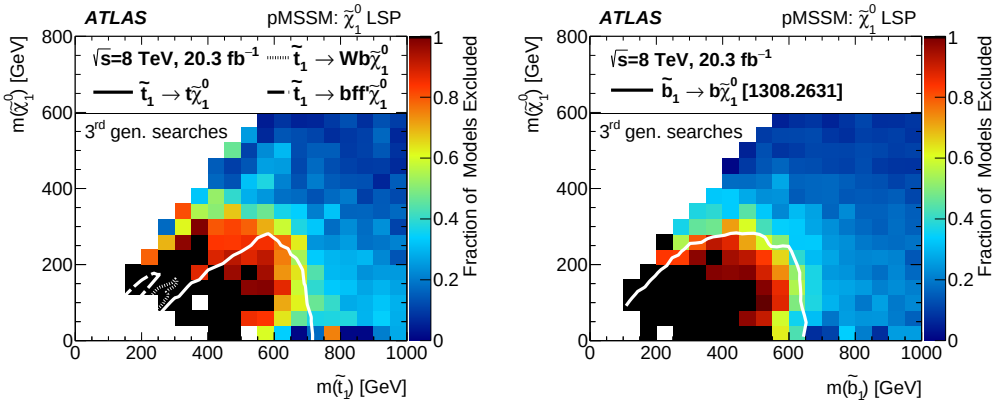

Figure B.7: Fraction of pMSSM points excluded by third generation searches in the $m_{\tilde{t}_1} - m_{\tilde{\chi}_1^0}$ plane (left) and in the $m_{\tilde{b}_1} - m_{\tilde{\chi}_1^0}$ plane (right) [158].

production (assuming left-right degeneration) where the sleptons decays only via $\tilde{\ell}^{\pm} \to \ell^{\pm}\tilde{\chi}_1^0$. The plot shows that EW searches have good sensitivity to light sleptons ($\lesssim$ 200 GeV) when $m_{\tilde{\chi}_1^0} < 75$ GeV. These low masses for the LSP are only achieved in Bino-like LSP models. On the other hand the exclusion power decreases near the diagonal, making it impossible to set any lower limit on slepton masses. The apparent reduction on the exclusion power of the pMSSM analysis compared to the simplified model, is again attributed to the oversimplification of the model, the mass degeneration between left and right light sleptons and the availability of only one kinematically reachable BR.

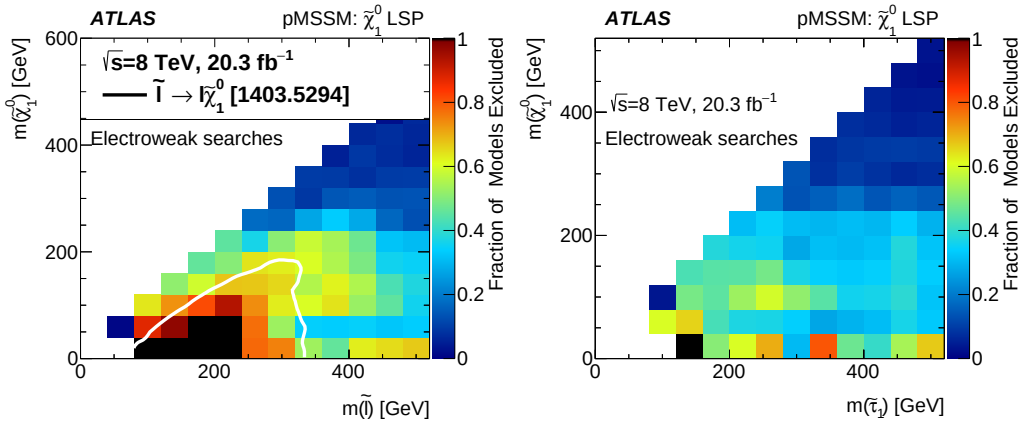

Figure B.8: Left: Fraction of pMSSM points excluded by electroweak searches in the $m_{\tilde{\ell}} - m_{\tilde{\chi}_1^0}$ plane. Right: Fraction of pMSSM points excluded by the combination of 8 TeV ATLAS searches in the $m_{\tilde{\tau}_1} - m_{\tilde{\chi}_1^0}$ plane. [158].

When the left and right states are allowed to be non degenerate in the simplified model, the pMSSM sensitivity looks much more in agreement with the simplified models limits. This is shown in figure B.9 where the left and right channels are plotted separately for the pMSSM and the white boundaries are taken from figures 8(a) and 8(b) of [174]. It is also very interesting to notice the wider sensitivity of the ATLAS searches to left handed sleptons.

For the lightest stau ($\tilde{\tau}_1$), no lower limit to $m_{\tilde{\tau}_1}$ could be set, as the ATLAS sensitivity to staus is quite limited. Backgrounds for stau searches are much larger than for the lighter

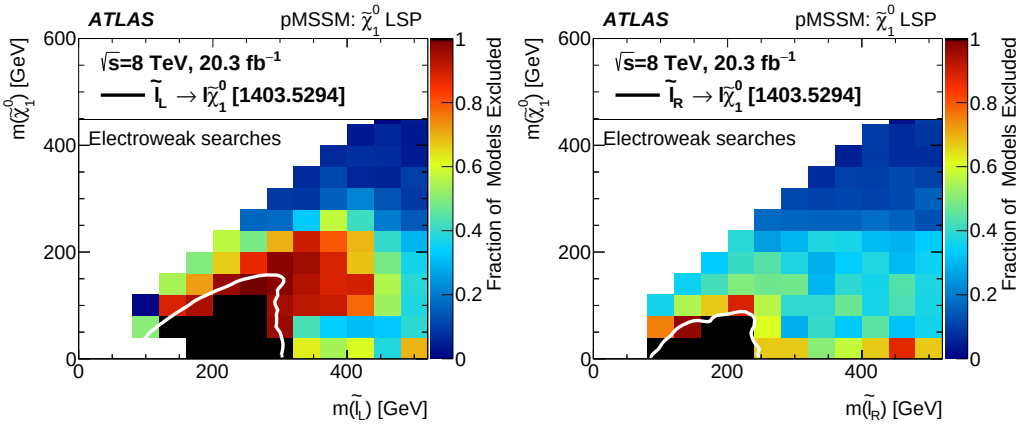

Figure B.9: Fraction of pMSSM points excluded by electroweak searches in the $m_{\tilde{\ell}_L} - m_{\tilde{\chi}_1^0}$ plane (left) and in the $m_{\tilde{\ell}_R} - m_{\tilde{\chi}_1^0}$ plane (right) [158].

sleptons, and it is very hard to trigger events coming from direct stau production. The poor ATLAS sensitivity to staus is clear in the right plot in figure B.8, where a large fraction of the models could not be excluded. In general, the results showed that ATLAS searches were quite sensitive restraining strongly interacting sparticles in specific regions of the phase space, for electroweakinos the searches tended to exclud models in wider regions. Additional results and plots as the fraction of excluded models projected in the $m_{\tilde{\chi}_2^0} - m_{\tilde{\chi}_1^0}$ or in the $m_{\tilde{\chi}_1^\pm} - m_{\tilde{\chi}_1^0}$ planes which are very interesting are no presented. Although there are large regions where all models were excluded, the regions were not distributed in a simple way and no exact limits were able to be defined. There is a lot of interesting phenomenology on these plots that is beyond the scope of this document. The interested reader is encouraged to find further interpretations of the results in the already cited bibliography.

B.4 Impact on long lived particles

Only the dedicated long lived particle searches [179, 180] were considered for testing the sensitivity to pMSSM models with long lived sparticles. These analyses showed to be very sensitive to the $\sim 3K$ long lived pMSSM points created, from which $\sim 92\%$ have a Bino-Like LSP. The best sensitivity was found for long lived sbottoms, where 77% of the models were excluded. In almost all of the models (99.6%) with long lived sbottoms, their lifetimes are long enough for them to pass through the detector before decaying. On the other hand, in the case of gluinos, only 5.1% of the models included gluinos with long enough lifetimes and the long lived searches excluded only 5% of the models.

B.5 Impact on heavy neutral higgs bosons

The impact on the heavy neutral boson higgs A is presented in figure B.10 in the $m_A - \tan\beta$ plane, where the fraction of excluded models by the combination of SUSY searches is shown. The white reference line corresponds to the observed limit from the $H/A \rightarrow \tau^+\tau^-$ search [181] for the m_h^{max} benchmark scenario [242, 243]. The plot shows a very close shape coherence between the observed limit represented by the white line, and the region of the pMSSM space almost completely excluded by the ATLAS searches. There are few mass bins scattered above

the white line for which not 100% of the plots have been excluded. The vast majority of points above the white line were excluded by the $H/A \to \tau^+\tau^-$ search.

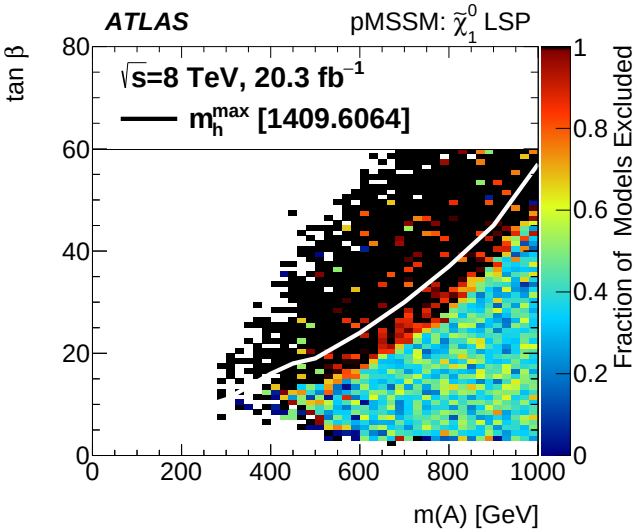

Figure B.10: Fraction of pMSSM points excluded by the combination of ATLAS searches in the $m_A - \tan\beta$ plane [158]

B.6 Impact on dark matter

As already discussed, the nature of the LSP plays a crucial role on the DM relic density. In the left plot in figure B.11 the distribution of points before the ATLAS constraints is

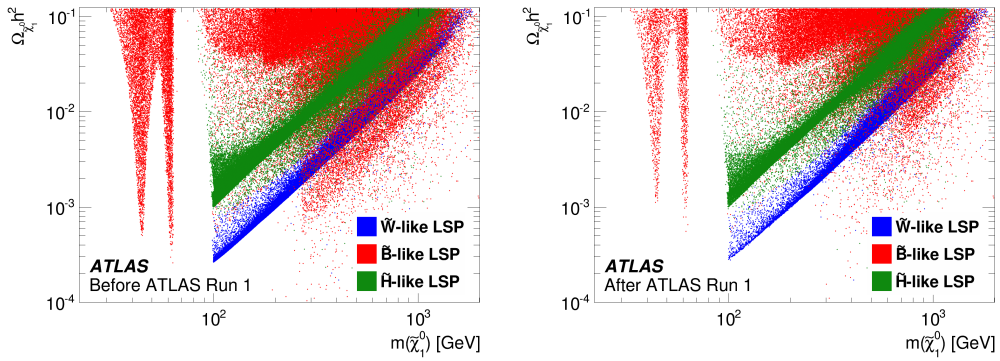

Figure B.11: Left: Distribution of models before the ATLAS constraints in the $m_{\tilde{\chi}_1^0}$ vs relic density ($\Omega_{\tilde{\chi}_1^0}h^2$) plane. Right: Distribution of models after applying the ATLAS constraints. [158].

presented in the LSP mass vs LSP relic density plane. The different shapes show how the LSP type is determinant for DM parameters. Bino-like LSP models presented in red, are the only points below the $\sim$ 200 GeV mass region, due to possible annihilation in the h and Z *funnels*. Wino- and Higgsino-like LSP models are presented in blue and green respectively. Above $\sim$ 200 GeV there are regions on the plane with presence of red points with different densities.

Such regions are created by the variety of annihilation processes for Bino-like DM as shown in figure in figure B.12 where the models have been categorized depending on the dominant annihilation mechanism of the DM candidate. The orange points labeled as *light flavor* refers to co-annihilation with light gluinos or squarks with masses similar to the LSP mass. The 200 GeV lower limit for squarks and the ~ 200 GeV lower limit for charged particles required by the experimental constraints shown on table 6.6 are clearly visible as vertical limits for the different annihilation mechanisms.

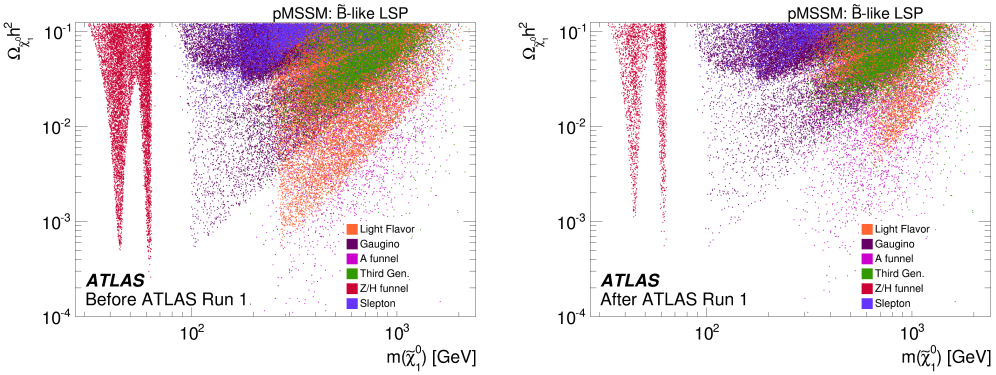

`Figure B.12:` Distribution of Bino-like models before (left) and after (right) the ATLAS constraints in the $m_{\tilde{\chi}_1^0}$ vs $\Omega_{\tilde{\chi}_1^0}h^2$ plane categorized by the annihilation processes type [158].

In the right plot in figure B.11, the effect of all ATLAS searches is presented. For Bino-like LSP models almost $\sim 67\%$ of the points below $m_{\tilde{\chi}_1^0} < 100$ GeV can be excluded. Also as seen on figure B.12 the ATLAS searches are very sensitive to light squark or gluino co-annihilation (mainly because of the mono-jet analyses). In the case of Wino-like LSP models, the sensitivity reaches values as high as $m_{\tilde{\chi}_1^0} \sim 800$ GeV, excluding around 80% of the models with $m_{\tilde{\chi}_1^0} \lesssim 220$ GeV thanks to the disappearing track analysis. For Higgsino-like LSP models, the disappearing track search has lower sensitivity because of the shorter $\tilde{\chi}_1^\pm$ lifetimes.

B.7 Impact on precision measurements

In figure B.13 the effect of the ATLAS searches on the expected values of the precision variables presented in table 6.6 is presented. In most of the plots, the reduction of models after ATLAS constraints is uniform through the whole range of the variableś. This means that ATLAS searches are no sensitivity to the predicted values of these variables. Most of these parameters depend on electroweakino spectrum more than on gluinos or squarks parameters. It has been commented that ATLAS searches are quite sensitive when restraining strongly interacting sparticles in certain regions of the phase space, while for electroweakinos the searches excluded models in much wider regions.

In the upper-left plot in figure B.13, the effects of atlas searches is shown projected in to the expected value of the $\Delta\rho$ parameter. Most of the sampled points are near the SM prediction ($\Delta\rho \sim 0$). Looking at the bottom panel where the fraction of excluded models is depicted, it appears as ATLAS searches sensitivity grows higher for models with large $\Delta\rho$. Nevertheless, this behavior occurs in the tail of the distribution, where the number of models in each bin is quite reduced. This apparent higher sesitivity in the tail, might only be statistical oscilation, as in the low $\Delta\rho$ region where there are more than 100 models per bin, the ratio distribution looks flat.

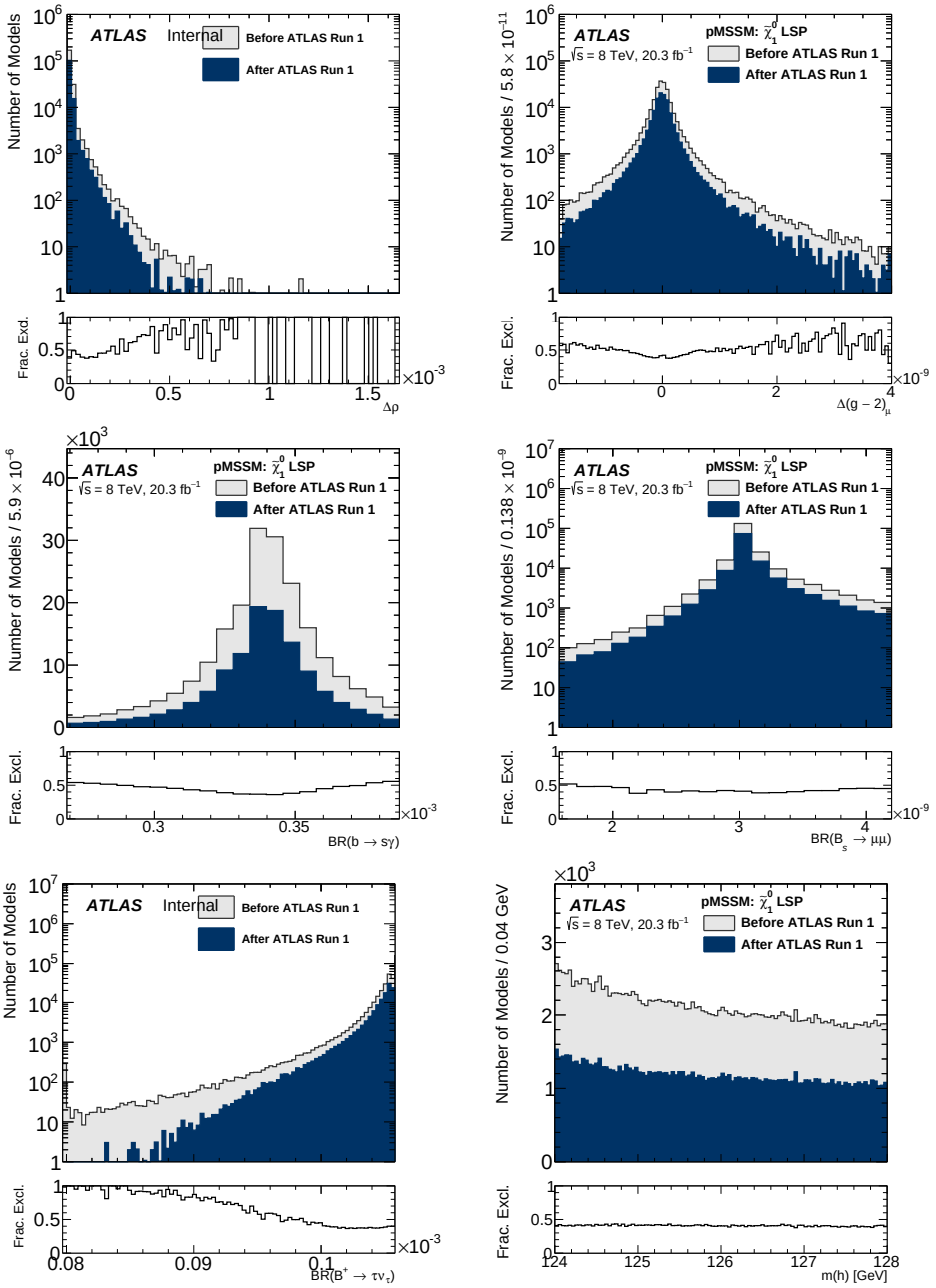

Figure B.13: Number of pMSSM models projected into the expected values of the variables $\Delta\rho$ (upper-left) [241], $\Delta(g_\mu - 2)$ (upper-right) [158], $BR(b \to s\gamma)$ (center-left) [158], $BR(B_s \to \mu^+\mu^-)$ (center-right) [158], $BR(B^+ \to \tau^+\nu_\tau)$ (lower-left) [241] and m_h (lower-right) [158].

In the top-right, center-left and center-right plots of figure B.13, the results are presented for $\Delta(g_\mu - 2)$, $BR(b \to s\gamma)$ and $BR(B_s \to \mu^+\mu^-)$ respectively. In all these plots the fraction of excluded models alond the expected values of the variables is quite flat, showing only minor SUSY contributions to the observables. Indeed for the $\Delta(g_\mu - 2)$ and $BR(b \to s\gamma)$ there is a tendency of higher sensitivity for the models on the tails of the distributions. This is an already known feature of SUSY, these models generaly contain light SUSY particles contributing via loop diagrams to the variables.

In the bottom-right plot in figure B.13 the effects are shown for $BR(B^+ \to \tau^+\nu_\tau)$. The plot shows an apparently higher SUSY sensitivity to models with low $BR(B^+ \to \tau^+\nu_\tau)$. Similar to what was discussed for the $\Delta\rho$ parameter, in the region where the number of models per bin is higher than 100 the distribution looks rather flat.

Finally, in the bottom-right plot in figure B.13 the results are presented with respect to the lighter higgs mass m_h. As seen on the bottom panel of the plot, the fraction of excluded models distribution is extraordinarily flat. This plot demonstrates that mass range used for restraining the higgs mass used in table 6.6 does not make a big impact and that having used an outdated value for the higgs mass was not major problem.

Appendix C

Additional $13\ TeV$ one lepton material

C.1 Kinematic distributions in CRs

In this section the kinematic distributions for all relevant 1 hard lepton variables is presented in all CRs in figures C.3 - C.14. In general the CRs have rather tight statistics, this makes the distributions to be sometimes not so smooth. Nevertheless It can be seen in all plots that data and MC agree within uncertainty bands. MC bands includes both statistical and systematic uncertainties.

C.1.1 Kinematic distributions in the 4-jet low-x TCR

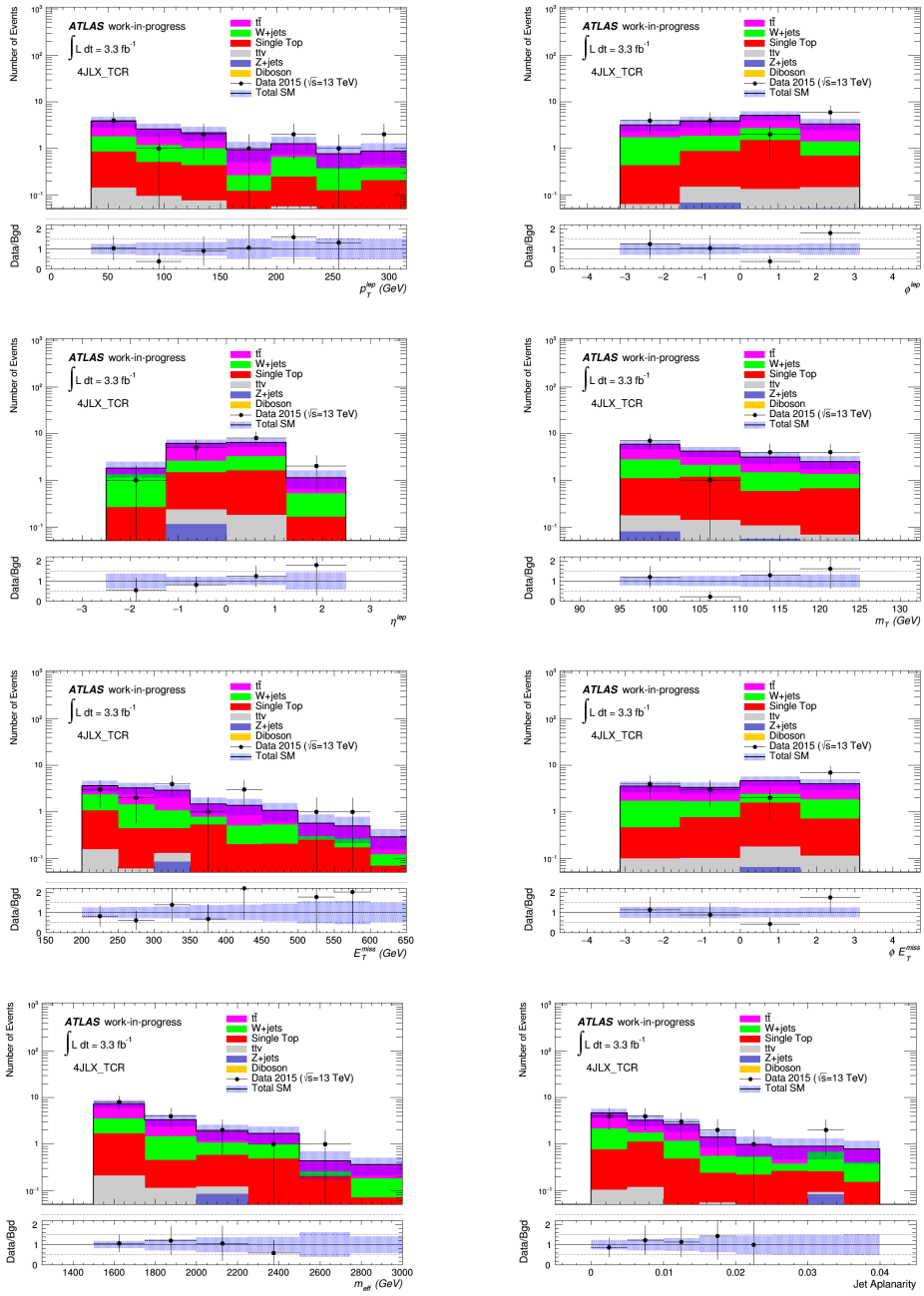

Figure C.1: Kinematic distributions of variables in the 4-jet low-x *top* CR after background fit.

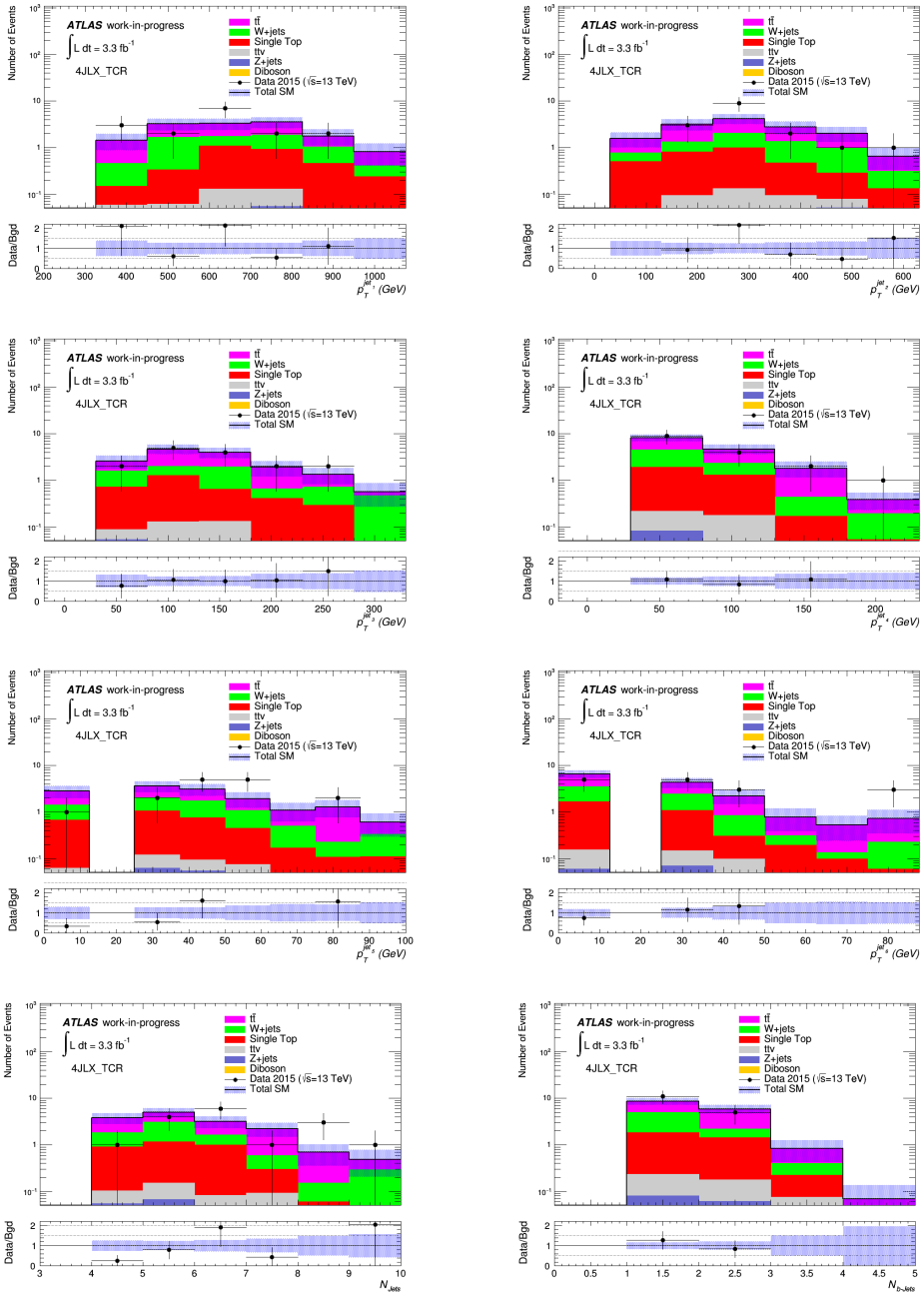

Figure C.2: Kinematic distributions of variables in the 4-jet low-x *top* CR after background fit.

C.1.2 Kinematic distributions in the 4-jet low-x WCR

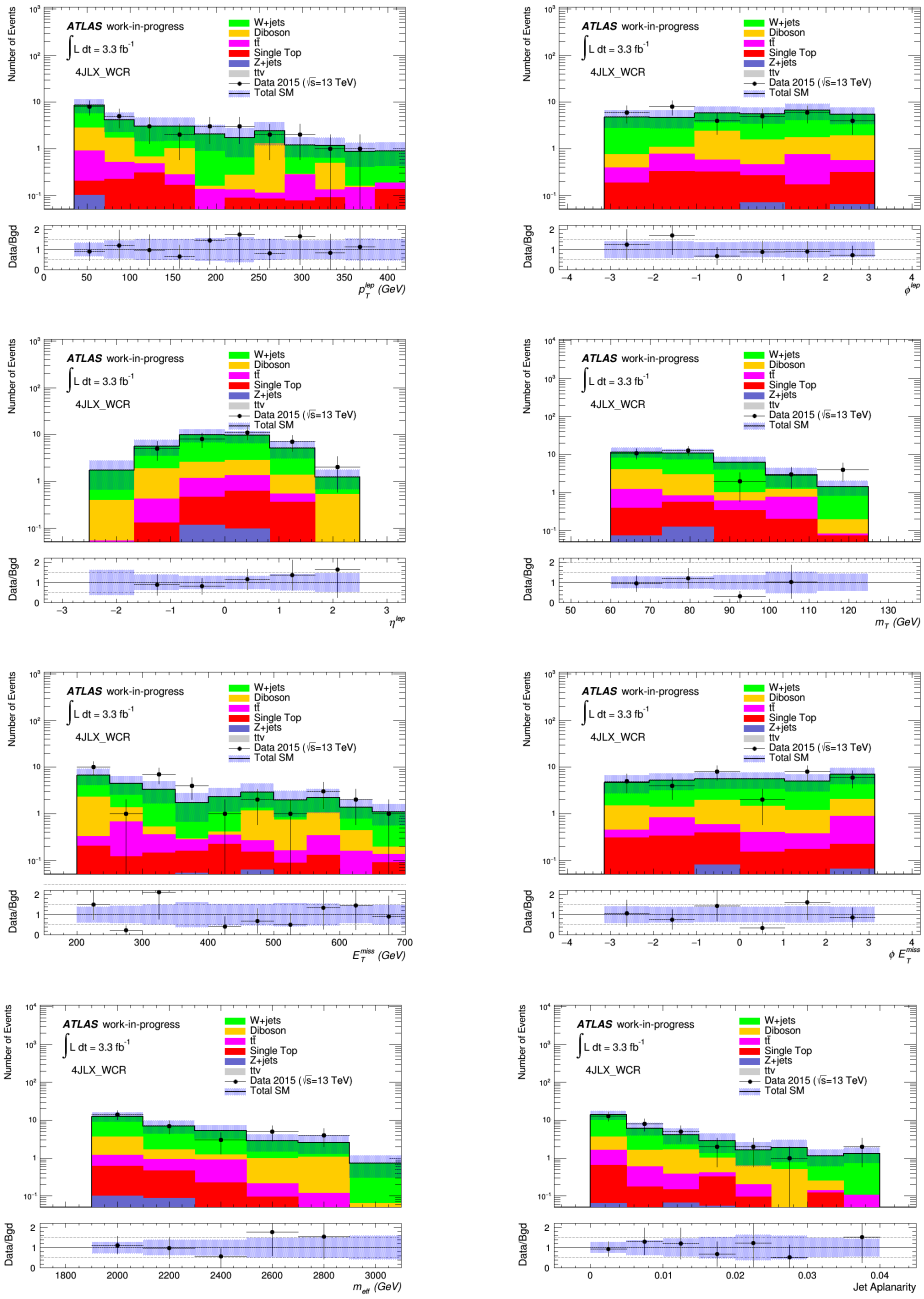

Figure C.3: Kinematic distributions of variables in the 4-jet low-x W CR after background fit.

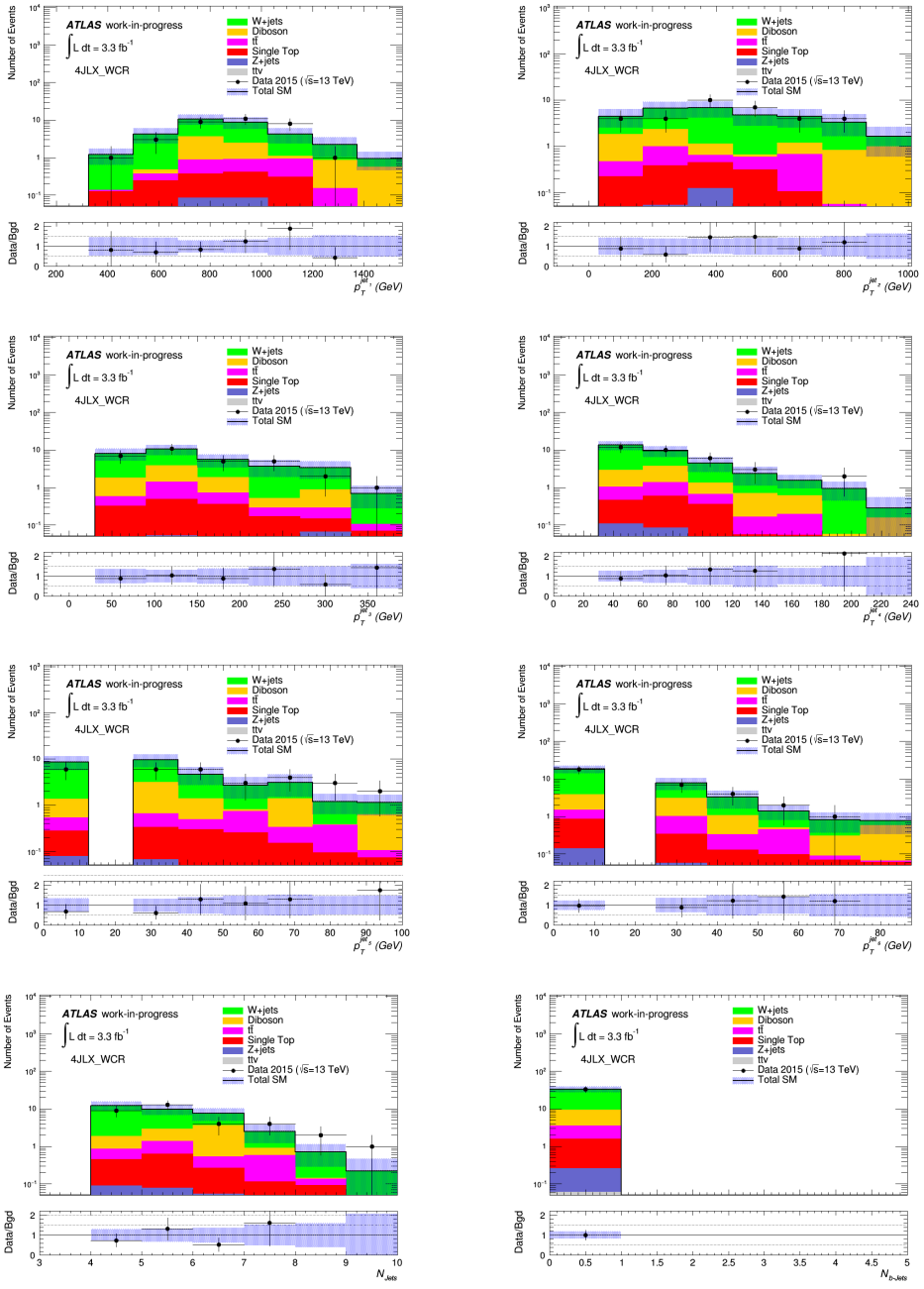

Figure C.4: Kinematic distributions of variables in the 4-jet low-x W CR after background fit.

C.1.3 Kinematic distributions in the 4-jet high-x TCR

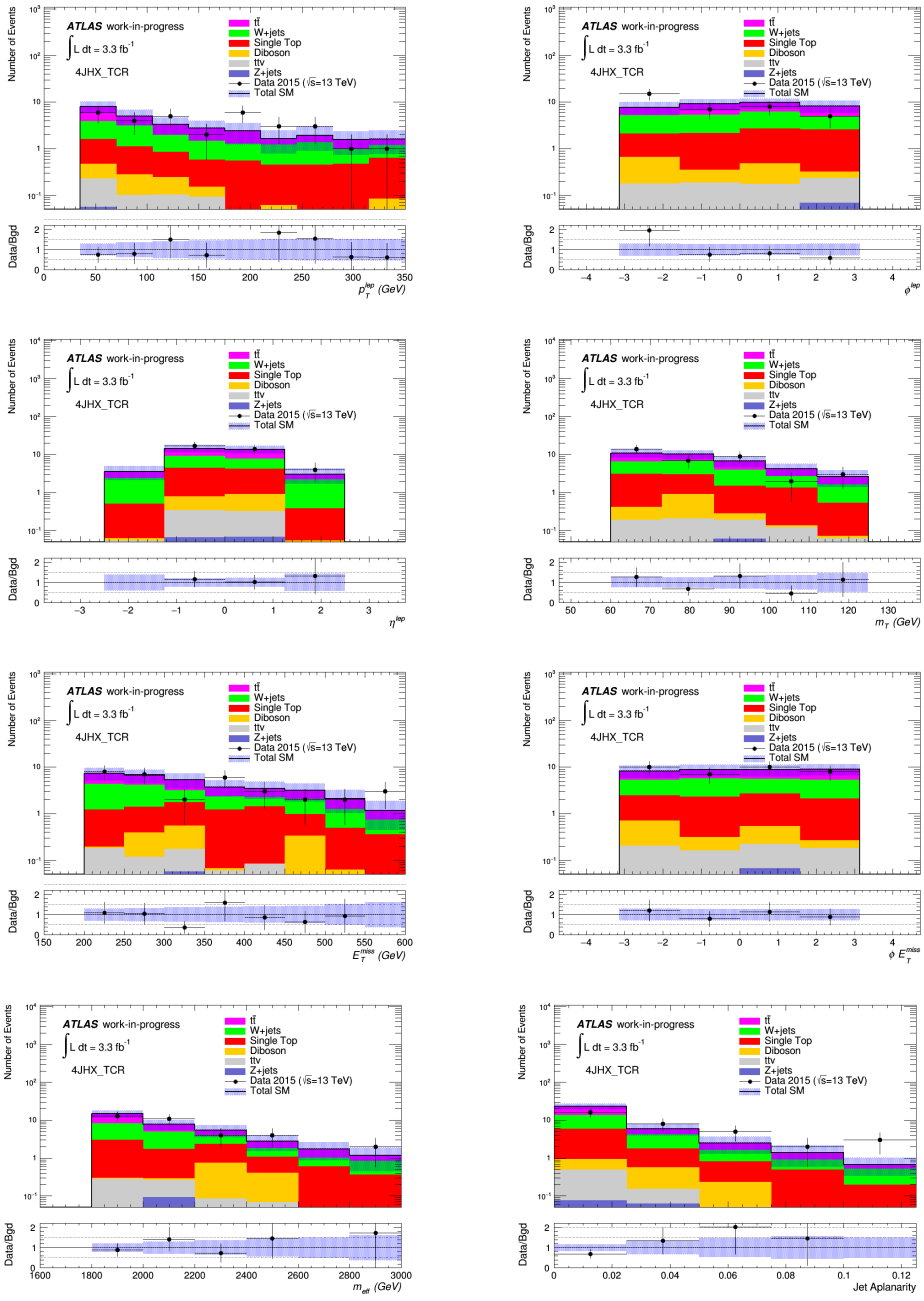

Figure C.5: Kinematic distributions of variables in the 4-jet high-x *top* CR after background fit.

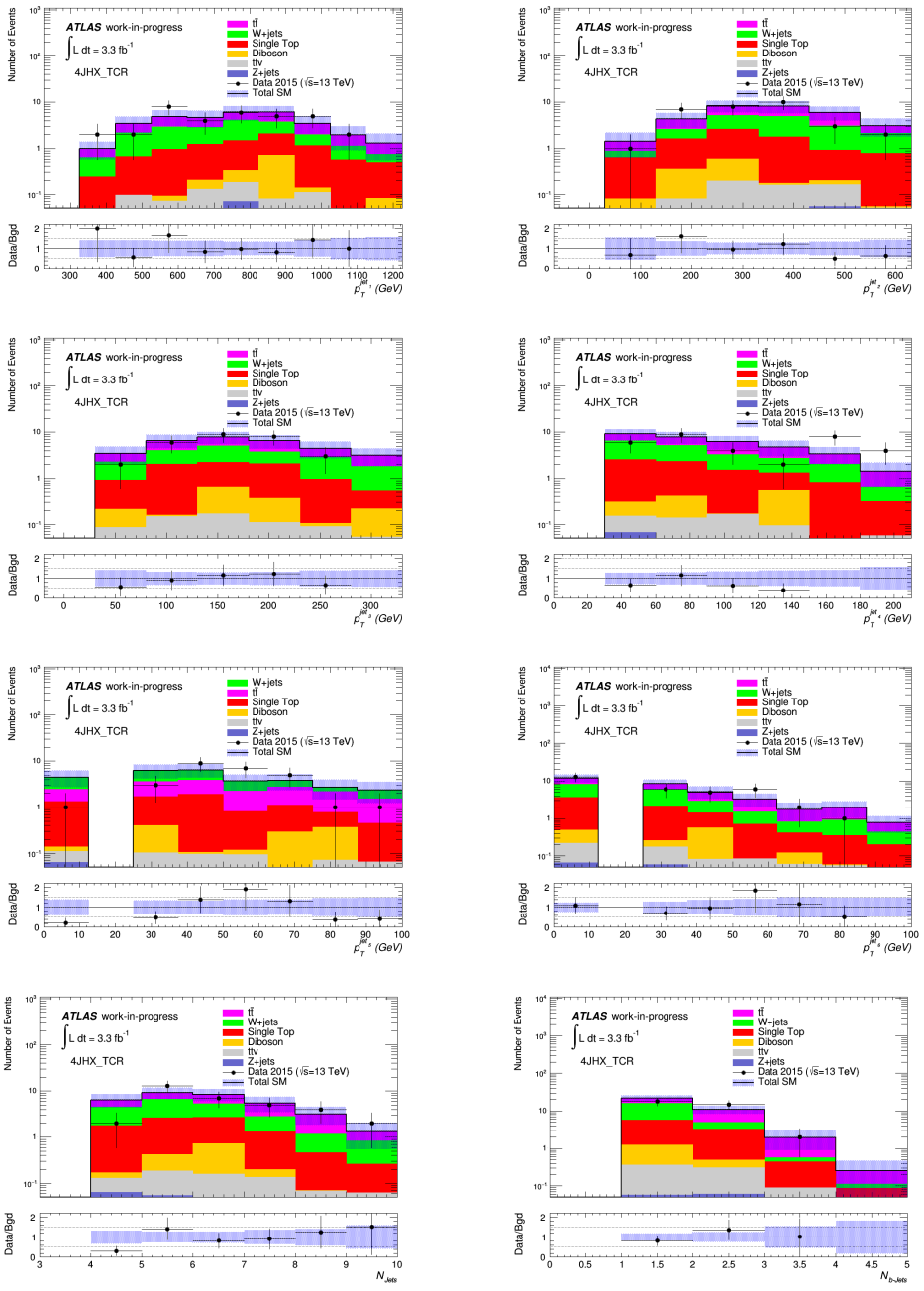

Figure C.6: Kinematic distributions of variables in the 4-jet high-x *top* CR after background fit.

C.1.4 Kinematic distributions in the 4-jet high-x WCR

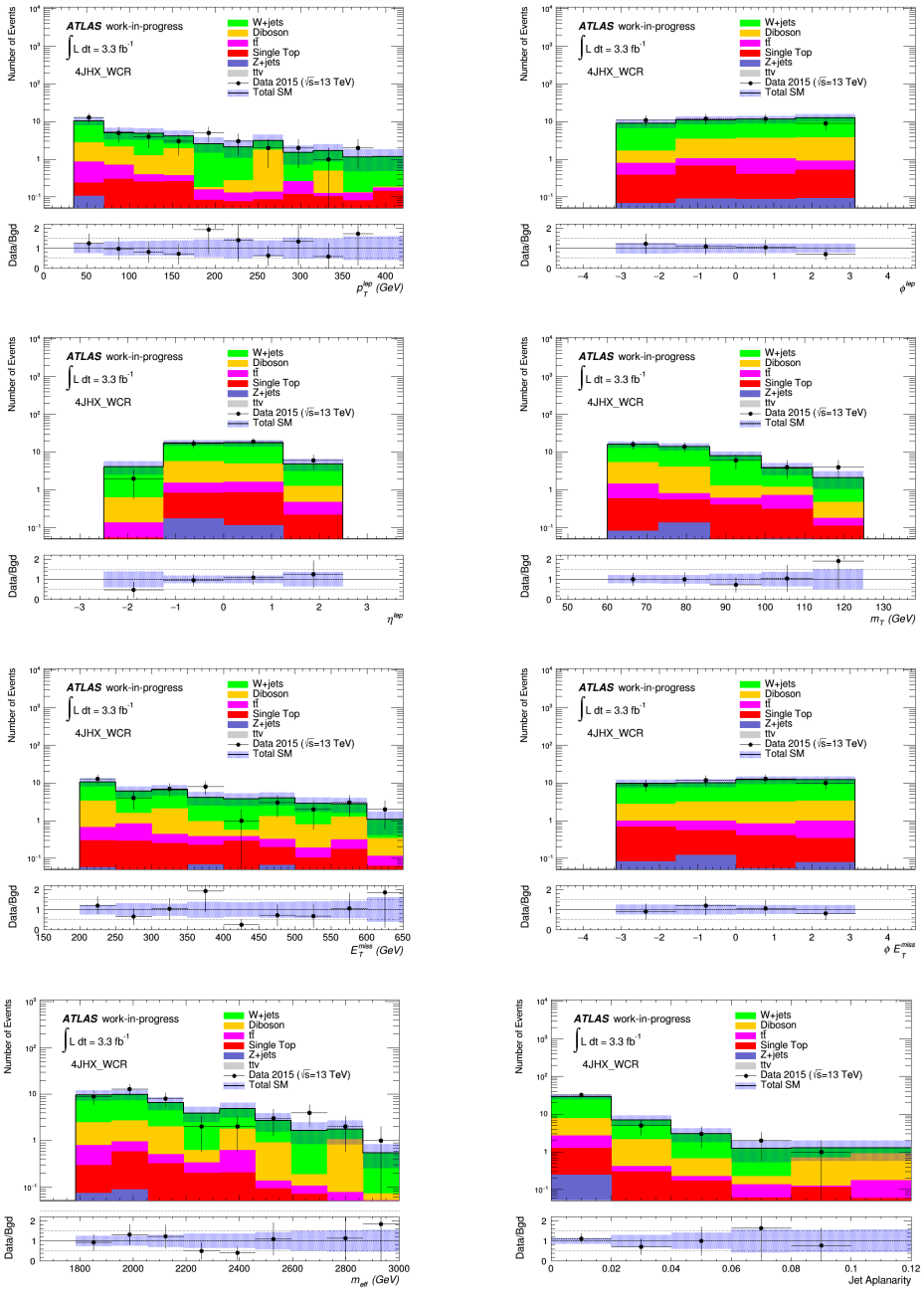

Figure C.7: Kinematic distributions of variables in the 4-jet high-x W CR after background fit.

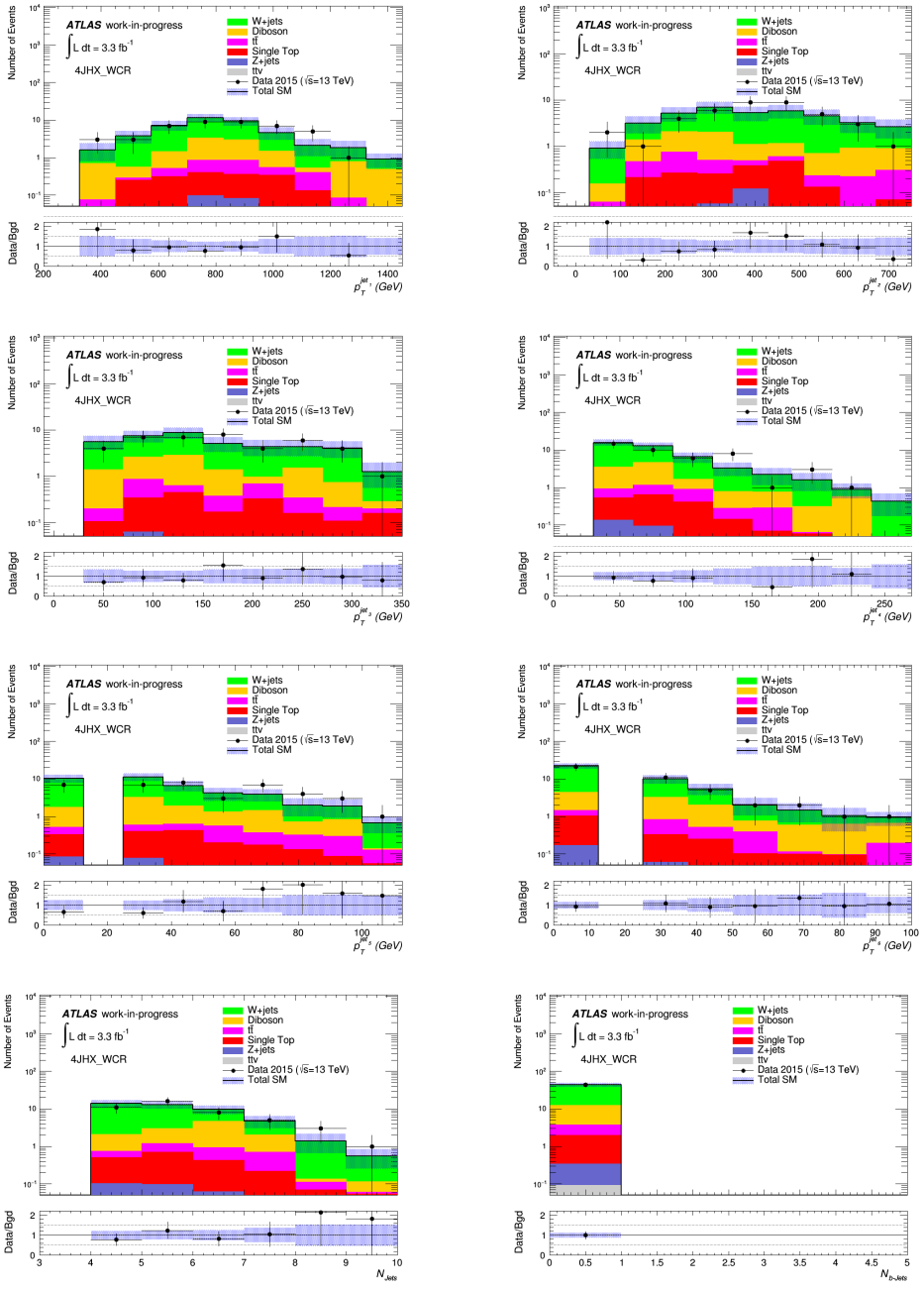

Figure C.8: Kinematic distributions of variables in the 4-jet high-x W CR after background fit.

C.1.5 Kinematic distributions in the 5-jet TCR

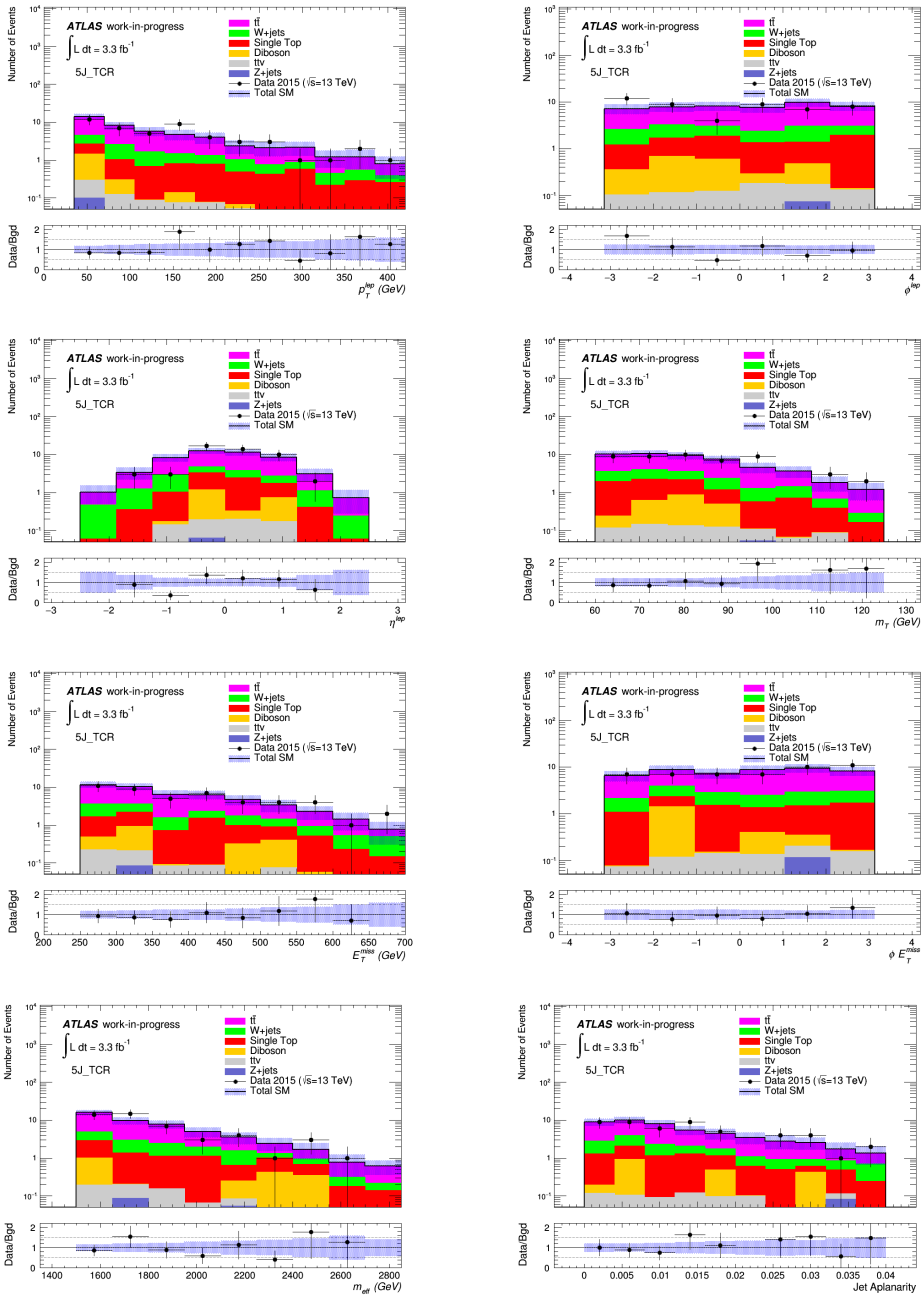

Figure C.9: Kinematic distributions of variables in the 5-jet *top* CR after background fit.

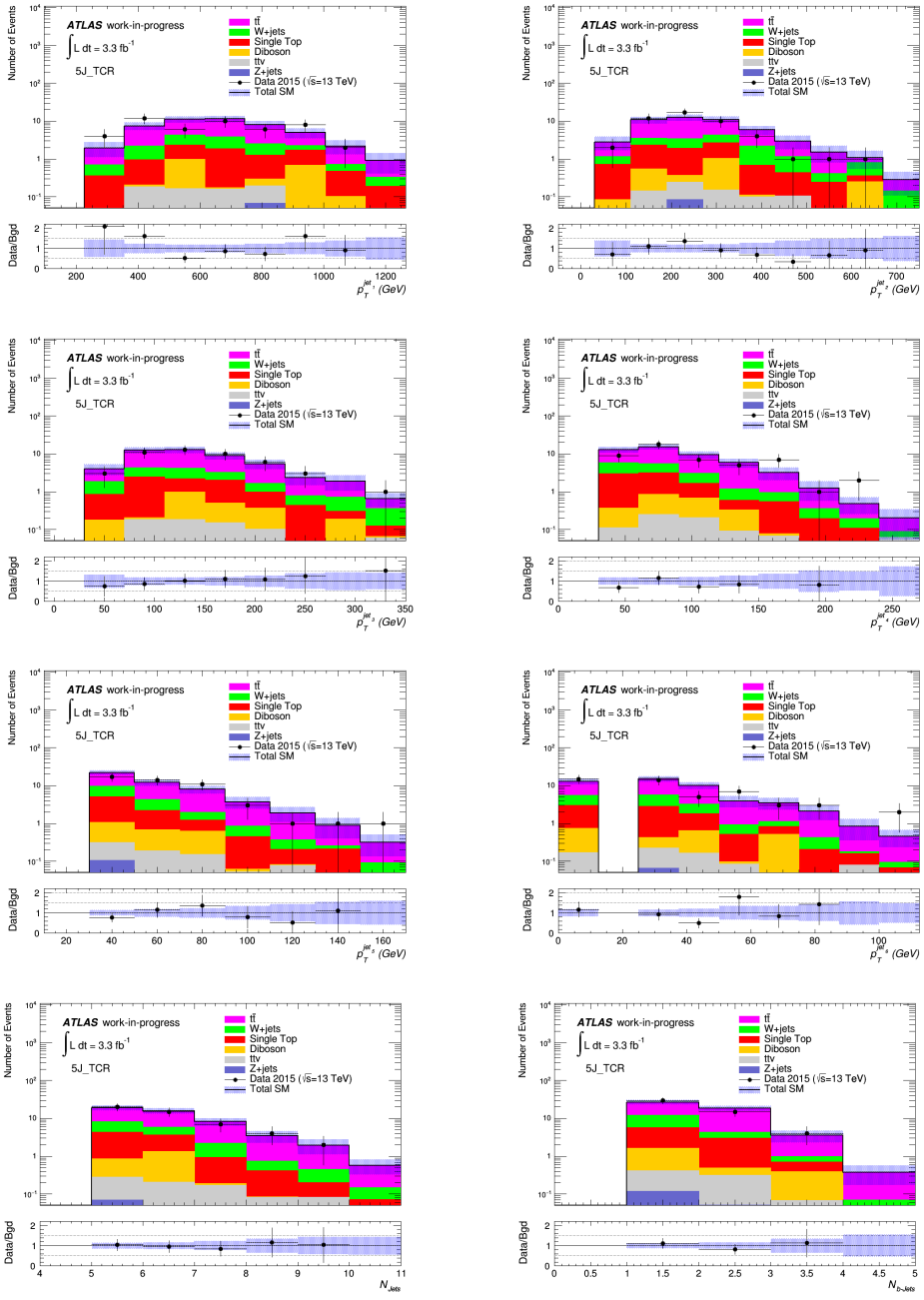

Figure C.10: Kinematic distributions of variables in the 5-jet *top* CR after background fit.

C.1.6 Kinematic distributions in the 5-jet WCR

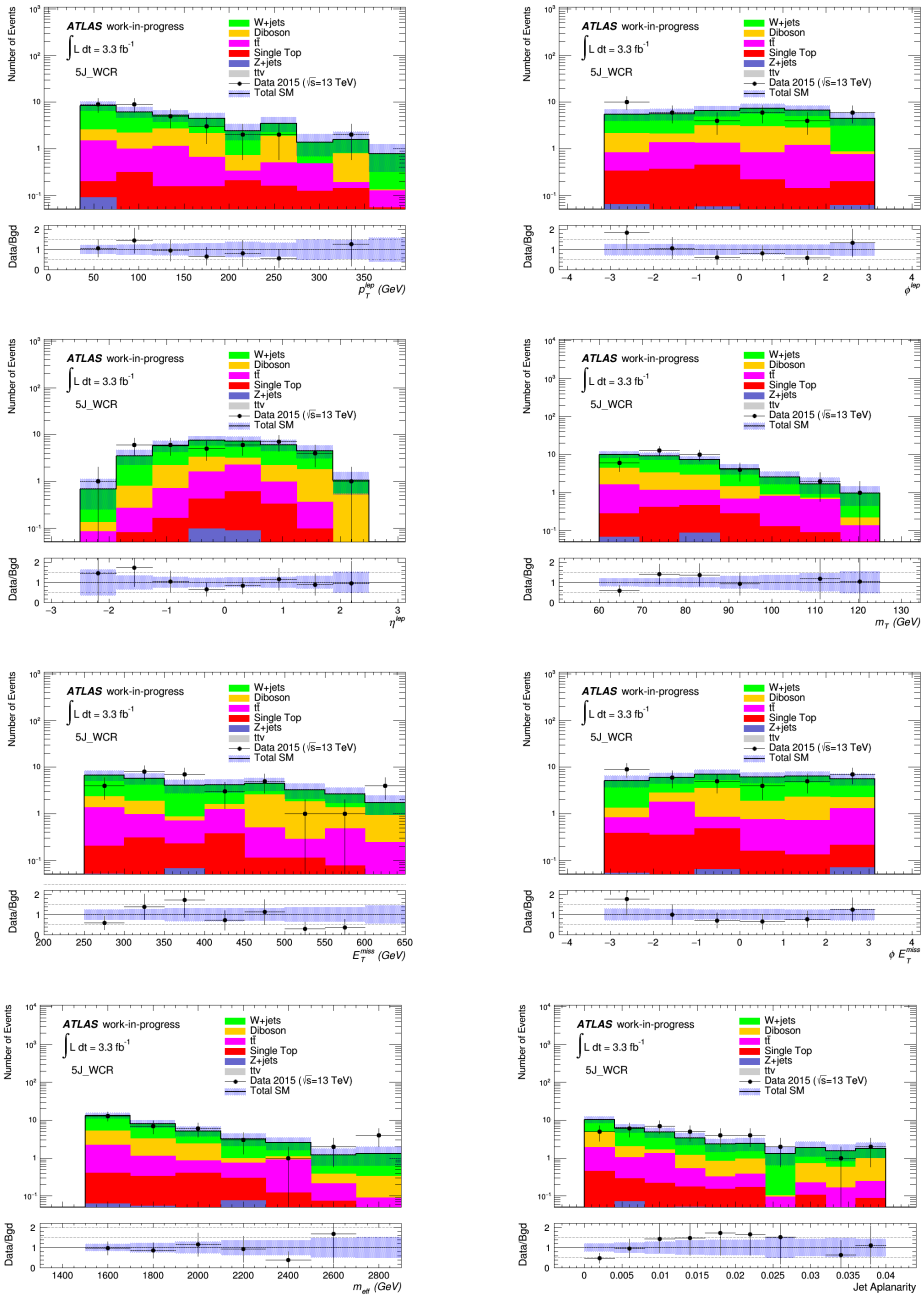

Figure C.11: Kinematic distributions of variables in the 5-jet W CR after background fit.

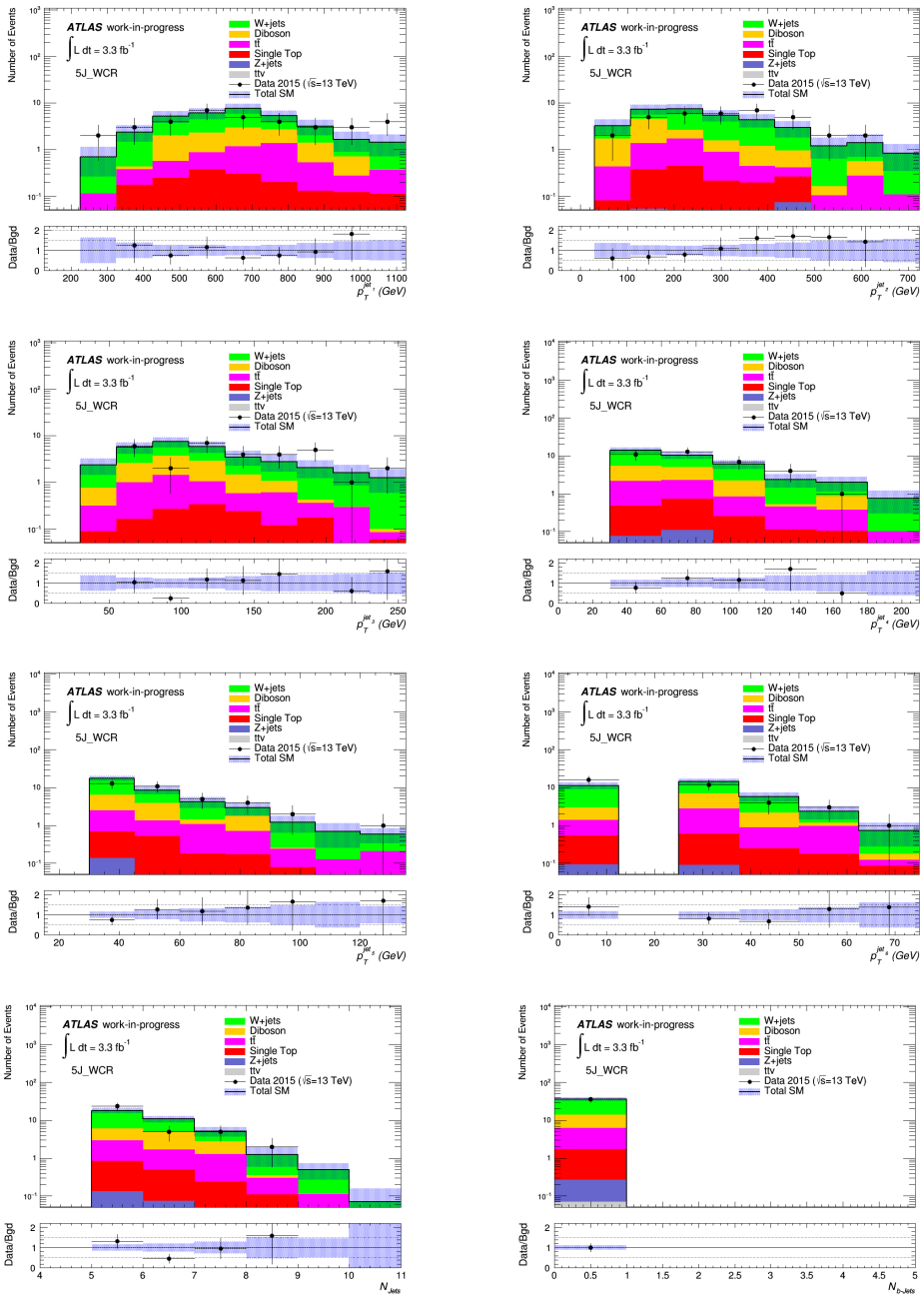

Figure C.12: Kinematic distributions of variables in the 5-jet W CR after background fit.

C.1.7 Kinematic distributions in the 6-jet TCR

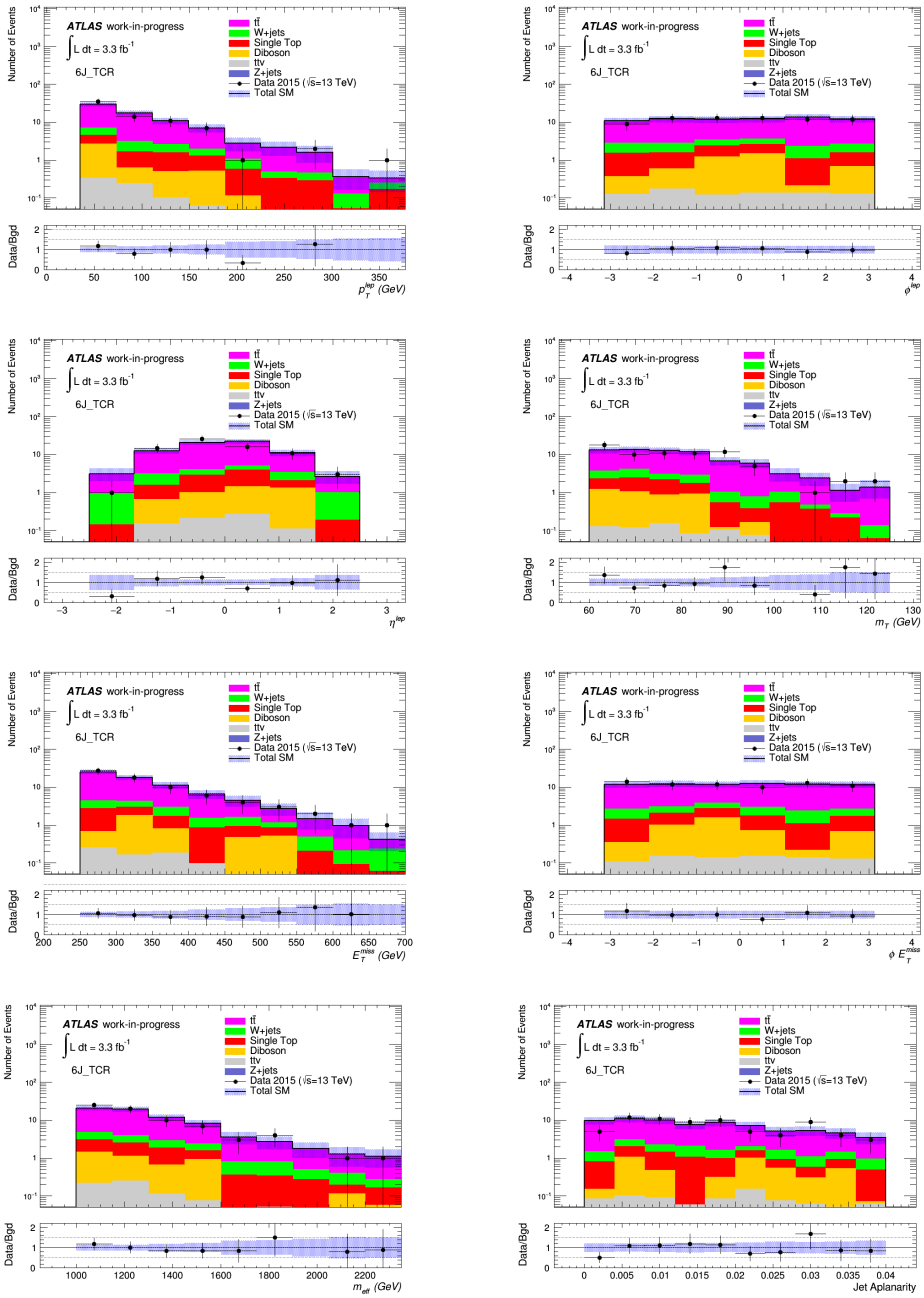

Figure C.13: Kinematic distributions of variables in the 6-jet *top* CR after background fit.

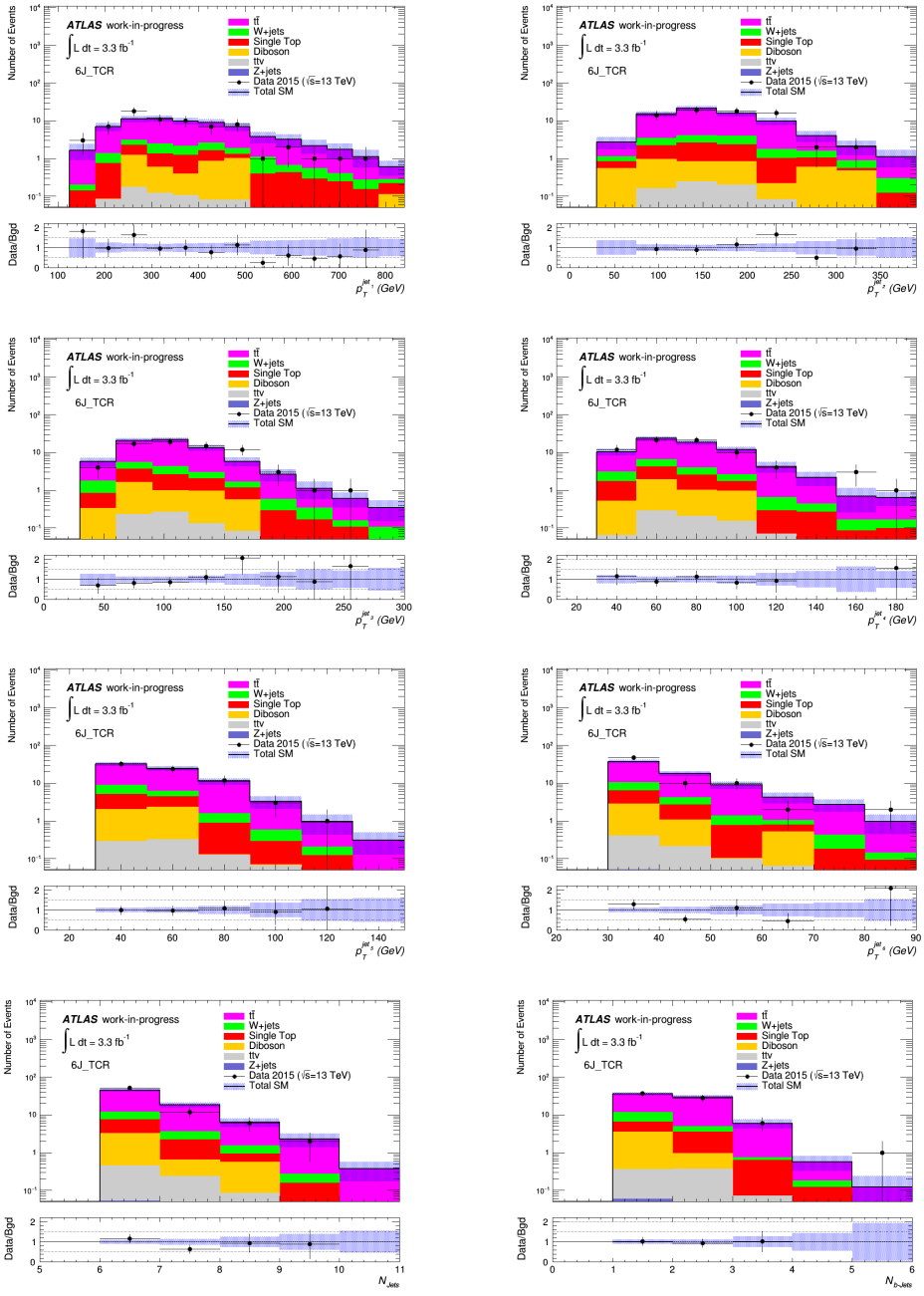

Figure C.14: Kinematic distributions of variables in the 6-jet *top* CR after background fit.

C.1.8 Kinematic distributions in the 6-jet WCR

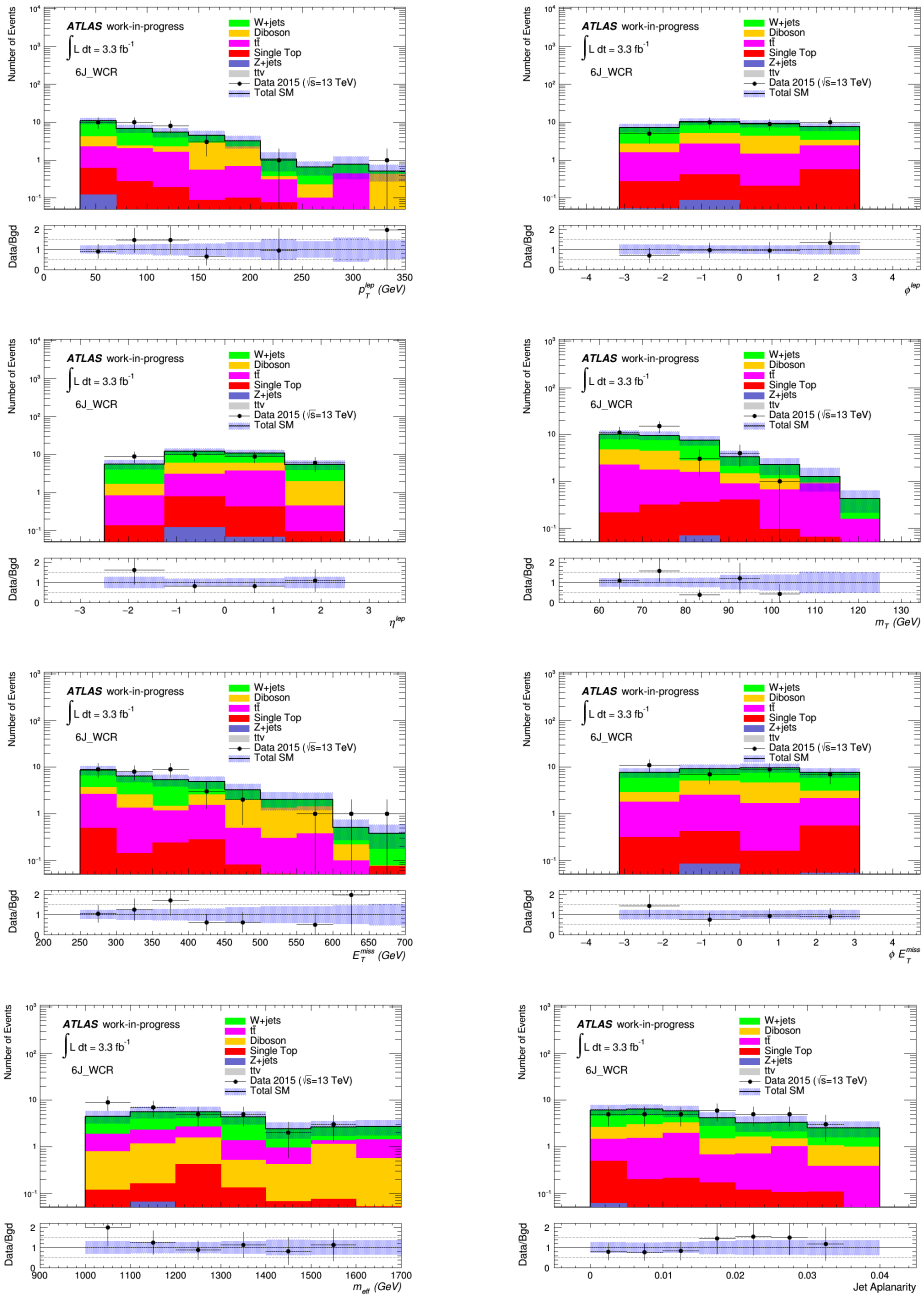

Figure C.15: Kinematic distributions of variables in the 6-jet W CR after background fit.

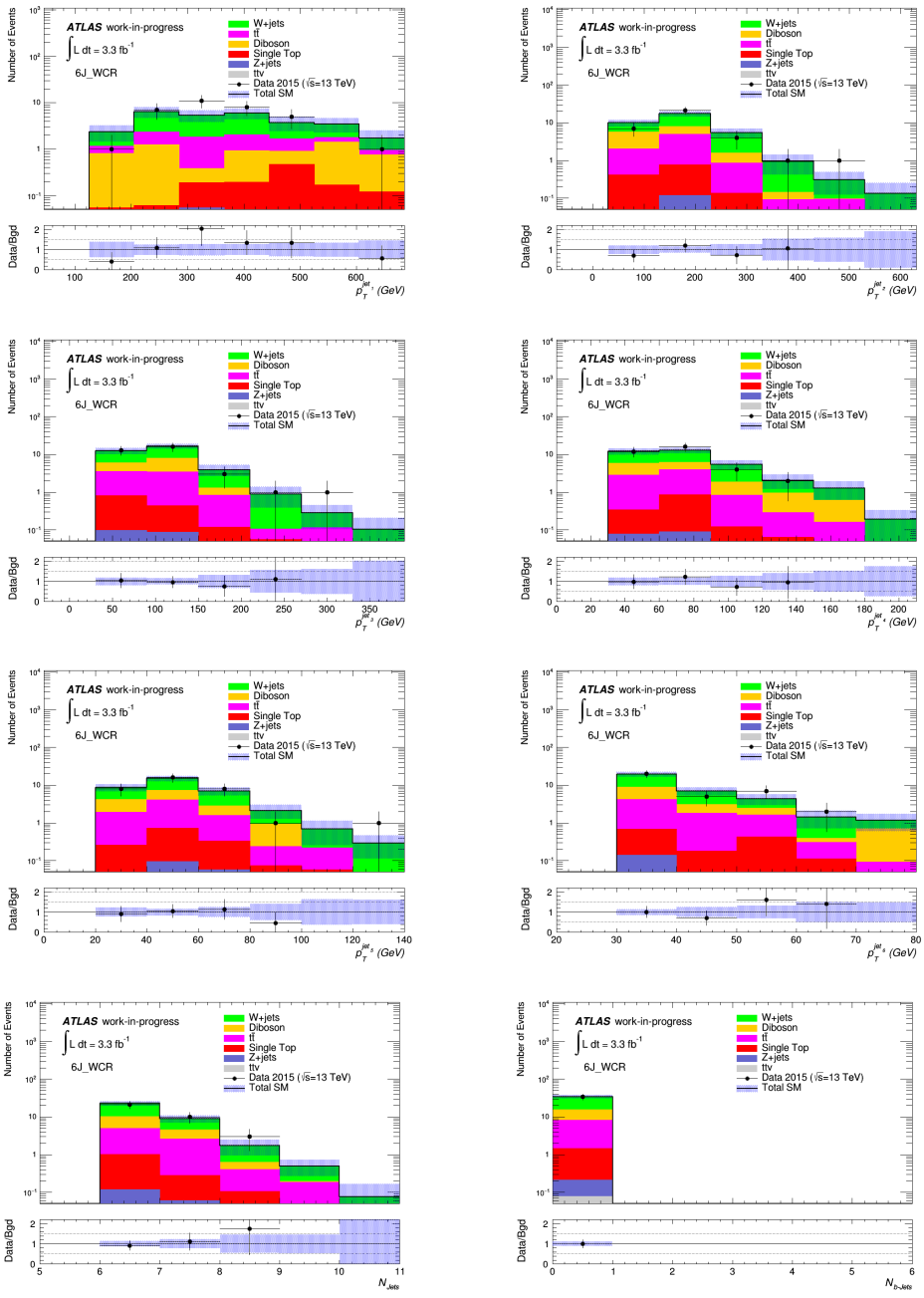

Figure C.16: Kinematic distributions of variables in the 6-jet W CR after background fit.

C.2 Additional background-only fit results.

In this section the Background-only fit results are presented for each of the different regions based on jet multiplicities. These results includes the fit parameters for normalization and nuisance parameters plus the correlation matrix between the parameters for each of the fits. Yields tables are included here for the soft lepton analysis.

C.2.1 4-jet low-x region

Parameter	Initial value	Fitted value	Up error	Down error
alpha_DibosonsScalesVar_TR4Jlowx	0.0000e+00	1.7184e-05	+1.00e+00	-1.00e+00
alpha_DibosonsScalesVar_WR4Jlowx	0.0000e+00	-8.1596e-04	+1.00e+00	-9.99e-01
alpha_Dibosons_TR4Jlowx	0.0000e+00	9.4065e-05	+1.00e+00	-1.00e+00
alpha_Dibosons_WR4Jlowx	0.0000e+00	-2.9883e-03	+1.00e+00	-9.97e-01
alpha_EG_RESOLUTION_ALL	0.0000e+00	-2.6361e-04	+1.00e+00	-1.00e+00
alpha_EG_SCALE_ALL	0.0000e+00	1.8664e-04	+1.00e+00	-1.00e+00
alpha_EL_Eff_ID	0.0000e+00	2.5562e-05	+1.00e+00	-1.00e+00
alpha_EL_Eff_Iso	0.0000e+00	1.1288e-03	+9.99e-01	-1.00e+00
alpha_EL_Eff_Reco	0.0000e+00	-2.0983e-05	+1.00e+00	-1.00e+00
alpha_JER	0.0000e+00	-5.1152e-04	+1.00e+00	-1.00e+00
alpha_JES_Group1	0.0000e+00	-1.2063e-03	+1.00e+00	-9.99e-01
alpha_JES_Group2	0.0000e+00	-4.1469e-03	+1.00e+00	-9.96e-01
alpha_JES_Group3	0.0000e+00	-3.6598e-03	+1.00e+00	-9.97e-01
alpha_MET_SoftTrk	0.0000e+00	-5.2922e-04	+1.00e+00	-1.00e+00
alpha_MET_SoftTrk_ResoPara	0.0000e+00	2.7904e-03	+9.97e-01	-1.00e+00
alpha_MET_SoftTrk_ResoPerp	0.0000e+00	-9.2836e-04	+1.00e+00	-9.99e-01
alpha_MUONS_ID	0.0000e+00	5.3299e-05	+1.00e+00	-1.00e+00
alpha_MUONS_MS	0.0000e+00	-1.3721e-03	+1.00e+00	-9.99e-01
alpha_MUONS_SCALE	0.0000e+00	1.2533e-05	+1.00e+00	-1.00e+00
alpha_MUON_Eff_Iso_stat	0.0000e+00	5.1852e-06	+1.00e+00	-1.00e+00
alpha_MUON_Eff_Iso_sys	0.0000e+00	1.2492e-05	+1.00e+00	-1.00e+00
alpha_MUON_Eff_stat	0.0000e+00	-2.3936e-06	+1.00e+00	-1.00e+00
alpha_MUON_Eff_stat_lowpt	0.0000e+00	0.0000e+00	+1.00e+00	-1.00e+00
alpha_MUON_Eff_sys	0.0000e+00	-1.1632e-05	+1.00e+00	-1.00e+00
alpha_MUON_Eff_sys_lowpt	0.0000e+00	0.0000e+00	+1.00e+00	-1.00e+00
alpha_ZjetsScalesVar_TR4Jlowx	0.0000e+00	6.8810e-05	+1.00e+00	-1.00e+00
alpha_ZjetsScalesVar_WR4Jlowx	0.0000e+00	-4.3300e-05	+1.00e+00	-1.00e+00
alpha_ZjetsTheo_TR4Jlowx	0.0000e+00	2.5298e-04	+1.00e+00	-1.00e+00
alpha_ZjetsTheo_WR4Jlowx	0.0000e+00	-1.6363e-04	+1.00e+00	-1.00e+00
alpha_btag_BT	0.0000e+00	-1.3120e-02	+1.01e+00	-9.87e-01
alpha_btag_CT	0.0000e+00	-1.2985e-03	+1.00e+00	-9.99e-01
alpha_btag_Extrapolation	0.0000e+00	2.1300e-03	+9.98e-01	-1.00e+00
alpha_btag_LightT	0.0000e+00	-2.8451e-03	+1.00e+00	-9.97e-01
alpha_h1L_DBXsec	0.0000e+00	-1.1657e-03	+1.00e+00	-9.99e-01
alpha_h1L_SingleTopComm	0.0000e+00	1.6169e-03	+9.99e-01	-1.00e+00
alpha_h1L_ZjetsXsec	0.0000e+00	1.8209e-05	+1.00e+00	-1.00e+00
alpha_h1L_ttvComm	0.0000e+00	6.8129e-04	+1.00e+00	-1.00e+00
alpha_pileup	0.0000e+00	6.0405e-03	+9.94e-01	-1.01e+00
gamma_stat_TR4JlowxEM_cuts_bin_0	1.0000e+00	1.0007e+00	+6.89e-02	-7.03e-02
gamma_stat_WR4JlowxEM_cuts_bin_0	1.0000e+00	1.0001e+00	+6.48e-02	-6.51e-02
mu_Top	1.0000e+00	5.1899e-01	+3.82e-01	-3.21e-01
mu_W	1.0000e+00	9.8339e-01	+3.39e-01	-3.23e-01

`Table C.1:` Background only fit results in the 4-jet low-x regions

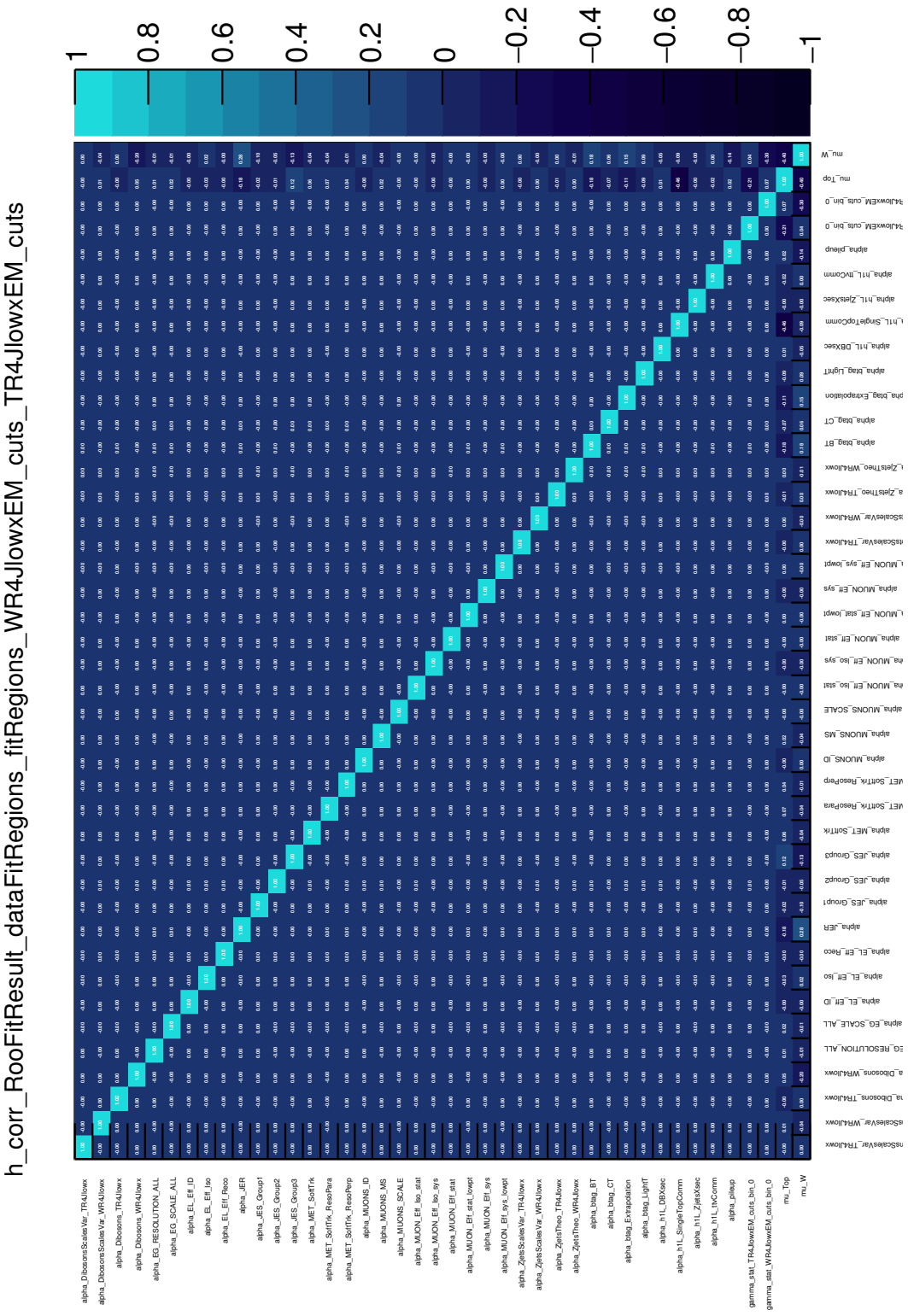

Figure C.17: Correlation matrix for the background-only fit in the 4-jet low-x region.

Uncertainty of channel	**4-jet low-x SR**
Total background expectation	1.27
Total statistical($\sqrt{N_{exp}}$)	± 1.13
Total background systematic	± 0.50 [39.80%]
alpha_h1L_SingleTopComm	± 0.43 [33.8%]
mu_Top	± 0.27 [21.4%]
gamma_stat_SR4JlowxEM_cuts_bin_0	± 0.20 [16.0%]
alpha_JES_Group1	± 0.15 [11.9%]
alpha_JES_Group3	± 0.10 [8.1%]
alpha_MET_SoftTrk	± 0.10 [8.1%]
alpha_MET_SoftTrk_ResoPerp	± 0.08 [6.6%]
mu_W	± 0.06 [5.1%]
alpha_JER	± 0.06 [5.1%]
alpha_HadFrag_SR4Jhighx	± 0.06 [4.7%]
alpha_FactRenScaleISRFSR_SR4Jhighx	± 0.06 [4.7%]
alpha_MET_SoftTrk_ResoPara	± 0.06 [4.7%]
alpha_Wjets_SR4Jhighx	± 0.06 [4.5%]
alpha_EG_SCALE_ALL	± 0.05 [4.3%]
alpha_MUONS_MS	± 0.05 [4.2%]
alpha_pileup	± 0.03 [2.6%]
alpha_HardScatteringGen_SR4Jhighx	± 0.03 [2.5%]
alpha_JES_Group2	± 0.03 [2.5%]
alpha_Dibosons_SR4Jlowx	± 0.02 [1.6%]
alpha_h1L_ttvComm	± 0.01 [1.1%]
alpha_MUON_Eff_Iso_sys	± 0.01 [1.1%]
alpha_ZjetsTheo_SR4Jlowx	± 0.01 [0.91%]
alpha_WJetsScaleVar_SR4Jhighx	± 0.01 [0.75%]
alpha_MUON_Eff_sys	± 0.01 [0.72%]
alpha_EG_RESOLUTION_ALL	± 0.01 [0.71%]
alpha_MUONS_ID	± 0.01 [0.53%]
alpha_EL_Eff_Iso	± 0.01 [0.53%]
alpha_EL_Eff_ID	± 0.01 [0.42%]
alpha_h1L_DBXsec	± 0.00 [0.27%]
alpha_ZjetsScalesVar_SR4Jlowx	± 0.00 [0.25%]
alpha_DibosonsScalesVar_SR4Jlowx	± 0.00 [0.23%]
alpha_EL_Eff_Reco	± 0.00 [0.18%]
alpha_h1L_ZjetsXsec	± 0.00 [0.17%]

`Table C.2:` Background only fit results in the 4-jet low-x regions

C.2.2 4-jet high-x region

Parameter	Initial value	Fitted value	Up error	Down error
alpha_DibosonsScalesVar_TR4Jhighx	0.0000e+00	-1.7532e-04	+1.00e+00	-1.00e+00
alpha_DibosonsScalesVar_WR4Jhighx	0.0000e+00	-3.9457e-04	+1.00e+00	-1.00e+00
alpha_Dibosons_TR4Jhighx	0.0000e+00	-1.8060e-03	+1.00e+00	-9.98e-01
alpha_Dibosons_WR4Jhighx	0.0000e+00	-4.4630e-03	+1.00e+00	-9.96e-01
alpha_EG_RESOLUTION_ALL	0.0000e+00	1.0863e-02	+9.89e-01	-1.01e+00
alpha_EG_SCALE_ALL	0.0000e+00	3.4408e-03	+9.97e-01	-1.00e+00
alpha_EL_Eff_ID	0.0000e+00	-3.4972e-04	+1.00e+00	-1.00e+00
alpha_EL_Eff_Iso	0.0000e+00	-3.2772e-04	+1.00e+00	-1.00e+00
alpha_EL_Eff_Reco	0.0000e+00	-1.3070e-04	+1.00e+00	-1.00e+00
alpha_JER	0.0000e+00	-6.3190e-03	+1.01e+00	-9.94e-01
alpha_JES_Group1	0.0000e+00	5.6110e-03	+9.95e-01	-1.01e+00
alpha_JES_Group2	0.0000e+00	5.3629e-03	+9.95e-01	-1.01e+00
alpha_JES_Group3	0.0000e+00	3.9412e-03	+9.96e-01	-1.00e+00
alpha_MET_SoftTrk	0.0000e+00	1.0007e-03	+9.99e-01	-1.00e+00
alpha_MET_SoftTrk_ResoPara	0.0000e+00	6.2300e-04	+1.00e+00	-1.00e+00
alpha_MET_SoftTrk_ResoPerp	0.0000e+00	1.5247e-03	+9.99e-01	-1.00e+00
alpha_MUONS_ID	0.0000e+00	1.6685e-03	+9.99e-01	-1.00e+00
alpha_MUONS_MS	0.0000e+00	1.8383e-03	+9.98e-01	-1.00e+00
alpha_MUONS_SCALE	0.0000e+00	-4.0007e-05	+1.00e+00	-1.00e+00
alpha_MUON_Eff_Iso_stat	0.0000e+00	-3.1415e-05	+1.00e+00	-1.00e+00
alpha_MUON_Eff_Iso_sys	0.0000e+00	-2.3978e-04	+1.00e+00	-1.00e+00
alpha_MUON_Eff_stat	0.0000e+00	-4.4559e-05	+1.00e+00	-1.00e+00
alpha_MUON_Eff_stat_lowpt	0.0000e+00	0.0000e+00	+1.00e+00	-1.00e+00
alpha_MUON_Eff_sys	0.0000e+00	-3.0095e-04	+1.00e+00	-1.00e+00
alpha_MUON_Eff_sys_lowpt	0.0000e+00	0.0000e+00	+1.00e+00	-1.00e+00
alpha_ZjetsScalesVar_TR4Jhighx	0.0000e+00	-6.3509e-05	+1.00e+00	-1.00e+00
alpha_ZjetsScalesVar_WR4Jhighx	0.0000e+00	-5.7261e-05	+1.00e+00	-1.00e+00
alpha_ZjetsTheo_TR4Jhighx	0.0000e+00	-1.7660e-04	+1.00e+00	-1.00e+00
alpha_ZjetsTheo_WR4Jhighx	0.0000e+00	-1.5869e-04	+1.00e+00	-1.00e+00
alpha_btag_BT	0.0000e+00	2.7557e-03	+9.97e-01	-1.00e+00
alpha_btag_CT	0.0000e+00	-2.5267e-04	+1.00e+00	-1.00e+00
alpha_btag_Extrapolation	0.0000e+00	-6.1686e-04	+1.00e+00	-1.00e+00
alpha_btag_LightT	0.0000e+00	4.9437e-03	+9.95e-01	-1.01e+00
alpha_h1L_DBXsec	0.0000e+00	-1.1248e-03	+1.00e+00	-9.99e-01
alpha_h1L_SingleTopComm	0.0000e+00	3.1865e-03	+9.97e-01	-1.00e+00
alpha_h1L_ZjetsXsec	0.0000e+00	-7.5426e-05	+1.00e+00	-1.00e+00
alpha_h1L_ttvComm	0.0000e+00	-9.5328e-04	+1.00e+00	-9.99e-01
alpha_pileup	0.0000e+00	-6.0790e-03	+1.01e+00	-9.94e-01
gamma_stat_TR4JhighxEM_cuts_bin_0	1.0000e+00	9.9980e-01	+4.45e-02	-4.41e-02
gamma_stat_WR4JhighxEM_cuts_bin_0	1.0000e+00	9.9996e-01	+5.92e-02	-5.91e-02
mu_Top	1.0000e+00	3.3688e-01	+2.83e-01	-2.47e-01
mu_W	1.0000e+00	1.0404e+00	+3.24e-01	-3.09e-01

`Table C.3:` Background only fit results in the 4-jet high-x regions

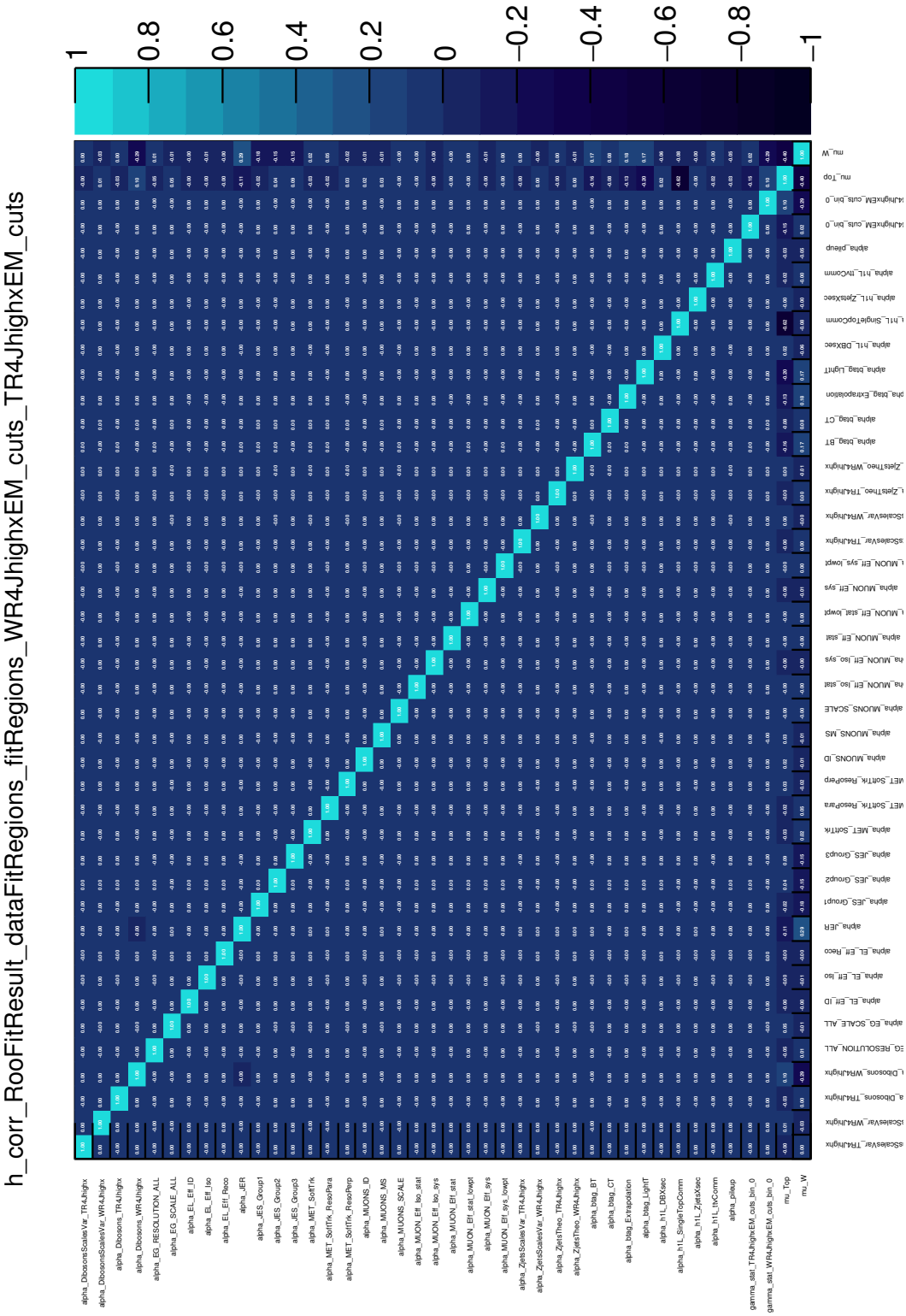

Figure C.18: Correlation matrix for the background-only fit in the 4-jet high-x region.

Uncertainty of channel	**4-jet high-x SR**
Total background expectation	0.92
Total statistical($\sqrt{N_{exp}}$)	± 0.96
Total background systematic	± 0.50 [54.49%]
gamma_stat_SR4JhighxEM_cuts_bin_0	± 0.30 [32.6%]
alpha_MUONS_MS	± 0.25 [27.7%]
mu_W	± 0.23 [24.7%]
alpha_Wjets_SR4Jhighx	± 0.22 [24.3%]
mu_Top	± 0.07 [7.1%]
alpha_WJetsScaleVar_SR4Jhighx	± 0.04 [4.1%]
alpha_MUON_Eff_sys	± 0.03 [3.3%]
alpha_h1L_SingleTopComm	± 0.03 [3.2%]
alpha_JES_Group3	± 0.03 [3.2%]
alpha_MUON_Eff_Iso_sys	± 0.02 [2.4%]
alpha_pileup	± 0.02 [2.4%]
alpha_JER	± 0.02 [2.3%]
alpha_HadFrag_SR4Jhighx	± 0.01 [1.4%]
alpha_FactRenScaleISRFSR_SR4Jhighx	± 0.01 [1.4%]
alpha_JES_Group1	± 0.01 [1.1%]
alpha_EL_Eff_Iso	± 0.01 [1.1%]
alpha_h1L_ttvComm	± 0.01 [0.78%]
alpha_HardScatteringGen_SR4Jhighx	± 0.01 [0.72%]
alpha_ZjetsTheo_SR4Jhighx	± 0.01 [0.68%]
alpha_MET_SoftTrk_ResoPara	± 0.01 [0.56%]
alpha_EG_RESOLUTION_ALL	± 0.00 [0.54%]
alpha_JES_Group2	± 0.00 [0.40%]
alpha_MUONS_SCALE	± 0.00 [0.26%]
alpha_ZjetsScalesVar_SR4Jhighx	± 0.00 [0.25%]
alpha_EL_Eff_ID	± 0.00 [0.24%]
alpha_MET_SoftTrk	± 0.00 [0.19%]
alpha_h1L_ZjetsXsec	± 0.00 [0.18%]
alpha_MET_SoftTrk_ResoPerp	± 0.00 [0.17%]
alpha_EL_Eff_Reco	± 0.00 [0.11%]
alpha_Dibosons_SR4Jhighx	± 0.00 [0.07%]
alpha_MUONS_ID	± 0.00 [0.07%]
alpha_MUON_Eff_stat	± 0.00 [0.05%]
alpha_EG_SCALE_ALL	± 0.00 [0.02%]

`Table C.4:` Dominant systematic uncertainties in the 4-jet high-x SR. Individual uncertainties can correlate, and do not add up quadratically to the total background uncertainty.

C.2.3 5-jet region

Parameter	Initial value	Fitted value	Up error	Down error
alpha_DibosonsScalesVar_TR5J	0.0000e+00	-8.6614e-06	+1.00e+00	-1.00e+00
alpha_DibosonsScalesVar_WR5J	0.0000e+00	1.8588e-03	+9.99e-01	-1.00e+00
alpha_Dibosons_TR5J	0.0000e+00	1.9907e-04	+1.00e+00	-1.00e+00
alpha_Dibosons_WR5J	0.0000e+00	1.3242e-02	+9.88e-01	-1.01e+00
alpha_EG_RESOLUTION_ALL	0.0000e+00	-3.5997e-04	+1.00e+00	-1.00e+00
alpha_EG_SCALE_ALL	0.0000e+00	-3.6093e-03	+1.00e+00	-9.97e-01
alpha_EL_Eff_ID	0.0000e+00	1.0701e-03	+1.00e+00	-1.00e+00
alpha_EL_Eff_Iso	0.0000e+00	1.0746e-03	+1.00e+00	-1.00e+00
alpha_EL_Eff_Reco	0.0000e+00	4.5385e-04	+1.00e+00	-1.00e+00
alpha_JER	0.0000e+00	3.0361e-04	+1.00e+00	-1.00e+00
alpha_JES_Group1	0.0000e+00	2.9401e-03	+9.98e-01	-1.00e+00
alpha_JES_Group2	0.0000e+00	1.7231e-04	+1.00e+00	-1.00e+00
alpha_JES_Group3	0.0000e+00	8.7676e-03	+9.92e-01	-1.01e+00
alpha_MET_SoftTrk	0.0000e+00	-8.0635e-04	+1.00e+00	-1.00e+00
alpha_MET_SoftTrk_ResoPara	0.0000e+00	-7.8009e-04	+1.00e+00	-1.00e+00
alpha_MET_SoftTrk_ResoPerp	0.0000e+00	-1.8092e-03	+1.00e+00	-9.99e-01
alpha_MUONS_ID	0.0000e+00	1.6543e-04	+1.00e+00	-1.00e+00
alpha_MUONS_MS	0.0000e+00	-3.1342e-04	+1.00e+00	-1.00e+00
alpha_MUONS_SCALE	0.0000e+00	2.1605e-04	+1.00e+00	-1.00e+00
alpha_MUON_Eff_Iso_stat	0.0000e+00	5.1134e-05	+1.00e+00	-1.00e+00
alpha_MUON_Eff_Iso_sys	0.0000e+00	3.1748e-04	+1.00e+00	-1.00e+00
alpha_MUON_Eff_stat	0.0000e+00	7.5159e-05	+1.00e+00	-1.00e+00
alpha_MUON_Eff_stat_lowpt	0.0000e+00	0.0000e+00	+1.00e+00	-1.00e+00
alpha_MUON_Eff_sys	0.0000e+00	4.7478e-04	+1.00e+00	-1.00e+00
alpha_MUON_Eff_sys_lowpt	0.0000e+00	0.0000e+00	+1.00e+00	-1.00e+00
alpha_ZjetsScalesVar_TR5J	0.0000e+00	-2.0733e-05	+1.00e+00	-1.00e+00
alpha_ZjetsScalesVar_WR5J	0.0000e+00	1.5237e-04	+1.00e+00	-1.00e+00
alpha_ZjetsTheo_TR5J	0.0000e+00	-4.7265e-05	+1.00e+00	-1.00e+00
alpha_ZjetsTheo_WR5J	0.0000e+00	3.6585e-04	+1.00e+00	-1.00e+00
alpha_btag_BT	0.0000e+00	-2.6678e-02	+1.03e+00	-9.74e-01
alpha_btag_CT	0.0000e+00	-8.7899e-03	+1.01e+00	-9.92e-01
alpha_btag_Extrapolation	0.0000e+00	-1.1373e-02	+1.01e+00	-9.90e-01
alpha_btag_LightT	0.0000e+00	-9.9444e-03	+1.01e+00	-9.91e-01
alpha_h1L_DBXsec	0.0000e+00	3.7080e-03	+9.97e-01	-1.00e+00
alpha_h1L_SingleTopComm	0.0000e+00	9.3328e-03	+9.92e-01	-1.01e+00
alpha_h1L_ZjetsXsec	0.0000e+00	8.2174e-05	+1.00e+00	-1.00e+00
alpha_h1L_ttvComm	0.0000e+00	8.7297e-05	+1.00e+00	-1.00e+00
alpha_pileup	0.0000e+00	-1.4596e-03	+1.00e+00	-9.99e-01
gamma_stat_TR5JEM_cuts_bin_0	1.0000e+00	9.9964e-01	+3.31e-02	-3.23e-02
gamma_stat_WR5JEM_cuts_bin_0	1.0000e+00	1.0004e+00	+5.46e-02	-5.54e-02
mu_Top	1.0000e+00	6.5232e-01	+2.33e-01	-2.16e-01
mu_W	1.0000e+00	7.6075e-01	+2.87e-01	-2.56e-01

`Table C.5:` Background only fit results in the 5-jet regions

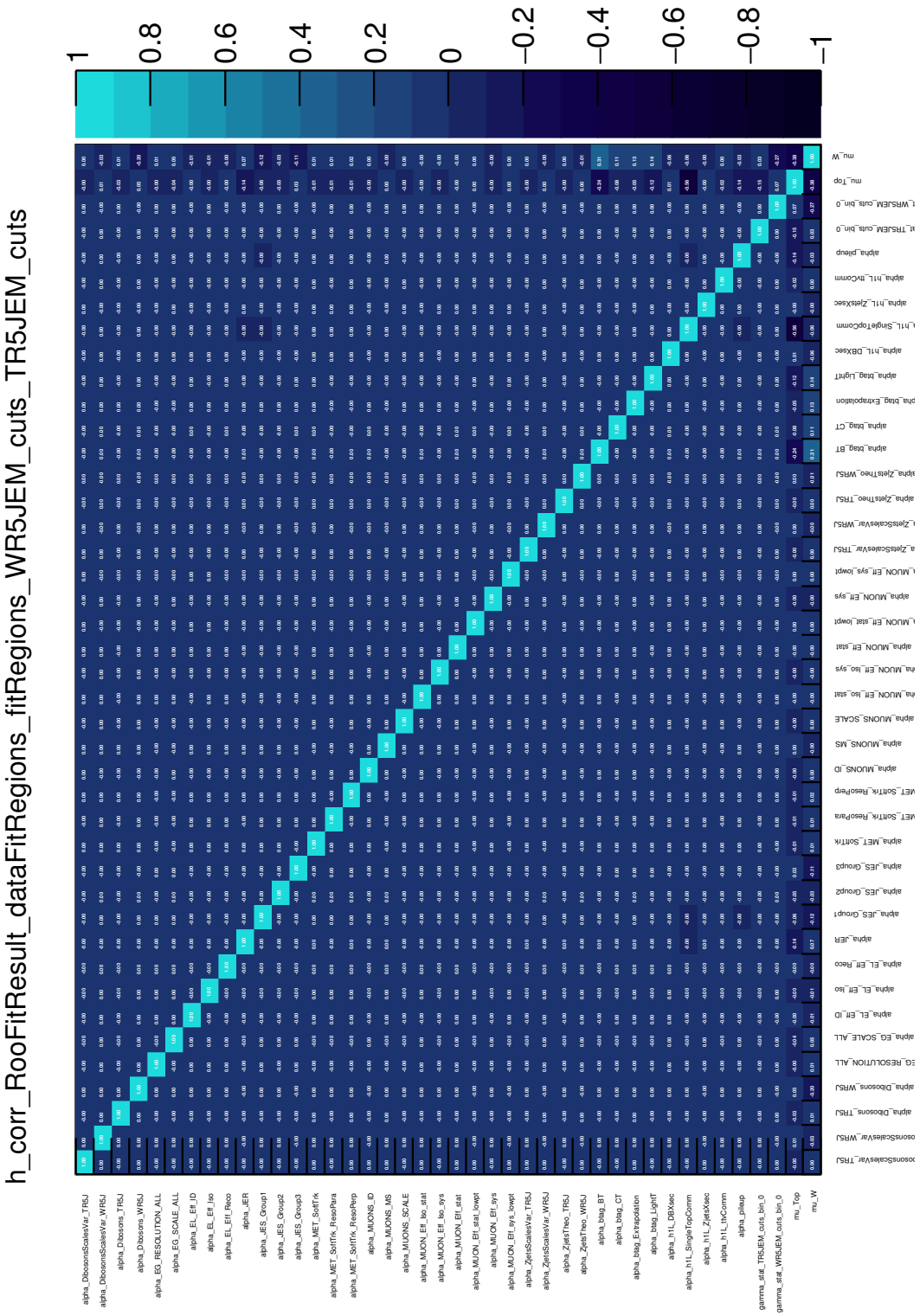

Figure C.19: Correlation matrix for the background-only fit in the 5-jet region.

Uncertainty of channel	**5-jet SR**
Total background expectation	1.27
Total statistical($\sqrt{N_{exp}}$)	± 1.13
Total background systematic	± 0.55 [43.33%]
gamma_stat_SR5JEM_cuts_bin_0	± 0.30 [23.6%]
alpha_MUONS_MS	± 0.28 [22.3%]
alpha_pileup	± 0.28 [21.8%]
alpha_h1L_SingleTopComm	± 0.18 [14.4%]
mu_Top	± 0.14 [10.9%]
alpha_JES_Group1	± 0.10 [7.6%]
alpha_JES_Group3	± 0.08 [6.7%]
alpha_Dibosons_SR5J	± 0.08 [6.6%]
alpha_JES_Group2	± 0.08 [6.4%]
alpha_HardScatteringGen_SR5J	± 0.08 [6.3%]
alpha_HadFrag_SR5J	± 0.06 [4.7%]
mu_W	± 0.06 [4.6%]
alpha_MUONS_ID	± 0.06 [4.3%]
alpha_FactRenScaleISRFSR_SR5J	± 0.05 [4.1%]
alpha_Wjets_SR5J	± 0.05 [3.7%]
alpha_MUON_Eff_Iso_sys	± 0.04 [2.8%]
alpha_WJetsScaleVar_SR5J	± 0.02 [1.9%]
alpha_h1L_DBXsec	± 0.02 [1.7%]
alpha_MUON_Eff_sys	± 0.02 [1.7%]
alpha_MET_SoftTrk_ResoPerp	± 0.02 [1.5%]
alpha_MET_SoftTrk_ResoPara	± 0.02 [1.4%]
alpha_h1L_ttvComm	± 0.02 [1.4%]
alpha_EG_RESOLUTION_ALL	± 0.02 [1.3%]
alpha_DibosonsScalesVar_SR5J	± 0.01 [1.1%]
alpha_ZjetsTheo_SR5J	± 0.01 [1.1%]
alpha_JER	± 0.01 [1.0%]
alpha_ZjetsScalesVar_SR5J	± 0.01 [0.46%]
alpha_h1L_ZjetsXsec	± 0.00 [0.28%]
alpha_EG_SCALE_ALL	± 0.00 [0.20%]
alpha_EL_Eff_ID	± 0.00 [0.15%]
alpha_MET_SoftTrk	± 0.00 [0.09%]
alpha_MUON_Eff_stat	± 0.00 [0.09%]
alpha_EL_Eff_Reco	± 0.00 [0.04%]
alpha_EL_Eff_Iso	± 0.00 [0.03%]
alpha_MUON_Eff_Iso_stat	± 0.00 [0.01%]

`Table C.6:` Dominant systematic uncertainties in the 5-jet SR. Individual uncertainties can correlate, and do not add up quadratically to the total background uncertainty.

C.2.4 6-jet region

Parameter	Initial value	Fitted value	Up error	Down error
alpha_DibosonsScalesVar_TR6J	0.0000e+00	1.0635e-03	+1.00e+00	-1.00e+00
alpha_DibosonsScalesVar_WR6J	0.0000e+00	-1.0462e-03	+1.00e+00	-1.00e+00
alpha_Dibosons_TR6J	0.0000e+00	9.3037e-03	+9.92e-01	-1.01e+00
alpha_Dibosons_WR6J	0.0000e+00	-6.8358e-03	+1.01e+00	-9.94e-01
alpha_EG_RESOLUTION_ALL	0.0000e+00	2.6248e-03	+9.98e-01	-1.00e+00
alpha_EG_SCALE_ALL	0.0000e+00	-2.1016e-04	+1.00e+00	-1.00e+00
alpha_EL_Eff_ID	0.0000e+00	3.2399e-05	+1.00e+00	-1.00e+00
alpha_EL_Eff_Iso	0.0000e+00	-8.5266e-05	+1.00e+00	-1.00e+00
alpha_EL_Eff_Reco	0.0000e+00	1.3119e-05	+1.00e+00	-1.00e+00
alpha_JER	0.0000e+00	-5.5928e-03	+1.01e+00	-9.95e-01
alpha_JES_Group1	0.0000e+00	-1.1782e-02	+1.01e+00	-9.89e-01
alpha_JES_Group2	0.0000e+00	-5.6769e-03	+1.01e+00	-9.95e-01
alpha_JES_Group3	0.0000e+00	2.9914e-04	+1.00e+00	-1.00e+00
alpha_MET_SoftTrk	0.0000e+00	2.3346e-03	+9.99e-01	-1.00e+00
alpha_MET_SoftTrk_ResoPara	0.0000e+00	2.9555e-03	+9.98e-01	-1.00e+00
alpha_MET_SoftTrk_ResoPerp	0.0000e+00	3.9930e-03	+9.97e-01	-1.00e+00
alpha_MUONS_ID	0.0000e+00	1.1473e-04	+1.00e+00	-1.00e+00
alpha_MUONS_MS	0.0000e+00	-1.3938e-03	+1.00e+00	-1.00e+00
alpha_MUONS_SCALE	0.0000e+00	3.9733e-05	+1.00e+00	-1.00e+00
alpha_MUON_Eff_Iso_stat	0.0000e+00	1.6986e-05	+1.00e+00	-1.00e+00
alpha_MUON_Eff_Iso_sys	0.0000e+00	7.5211e-05	+1.00e+00	-1.00e+00
alpha_MUON_Eff_stat	0.0000e+00	2.0365e-05	+1.00e+00	-1.00e+00
alpha_MUON_Eff_stat_lowpt	0.0000e+00	0.0000e+00	+1.00e+00	-1.00e+00
alpha_MUON_Eff_sys	0.0000e+00	1.0769e-04	+1.00e+00	-1.00e+00
alpha_MUON_Eff_sys_lowpt	0.0000e+00	0.0000e+00	+1.00e+00	-1.00e+00
alpha_ZjetsScalesVar_TR6J	0.0000e+00	5.3625e-05	+1.00e+00	-1.00e+00
alpha_ZjetsScalesVar_WR6J	0.0000e+00	-4.9623e-05	+1.00e+00	-1.00e+00
alpha_ZjetsTheo_TR6J	0.0000e+00	1.0799e-04	+1.00e+00	-1.00e+00
alpha_ZjetsTheo_WR6J	0.0000e+00	-9.9632e-05	+1.00e+00	-1.00e+00
alpha_btag_BT	0.0000e+00	1.4843e-02	+9.86e-01	-1.02e+00
alpha_btag_CT	0.0000e+00	5.0953e-03	+9.96e-01	-1.01e+00
alpha_btag_Extrapolation	0.0000e+00	2.6083e-03	+9.98e-01	-1.00e+00
alpha_btag_LightT	0.0000e+00	7.2873e-03	+9.94e-01	-1.01e+00
alpha_h1L_DBXsec	0.0000e+00	4.4096e-05	+1.00e+00	-1.00e+00
alpha_h1L_SingleTopComm	0.0000e+00	5.4745e-03	+9.95e-01	-1.01e+00
alpha_h1L_ZjetsXsec	0.0000e+00	1.8052e-06	+1.00e+00	-1.00e+00
alpha_h1L_ttvComm	0.0000e+00	1.9364e-03	+9.99e-01	-1.00e+00
alpha_pileup	0.0000e+00	-1.8650e-02	+1.02e+00	-9.82e-01
gamma_stat_TR6JEM_cuts_bin_0	1.0000e+00	1.0005e+00	+3.28e-02	-3.39e-02
gamma_stat_WR6JEM_cuts_bin_0	1.0000e+00	9.9969e-01	+6.03e-02	-5.96e-02
mu_Top	1.0000e+00	8.1805e-01	+1.85e-01	-1.62e-01
mu_W	1.0000e+00	7.1967e-01	+3.11e-01	-3.33e-01

`Table C.7:` Background only fit results in the 6-jet regions

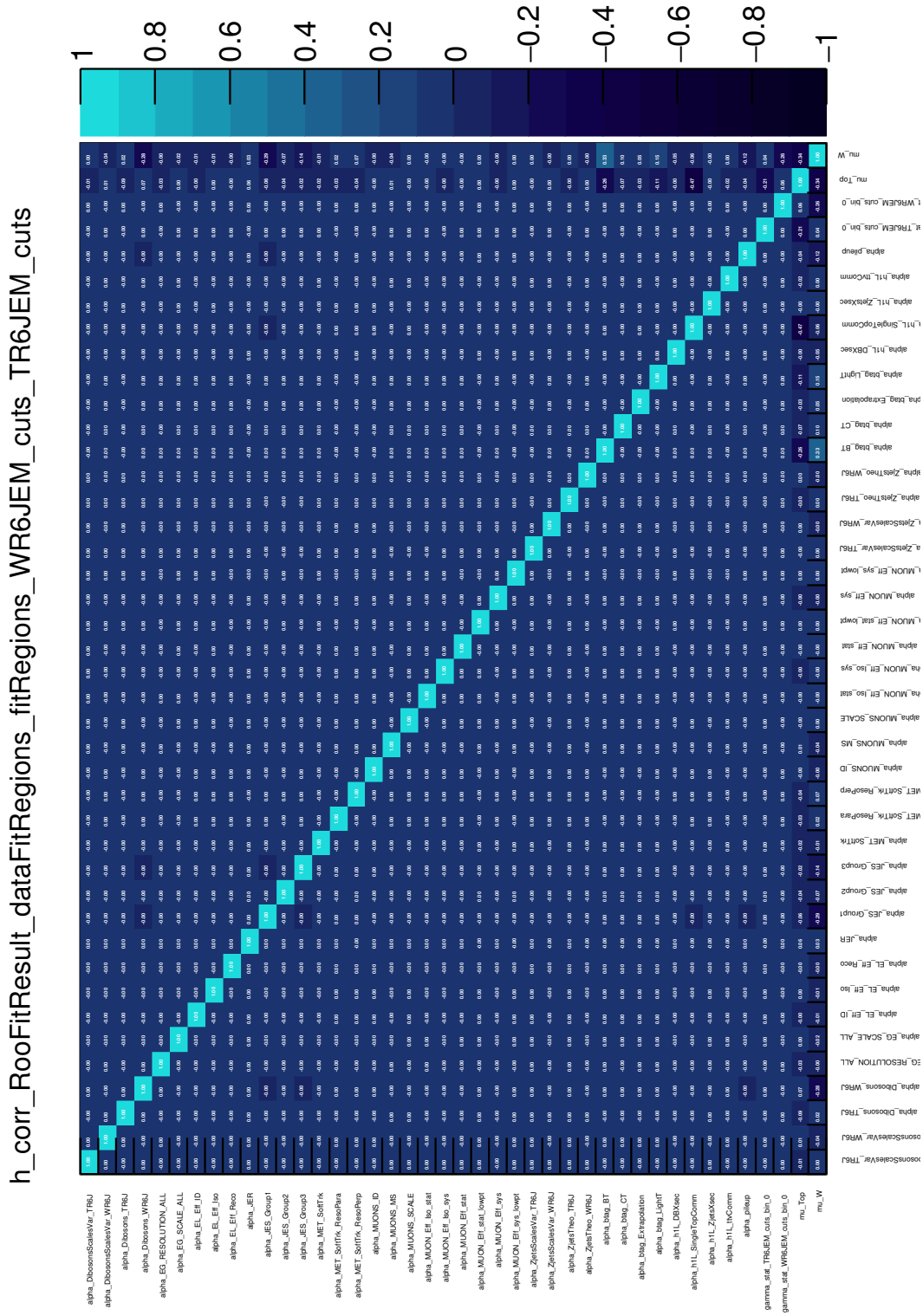

Figure C.20: Correlation matrix for the background-only fit in the 6-jet region.

Uncertainty of channel	**6-jet SR**
Total background expectation	4.37
Total statistical($\sqrt{N_{exp}}$)	± 2.09
Total background systematic	± 1.01 [23.15%]
mu_Top	± 0.54 [12.3%]
gamma_stat_SR6JEM_cuts_bin_0	± 0.49 [11.3%]
alpha_HardScatteringGen_SR6J	± 0.43 [9.8%]
alpha_MUONS_MS	± 0.37 [8.4%]
alpha_h1L_SingleTopComm	± 0.34 [7.8%]
alpha_Dibosons_SR6J	± 0.26 [6.0%]
alpha_pileup	± 0.24 [5.6%]
alpha_JER	± 0.20 [4.6%]
alpha_JES_Group3	± 0.16 [3.6%]
alpha_MET_SoftTrk_ResoPara	± 0.16 [3.6%]
alpha_HadFrag_SR6J	± 0.15 [3.5%]
mu_W	± 0.10 [2.3%]
alpha_FactRenScaleISRFSR_SR6J	± 0.10 [2.3%]
alpha_h1L_ttvComm	± 0.07 [1.6%]
alpha_Wjets_SR6J	± 0.07 [1.6%]
alpha_JES_Group2	± 0.07 [1.6%]
alpha_MET_SoftTrk	± 0.05 [1.2%]
alpha_h1L_DBXsec	± 0.05 [1.1%]
alpha_WJetsScaleVar_SR6J	± 0.05 [1.0%]
alpha_EG_SCALE_ALL	± 0.04 [1.0%]
alpha_EG_RESOLUTION_ALL	± 0.04 [1.0%]
alpha_DibosonsScalesVar_SR6J	± 0.04 [0.99%]
alpha_JES_Group1	± 0.04 [0.92%]
alpha_MUON_Eff_Iso_sys	± 0.02 [0.42%]
alpha_MET_SoftTrk_ResoPerp	± 0.02 [0.41%]
alpha_ZjetsTheo_SR6J	± 0.02 [0.39%]
alpha_MUON_Eff_sys	± 0.02 [0.39%]
alpha_ZjetsScalesVar_SR6J	± 0.01 [0.20%]
alpha_EL_Eff_ID	± 0.01 [0.15%]
alpha_EL_Eff_Iso	± 0.00 [0.09%]
alpha_h1L_ZjetsXsec	± 0.00 [0.09%]
alpha_EL_Eff_Reco	± 0.00 [0.05%]
alpha_MUON_Eff_stat	± 0.00 [0.04%]

`Table C.8:` Dominant systematic uncertainties in the 6-jet SR. Individual uncertainties can correlate, and do not add up quadratically to the total background uncertainty.

C.2.5 2-jet soft-lepton region

Regions	TR 2-jet soft-lepton	WR 2-jet soft-lepton
Observed events	264	1216
Fitted bkg events	264.075 ± 16.191	1216.194 ± 34.976
Fitted ttbar events	96.509 ± 35.997	28.962 ± 13.622
Fitted wjets events	132.744 ± 22.661	1136.314 ± 42.675
Fitted zjets events	1.382 ± 0.426	$3.382^{+6.008}_{-3.382}$
Fitted singletop events	23.960 ± 19.329	10.261 ± 8.370
Fitted diboson events	9.076 ± 4.153	37.171 ± 15.937
Fitted ttv events	0.404 ± 0.128	0.103 ± 0.035
MC exp. SM events	302.613 ± 30.241	1228.907 ± 29.473
MC exp. ttbar events	134.801 ± 6.863	40.393 ± 6.864
MC exp. wjets events	132.876 ± 18.844	1137.376 ± 18.844
MC exp. zjets events	1.381 ± 0.425	$3.386^{+5.985}_{-3.386}$
MC exp. singletop events	24.091 ± 19.380	10.305 ± 8.382
MC exp. diboson events	9.059 ± 4.149	37.344 ± 15.977
MC exp. ttv events	0.404 ± 0.128	0.103 ± 0.035

`Table C.9:` Background fit results for the region(s), for an integrated luminosity of 3.2 fb^{-1} for ISR-type. Nominal MC expectations (normalized to MC cross-sections) are given for comparison. The errors shown are the statistical plus systematic uncertainties. Uncertainties on the fitted yields are symmetric by construction, where the negative error is truncated when reaching to zero event yield.

Parameter	Initial value	Fitted value	Up error	Down error
alpha_DibosonsScaleVarTheo_TR2J	0.0000e+00	-7,81E+00	+1.00e+00	-9.99e-01
alpha_DibosonsScaleVarTheo_WR2J	0.0000e+00	-2,03E+01	+1.00e+00	-9.98e-01
alpha_DibosonsTheo_TR2J	0.0000e+00	4,38E+01	+9.96e-01	-1.00e+00
alpha_DibosonsTheo_WR2J	0.0000e+00	-1,24E+02	+1.01e+00	-9.88e-01
alpha_EG_RESOLUTION_ALL	0.0000e+00	6,05E+00	+1.00e+00	-1.00e+00
alpha_EG_SCALE_ALL	0.0000e+00	-3,94E+00	+1.00e+00	-1.00e+00
alpha_EL_Eff_ID	0.0000e+00	-1,22E+01	+1.00e+00	-9.99e-01
alpha_EL_Eff_Iso	0.0000e+00	-3,12E+00	+1.00e+00	-1.00e+00
alpha_EL_Eff_Reco	0.0000e+00	-4,75E+00	+1.00e+00	-1.00e+00
alpha_JER	0.0000e+00	2,59E+01	+9.98e-01	-1.00e+00
alpha_JES_Group1	0.0000e+00	9,14E+01	+9.91e-01	-1.01e+00
alpha_JES_Group2	0.0000e+00	-1,01E+01	+1.00e+00	-9.99e-01
alpha_JES_Group3	0.0000e+00	3,83E+01	+9.96e-01	-1.00e+00
alpha_MET_SoftTrk	0.0000e+00	5,57E+00	+1.00e+00	-1.00e+00
alpha_MET_SoftTrk_ResoPara	0.0000e+00	-4,26E+01	+1.00e+00	-9.96e-01
alpha_MET_SoftTrk_ResoPerp	0.0000e+00	2,35E+01	+9.98e-01	-1.00e+00
alpha_MUONS_ID	0.0000e+00	-2,28E+00	+1.00e+00	-1.00e+00
alpha_MUONS_MS	0.0000e+00	-4,82E+00	+1.00e+00	-1.00e+00
alpha_MUONS_SCALE	0.0000e+00	7,86E-01	+1.00e+00	-1.00e+00
alpha_MUON_Eff_Iso_stat	0.0000e+00	-2,73E-01	+1.00e+00	-1.00e+00
alpha_MUON_Eff_Iso_sys	0.0000e+00	-6,14E+00	+1.00e+00	-1.00e+00
alpha_MUON_Eff_stat	0.0000e+00	-4,15E-01	+1.00e+00	-1.00e+00
alpha_MUON_Eff_stat_lowpt	0.0000e+00	-8,36E-01	+1.00e+00	-1.00e+00
alpha_MUON_Eff_sys	0.0000e+00	-7,08E-01	+1.00e+00	-1.00e+00
alpha_MUON_Eff_sys_lowpt	0.0000e+00	-9,15E-01	+1.00e+00	-1.00e+00
alpha_ZjetsScaleVarTheo_TR2J	0.0000e+00	-9,76E-01	+1.00e+00	-1.00e+00
alpha_ZjetsScaleVarTheo_WR2J	0.0000e+00	-1,73E+00	+1.00e+00	-1.00e+00
alpha_ZjetsTheo_TR2J	0.0000e+00	-2,89E+00	+1.00e+00	-1.00e+00
alpha_ZjetsTheo_WR2J	0.0000e+00	-5,17E+00	+1.00e+00	-1.00e+00
alpha_btag_BT	0.0000e+00	-8,08E+01	+1.01e+00	-9.92e-01
alpha_btag_CT	0.0000e+00	-1,16E+01	+1.00e+00	-9.99e-01
alpha_btag_Extra	0.0000e+00	-6,46E+00	+1.00e+00	-1.00e+00
alpha_btag_LightT	0.0000e+00	1,90E+01	+9.98e-01	-1.00e+00
alpha_h1L_DBXsec	0.0000e+00	-2,11E+01	+1.00e+00	-9.98e-01
alpha_h1L_SingleTopComm	0.0000e+00	-5,98E+01	+1.01e+00	-9.94e-01
alpha_h1L_ZjetsXsec	0.0000e+00	-2,70E+00	+1.00e+00	-1.00e+00
alpha_h1L_ttbarVComm	0.0000e+00	-1,85E+00	+1.00e+00	-1.00e+00
alpha_pileup	0.0000e+00	-6,55E+01	+1.01e+00	-9.94e-01
mu_Top	1,00E+04	7,16E+03	+2.93e-01	-2.61e-01
mu_W	1,00E+04	9,99E+03	+4.39e-02	-4.46e-02

`Table C.10:` Background only fit results in the 2-jet soft-lepton regions

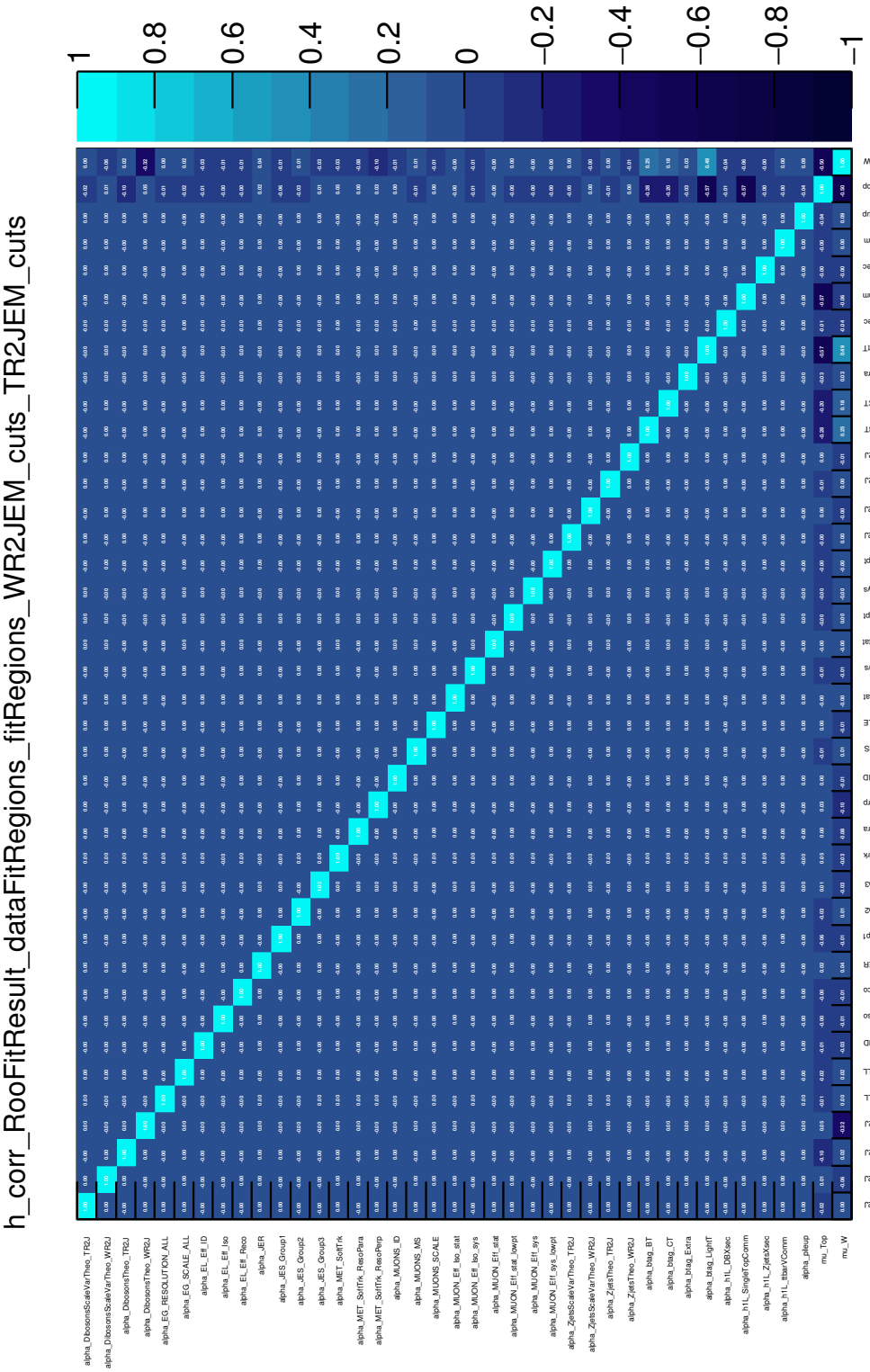

Figure C.21: Correlation matrix for the background-only fit in the 2-jet soft-lepton region.

Uncertainty of channel	**2-jet soft-lepton SR**
Total background expectation	3.60
Total statistical($\sqrt{N_{exp}}$)	± 1.90
Total background systematic	± 0.71 [19.81%]
gamma_stat_SR2JEM_cuts_bin_0	± 0.43 [11.9%]
alpha_WjetsTheo_2J	± 0.34 [9.3%]
alpha_WjetsScaleVarTheo_2J	± 0.26 [7.3%]
mu_Top	± 0.25 [6.9%]
alpha_HardScatteringGenTTbar_2J	± 0.16 [4.5%]
alpha_JES_Group1	± 0.15 [4.3%]
alpha_DibosonsTheo_SR2J	± 0.15 [4.2%]
alpha_h1L_SingleTopComm	± 0.12 [3.4%]
alpha_pileup	± 0.10 [2.8%]
alpha_FactRenScaleISRFSRTTbar_2J	± 0.10 [2.7%]
mu_W	± 0.08 [2.3%]
alpha_ZjetsTheo_SR2J	± 0.07 [2.0%]
alpha_MUONS_MS	± 0.07 [1.8%]
alpha_MET_SoftTrk	± 0.06 [1.7%]
alpha_JES_Group3	± 0.04 [1.2%]
alpha_HadFragTTbar_2J	± 0.04 [1.1%]
alpha_DibosonsScaleVarTheo_SR2J	± 0.03 [0.84%]
alpha_JER	± 0.03 [0.82%]
alpha_h1L_ttbarVComm	± 0.02 [0.69%]
alpha_ZjetsScaleVarTheo_SR2J	± 0.02 [0.65%]
alpha_h1L_ZjetsXsec	± 0.02 [0.65%]
alpha_h1L_DBXsec	± 0.02 [0.63%]
alpha_JES_Group2	± 0.02 [0.59%]
alpha_MET_SoftTrk_ResoPerp	± 0.02 [0.52%]
alpha_MET_SoftTrk_ResoPara	± 0.02 [0.43%]
alpha_EG_SCALE_ALL	± 0.01 [0.37%]
alpha_EG_RESOLUTION_ALL	± 0.01 [0.34%]
alpha_MUON_Eff_Iso_sys	± 0.01 [0.31%]
alpha_EL_Eff_ID	± 0.01 [0.15%]

`Table C.11:` Dominant systematic uncertainties in the 2-jet soft-lepton SR. Individual uncertainties can correlate, and do not add up quadratically to the total background uncertainty.

C.2.6 5-jet soft-lepton region

Regions	TR 5-jet soft-lepton	WR 5-jet soft-lepton
Observed events	134	55
Fitted bkg events	134.030 ± 11.548	55.026 ± 7.448
Fitted ttbar events	108.460 ± 14.850	8.828 ± 3.232
Fitted wjets events	10.337 ± 3.779	36.006 ± 8.970
Fitted zjets events	0.492 ± 0.252	2.216 ± 0.918
Fitted singletop events	9.004 ± 7.416	1.024 ± 0.882
Fitted diboson events	4.427 ± 1.967	6.824 ± 2.329
Fitted ttv events	1.311 ± 0.421	0.127 ± 0.056
MC exp. SM events	148.157 ± 8.645	71.741 ± 7.184
MC exp. ttbar events	118.038 ± 2.818	9.613 ± 2.874
MC exp. wjets events	14.910 ± 2.254	51.940 ± 3.786
MC exp. zjets events	0.491 ± 0.252	2.216 ± 0.918
MC exp. singletop events	8.980 ± 7.405	1.022 ± 0.881
MC exp. diboson events	4.427 ± 1.966	6.821 ± 2.328
MC exp. ttv events	1.311 ± 0.421	0.128 ± 0.057

`Table C.12:` Background fit results for the region(s), for an integrated luminosity of 3.2 fb^{-1} for 5J-type. Nominal MC expectations (normalized to MC cross-sections) are given for comparison. The errors shown are the statistical plus systematic uncertainties. Uncertainties on the fitted yields are symmetric by construction, where the negative error is truncated when reaching to zero event yield.

Parameter	Initial value	Fitted value	Up error	Down error
alpha_DibosonsScaleVarTheo_TR5J	0.0000e+00	-6.0687e-04	+1.00e+00	-9.99e-01
alpha_DibosonsScaleVarTheo_WR5J	0.0000e+00	1.9238e-04	+1.00e+00	-1.00e+00
alpha_DibosonsTheo_TR5J	0.0000e+00	-1.7044e-03	+1.00e+00	-9.98e-01
alpha_DibosonsTheo_WR5J	0.0000e+00	1.8454e-03	+9.98e-01	-1.00e+00
alpha_EG_RESOLUTION_ALL	0.0000e+00	1.8931e-05	+1.00e+00	-1.00e+00
alpha_EG_SCALE_ALL	0.0000e+00	8.3161e-05	+1.00e+00	-1.00e+00
alpha_EL_Eff_ID	0.0000e+00	-2.7952e-04	+1.00e+00	-1.00e+00
alpha_EL_Eff_Iso	0.0000e+00	-5.9166e-05	+1.00e+00	-1.00e+00
alpha_EL_Eff_Reco	0.0000e+00	-1.0915e-04	+1.00e+00	-1.00e+00
alpha_JER	0.0000e+00	2.1427e-03	+9.98e-01	-1.00e+00
alpha_JES_Group1	0.0000e+00	-4.6446e-04	+1.00e+00	-1.00e+00
alpha_JES_Group2	0.0000e+00	6.9660e-04	+9.99e-01	-1.00e+00
alpha_JES_Group3	0.0000e+00	2.7772e-03	+9.97e-01	-1.00e+00
alpha_MET_SoftTrk	0.0000e+00	1.1399e-04	+1.00e+00	-1.00e+00
alpha_MET_SoftTrk_ResoPara	0.0000e+00	2.7293e-04	+1.00e+00	-1.00e+00
alpha_MET_SoftTrk_ResoPerp	0.0000e+00	-2.5959e-04	+1.00e+00	-1.00e+00
alpha_MUONS_ID	0.0000e+00	4.6174e-05	+1.00e+00	-1.00e+00
alpha_MUONS_MS	0.0000e+00	-4.5138e-05	+1.00e+00	-1.00e+00
alpha_MUONS_SCALE	0.0000e+00	2.9772e-05	+1.00e+00	-1.00e+00
alpha_MUON_Eff_Iso_stat	0.0000e+00	-6.0425e-06	+1.00e+00	-1.00e+00
alpha_MUON_Eff_Iso_sys	0.0000e+00	-9.0646e-05	+1.00e+00	-1.00e+00
alpha_MUON_Eff_stat	0.0000e+00	-1.0622e-05	+1.00e+00	-1.00e+00
alpha_MUON_Eff_stat_lowpt	0.0000e+00	-1.2832e-05	+1.00e+00	-1.00e+00
alpha_MUON_Eff_sys	0.0000e+00	-1.8399e-05	+1.00e+00	-1.00e+00
alpha_MUON_Eff_sys_lowpt	0.0000e+00	-1.7399e-05	+1.00e+00	-1.00e+00
alpha_ZjetsScaleVarTheo_TR5J	0.0000e+00	-5.1596e-05	+1.00e+00	-1.00e+00
alpha_ZjetsScaleVarTheo_WR5J	0.0000e+00	2.5608e-05	+1.00e+00	-1.00e+00
alpha_ZjetsTheo_TR5J	0.0000e+00	-1.6569e-04	+1.00e+00	-1.00e+00
alpha_ZjetsTheo_WR5J	0.0000e+00	3.5338e-04	+1.00e+00	-1.00e+00
alpha_btag_BT	0.0000e+00	2.8944e-03	+9.97e-01	-1.00e+00
alpha_btag_CT	0.0000e+00	8.8228e-04	+9.99e-01	-1.00e+00
alpha_btag_Extra	0.0000e+00	-2.2553e-05	+1.00e+00	-1.00e+00
alpha_btag_LightT	0.0000e+00	3.9082e-03	+9.96e-01	-1.00e+00
alpha_h1L_DBXsec	0.0000e+00	-2.6535e-04	+1.00e+00	-1.00e+00
alpha_h1L_SingleTopComm	0.0000e+00	2.5753e-03	+9.97e-01	-1.00e+00
alpha_h1L_ZjetsXsec	0.0000e+00	-1.7799e-05	+1.00e+00	-1.00e+00
alpha_h1L_ttbarVComm	0.0000e+00	-5.9120e-04	+1.00e+00	-9.99e-01
alpha_pileup	0.0000e+00	5.0229e-04	+1.00e+00	-1.00e+00
gamma_stat_WR5JEM_cuts_bin_0	1.0000e+00	1.0002e+00	+5.84e-02	-5.88e-02
mu_Top	1.0000e+00	9.1880e-01	+1.38e-01	-1.23e-01
mu_W	1.0000e+00	6.9314e-01	+1.97e-01	-1.88e-01

`Table C.13:` Background only fit results in the 5-jet soft-lepton regions

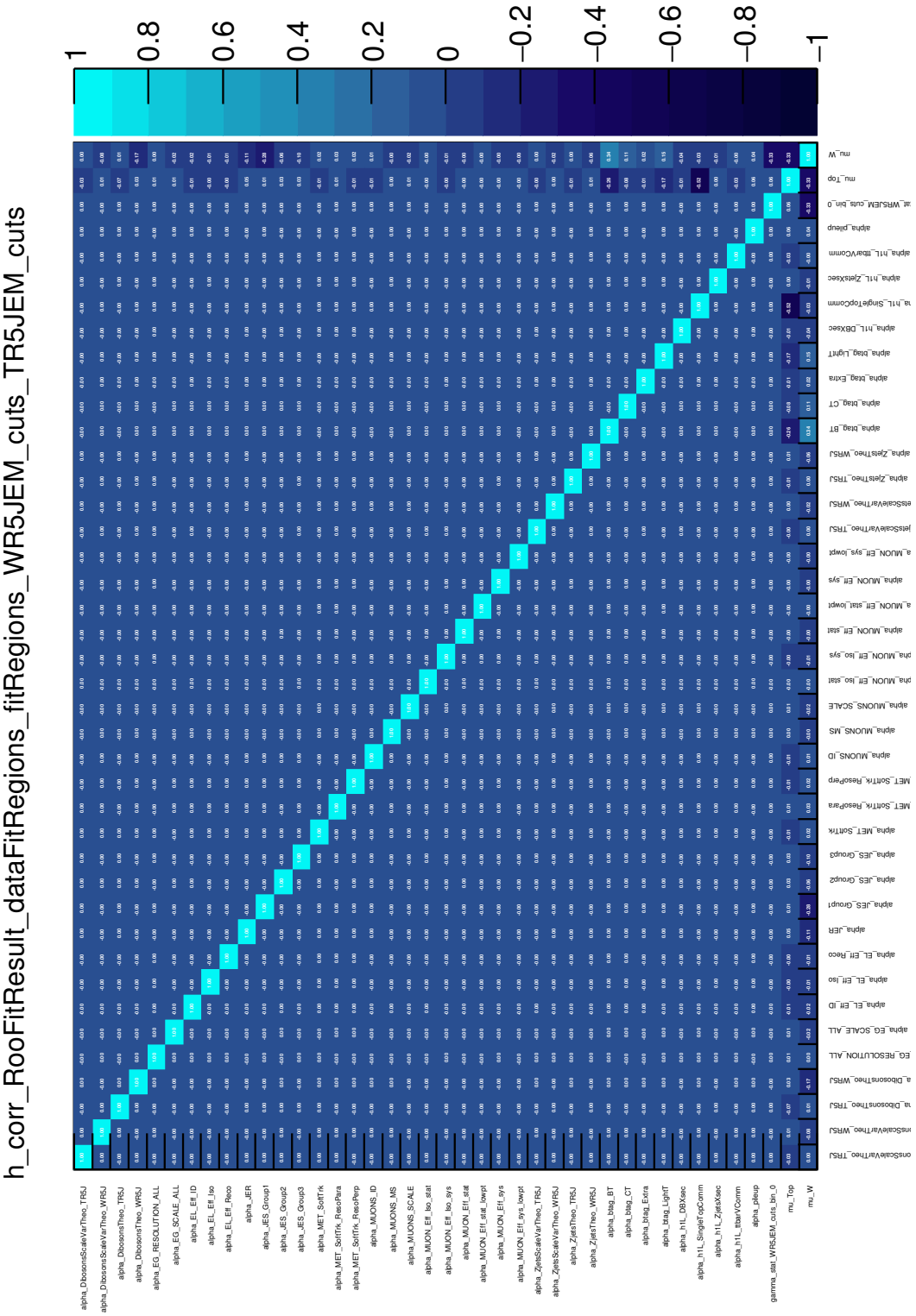

Figure C.22: Correlation matrix for the background-only fit in the 5-jet soft-lepton region.

Uncertainty of channel	**5-jet soft-lepton SR**
Total background expectation	7.68
Total statistical($\sqrt{N_{exp}}$)	± 2.77
Total background systematic	± 1.89 [24.59%]
gamma_stat_SR5JEM_cuts_bin_0	± 1.03 [13.4%]
alpha_WjetsTheo_SR5J	± 0.86 [11.2%]
alpha_FactRenScaleISRFSRTTbar_SR5J	± 0.73 [9.5%]
mu_W	± 0.70 [9.2%]
alpha_HardScatteringGenTTbar_SR5J	± 0.55 [7.1%]
mu_Top	± 0.52 [6.7%]
alpha_pileup	± 0.38 [5.0%]
alpha_h1L_SingleTopComm	± 0.32 [4.2%]
alpha_WjetsScaleVarTheo_SR5J	± 0.28 [3.6%]
alpha_JES_Group2	± 0.27 [3.6%]
alpha_JES_Group1	± 0.23 [3.0%]
alpha_DibosonsTheo_SR5J	± 0.22 [2.9%]
alpha_HadFragTTbar_SR5J	± 0.18 [2.4%]
alpha_JES_Group3	± 0.16 [2.0%]
alpha_DibosonsScaleVarTheo_SR5J	± 0.10 [1.3%]
alpha_JER	± 0.08 [1.1%]
alpha_MUON_Eff_Iso_sys	± 0.06 [0.79%]
alpha_h1L_DBXsec	± 0.05 [0.70%]
alpha_MET_SoftTrk_ResoPerp	± 0.03 [0.36%]
alpha_ZjetsTheo_SR5J	± 0.02 [0.31%]
alpha_h1L_ttbarVComm	± 0.02 [0.26%]
alpha_MUONS_MS	± 0.02 [0.20%]
alpha_MUONS_ID	± 0.02 [0.20%]
alpha_MUONS_SCALE	± 0.01 [0.19%]
alpha_MET_SoftTrk	± 0.01 [0.13%]
alpha_ZjetsScaleVarTheo_SR5J	± 0.01 [0.10%]
alpha_EL_Eff_ID	± 0.01 [0.09%]
alpha_EL_Eff_Reco	± 0.01 [0.09%]
alpha_EG_RESOLUTION_ALL	± 0.01 [0.09%]
alpha_MET_SoftTrk_ResoPara	± 0.01 [0.08%]
alpha_MUON_Eff_sys_lowpt	± 0.00 [0.06%]
alpha_h1L_ZjetsXsec	± 0.00 [0.06%]
alpha_MUON_Eff_stat_lowpt	± 0.00 [0.04%]
alpha_EL_Eff_Iso	± 0.00 [0.03%]
alpha_MUON_Eff_Iso_stat	± 0.00 [0.02%]
alpha_MUON_Eff_stat	± 0.00 [0.01%]
alpha_EG_SCALE_ALL	± 0.00 [0.01%]
alpha_MUON_Eff_sys	± 0.00 [0.01%]

`Table C.14:` Dominant systematic uncertainties in the 5-jet soft-lepton SR. Individual uncertainties can correlate, and do not add up quadratically to the total background uncertainty.

C.3 $t\bar{t}$ modeling and p_T re-weighting

C.3.1 $t\bar{t}$ re-weighting

Based on the low normalization factors for $t\bar{t}$ in the fits, on the slopes found for the hardest jet p_T distribution when comparing data to MC in the TCRs and in looser top controlled regions, also on previous similar results, and on the theoretical results presented in [287], there was a was clear hint for a miss modeling of $t\bar{t}$ processes in the simulations.

Initially, inspired by the work presented in [287], where the STRIPPER (SecToR Improved Phase sPacE for real Radiation) subtraction scheme [288] is used for the evaluation of NNLO QCD contributions, a theory based $t\bar{t}$ re-weighting procedure was tested. As seen in figure C.23 there is a clear slope in the $t\bar{t}$ system p_T when comparing results using only NLO and NNLO QCD. The slope was parametrized by a linear function given by $y = -0.0004x + 1.107$.

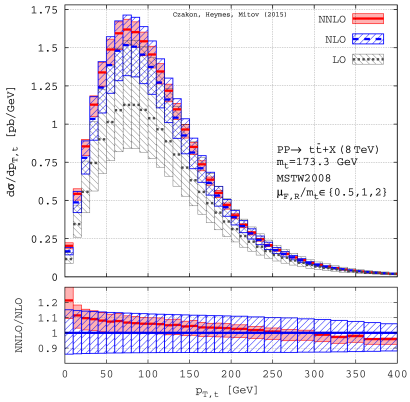

Figure C.23: $t\bar{t}$ system p_T distribution with LO, NLO and NNLO QCD from [287].

Even though the cross section fot $t\bar{t}$ is calculated at NNLO+NNLL level, the shape of the $t\bar{t}$ samples used for the analysis are only NLO. As the slope was found for theoretical top p_T, the re-weighting must be done on truth top p_T from $t\bar{t}$ samples. First a weight per event was stored using the linear function found to fit the slope. To properly re-weight, the new and old total $t\bar{t}$ weighted yields before selection are saved, and an additional overall weight is applied to to keep the cross section constant. The re-weighting showed to move the shapes in the proper direction, scaling down $t\bar{t}$ and reducing the slope, but the effect was lower than expected. The slope found in [287] was found on top p_T and the correlation to the hardest jest p_T remained unknown. Besides, the results from the STRIPPER method presented slopes only for low top p_T, while the reach of the regions on this work is higher. In addition, the slopes were calculated for 8 TeV as no for 13 TeV result was available yet.

Nevertheless, motivated by the same results a second re-weighting procedure is tested. The second procedure is a data driven $t\bar{t}$ re-weighting using reconstructed top p_T binned in truth top p_T bins. To perform the data driven approach, a two top region is defined to increase the top purity of the sample. The region is selected by requiring at least two b-jets in addition to the following requirements: Lepton $p_T > 35$ GeV, at least four jets with $p_T > 30$ GeV, 60 GeV $< mt <$ 125 GeV and $E_T miss > 200$ GeV. As the problem seems to come from the modeling, the approach of using truth top p_T bins is kept. First, the top p_T is reconstructed using TtresChi2 package from the TopEventReconstructionTool, for the semi-leptonic top, the neutrinos are built with the TtresNeutrinoBuilder package. Then the reconstructed top p_T is divided by truth top Pt bins, using a spatial matching

between truth and reconstructed objects. Figure C.24 shows the splitting of the top p_T, where the p_T distribution of the reconstructed semileptonic top is presented in red, while the reconstructed p_T distribution for different truth p_T bins are presented with different colors. To validate the splitting, she sum of all truth p_T bins is presented in black, and it is clear by looking at the superimposition of the black points in top of the red that the splitting is under control.

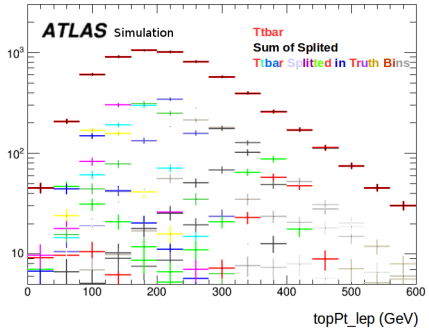

Figure C.24: Splitting of the reconstructed semi-leptonic top p_T in bins of truth top p_T.

After dividing the sample in truth top p_T bins, the fit of $t\bar{t}$+BG(fixed) to data is performed for reconstructed top p_T using a linear function, such that each bin gets its own normalization factor. The fit result is parametrized by a linear function with a slope of $m = -7.528 \times 10^{-4} \pm 10^{-7}$ with a vertical intercept of $n = 1.06081 \pm 10^{-4}$ where x represents the truth top p_T bin. The fit results showed an improvement of other possible related slopes, and helps reducing the top normalization factors in control regions. Figure C.25 shows few interesting distributions before the fit is applied, while the plots after the fit are presented in figure C.26. The remaining distributions were studied before and after fit to check for consistency. For all the distributions not presented here, only an overall scaling without any significant shape variation is observed. As it can be seen on the plots, there is a clear improvement on jet p_T, E_T^{miss} and m_{eff} distributions without spoiling well behaved distributions such as m_T. Additional distributions not presented, show the same behavior after fit. Looking at the lepton p_T distributions on both plots, there might be an artifact from the fit possibly inducing an upward slope. This behavior must be carefully studied, possibly including a higher order correction for the top p_T re-weighting. Nevertheless in general the re-weighting keeps the lepton p_T distribution after fit well within uncertainties, while improving jet p_T and E_T^{miss} slopes reducing also the normalization factors.

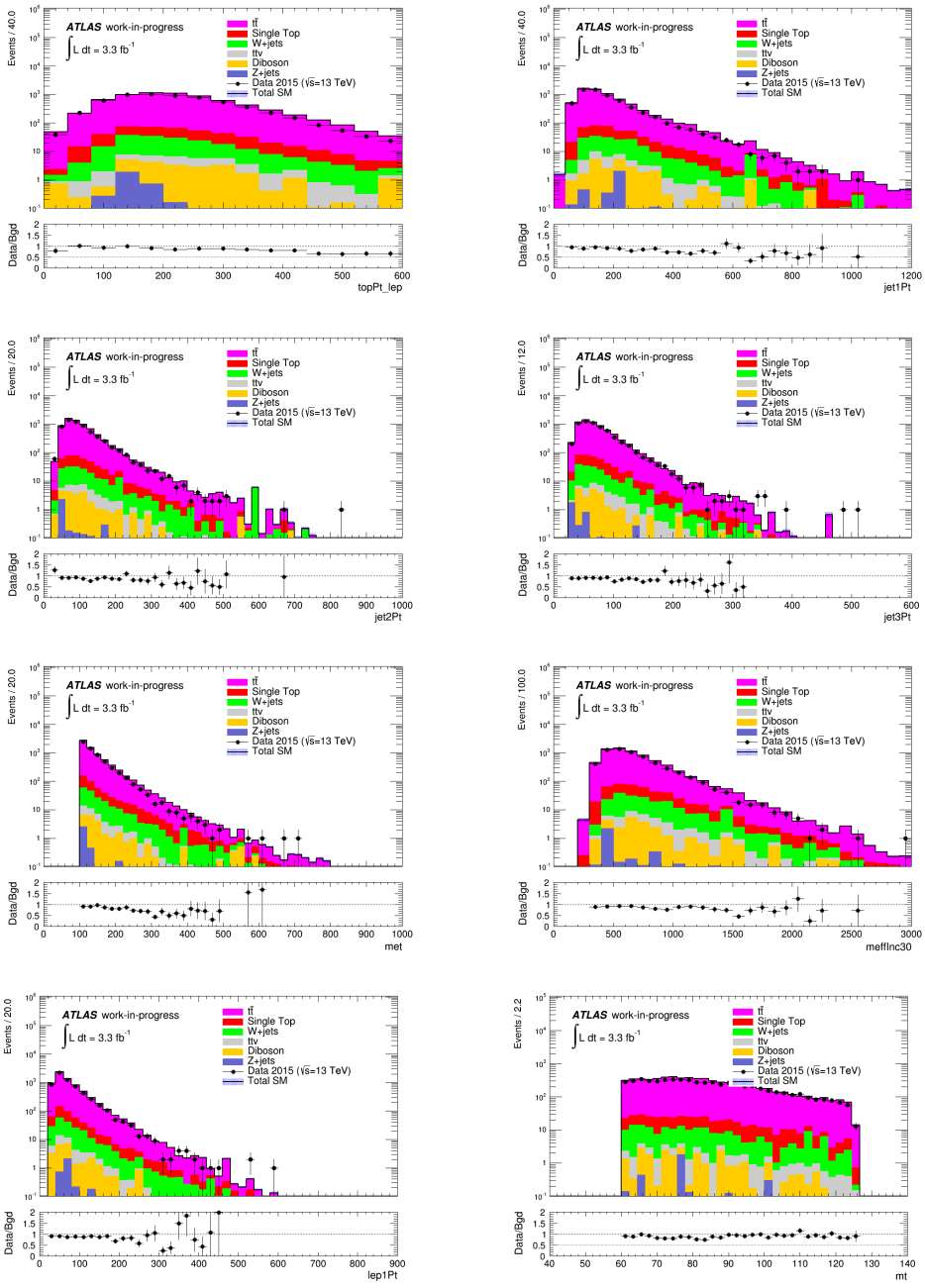

Figure C.25: Kinematic distributions in the di-top region before $t\bar{t}$ data driven re-weighting, using reconstructed top p_T binned in truth top p_T.

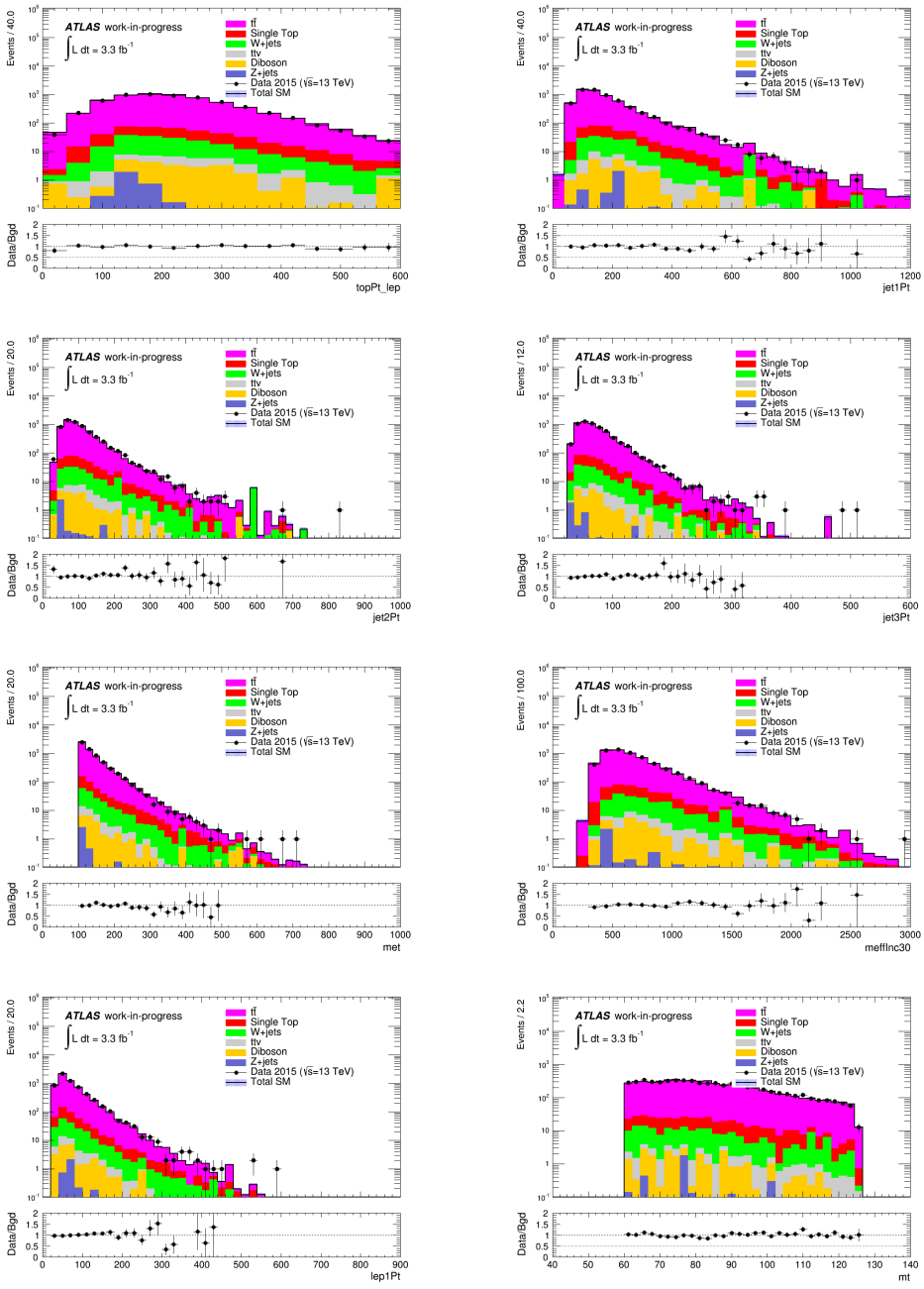

Figure C.26: Kinematic distributions in the di-top region after $t\bar{t}$ data driven re-weighting, using reconstructed top p_T binned in truth top p_T.

C.3.2 $t\bar{t}$ dominant decays in the different 6 jet regions

As presented in table C.15, the dominant $t\bar{t}$ decay channels are not the same in the 6 jet TCR and in the 6 jet SR. A loosen di-lepton control region was studied, to check if the $t\bar{t}$ di-lepton kinematics distributions are well described by simulation. It was found that MC describes kinematics correctly. A possible solution to properly control $t\bar{t}$ kinematics before extrapolating to SRs, would be to include a di-lepton CRs, as it has been done in previous similar analysis. Unfortunately, due to the limited statistics, these regions do not have the enough event content to properly estimate BG uncertainties for a robust transfer factor extrapolation to SRs.

% of $t\bar{t}$ events per channel				
Channel	6-jet TCR	6-jet VR Apl.	6-jet VR m_T	6-jet SR
LEPLEP	6 ± 2	4 ± 1	23 ± 6	14 ± 6
LEPLTAU	1 ± 0	1 ± 0	14 ± 3	22 ± 8
LTAULTAU	1 ± 1	0 ± 0	1 ± 1	0 ± 0
LEPHAD	81 ± 4	83 ± 6	6 ± 2	0 ± 0
LEPHTAU	7 ± 1	8 ± 4	52 ± 5	63 ± 15
LTAUHAD	4 ± 1	4 ± 1	0 ± 0	0 ± 0
LTAUHTAU	0 ± 0	0 ± 0	4 ± 2	1 ± 1
HADHAD	0 ± 0	0 ± 0	0 ± 0	0 ± 0
HADHTAU	0 ± 0	0 ± 0	0 ± 0	0 ± 0
HTAUHTAU	0 ± 0	0 ± 0	0 ± 0	0 ± 0

`Table C.15:` Dominant $t\bar{t}$ decay channels per region. The dominant channels in the 6-jet VR Jet Aplanarity and in the 6-jet SR, are different than in the 4-jet TCR.

Bibliography

[1] C. Patrignani et al. “Particle Data Group”,
Chinese Physics C, 40, 100001 (2016)

[2] B. Pontecorvo, “Mesonium and anti-mesonium”,
B. Sov.Phys.JETP **6** 429; Zh.Eksp.Teor.Fiz. 33 549-551 (1957)

[3] B. Pontecorvo, “Inverse beta processes and nonconservation of lepton charge”,
B. Sov.Phys.JETP **7** 172-173 (1958), Zh.Eksp.Teor.Fiz. **34** 247 (1957)

[4] Z. Maki, M. Nakagawa, and S. Sakata, “Remarks on the Unified Model of Elementary Particles”,
Prog. Theor. Phys. **28**, 870 (1962)

[5] The Planck Collaboration, “Planck 2015 results XVIII. Background geometry and topology.”;
arXiv:1502.01593 (2015)

[6] H.-X. Chen, W. Chen, X. Liu, S.-L. Zhu, “The hidden-charm pentaquark and tetraquark states”
Phys. Rept. 639 (2016) 1-121; doi:10.1016/j.physrep.2016.05.004; arXiv:1601.02092

[7] S. Weinberg, “A MODEL OF LEPTONS”,
Phys. Rev. Lett. **19**, 1264 (1967).

[8] P. A. M. Dirac, “The Quantum Theory of the Emission and Absorption of Radiation”,
Proc. Roy. Soc. **A114**, 243 (1927); idem, **A114**, 710 (1927).

[9] C. S. Wu et al., “Experimental Test of Parity Conservation in Beta Decay”,
Phys. Rev. **105**, 1413 (1957)

[10] J. H. Christenson, J. W. Cronin, V. L. Fitch, and R. Turlay, “Evidence for the 2π Decay of the K_2^0 Meson”,
Phys. Rev. Lett. **13**, 138 (1964).

[11] J. Ellis, M. K. Gaillardb, D. V. Nanopoulos, “A Historical Profile of the Higgs Boson”,
arXiv:hep-ph/1201.6045

[12] G. Altarelli and G. Parisi. “Asymptotic Freedom in Parton Language”,
Nucl.Phys. B126:298 (1977)
Yu.L. Dokshitzer. “ Calculation of the Structure Functions for Deep Inelastic Scattering and $e+e-$ Annihilation by Perturbation Theory in Quantum Chromodynamics”,

Sov.Phys.JETP **46** 641-653 (1977); Zh.Eksp.Teor.Fiz. **73** 1216-1240 (1977)

V.N. Gribov, L.N. Lipatov. "Deep inelastic *ep* scattering in perturbation theory",

Zh.Eksp.Teor.Fiz. **73** 1216-1240 (1972); Sov.J.Nucl.Phys. **15** 438-450 (1972)

[13] S. Weinberg, "Gauge hierarchies",

Phys. Lett. **82B**, 387 (1979)

[14] E. Gildener , "Gauge Symmetry Hierarchies",

Phys. Rev. **D14**, 1667 (1976).

[15] The ATLAS Collaboration, "Observation of a New Particle in the Search for the Standard Model Higgs Boson with the ATLAS Detector at the LHC",

Phys. Lett. **B716** (2012) 1-29, arXiv:hep-ex/1207.7214v2

[16] The CMS Collaboration, "Observation of a new boson at a mass of 125 GeV with the CMS experiment at the LHC",

Phys. Lett. **B716** (2012) 30-61, arXiv:hep-ex/1207.7235

[17] Peter W. Higgs, "Broken Symmetries and the Masses of Gauge Bosons",

Phys. Rev. Lett. **13**, 508 (1964)

[18] F. Englert and R. Brout, "Broken Symmetry and the Mass of Gauge Vector Mesons",

Phys. Rev. Lett. **13**, 321 (1964)

[19] G. 't Hooft, "Renormalizable Lagrangians for massive Yang-Mills fields",

Nucl. Phys. **B35**, 167 (1971)

[20] J. Pati and A. Salam, "Unified Lepton-Hadron Symmetry and a Gauge Theory of the Basic Interactions",

Phys. Rev. **D8**, 1240 (1973);

[21] H. Georgi and S.L. Glashow, "Unity of All Elementary-Particle Forces",

Phys. Rev. Lett. **32**, 438 (1974).

[22] Zwicky, F. 1933, "Die Rotverschiebung von extragalaktischen Nebeln",

Helvetica Physica Acta, **6**, 110.

Zwicky, F. 1937, "On the Masses of Nebulae and of Clusters of Nebulae",

ApJ, **86**, 217

[23] Edvige Corbelli and Paolo Salucci, "The extended rotation curve and the dark matter halo of M33",

MNRAS **311** (2): 441-447 (2000)

[24] Douglas Clowe et al., "A direct empirical proof of the existence of dark matter",

ApJ **648** (2006) L109; arXiv:astro-ph/0608407

[25] The WMAP Collaboration, "Seven-Year Wilkinson Microwave Anisotropy Probe (WMAP) Observations: Cosmological Interpretation",

ApJS **192** (2011) 18, arXiv:astro-ph.CO/1001.4538

[26] H. E. Haber, "The Supersymmetric top ten lists",
SCIPP-93-22, C93-04-13.1; arXiv:hep-ph/9308209 (1993)

[27] H. E. Haber, "Introductory low-energy supersymmetry",
SCIPP-92-33, C92-06-03.1; arXiv:hep-ph/9306207 (1993)

[28] Stephen P. Martin, "A Supersymmetry Primer",
Adv. Ser. Direct. High Energy Phys. **21** (2010) 1-153; Adv. Ser. Direct. High Energy Phys. **18** (1998) 1-98; arXiv:hep-ph/9709356v6 (2010)

[29] Y. A. Golfand and E. P. Likhtman, "Extension Of The Algebra Of Poincare Group Generators And Violation Of P Invariance",
JETP Lett. **13**, 323 (1971); [Pisma Zh. Eksp. Teor. Fiz. **13**, 452 (1971)].

[30] D. V. Volkov and V. P. Akulov, "Possible Universal Neutrino Interaction",
JETP Lett. **16**, 438 (1972).

[31] J. Wess and B. Zumino, "Supergauge Transformations In Four-Dimensions",
Nucl. Phys. **B70**, 39 (1974).

[32] H. P. Nilles, "Supersymmetry, Supergravity And Particle Physics",
Phys. Rept. **110** (1984) 1

[33] G. F. Giudice and R. Rattazzi, "Theories with gauge-mediated supersymmetry breaking,"
Phys. Rept. **322** (1999) 419; arXiv:hep-ph/9801271

[34] L. Randall and R. Sundrum, "Out of this world supersymmetry breaking"
Nucl. Phys. **B557** (1999) 79; arXiv:hep-th/9810155

[35] B. C. Allanach et al., "The Snowmass points and slopes: Benchmarks for SUSY searches",
Eur. Phys. J. **C25** (2002) 113; arXiv:hep-ph/0202233

[36] D. Alves et al., "Simplified Models for LHC New Physics Searches",
J. Phys. **G39**, (2012) 105005; arXiv:hep-ph/1105.2838

[37] J. Alwall et al., "Searching for Directly Decaying Gluinos at the Tevatron",
Phys. Lett. **B666** (2008) 34, arXiv:hep-ph/0803.0019

[38] J. Alwall, P. Schuster and N. Toro, "Simplified Models for a First Characterization of New Physics at the LHC",
Phys. Rev. **D79** (2009) 075020, arXiv:hep-ph/0810.3921

[39] D. Alves et al., "Simplified Models for LHC New Physics Searches",
J. Phys. G: Nucl. Part. Phys. **39** (2012) 105005, arXiv:hep-ph/1105.2838

[40] G. D'Ambrosio, G.F. Giudice, G. Isidori, A. Strumia, "Minimal Flavor Violation: an effective field theory approach",
Nucl. Phys. **645** 155 (2002)

[41] A. Djouadi, J. L. Kneur and G. Moultaka. "SuSpect: A Fortran code for the supersymmetric and Higgs particle spectrum in the MSSM".
Comput. Phys. Commun. **176** (2007), p. 426-455; arXiv:hep-ph/0211331

[42] C. F. Berger et al. “Supersymmetry without prejudice”,
JHEP **0902** (2009), p. 023; arXiv:hep-ph/0812.0980

[43] M. W. Cahill-Rowley et al. “The New Look pMSSM with Neutralino and Gravitino LSPs”,
Eur. Phys. J. **C72** (2012), p. 2156; arXiv:hep-ph/206.4321

[44] The ATLAS Collaboration, “Search for squarks and gluinos with the ATLAS detector in final states with jets and missing transverse momentum using $\sqrt{s} = 8$TeV proton-proton collision data”,
JHEP **09** (2014) 176; arXiv:hep-ex/1405.7875

[45] The ATLAS Collaboration, “Summary of the searches for squarks and gluinos using $\sqrt{s} = 8$TeV pp collisions with the ATLAS experiment at the LHC”,
JHEP **10** (2015) 054 ; arXiv:hep-ex/1507.05525

[46] The ATLAS Collaboration, ATLAS Supersymmetry Public Results webpage,
https://twiki.cern.ch/twiki/bin/view/AtlasPublic/SupersymmetryPublicResults

[47] The CMS Collaboration, CMS Supersymmetry Public Results webpage,
https://cms-results.web.cern.ch/cms-results/public-results/publications/SUS/index.html

[48] The ATLAS Collaboration, “Search for squarks and gluinos in events with isolated leptons, jets and missing transverse momentum at $\sqrt{s} = 8$ TeV with the ATLAS detector”,
JHEP **1504** (2015), p. 116; arXiv:hep-ex/1501.03555 (2015)

[49] The ATLAS Collaboration, “Summary of the searches for squarks and gluinos using $\sqrt{s} = 8$TeV pp collisions with the ATLAS experiment at the LHC”,
JHEP **1510** (2015), 054; arXiv:hep-ex/1507.05525

[50] L.Evans, “The Large Hadron Collider: A Marvel of Technology”,
CERN, EPFL Press (2009)

[51] The LHC Study Group, “The Large Hadron Collider : conceptual design”,
CERN-AC-95-05-LHC; https://cds.cern.ch/record/291782 (1995)

[52] L. Evans and P. Bryant, “LHC Machine”,
JINST 3 (2008) S08001

[53] O. Brüning, P. Collier, P. Lebrun, S. Myers, R. Ostojic, J. Poole, P. Proudlock “LHC Design Report v.1 : the LHC Main Rings”,
CERN-2004-003-V-1; https://cds.cern.ch/record/782076 (2004)

[54] H. Schopper, “LEP - The Lord of the Collider Rings at CERN 1980-2000”,
Springer (2009)

[55] K. Schindl, “The Injector Chain for the LHC”,
CERN-PS-99-018-DI; https://cds.cern.ch/record/384396 (1999)

[56] B. Couturier, A. Lombardi, “Proposal for a new proton injector for LINAC2”,
ACERN-PS-HP-NOTE-97-06; https://cds.cern.ch/record/2111352 (1997)

[57] K. Schindl, "The PS Booster as Pre-Injector for LHC",
CERN-PS-97-011-DI T; https://cds.cern.ch/record/323757 (1997)

[58] D. Cundy and S. Gilardoni, "The Proton Synchrotron (PS): At the Core of the CERN Accelerators",
Adv. Ser. Direct. High Energy Phys. **27** 39 (2017); doi:10.1142/9789814749145_0003

[59] P. Collier et al., "The SPS as injector for LHC: Conceptual design",
CERN-SL-97-007-DI, CERN-SL-97-07-DI, CERN-SL-97-7-DI.

[60] LHeC Study Group, J L Abelleira Fernandez et al., "A Large Hadron Electron Collider at CERN: Report on the Physics and Design Concepts for Machine and Detector",
J. Phys. G: Nucl. Part. Phys. **39** (2012) 075001

[61] ATLAS Collaboration, "The ATLAS Experiment at the CERN Large Hadron Collider",
JINST 3 (2008) S08003.

[62] ATLAS Collaboration, "ATLAS detector and physics performance : Technical Design Report, 1",
ATLAS-TDR-14; CERN-LHCC-99-014; https://cds.cern.ch/record/391176 (1999)

[63] ATLAS Collaboration, "ATLAS detector and physics performance : Technical Design Report, 2",
ATLAS-TDR-15 ; CERN-LHCC-99-015; https://cds.cern.ch/record/391177 (1999)

[64] ALICE Collaboration, "The ALICE experiment at the CERN LHC",
JINST 3 (2008) S08002

[65] CMS Collaboration, "The CMS experiment at the CERN LHC",
JINST 3 (2008) S08004

[66] The LHCb Collaboration, "The LHCb Detector at the LHC",
JINST 3 (2008) S08005

[67] T. Taylor, "Superconducting magnets and RF cavities for the LHC",
CERN-LHC-PROJECT-REPORT-379

[68] LHC MACHINE OUTREACH: https://lhc-machine-outreach.web.cern.ch/lhc-machine-outreach/components/magnets.htm

[69] Taking a closer look at LHC: https://www.lhc-closer.es/taking_a_closer_look_at_lhc/0.magnetic_dipoles

[70] Mike Lamont on behalf of the LHC team, "The LHC's first long run",
CERN Courier, Aug 19, 2013

[71] ATLAS Collaboration, "Luminosity Public Results Run 2",
https://twiki.cern.ch/twiki/bin/view/AtlasPublic/LuminosityPublicResultsRun2

[72] ATLAS Collaboration, "THE ATLAS Insertable B-Layer Technical Design Report",
ATLAS-TDR-19; CERN-LHCC-2010-013; https://cds.cern.ch/record/1291633 (2010)

[73] ATLAS Collaboration, "ATLAS Insertable B-Layer Technical Design Report",
ATLAS TDR 19-ADD-1; CERN/LHCC 2012-009; https://cds.cern.ch/record/1451888 (2012)

[74] ATLAS Collaboration, "Technical Design Report of the ATLAS Pixel Detector",
ATLAS TDR 11; CERN/LHCC 98-13; https://cds.cern.ch/record/381263 (1998)

[75] I Ibragimov, The ATLAS collaboration "Timing behavior of the ATLAS Pixel Detector in calibration, cosmic-ray and collision data"
ATL-INDET-PROC-2010-021; http://cds.cern.ch/record/1290098 (2010)

[76] The ATLAS collaboration, "ATLAS Strip Detector: Operational Experience and Run1-> Run2 Transition",
ATL-INDET-PROC-2014-018; http://cds.cern.ch/record/1972027 (2014)

[77] The ATLAS collaboration, "Operation and performance of the ATLAS semiconductor tracker",
JINST 9 (2014) P08009; http://iopscience.iop.org/1748-0221/9/08/P08009

[78] A. Ahmad, et al., "The Silicon Microstrip Sensors of the ATLAS SemiConductor Tracker",
ATL-INDET-PUB-2007-007; ATL-COM-INDET-2007-008; CERN-ATL-COM-INDET-2007-008; Nucl. Instrum. Methods Phys. Res., A **578** (2007), 98-118

[79] E. Abat et al., "The ATLAS Transition Radiation Tracker (TRT) proportional drift tube: Design and performance",
JINST 3 (2008) P02013

[80] The ATLAS COllaboration, "Performance of the ATLAS Transition Radiation Tracker in Run 1 of the LHC: tracker properties"
ATL-COM-INDET-2015-041 (2016)

[81] Abat et al., "The ATLAS TRT barrel detector",
JINST 3 (2008) P02014

[82] E. Abat et al., "The ATLAS TRT end-cap detectors",
JINST 3 (2008) P10003

[83] ATLAS Collaboration, "ATLAS central solenoid : Technical Design Report"
ATLAS-TDR-9; CERN-LHCC-97-021; https://cds.cern.ch/record/331067 (1997)

[84] The ATLAS collaboration, "Track Reconstruction Performance of the ATLAS Inner Detector at $\sqrt{s} = 13$TeV",
ATL-PHYS-PUB-2015-018; https://cds.cern.ch/record/2037683 (2015)

[85] The ATLAS collaboration, "The Pixel Detector of the ATLAS experiment for LHC Run-2",
JINST 10 (2015) C06012; http://iopscience.iop.org/1748-0221/10/06/C06012

[86] The ATLAS collaboration, "Prototype ATLAS IBL modules using the FE-I4A front-end readout chip",
JINST 7 (2012) P11010; arXiv:1209.1906

[87] The ATLAS collaboration, “Study of the mechanical stability of the ATLAS Insertable B-Layer”, ATLAS-INDET-PUB-2015-001; https://cds.cern.ch/record/2022587 (2015)

[88] The ATLAS Collaboration, ”Studies of the performance of the ATLAS detector using cosmic-ray muons“,

Eur.Phys.J.C **71** (2011) 1593, arXiv:1011.6665

[89] The ATLAS Collaboration, ”ATLAS calorimeter performance Technical Design Report“,

CERN/LHCC 96-40; http://atlas.web.cern.ch/Atlas/TDR/caloperf/caloperf.html (1996)

[90] The ATLAS Collaboration, ”ATLAS liquid-argon calorimeter: Technical Design Report“,

CERN-LHCC-96-041; https://cds.cern.ch/record/331061/ (1996)

[91] The ATLAS Collaboration, ”ATLAS tile calorimeter : Technical Design Report“,

CERN-LHCC-96-042; https://cds.cern.ch/record/331062/ (1996)

[92] Artamonov, et al., ”The ATLAS forward calorimeter“,

JINST 3 (2008) P02010.

[93] ATLAS Collaboration, ”Expected Performance of the ATLAS Experiment - Detector, Trigger and Physics“,

CERN-OPEN-2008-020; arXiv:hep-ex/0901.0512 (2008)

[94] B. Aubert et al., ”Development and construction of large size signal electrodes for the ATLAS electromagnetic calorimeter“,

CERN-PH-EP-2004-019; Nucl.Instrum.Meth. **A539** (2005) 558-594

[95] J Abdallah et al., ”Mechanical construction and installation of the ATLAS tile calorimeter“,

JINST 8 (2013) T11001

[96] The ATLAS Collaboration, ”ATLAS: Muon Spectrometer Technical Design Report“,

CERNLHCC-97-022; https://cds.cern.ch/record/331068 (1997)

[97] Grazia Cabras, on the behalf of the LUCID group, ”LUCID: The ATLAS Luminosity Detector“,

TL-FWD-PROC-2018-003; https://cds.cern.ch/record/2626278 (2018)

[98] The ATLAS Collaboration, ”Luminosity determination in pp collisions at $\sqrt{s} = 13$ TeV using the ATLAS detector at the LHC“,

ATLAS-CONF-2019-02103; http://cdsweb.cern.ch/record/2677054/files/ATLAS-CONF-2019-021.pdf (2019)

[99] The ATLAS Luminosity and Forward Physics Community, ”ATLAS Forward Detectors for Measurement of Elastic Scattering and Luminosity“,

ATLAS TDR 018, CERN/LHCC (2008)

[100] ATLAS DBM collaboration, ”The ATLAS Diamond Beam Monitor“,

ATL-INDET-PROC-2013-021, https://cds.cern.ch/record/1630832 (2013)

[101] Cindro et al., "The ATLAS Beam Conditions Monitor",
JINST 3 P02004 (2004)

[102] E. Griesmayer, B. Dehning. "Diamonds for beam instrumentation",
TIPP 2011; https://doi.org/10.1016/j.phpro.2012.02.526 (2012)

[103] R. Achenbach et al., "The ATLAS Level-1 calorimeter trigger",
JINST 3 (2008) P03001

[104] W. Lampl et al., "Calorimeter Clustering Algorithms: Description and Performance"
ATL-LARG-PUB-2008-002; ATL-COM-LARG-2008-003; https://cds.cern.ch/record/1099735 (2008)

[105] E. Simioni et al., "Upgrade of the ATLAS Level-1 Trigger with event topology information",
Proceedings of CHEP2015 J. Phys.: Conf. Ser.; https://cds.cern.ch/record/2016644 (2015)

[106] Yu Nakahama on behalf of the ATLAS Collaboration, "The ATLAS Trigger System: Ready for Run-2"
J. Phys. Conf. Ser. **664** (2015) no.8, 082037

[107] R. Hauser, The ATLAS Collaboration, "The ATLAS Data Flow system for the second LHC run",
ATL-DAQ-SLIDE-2015-174; Proceedings of CHEP2015 J. Phys.: Conf. Ser.; https://cds.cern.ch/record/2007873 (2015)

[108] C. Schiavi, "ATLAS High-Level Trigger Algorithms for Run-2 Data Taking",
Proceedings of CHEP2015 J. Phys.: Conf. Ser.; https://cds.cern.ch/record/2007824 (2015)

[109] ATLAS Public Results: Level-1 Calorimeter Trigger Public Results, https://twiki.cern.ch/twiki/bin/view/AtlasPublic/L1CaloTriggerPublicResults

[110] E. Simioni et al. , "The Topological Processor for the future ATLAS Level-1 Trigger: from design to commissioning"
arXiv:1406.4316 (2014)

[111] Andreas Salzburger, "Optimisation of the ATLAS Track Reconstruction Software for Run-2"
J. Phys.: Conf. Ser. **664** (2015) 072042; ATL-SOFT-PROC-2015-056; https://cds.cern.ch/record/2018442

[112] The ATLAS Collaboration, "Measurement of performance of the pixel neural network clustering algorithm of the ATLAS experiment at $\sqrt{s} = 13$TeV"
ATL-PHYS-PUB-2015-044; https://cds.cern.ch/record/2054921 (2015)

[113] The ATLAS Collaboration, "The ATLAS Inner Detector commissioning and calibration",
Eur.Phys.J. **C70** (2010) 787-821; arXiv:physics.ins-det/1004.5293

[114] The ATLAS Collaboration, "Impact Parameter Resolution",

https://atlas.web.cern.ch/Atlas/GROUPS/PHYSICS/PLOTS/IDTR-2015-007 (2015)

[115] The ATLAS Collaboration, "The Optimization of ATLAS Track Reconstruction in Dense Environments",

ATL-PHYS-PUB-2015-006; https://cds.cern.ch/record/2002609 (2015)

[116] Gabriel Facini on behalf of the ATLAS Collaboration, "Novel Methods and Expected Run 2 Performance for ATLAS Track Reconstruction in Dense Environments",

ATL-INDET-PROC-2015-012; https://cds.cern.ch/record/2104001 (2015)

[117] The ATLAS Collaboration, "Performance of the ATLAS Inner Detector Track and Vertex Reconstruction in the High Pile-Up LHC Environments",

ATLAS-CONF-2012-042; https://cds.cern.ch/record/1435196 (2012)

[118] The ATLAS Collaboration, "First 2016 vertex reconstruction in data and comparison between 2015 and 2016 software release",

ATL-PHYS-PUB-2015-026; https://atlas.web.cern.ch/Atlas/GROUPS/PHYSICS/PLOTS/IDTR-2016-003 (2016)

[119] The ATLAS Collaboration, "Topological cell clustering in the ATLAS calorimeters and its performance in LHC Run 1",

CERN-PH-EP-2015-304; arXiv:1603.02934; http://cds.cern.ch/record/2138166 (2016)

[120] W Lampl et al., "Calorimeter clustering algorithms, description and performance",

ATL-LARG-PUB-2008-002; ATL-LARG-PUB-2008-002; http://cdsweb.cern.ch/record/1099735 (2008)

[121] The ATLAS Collaboration, "Total Noise in the Liquid Argon Detector at the Electron Scale (2015)",

https://twiki.cern.ch/twiki/pub/AtlasPublic/LArCaloPublicResultsDetStatus/lar-noise-2015data.pdf

[122] S. Menke, P. Strizenec, G. Unal, "Simulated Calorimeter Noise for Phase II",

ATL-COM-CAL-2013-003; https://cds.cern.ch/record/1562964 (2013)

[123] The ATLAS Collaboration, "Jet Calibration and Systematic Uncertainties for Jets Reconstructed in the ATLAS Detector at $\sqrt{s} = 13$TeV",

ATL-PHYS-PUB-2015-015; https://cds.cern.ch/record/2037613 (2015)

[124] The ATLAS Collaboration, "Properties of Jets and Inputs to Jet Reconstruction and Calibration with the ATLAS Detector Using Proton-Proton Collisions at $\sqrt{s} = 13$TeV",

ATL-PHYS-PUB-2015-036; http://cds.cern.ch/record/2044564 (2015)

[125] The ATLAS collaboration, "Monte Carlo Calibration and Combination of In-situ Measurements of Jet Energy Scale, Jet Energy Resolution and Jet Mass in ATLAS",

ATLAS-CONF-2015-037; http://cds.cern.ch/record/2044941 (2015)

[126] M. Cacciari, G. P. Salam and G. Soyez, "The Anti-k(t) jet clustering algorithm",

JHEP **04** (2008) 063, arXiv:hep-ex/0802.1189

[127] The ATLAS Collaboration, "Tagging and suppression of pileup jets with the ATLAS detector", ATLAS-CONF-2014-018; http://cds.cern.ch/record/1700870 (2014)

[128] M. Cacciari, G. P. Salam, "Pileup subtraction using jet areas",

Phys.Lett. **B659** (2008) 119-126; arXiv:hep-ph/0707.1378v2

[129] ATLAS Collaboration. "Pile-up subtraction and suppression for jets in ATLAS",

ATLAS-CONF-2013-083, http://cdsweb.cern.ch/record/1570994 (2013)

[130] M. Cacciari, G. P. Salam, G. Soyez, "The Catchment Area of Jets",

JHEP **0804** (2008) 005; arXiv:hep-ph/0802.1188

[131] Stephen D. Ellis, Davision E. Soper, "Successive Combination Jet Algorithm For Hadron Collisions",

CERN-TH-6860-93; Phys.Rev. **D48** (1993) 3160-3166; arXiv:hep-ph/9305266v1

[132] The ATLAS Collaboration, "Jet global sequential corrections with the ATLAS detector in proton-proton collisions at $\sqrt{s} = 8$TeV",

ATLAS-CONF-2015-002; https://cds.cern.ch/record/2001682 (2015)

[133] The CDF Collaboration, "First measurements of inclusive W and Z cross sections from Run II of the Tevatron collider",

Phys. Rev. Lett. **94** (2005) 091differecne between hadronic jets and simple jets hep803, arXiv:hep-ex/0406078

[134] The D$\emptyset$ Collaboration, "Measurement of the shape of the boson rapidity distribution for $p\bar{p} \to Z/\gamma^* \to e^+e^- + X$ events produced at $\sqrt{s} = 1.96$TeV"

Phys. Rev. **D76** (2007) 012003; arXiv:hep-ex/0702025

[135] M. Frate, B. Malaescu, D. Varouchas, M. Swiatlowski, D. Miller, C. Issever, "Jet in-situ correction comparison between 8 and 13 TeV",

ATL-COM-PHYS-2016-201; https://cds.cern.ch/record/2135332 (2016)

[136] The ATLAS Collaboration, "Expected performance of the ATLAS b-tagging algorithms in Run-2",

ATL-PHYS-PUB-2015-022 (2015), url: https://cds.cern.ch/record/2037697.

[137] The ATLAS Collaboration, "Commissioning of the ATLAS high-performance b-tagging algorithms in the 7 TeV collision data",

ATLAS-CONF-2011-102 (2011); https://cds.cern.ch/record/1369219

[138] The ATLAS Collaboration. "Electron efficiency measurements with the ATLAS detector using the 2015 LHC proton-proton collision data",

ATLAS-CONF-2016-024; https://cds.cern.ch/record/2157687 (2016)

[139] T. Cornelissen et al. "The global χ^2 track fitter in ATLAS",

J. Phys. Conf. Ser. **119** (2008) 032013

[140] The ATLAS Collaboration. "Improved electron reconstruction in ATLAS using the Gaussian Sum Filter-based model for bremsstrahlung",

ATLAS-CONF-2012-047, http://cdsweb.cern.ch/record/1449796 (2012)

[141] The ATLAS Collaboration. "Muon reconstruction performance in early $\sqrt{s}$ = 13TeV data",

ATL-PHYS-PUB-2015-037; http://cds.cern.ch/record/2047831 (2015)

[142] The ATLAS Collaboration. "Muon reconstruction performance of the ATLAS detector in proton–proton collision data at $\sqrt{s} = 13$TeV",

Eur. Phys. J. **C76** (2016) 292; CERN-EP-2016-033; arXiv:hep-ex/1603.05598;

[143] The ATLAS Collaboration. "Expected performance of missing transverse momentum reconstruction for the ATLAS detector at $\sqrt{s} = 13$TeV"

ATL-PHYS-PUB-2015-023, http://cds.cern.ch/record/2037700 (2015)

[144] The ATLAS Collaboration. "Performance of missing transverse momentum reconstruction with the ATLAS detector in first proton-proton collisions at $\sqrt{s} = 13$TeV"

ATL-PHYS-PUB-2015-027, http://cds.cern.ch/record/2037904 (2015)

[145] https://twiki.cern.ch/twiki/bin/view/AtlasProtected/SUSYFeynmanDiagrams

[146] V. Gribov and L. Lipatov. "Deep inelastic e p scattering in perturbation theory",

Sov. J. Nucl. Phys. **15** (1972) 438-450

[147] G. Altarelli and G. Parisi. "Asymptotic Freedom in Parton Language",

Nucl. Phys. **B126** (1977) 298

[148] Y. L. Dokshitzer, "Calculation of the Structure Functions for Deep Inelastic Scattering and e^+e^- Annihilation by Perturbation Theory in Quantum Chromodynamics. ",

Sov. Phys. JETP **46** (1977) 641-653

[149] C. Borschensky, M. Krämer, A. Kulesza, M. Mangano, S. Padhi, T. Plehn and X. Portell. "Squark and gluino production cross sections in pp collisions at $\sqrt{s} = 13$, 14, 33 and 100 TeV",

Eur. Phys. J. **C74** (2014) no.12, 3174; arXiv:hep-ph/1407.5066

[150] G. Cowan et al. "Asymptotic formulae for likelihood-based tests of new physics",

Eur. Phys. J. **C 71** (2011) 1554, arXiv:physics.data-an/1007.1727

[151] R. Bruneliere, M. Baak, J. Lundberg, M. C. Rammensee and T. J. Khoo, "Setting exclusion limits in ATLAS supersymmetry searches with a likelihood ratio based method",

ATL-PHYS-INT-2011-032, (2011); https://cds.cern.ch/record/1342545

[152] G. Cowan, K. Cranmer, E. Gross and O. Vitells. "Asymptotic formulae for likelihood-based tests of new physics",

Eur. Phys. J. **C71** (2011) 1554; arXiv:physics.data-an/1007.1727

[153] M. Baak et al. "HistFitter software framework for statistical data analysis",

Eur. Phys. J. **C75.4** (2015), p. 153; arXiv:1410.1280 [hep-ex]

[154] J. Neyman and E. Pearson. "On the Problem of the Most Efficient Tests of Statistical Hypotheses".

Philosophical Transactions of the Royal Society A: Mathematical, Physical and Engineering Sciences. **231** (694-706): 289-337; doi:10.1098/rsta.1933.0009. JSTOR 91247.

[155] A. L. Read. "Presentation of search results: the CL s technique",

Journal of Physics G: Nuclear and Particle Physics 28.10 (2002), p. 2693.

[156] M. Baak, G.J. Besjes, J. Lorenz, S. Pataraia, et al. "Introduction to statistics / statistical tools",

Hist Fitter Tutorial, DESY, (March 2015); https://indico.desy.de/materialDisplay.py?contribId=1&sessionId=

[157] K. Kranmer, "Practical Statistics for Particle Physics",

HCP Summer School, https://indico.cern.ch/event/226365/contributions/1533500/attachments/372527/5183 FermiLab-HCP_2013_L3.pdf (2013)

[158] The ATLAS Collaboration, "Summary of the ATLAS experiment's sensitivity to supersymmetry after LHC Run 1 - interpreted in the phenomenological MSSM",

JHEP **10** (2015) 134; arXiv:hep-ex/1508.06608v2

[159] The ATLAS Collaboration. "Search for squarks and gluinos with the ATLAS detector in final states with jets and missing transverse momentum using $\sqrt{s}$ =8 TeV proton-proton collision data",

JHEP **1409** (2014), p. 176; arXiv:hep-ex/1405.7875

[160] The ATLAS Collaboration. "Search for new phenomena in final states with large jet multiplicities and missing transverse momentum at $\sqrt{s}$ =8 TeV proton-proton collisions using the ATLAS experiment",

JHEP **10** (2013), p. 130; arXiv:hep-ex/1308.1841

[161] The ATLAS Collaboration. "Search for squarks and gluinos in events with isolated leptons, jets and missing transverse momentum at $\sqrt{s}$ =8 TeV with the ATLAS detector",

JHEP **1504** (2015), p. 116; arXiv:hep-ex/1501.03555

[162] The ATLAS Collaboration. "Search for supersymmetry in events with large missing transverse momentum, jets, and at least one tau lepton in 20 fb^{-1} of $\sqrt{s}$ =8 TeV proton-proton collision data with the ATLAS detector",

JHEP **1409** (2014), p. 103; arXiv:hep-ex/1407.0603

[163] The ATLAS Collaboration. "Search for supersymmetry at $\sqrt{s}$ =8 TeV in final states with jets and two same-sign leptons or three leptons with the ATLAS detector",

JHEP **1406** (2014), p. 035; arXiv:hep-ex/1404.2500

[164] ATLAS Collaboration. "Search for strong production of supersymmetric particles in final states with missing transverse momentum and at least three b-jets at $\sqrt{s}$ =8 TeV proton-proton collisions with the ATLAS detector",

JHEP **1410** (2014), p. 24, arXiv:hep-ex/1407.0600

[165] ATLAS Collaboration. "Search for new phenomena in final states with an energetic jet and large missing transverse momentum in pp collisions at $\sqrt{s}$ =8 TeV with the ATLAS detector",

Eur. Phys. J. **C75.7** (2015), p. 299; arXiv:hep-ex/1502.01518

[166] ATLAS Collaboration. "Search for direct pair production of the top squark in all-hadronic final states in proton-proton collisions at $\sqrt{s}$ =8 TeV with the ATLAS detector",

JHEP **1409** (2014), p. 015; arXiv:hep-ex/1406.1122

[167] ATLAS Collaboration. "Search for top squark pair production in final states with one isolated lepton, jets, and missing transverse momentum in $\sqrt{s}$ =8 TeV pp collisions with the ATLAS detector",

JHEP **11** (2014), p. 118; arXiv:hep-ex/1407.0583

[168] ATLAS Collaboration. "Search for direct top-squark pair production in final states with two leptons in pp collisions at $\sqrt{s}$ =8 TeV with the ATLAS detector",

JHEP **1406** (2014), p. 124; arXiv:hep-ex/1403.4853

[169] ATLAS Collaboration. "Search for pair-produced third-generation squarks decaying via charm quarks or in compressed supersymmetric scenarios in pp collisions at $\sqrt{s}$ =8 TeV with the ATLAS detector",

JHEP **1406** (2014), p. 124. arXiv:hep-ex/1403.4853

[170] ATLAS Collaboration. "Search for direct top squark pair production in events with a Z boson, b-jets and missing transverse momentum in $\sqrt{s}$ =8 TeV pp collisions with the ATLAS detector",

Eur. Phys. J. **C74.6** (2014), p. 2883; arXiv:hep-ex/1403.5222

[171] ATLAS Collaboration. "Search for direct third-generation squark pair production in final states with missing transverse momentum and two b-jets in $\sqrt{s}$ =8 TeV pp collisions with the ATLAS detector",

JHEP **1310** (2013), p. 189; arXiv:hep-ex/1308.2631

[172] ATLAS Collaboration. "ATLAS Run 1 searches for direct pair production of third-generation squarks at the Large Hadron Collider",

Eur. Phys. J. **C75** (2015), p. 510; arXiv:hep-ex/1506.08616

[173] ATLAS Collaboration. "Search for direct pair production of a chargino and a neutralino decaying to the 125 GeV Higgs boson in $\sqrt{s}$ =8 TeV pp collisions with the ATLAS detector",

Eur. Phys. J. **C75.5** (2015), p. 208; arXiv:hep-ex/1501.07110

[174] ATLAS Collaboration. "Search for direct production of charginos, neutralinos and sleptons in final states with two leptons and missing transverse momentum in pp collisions at $\sqrt{s}$ =8 TeV with the ATLAS detector",

JHEP **05** (2014), p. 071; arXiv:hep-ex/1403.5294

[175] ATLAS Collaboration. "Search for the direct production of charginos, neutralinos and staus in final states with at least two hadronically decaying taus and missing transverse momentum in pp collisions at $\sqrt{s}$ =8 TeV with the ATLAS detector",

JHEP **10** (2014), p. 96; arXiv:hep-ex/1407.0350

[176] ATLAS Collaboration. "Search for direct production of charginos and neutralinos in events with three leptons and missing transverse momentum in $\sqrt{s}$ =8 TeV pp collisions with the ATLAS detector",

JHEP **1404** (2014), p. 169; arXiv:hep-ex/1402.7029

[177] ATLAS Collaboration. "Search for supersymmetry in events with four or more leptons in $\sqrt{s}$ =8 TeV pp collisions with the ATLAS detector",

Phys. Rev. **D90.5** (2014), p. 299; arXiv:hep-ex/1405.5086

[178] ATLAS Collaboration. "Search for charginos nearly mass degenerate with the lightest neutralino based on a disappearing-track signature in pp collisions $\sqrt{s}$ =8 TeV with the ATLAS detector",

Phys. Rev. **D88.11** (2013), p. 112006; arXiv:hep-ex/1310.3675

[179] ATLAS Collaboration. "Searches for heavy long-lived sleptons and R-Hadrons with the ATLAS detector in pp collisions at $\sqrt{s}$ =7 TeV",

Phys. Lett. **B720** (2013), p. 277-308; arXiv:hep-ex/1211.1597

[180] ATLAS Collaboration. "Searches for heavy long-lived charged particles with the ATLAS detector in proton-proton collisions at $\sqrt{s}$ =8 TeV",

JHEP **01** (2015), p. 068; arXiv:hep-ex/1411.6795

[181] ATLAS Collaboration. "Search for neutral Higgs bosons of the minimal supersymmetric standard model in pp collisions at $\sqrt{s}$ =8 TeV with the ATLAS detector",

JHEP **1411** (2014), p. 056; arXiv:hep-ex/1409.6064

[182] ATLAS GRL page: http://atlasdqm.web.cern.ch/atlasdqm/grlgen/All_Good/

[183] S. Alioli, P. Nason, C. Oleari, and E. Re. "A general framework for implementing NLO calculations in shower Monte Carlo programs: the POWHEG BOX",

JHEP **06** (2010), p. 043; arXiv:hep-ph/1002.2581

[184] T. Sjostrand, S. Mrenna, and P. Skands. "PYTHIA 6.4 physics and manual",

JHEP **05** (2006), p. 026; arXiv:hep-ph/0603175

[185] T. Gleisberg et al. "Event generation with Sherpa 1.1",

JHEP **02** (2009), p. 007; arXiv:hep-ph/0811.4622

[186] M. L. Mangano, M. Moretti, F. Piccinini, R. Pittau, and A. D. Polosa. "ALPGEN, a generator for hard multiparton processes in hadronic collisions",

JHEP **07** (2003), p. 001; arXiv:hep-ph/0206293

[187] G. Corcella et al. "HERWIG 6: An Event generator for hadron emission reactions with interfering gluons (including supersymmetric processes)",

JHEP **01** (2001), p. 010; arXiv:hep-ph/0011363

[188] B. P. Kersevan and E. Richter-Was. "The Monte Carlo event generator AcerMC version 2.0 with interfaces to PYTHIA 6.2 and HERWIG 6.5" ,

arXiv:hep-ph/0405247 (2004)

[189] J. Alwall, M. Herquet, F. Maltoni, O. Mattelaer, and T. Stelzer. "MadGraph 5 : Going Beyond",

JHEP **06** (2011), p. 128; arXiv:hep-ph/1106.0522

[190] M. W. Cahill-Rowley, J. L. Hewett, S. Hoeche, A. Ismail, and T. G. Rizzo, "The New Look pMSSM with Neutralino and Gravitino LSPs",

Eur.Phys.J. **C72** (2012), p. 2156; arXiv:hep-ph/1206.4321

[191] P. Ade et al. "Planck 2015 results. XIII. Cosmological parameters",

Astron. Astrophys. **594**, A13 (2016); arXiv:astro-ph.CO/1502.01589

[192] B. Allanach. "SOFTSUSY: a program for calculating supersymmetric spectra",

Comput. Phys. Commun. **143** (2002), p. 305; arXiv:hep-ph/0104145

[193] G. Belanger et al. "MicrOMEGAs 2.0: A Program to calculate the relic density of dark matter in a generic model", Comput. Phys. Commun. **176** (2007), p. 367; arXiv:hep-ph/0607059 [hep-ph].

[194] G. Belanger et al. "micrOMEGAs: A Tool for dark matter studies",

Nuovo Cim. **C033N2** (2010), p. 111; arXiv:hep-ph/1005.4133

[195] F. E. Paige, S. D. Protopopescu, H. Baer, and X. Tata. "ISAJET 7.69: A Monte Carlo event generator for pp, anti-p p, and e+e- reactions,"

arXiv:hep-ph/0312045 (2003)

[196] [268] W. Porod. "SPheno, a program for calculating supersymmetric spectra, SUSY particle decays and SUSY particle production at e^+e^- colliders",

Comput. Phys. Commun. **153** (2003), p. 275; arXiv:hep-ph/0301101

[197] A. Djouadi, J.-L. Kneur, and G. Moultaka. "SuSpect: A Fortran code for the supersymmetric and Higgs particle spectrum in the MSSM",

Comput. Phys. Commun. **176** (2007), p. 426; arXiv:hep-ph/0211331

[198] S. Heinemeyer, W. Hollik and G. Weiglein. "FeynHiggs: A Program for the calculation of the masses of the neutral CP even Higgs bosons in the MSSM",

Comput. Phys. Commun. **124** (2000), p. 76; arXiv:hep-ph/9812320

[199] T. Hahn et al. "High-precision predictions for the light CP-even Higgs Boson Mass of the MSSM",

Phys. Rev. Lett. **112** (2014), p. 141801; arXiv:hep-ph/1312.4937

[200] A. Djouadi, M. Muhlleitner and M. Spira. "Decays of supersymmetric particles: The Program SUSY-HIT (SUspect-SdecaY-Hdecay-InTerface)",

Acta Phys. Polon. **B38** (2007), p. 635; arXiv:hep-ph/0609292

[201] C. Chen, M. Drees and J. Gunion. "Addendum/erratum for 'Searching for invisible and almost invisible particles at e^+e^- colliders' and 'A nonstandard string/SUSY scenario and its phenomenological implications' ",

arXiv:hep-ph/9902309 (1999)

[202] J. Alwall et al. "The automated computation of tree-level and next-to-leading order differential cross-sections, and their matching to parton shower simulations",

JHEP **1407** (2014), p. 079; arXiv:hep-ph/1405.0301

[203] D. Chowdhury et al. "Charge and color breaking constraints in MSSM after the Higgs Discovery at LHC",

JHEP **1402** (2014), p. 110; arXiv:hep-ph/1310.1932

[204] M. Baak et al. "The Electroweak Fit of the Standard Model after the Discovery of a New Boson at the LHC",

Eur. Phys. J. **C72** (2012), p. 2205; arXiv:hep-ph/1209.2716

[205] T. Aoyama, M. Hayakawa, T. Kinoshita, and M. Nio. "Complete Tenth-Order QED Contribution to the Muon $g-2$"

Phys.Rev.Lett. **109** (2012), p. 111808; arXiv:hep-ph/1205.5370

[206] Y. Amhis et al. "Averages of B-Hadron, C-Hadron, and tau-lepton properties as of early 2012",

arXiv:hep-ex/1207.1158 (2012)

[207] V. Khachatryan et al. "Observation of the rare $B_0 \to \mu^+\mu^-$ decay from the combined analysis of CMS and LHCb data",

Nature **522** (2015), p. 68; arXiv:hep-ex/1411.4413

[208] K. De Bruyn et al. "Probing new physics via the $B_0 \to \mu^+\mu^-$ Effective Lifetime",

Phys. Rev.Lett. **109** (2012), p. 041801; arXiv:hep-ph/1204.1737

[209] B. Aubert et al. "A Search for $B^+ \to \ell^+\nu_\ell$ Recoiling Against $B^- \to D^0\ell^-\bar{\nu}X$",

Phys. Rev. **D81** (2010), p. 051101; arXiv:hep-ex/0912.2453

[210] K. Hara et al. "Evidence for $B^- \to \tau^-\bar{\nu}$ with a Semileptonic Tagging Method", Phys. Rev. **D82** (2010), p. 071101; arXiv:hep-ex/1006.4201

[211] I. Adachi et al. "Evidence for $B^- \to \tau^-\bar{\nu}_\tau$ with a Hadronic Tagging Method Using the Full Data Sample of Belle", Phys. Rev. Lett. **110.13** (2013), p. 131801; arXiv:hep-ex/1208.4678

[212] J. Lees et al. "Evidence of $B^+ \to \tau^+\nu$ decays with hadronic B tags" Phys. Rev. **D88.3** (2013), p. 031102; arXiv:hep-ex/1207.0698

[213] F. Mahmoudi. "SuperIso v2.3: A Program for calculating flavor physics observables in Supersymmetry",

Comput. Phys. Commun. **180** (2009), p. 1579; arXiv:hep-ph/0808.3144

[214] J. Charles et al. "CP violation and the CKM matrix: Assessing the impact of the asymmetric B factories",

Eur. Phys. J. **C41** (2005) Updated results (2014) from http://ckmfitter.in2p3.fr, p. 1; arXiv:hep-ph/0406184

[215] S. Schael et al. "Precision electroweak measurements on the Z resonance",

Phys. Rept. **C427** (2006), p. 257; arXiv:hep-ex/0509008

[216] The LEP SUSY Working Group and the ALEPH, DELPHI, L3 and OPAL experiments,

LEPSUSYWG/01-03.1; http://lepsusy.web.cern.ch/lepsusy

[217] ATLAS, CMS Collaborations. "Combined Measurement of the Higgs Boson Mass in pp Collisions at $\sqrt{s} = 7$ and 8 TeV with the ATLAS and CMS Experiments",

Phys.Rev.Lett. **114** (2015) 191803; arXiv:hep-ex/1503.07589

[218] The ATLAS Collaboration. "Measurement of the Higgs boson mass from the $H \to \gamma\gamma$ and $H \to ZZ^* \to 4\ell$ channels in pp collisions at center-of-mass energies of 7 and 8 TeV with the ATLAS detector",

Phys. Rev. **D 90** (2014) 052004; arXiv:hep-ex/1406.3827

[219] M. Cirelli, N. Fornengo and A. Strumia. "Minimal dark matter",

Nucl. Phys. **B753** (2006), p. 178; arXiv:hep-ph/0512090

[220] M. Cirelli, A. Strumia and M. Tamburini. "Cosmology and Astrophysics of Minimal Dark Matter",

Nucl. Phys. **B787** (2007), p. 152; arXiv:hep-ph/0706.4071

[221] J. Hisano et al. "Non-perturbative effect on thermal relic abundance of dark matter", Phys. Lett. **B646** (2007), p. 34; arXiv:hep-ph/0610249

[222] W. Beenakker et al. "Squark and gluino production at hadron colliders",

Nucl. Phys. **B492** (1997), p. 51; arXiv:hep-ph/9610490

[223] W. Beenakker et al. "Stop production at hadron colliders",

Nucl. Phys. **B515** (1998), p. 3; arXiv:hep-ph/9710451

[224] W. Beenakker et al. "The Production of charginos/neutralinos and sleptons at hadron colliders",

Phys. Rev. Lett. **83** (1999), p. 3780; arXiv:hep-ph/9906298

[225] M. Spira. "Higgs and SUSY particle production at hadron colliders",

arXiv:hep-ph/0211145 (2002)

[226] T. Plehn. "Measuring the MSSM Lagrangean",

Czech. J. Phys. **55** (2005), B213-B220. arXiv:hep-ph/0410063

[227] S. Agostinelli et al. "GEANT4: A Simulation toolkit",

Nucl. Instrum. Meth. **A506** (2003), p. 250

[228] W. Lukas. "Fast Simulation for ATLAS: Atlfast-II and ISF",

ATL-SOFT-PROC-2012-065; ATL-COM-SOFT-2012-137;

[229] ATLAS Collaboration. "The ATLAS Simulation Infrastructure",

Eur. Phys. J. **C 70** (2010), p. 823; arXiv:hep-ex/1005.4568

[230] M. Krämer et al. "Supersymmetry production cross-sections in pp collisions at s = 7 TeV",

arXiv:hep-ph/1206.2892 (2012)

[231] A. Kulesza and L. Motyka. "Threshold resummation for squark-antisquark and gluino-pair production at the LHC",

Phys.Rev.Lett. **102** (2009) 111802, arXiv:hep-ph/0807.2405

[232] A. Kulesza and L. Motyka. "Soft gluon resummation for the production of gluino-gluino and squark-antisquark pairs at the LHC",

Phys.Rev. **D80** (2009) 095004, arXiv:hep-ph/0905.4749

[233] W. Beenakker, S. Brensing, M. Krämer, A. Kulesza, E. Laenen, et al. "Soft-gluon resummation for squark and gluino hadroproduction",

JHEP **0912** (2009) 041, arXiv:hep-ph/0909.4418

[234] W. Beenakker, S. Brensing, M. Krämer, A. Kulesza, E. Laenen, and I. Niessen. "Supersymmetric top and bottom squark production at hadron colliders",

JHEP. **1008** (2010) 098, arXiv:hep-ph/1006.4771

[235] W. Beenakker, S. Brensing, M. Krämer, A. Kulesza, E. Laenen, et al. "Squark and gluino hadroproduction",

Int.J.Mod.Phys. **A26** (2011) 2637-2664, arXiv:hep-ph/1105.1110

[236] LHC Higgs Cross Section Working Group et al. "Handbook of LHC Higgs Cross Sections: 1. Inclusive Observables",

arXiv:hep-ph/1101.0593 (2011)

[237] LHC Higgs Cross Section Working Group et al. "Handbook of LHC Higgs Cross Sections: 2. Differential Distributions",

CERN-2012-002 (2012); arXiv:hep-ph/1201.3084

[238] LHC Higgs Cross Section Working Group et al. "Handbook of LHC Higgs Cross Sections: 3. Higgs Properties",

CERN-2013-004 (2013); arXiv:hep-ph/1307.1347

[239] Corrected manual for SusHi:

R. V. Harlander, S. Liebler and H. Mantler. "SusHi 1.3.0: A program for the calculation of Higgs production in gluon fusion and bottom-quark annihilation in the Standard Model, the 2HDM and the MSSM",

Manual on the web page: sushi.hepforge.org/manual/SusHi130.pdf

Based on:

R. V. Harlander, S. Liebler and H. Mantler. "SusHi: A program for the calculation of Higgs production in gluon fusion and bottom-quark annihilation in the Standard Model and the MSSM"

Comput. Phys. Commun. **184** (2013), p. 1605; arXiv:hep-ph/1212.3249

[240] https://atlas.web.cern.ch/Atlas/GROUPS/PHYSICS/PAPERS/SUSY-2014-08

[241] The ATLAS Collaboration. "Summary of the ATLAS experiment's sensitivity to supersymmetry after LHC Run 1 interpreted in the phenomenological MSSM",

SUSY-2014-08, https://cds.cern.ch/record/1747267

[242] S. Heinemeyer, W. Hollik, and G. Weiglein. "Constraints on tan Beta in the MSSM from the upper bound on the mass of the lightest Higgs boson",

JHEP **06** (2000), p. 009; arXiv:hep-ph/9909540

[243] M. Carena, S. Heinemeyer, C. E. M. Wagner and G. Weiglein. "Suggestions for benchmark scenarios for MSSM Higgs boson searches at hadron colliders",

Eur. Phys. J. **C 26** (2003), p. 601; arXiv:hep-ph/0202167

[244] The ATLAS Collaboration, "Search for gluinos in events with an isolated lepton, jets and missing transverse momentum at $\sqrt{s} = 13$ TeV with the ATLAS detector",

Eur. Phys. J. **C76** 565 (2016); DOI: 10.1140/epjc/s10052-016-4397-x; arXiv:hep-ex/1605.04285

[245] CMS Collaboration. "Search for new physics in events with same-sign dileptons and jets in pp collisions at $\sqrt{s} = 8\ TeV$",

JHEP **01** (2014) 163; arXiv:hep-ex 1311.6736.

[246] CMS Collaboration, "Search for new physics in the multijet and missing transverse momentum final state in proton-proton collisions at $\sqrt{s} = 8\ TeV$",

JHEP **06** (2014) 055; arXiv:hep-ex/1402.4770.

[247] CMS Collaboration. "Inclusive search for supersymmetry using the razor variables at $\sqrt{s} = 13\ TeV$",

https://cds.cern.ch/record/2114815/files/SUS-15-004-pas.pdf; CMS-PAS-SUS-15-004 (2015)

[248] CMS Collaboration, "Search for supersymmetry in pp collisions at $\sqrt{s} = 8\ TeV$ in the single-lepton final state using the sum of masses of large radius jets"

https://cds.cern.ch/record/2114814/files/SUS-15-007-pas.pdf; CMS-PAS-SUS-15-007 (2015)

[249] CMS Collaboration, "Search for SUSY in same-sign dilepton events at $\sqrt{s} = 13\ TeV$",

https://cds.cern.ch/record/2114813/files/SUS-15-008-pas.pdf; CMS-PAS-SUS-15-008 (2015)

[250] H-L Lai et al. "New parton distributions for collider physics",

Phys. Rev. **D82** (2010) 074024; arXiv:hep-ph/1007.2241

[251] J. Pumplin et al. "New generation of parton distributions with uncertainties from global QCD analysis",

JHEP **07** (2002) 012; arXiv:hep-ph/0201195

[252] P. Z. Skands, "Tuning Monte Carlo Generators: The Perugia Tunes",

Phys. Rev. **D82**, 074018 (2010); arXiv:hep-ph/1005.3457

[253] M. Czakon and A. Mitov, "Top++: A Program for the Calculation of the Top-Pair Cross-Section at Hadron Colliders",

Comput. Phys. Commun. **185**, 2930 (2014); arXiv:hep-ph/1112.5675

[254] T. Gleisberg and S. HÃűche, "Comix, a new matrix element generator",

JHEP **0812** (2008) 039; arXiv:hep-ph/0808.3674

[255] F. Cascioli, P. Maierhofer and S. Pozzorini, "Scattering Amplitudes with Open Loops",

Phys. Rev. Lett. **108** (2012) 111601; arXiv:hep-ph/1111.5206

[256] S. Schumann and F. Krauss, "A Parton shower algorithm based on Catani-Seymour dipole factorisation",

JHEP **0803** (2008) 038; arXiv:hep-ph/0709.1027

[257] S. Höche et al., "QCD matrix elements + parton showers: The NLO case",

JHEP **04** (2013) 027; arXiv:hep-ph/1207.5030

[258] ATLAS Collaboration, "ATLAS Pythia 8 tunes to 7 TeV data",

ATL-PHYS-PUB-2014-021, 2014; http://cdsweb.cern.ch/record/1966419

[259] R. D. Ball et al. "Parton distributions with LHC data",
Nucl. Phys. **B867** (2013) 244; arXiv:hep-ph/1207.1303

[260] A. Sherstnev and R. Thorne. "Parton Distributions for LO Generators",
Eur. Phys. J. **C 55** (2008) 553, arXiv:hep-ph/0711.2473

[261] L. Lonnblad and S. Prestel, "Matching Tree-Level Matrix Elements with Interleaved Showers",
JHEP **03** (2012) 019, arXiv:hep-ph/1109.4829

[262] ATLAS Collaboration. "Summary of ATLAS Pythia 8 tunes",
ATL-PHYS-PUB-2012-003 (2012); https://cds.cern.ch/record/1474107

[263] M. Krämer et al. "Supersymmetry production cross sections in pp collisions at $\sqrt{s} = 7\ TeV$"
arXiv:hep-ph/1206.2892, 2012

[264] C. Borschensky et al. "Squark and gluino production cross sections in pp collisions at $\sqrt{s} = 13, 14, 33$ and 100 TeV",
Eur. Phys. J. **C74.12** (2014) 3174; arXiv:hep-ph/1407.5066

[265] The ATLAS Collaboration. "Performance of the ATLAS fast simulation ATLFAST",
Tech. rep. ATL-PHYS-INT-2007-0-5. Geneva: CERN, 2007.

[266] W. Lukas, "Fast Simulation for ATLAS: Atlfast-II and ISF",
ATL-SOFT-PROC-2012-065 (2012), https://cds.cern.ch/record/1458503/files/ATL-SOFT-PROC-2012-065.pdf

[267] The ATLAS Collaboration, "Selection of jets produced in 13 TeV proton-proton collisions with the ATLAS detector",
ATLAS-CONF-2015-029 (2015), https://cds.cern.ch/record/2037702

[268] D. W. Miller, A. Schwartzman and D. Su. "Jet-Vertex Association Algorithm",
ATL-COM-PHYS-2008-008 (2008), https://cds.cern.ch/record/1082880

[269] The ATLAS Collaboration, "Expected sensitivity studies for gluino and squark searches using the early LHC 13 TeV Run-2 dataset with the ATLAS experiment",
ATL-PHYS-PUB-2015-005 (2015); https://cds.cern.ch/record/2002608/files/ATL-PHYS-PUB-2015-005.pdf

[270] Andreas Hoecker, "Physics at the LHC Run-2 and Beyond",
CERN-YELLOW-REPORT-CERN-2017-009-SP (2016); arXiv:hep-ex/1611.07864

[271] L. Moneta et al. "The RooStats Project", arXiv:physics.data-an/1009.1003 (2011)

[272] M. Backes et al. "Search for gluinos in events with isolated leptons, jets and missing transverse momentum at $\sqrt{s} = 13\ TeV$ with the ATLAS detector",
SUSY-2015-08 (2015); https://cds.cern.ch/record/2058272

[273] The ATLAS Collaboration, "Minimal representations of ATLAS experimental uncertainties",
ATL-COM-PHYS-2015-374 (2015); https://cds.cern.ch/record/2014656

[274] R. Beran, "Bootstrap methods in statistics",

Jber. d. Dt. Math. Verein 86, 14-30 (1984)

[275] The ATLAS Collaboration, "Measurement of top quark pair differential cross sections in the dilepton channel in *pp* collisions at $\sqrt{s} = 7$ and 8 TeV with ATLAS",

Phys. Rev. D. **94** (2016) 092003; arXiv:hep-ex/1607.07281

[276] M. Bahr et al. "Herwig++ Physics and Manual",

Eur. Phys. J. **C58** (2008) 639; arXiv:hep-ph/0803.0883

[277] S. Frixione and B. R. Webber, "Matching NLO QCD computations and parton shower simulations",

JHEP **06** (2002) 029, arXiv:hep-ph/0204244

[278] E. Bothmann, M. Schönherr and S. Schumann, "Reweighting QCD matrix-element and parton-shower calculations",

S. Eur. Phys. J. **C76** (2016) 590; arXiv:hep-ph/1606.08753

[279] The ATLAS Collaboration, "Measurement of W and Z Boson Production Cross Sections in *pp* Collisions at $\sqrt{s} = 13\ TeV$ in the ATLAS Detector",

ATLAS-CONF-2015-039 (2015); https://cds.cern.ch/record/2045487

[280] P. Kant et al. "HatHor for single top-quark production: Updated predictions and uncertainty estimates for single top-quark production in hadronic collisions",

Comput. Phys. Commun. **191** (2015) 74, arXiv:hep-ph/1406.4403

[281] C. Borschensky, M. Krämer, A. Kulesza, M. Mangano, S. Padhi, T. Plehn and X. Portell, "Squark and gluino production cross sections in pp collisions at $\sqrt{s} = 13$, 14, 33 and 100 TeV",

Eur. Phys. J. **C74** (2014) no.12 3174; arXiv:hep-ph/1407.5066

[282] The ATLAS Collaboration, "Measurements of top quark pair relative differential cross-sections with ATLAS in pp collisions at $\sqrt{s} = 7\ TeV$",

Eur.Phys.J. **C73** (2013) 2261, arXiv:hep-ex/1207.5644

[283] The ATLAS Collaboration, "Measurements of normalized differential cross-sections for $t\bar{t}$ production in pp collisions at $\sqrt{s} = 7\ TeV$ TeV using the ATLAS detector",

Phys.Rev. **D90** (2014) 072004, arXiv:hep-ex/1407.0371

[284] The ATLAS Collaboration, "Measurements of top-quark pair differential cross-sections in the lepton+jets channel in pp collisions at $\sqrt{s} = 8\ TeV$ using the ATLAS detector",

Eur.Phys.J. **C76** (2016) no.10, 538 arXiv:hep-ex/1511.04716

[285] The ATLAS Collaboration, "Measurements of the W production cross sections in association with jets with the ATLAS detector",

Eur.Phys.J. **C75** (2015) 82 arXiv:hep-ex/1409.8639

[286] The ATLAS Collaboration, "Search for gluinos in events with an isolated lepton, jets and missing transverse momentum at $\sqrt{s} = 13\ TeV$ with the ATLAS detector",

ATLAS-CONF-2015-076; https://cds.cern.ch/record/2114848 (2015)

[287] M. Czakon, D. Heymes and A. Mitov, "High-precision differential predictions for top-quark pairs at the LHC"

Phys. Rev. Lett. 116, 082003 (2016); arXiv:hep-ph/1511.00549

[288] M. Czakon, "A novel subtraction scheme for double-real radiation at NNLO"

Physics Letters **B** 693(3); arXiv:hep-ph/1005.0274 2010

[289] Alan Barr, Jesse Liu, "First interpretation of 13 TeV supersymmetry searches in the pMSSM",

arXiv:1605.09502 [hep-ph]

[290] The ATLAS Collaboration, "Search for squarks and gluinos in events with an isolated lepton, jets, and missing transverse momentum at $\sqrt{s} = 13$ TeV with the ATLAS detector",

Phys. Rev. **D96**, 112010 (2017); DOI:10.1103/PhysRevD.96.112010; arXiv:hep-ex/1708.08232